Open Charm Production in Inclusive and Diffractive Deep-Inelastic Scattering at HERA

Paul Thompson

Thesis submitted for the degree of
Doctor of Philosophy

June 1999

School of Physics and Space Research
Faculty of Science
University of Birmingham

Abstract

A measurement is presented of the total and differential cross sections for inclusive and diffractive $D^{*\pm}$ production based on an analysis of 1995, 1996 and 1997 data from the HERA experiment H1. The decay channel $D^{*\pm} \to K^{\mp}\pi^{\pm}\pi^{\pm}$ is used.

The measurement of the inclusive D^* cross section, which is the first to use the 1997 data sample, is found to be consistent with both the prediction of LO QCD based on the gluon distribution in the proton, and with published data which used a smaller data sample. For the measurement of the diffractive D^* cross section, the forward components of the H1 detector are used to select events on the basis of a large gap in the pseudo-rapidity distribution of final state hadrons adjacent to the leading proton. The cross section is measured in the diffractive kinematic range $M_Y < 1.6$ GeV, $|t| < 1$ GeV^2 and $x_{I\!P} < 0.04$, and is found to contribute around 5% to the inclusive D^* cross section. The normalisation of the diffractive cross section is a factor two to three smaller than the QCD prediction based on factorisable pomeron parton distributions obtained from a QCD fit to the H1 measurement of $F_2^{D(3)}$. However, the shape of the differential distributions for diffractive D^* production, which are measured for the first time, are well modelled by the factorisable pomeron model. The model is able to describe the shapes of the cross sections differential in final state hadronic variables which are sensitive to the mass of the diffractively scattered system.

A note on the author's contribution

The collaborative nature of experimental high-energy physics is such that the work presented in this thesis would not be possible without the input of very many people from the H1 collaboration. Here, I wish to acknowledge specific contributions from a number of people, more general acknowledgements are found at end of this thesis.

The basis for the D^* finding algorithm, used in the analysis, was written by Ben Waugh. The calibration of the forward detectors described in chapter 7 was performed in collaboration with Andrew Mehta. The invariant mass reconstruction method and noise suppression techniques were developed by Paul Newman, Andrew Mehta and Julian Phillips. All other features are the work of the author.

I am grateful to Paul Newman and Ian Kenyon for proof-reading all or part of this thesis, and for making many helpful suggestions.

A note on Units

In this work, a system of natural units will be used, whereby $\hbar = c = 1$

This work was supported financially by the UK Particle Physics and Astronomy Research Council (P.P.A.R.C).

Dedicated to

Asia

and

William.

Contents

1 The H1 Experiment **4**

1.1 Introduction 4

1.2 The HERA Accelerator 4

1.3 Overview of H1 5

1.3.1 Requirements for ep Scattering 5

1.3.2 The Layout of H1 6

1.4 Tracking 8

1.4.1 The Central Tracking Detector 9

1.4.2 The Forward Tracker 11

1.4.3 Backward Drift Chamber 11

1.5 Calorimetry 12

1.5.1 The Liquid Argon Calorimeter 13

1.5.2 The Tail Catcher 14

1.5.3 The Plug Calorimeter 15

1.5.4 SPACAL 15

1.5.5 Energy Calibration of the SPACAL 17

1.6 Muon Detectors 18

1.6.1 Instrumented Iron 18

1.6.2 Forward Muon Detector 18

1.7 Time-of-Flight Detectors 19

1.8 The Luminosity System 20

1.9 The Very Forward Detectors 21

1.9.1 The Proton Remnant Tagger 21

1.9.2 The Forward Proton Spectrometer 21

1.9.3 Forward Neutron Counter 22

1.10 Triggering and Data Acquisition 22

1.11 Trigger Sub-Systems 25

1.11.1 The SPACAL Trigger 25

1.11.2 The z-vertex Trigger 26

1.11.3 The Central Drift Chamber Trigger 27

2 HERA Physics **28**

2.1 Introduction 28

2.2 DIS kinematics 28

2.3 Proton Structure 31

2.3.1 The Quark Parton Model 32

2.3.2 Violation of Scaling and QCD Evolution 34

2.4 Low x Phenomenology 35

2.4.1 The DGLAP Evolution Formalism 35

2.4.2 The BFKL Evolution Formalism 37

2.4.3 The Gluon distribution at Low x 38

2.5 The Hadronic Final State 39

2.6 Monte Carlo Generators 40

2.6.1 Fragmentation Models 41

2.6.2 Hadronisation 42

2.7 Forward Energy Flow 42

2.8 Charm Production 45

2.8.1 Charm Production Mechanisms 45

2.8.2 The Charm Structure Function 46

2.8.3 Determination of the Gluon Density 49

2.9 Summary 54

3 Diffraction **56**

3.1 Introduction 56

3.2 Regge Theory 57

3.3 Structure of the Pomeron 61

3.3.1 Diffractive DIS Kinematics 61

3.3.2 Diffractive Structure Function 62

3.4 Dipole Models 68

3.4.1 A Two Gluon Exchange Model 69

3.4.2 A Semi-Classical Model 69

3.5 Soft Colour Interactions 72

3.6 The Hadronic Final State in Diffraction 72

3.7 Diffractive Charm Production Models 74

3.7.1 Definition of Variables 75

3.7.2 Factorisable Pomeron Predictions 75

3.7.3 SCI Predictions 77

3.7.4 Perturbative Two Gluon Exchange Predictions 78

3.8 Summary 79

4 Event Selection and Kinematic Reconstruction of DIS Events 80

4.1 Introduction 80

4.2 Selection of Quality Data 81

4.3 The Event Classification 83

4.3.1 Level 4 Downscaling 83

4.3.2 The 'Inclusive Final State' Event Class 83

4.4 The Analysis Sub-Trigger 85

4.5 Selection of DIS Events 86

4.5.1 The Electron Candidate 86

4.5.2 The $\sum(E - p_z)$ of the Final State 88

4.5.3 The Event Vertex 89

4.6 Kinematic Reconstruction 89

4.6.1 The DIS Kinematic Range 90

5 The Reconstruction of D^* Mesons 92

5.1 Introduction 92

5.2 The D^* Decay Mode 92

5.3 The Kinematic Range for D^* Cross Section Measurements 93

5.4 Monte Carlo Models for Charm Production 94

5.4.1 AROMA 94

5.4.2 RAPGAP 94

5.5 The Kinematics of the D^* in the Final State 95

5.6 Reconstruction of D^* Decays in the Central Tracking Detector 96

5.7 Determination of the Number of D^* Mesons 97

6 Measurement of the Inclusive D^* Cross Section **101**

6.1 Introduction 101

6.2 Calculation of the Cross Section ($ep \to eD^*X$) 101

6.3 Calculation of the 'Smeared' Acceptance - A_{tot} 102

6.4 Simulation of the Central Tracking Detector 108

6.4.1 Hit Multiplicities Per Track 108

6.4.2 Asymmetry in the Width of the ΔM Distribution as a function of ϕ 108

6.5 Efficiency of the Track Cuts 110

6.5.1 Distance of Closest Approach 111

6.5.2 Radial Track Length 112

6.5.3 Track Start 113

6.5.4 Combined Efficiency 114

6.6 Studies of Vertex and Track Reconstruction Efficiency 115

6.7 Evaluation of the Trigger Efficiency 116

6.7.1 Electron Trigger Efficiency 116

6.7.2 Track Trigger Efficiency 117

6.8 DIS Control Distributions 120

6.9 The Background Correction - r 122

6.10 Error Determination 123

6.11 Results 126

6.12 Stability of the Cross Section 126

6.13 Conclusion 127

7 Selection and Reconstruction of Diffractive Events 135

7.1 Introduction 135

7.2 Monte Carlo Models 136

7.2.1 RAPGAP 136

7.2.2 DIFFVM 137

7.2.3 AROMA 137

7.3 Large Rapidity Gap Event Selection 137

7.3.1 Separation of the System X and System Y 137

7.3.2 Final State Rapidity Distributions 138

7.3.3 The η_{max} cut 139

7.4 The Forward Detector Selection 140

7.4.1 Forward Detector Run Selection 142

7.4.2 Residual Noise in the Forward Detectors 142

7.4.3 The Forward Muon Detector (FMD) 142

7.4.4 The Proton Remnant Tagger (PRT) 143

7.4.5 The Liquid Argon Calorimeter 143

7.5 Performance of the Forward Detectors 144

7.5.1 Monte Carlo Comparison 147

7.5.2 Correction of the Proton Remnant Tagger Simulation 148

7.5.3 Performance History of the Proton Remnant Tagger 149

7.5.4 Correction of the Individual Scintillators 150

7.5.5 Overall Correction of the PRT efficiency 151

7.5.6 Summary of the Calibration 152

7.6 The Kinematic Range in M_Y and t 152

7.7 Kinematic Reconstruction 156

7.8 Summary 158

8 Measurement of the Diffractive D^* Cross Section **159**

8.1 Introduction 159

8.2 Calculation of $\sigma(ep \to e(D^{*\pm}X)Y)$ 159

8.3 Reconstruction of $z_{I\!P}$ 160

8.4 Evaluation of the Number of D^* Mesons - N_{obs} 161

8.5 Calculation of the 'Smeared' Acceptance - A_{tot} 161

8.6 Error Determination 162

8.7 Cross Section Result 164

8.8 Stability of the Cross Section Measurement 165

8.9 The Ratio to the Inclusive D^* Cross Section 165

8.10 Model Comparison 166

8.11 Conclusion 168

Introduction

The scattering of electrons from protons has been integral to the understanding of the structure of matter. Electrons have proved extremely useful probes, from a practical viewpoint because they are stable and so can be accelerated and stored indefinitely, and theoretically, because the interactions of the point-like electron are well described by the electroweak sector of the Standard Model [1].

High energy inelastic electron-proton scattering at SLAC [2], presented the first evidence of substructure of the proton. The inelastic cross section was observed to show only a weak dependence on the magnitude of the squared four-momentum transfer, Q^2, after factorising out the $1/Q^4$ photon propagator term. This was interpreted as being evidence for the scattering of the electron from point-like objects in the proton.

Within the Standard Model the proton consists of point-like spin-half *quarks* with fractional electric charge that interact with one another via the strong force. The strong force is described by the theory of Quantum Chromodynamics (QCD) which is mediated by the exchange of massless vector bosons, or *gluons*. In electron-proton scattering when the electron interacts with a quark of the proton directly, as opposed to the proton as a whole, the reaction is said to be *deeply-inelastic*. Deep-Inelastic Scattering (DIS) interactions are most often described in terms of Q^2 and the Bjorken scaling variable x. In the infinite momentum frame of the proton, x is interpreted as the fraction of the proton's momentum carried by the charged objects within the proton. For example, the structure of the proton is described most often in terms of the DIS *structure function* $F_2(x, Q^2)$. The evolution in x and Q^2 of the structure function of the proton provides an important test of QCD.

The most recently built facility for the study of electron-proton collisions is the Hadron Electron Ring Accelerator (HERA) located at the DESY laboratory in Hamburg, Germany. Operational since 1992, the HERA accelerator is the first to collide beams of electrons and protons and therefore achieves far larger centre of mass energies than fixed target experiments. This allows the proton structure function to be probed in new kine-

matic regions, in particular at low x and high Q^2. A further advantage of the HERA accelerator, over fixed target experiments, is that the hadronic final state can be measured in detail in DIS for the first time.

The production of charm quarks in the hadronic final state is an important tool for studying the gluon distribution of the proton because boson-gluon fusion is the dominant production mechanism for charm at HERA. For example, the tagging of charm quarks by reconstructing the decay of $D^{*\pm}$ mesons, via the chain $D^{*\pm} \to D^0\pi^\pm \to K^\mp\pi^\pm\pi^\pm$, allows a direct measurement of the gluon density of the proton. In this thesis, an analysis is presented of $D^{*\pm}$ production in DIS, the results of which are compared to a leading order QCD model based on the boson-gluon fusion mechanism and the gluon distribution in the proton.

Considerable interest has been generated by the observation at HERA of a class of DIS events in which there is a rapidity gap adjacent to the proton direction in which no hadrons emerge. These events must involve colour singlet exchange. Such processes are found to contribute significantly to high energy hadron-hadron and also photoproduction interactions, and have been successfully parameterised in terms of phenomenological Regge theory [3]. The dominant contribution to the cross section at high energy arises from the exchange of the *pomeron* - an object with the quantum numbers of the vacuum. Processes involving pomeron exchange are referred to as *diffractive*. When DIS events with rapidity gaps are selected the photon can be viewed as probing the structure of the pomeron rather than that of the whole proton. The study of diffractive scattering in DIS therefore offers the possibility to understand the partonic structure of the pomeron within QCD. For example, the simplest realisation of the pomeron in QCD is the exchange of two gluons in a net colour singlet state. The measurement and subsequent QCD analysis of the diffractive structure function [4], which is analogous to the proton structure function but for the pomeron, supports the hypothesis that gluons carry most of the pomeron momentum. In this thesis, an analysis is presented of $D^{*\pm}$ production in diffractive DIS and information about the gluon content of the pomeron is thus inferred.

Chapter 1 contains a brief description of the HERA accelerator, and a fuller review of the H1 experiment, which is built around one of the beam-crossing points. Chapter 2 presents a basic overview of the physics topics investigated at HERA, with emphasis on DIS and the measurement of the hadronic final state. In particular, it is explained how tagging charm quarks in the final state leads to a direct measurement of the gluon content of the proton. Chapter 3 contains a discussion of diffractive scattering, detailing the importance of measuring charm in the final state to reveal the gluon structure of the pomeron.

In chapter 4 the method of kinematic reconstruction and data selection for DIS events used in the analyses subsequently performed in the thesis are discussed. Chapter 5 is concerned with the tagging of charm by reconstructing the decay products of D^* mesons in the H1 tracking detector. Chapter 6 presents the measurement of the inclusive total and differential D^* cross sections using H1 data from the 1995, 1996 and 1997 running periods. In chapter 7, the experimental techniques used in the selection and kinematic reconstruction of diffractive events are described. In chapter 8, the total and differential cross sections for D^* meson production in diffractive DIS are presented.

Chapter 1

The H1 Experiment

1.1 Introduction

H1 is one of the two experiments, located at one of the four interaction points of the HERA accelerator, which is devoted to the study of the collision of electrons with protons. The first part of this chapter is devoted to a brief description of the HERA accelerator, the requirements in the design of the H1 detector, and a description of its layout. The second part will entail a more detailed discussion of the components of H1 divided as follows; tracking, calorimetry, muon detectors, time-of-flight detectors, the luminosity measurement system, the very forward detectors and triggering and data acquisition. Finally, the sub-trigger systems used in the analysis presented in this thesis are described.

1.2 The HERA Accelerator

The electron and proton beams are accelerated and stored in separate beam lines in a tunnel of 6.3 km circumference. The electrons can be accelerated to 30 GeV with conventional magnets, however the 820 GeV[1] protons require super-conducting magnets to produce the required 4.6 T field. The cross section for ep interactions is small and so very high fluxes of electrons and protons are required. The electrons, with a typical current of around 30 mA, and the protons, with a current of around 80 mA, are stored in bunches which are collided. The bunch crossing interval is 96 ns. The design maximum luminosity producible is 1.4×10^{30} cm^{-2}s^{-1}.

Some bunches are left empty so that a proton or electron bunch may arrive in the detector

[1]Since 1998 the HERA accelerator has operated with 920 GeV protons.

without an interaction partner. These 'pilot' bunches are used to estimate backgrounds coming from beam interactions with residual gas in the beam-pipe ('beam-gas') and those from collisions with the beam-wall and other apertures ('beam-wall'). Beam-gas interactions occur typically at a rate of greater than 10 kHz.

1.3 Overview of H1

1.3.1 Requirements for *ep* Scattering

Because the H1 detector is designed to study a wide range of physics processes occurring in ep scattering, it was built to satisfy certain basic requirements. In DIS physics, where electrons of moderate Q^2 are scattered in the backward[2] direction, a high efficiency for identification and good resolution of the scattered electron is of paramount importance, because the angle and energy of the electron are often used to calculate the kinematical variables x and Q^2. A high resolution measurement of the electron, extending to scattering angles as small as possible, will increase the acceptance and decrease the systematic uncertainty for low x and low Q^2 measurements of the proton structure function. Further instrumentation is also necessary downstream in the electron direction, to detect electrons scattered through very small angles. Such electrons are used for the measurement of the luminosity and photoproduction ($Q^2 \sim 0$) processes.

It is essential that the calorimetry is hermetic in order to measure missing transverse energy, which is the signature for charged current[3] DIS events. This calorimetry must have high granularity if a good reconstruction of the final state is to be made. This is crucial, for example, in the measurement of hadron jet angular distributions and profiles of hadrons within the jet. High resolution tracking detectors with the largest angular coverage possible, located in a magnetic field, are required for the measurement of charged particle momentum, particle multiplicities and particle identification through the rate of energy loss. The tracking and calorimetry can be seen as partly complementary since neutral particles, undetected in the tracking chambers, will have their energy measured in the calorimeter. Low momentum charged particles, poorly resolved in the calorimeter, will have small radii of curvature in the tracking system and hence will be well measured. Muon detection over the full solid angle is required for the detection of heavy flavour processes and the search for new and exotic particle production. Enhanced detection in the forward direction is required because the density of final state particles is a maximum

[2] At H1, the direction from the interaction point is referred to as forward (backward) in the direction of the proton (electron) beam.

[3] See section 2.2 for a description of charged current interactions.

there due to the asymmetry in the beam energies. Detectors in the forward region are also utilised, although they are not always specifically designed for the purpose, to detect diffractive[4] processes, where the activity close to the beam-pipe in the proton direction must be measured.

The experiment must also be able to distinguish ep interactions from the large backgrounds present. As well as beam-gas and beam-wall backgrounds there is background originating from cosmic rays. With such a high background rate and short time interval between bunch crossings the development of a sophisticated trigger system is essential to minimise the deadtime[5] in the experiment.

1.3.2 The Layout of H1

The layout of the main components of the H1 detector is shown in figure 1.1. Around the interaction point are the tracking systems, consisting of the central [2], and forward [3] trackers. The SPACAL electromagnetic and hadronic calorimeter [12] is located around the beam-pipe in the backward direction. The Liquid Argon (LAr) calorimeter, with both electromagnetic [4] and hadronic [5] sections, is situated outside the trackers and extends round to cover the space in front of the forward tracker. The plug calorimeter [13] extends the range of the forward calorimetry closer to the beam-pipe. A superconducting coil [6], of radius 3 m, loops around the LAr calorimeter and provides a field of 1.15 T along the tracking region. The field fluctuations are of the order of 1% and are more pronounced at the ends of the magnet, i.e. in the region of the forward tracker. The iron return yoke of the magnet [10] is instrumented with streamer tubes and detects muons, which leave only minimum ionization in the calorimeter, and also measures the leakage of hadrons from the hadronic calorimeters. The forward muon detector [11] identifies and measures the momentum of penetrating muons in the forward direction through the use of drift chambers and a toroidal magnet.

As described in figure 1.1, at H1, a right handed co-ordinate system is used with the origin at the interaction point. Positive z is defined as being along the proton beam direction and y vertically upwards. The positive z axis corresponds to $\theta = 0$, and the positive x axis to $\phi = 0$ when using cylindrical polar co-ordinates.

[4] See chapter 3 for a description of diffraction.
[5] See section 1.10 for a discussion of the trigger system and the concept of deadtime.

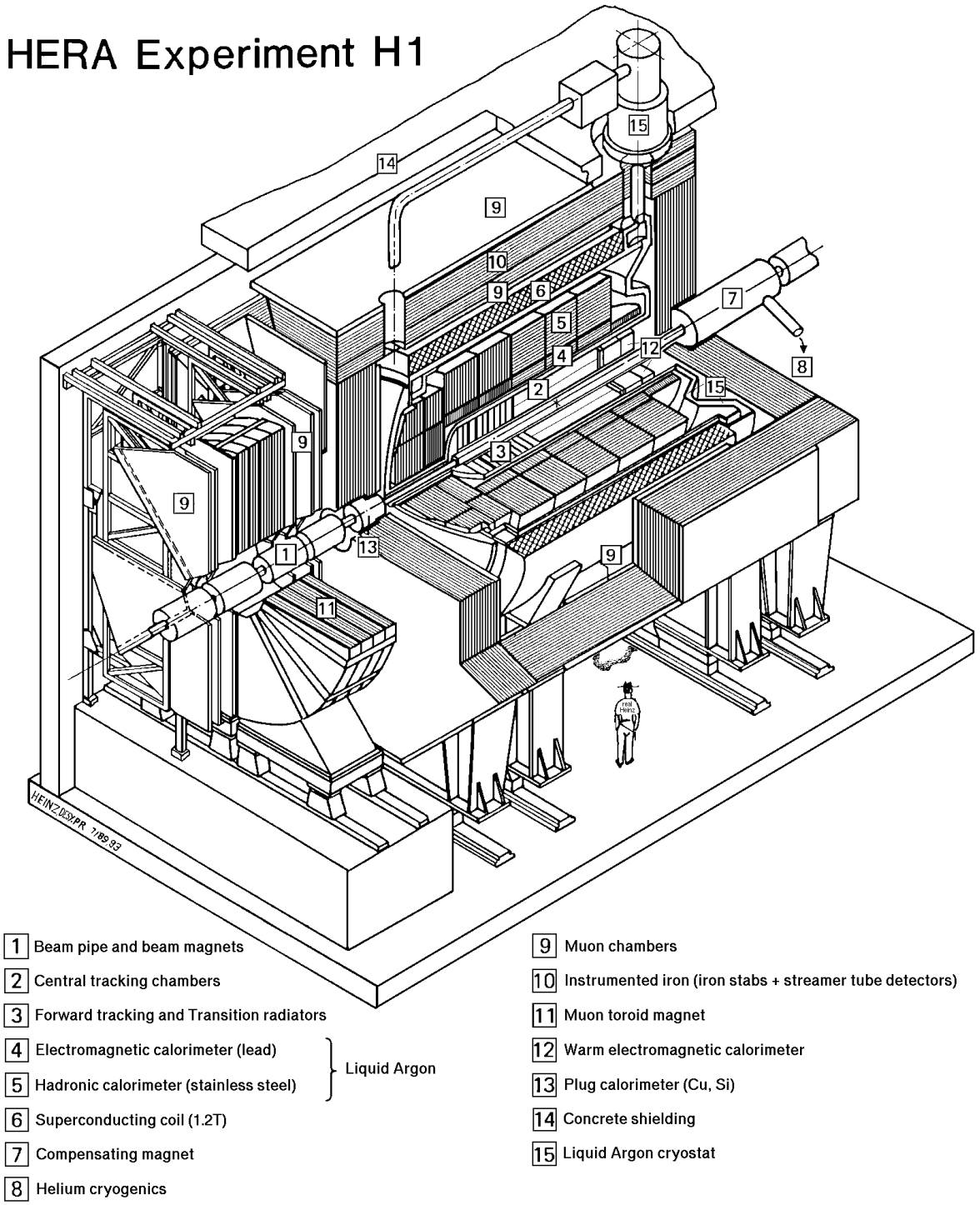

Figure 1.1: A view of the H1 detector. The co-ordinate system is defined as having the $+z$ axis along the proton (forward) direction. The protons in this picture travel from right to left.

1.4 Tracking

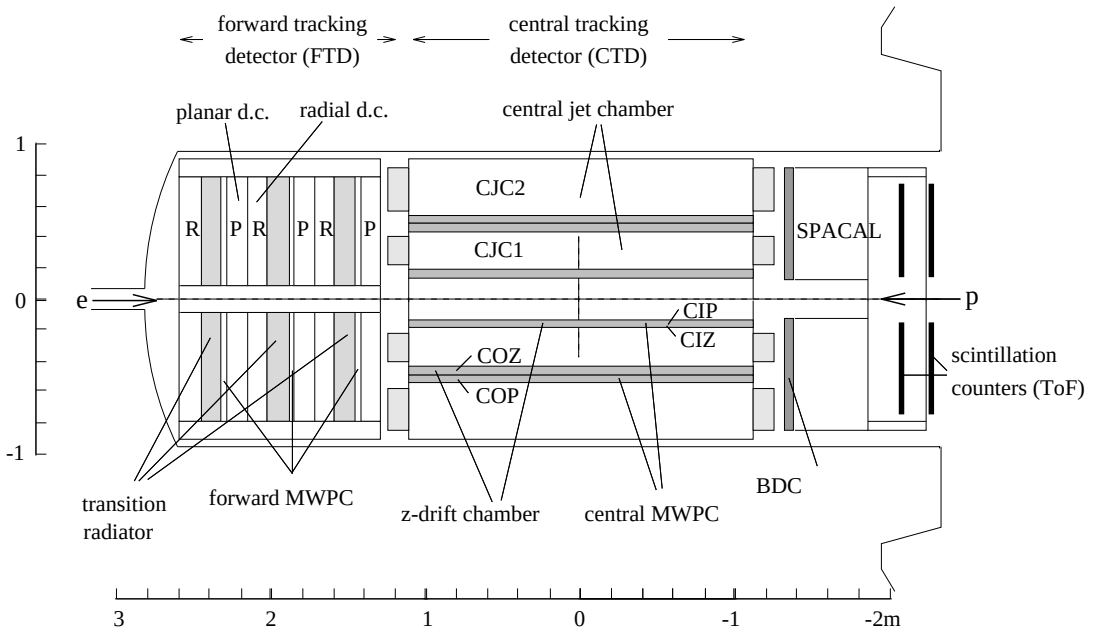

Figure 1.2: A cross-sectional view of the H1 tracking system, showing the central and forward trackers, and the BDC.

The tracking system at H1 utilises two main types of tracking detector, multi-wire proportional chambers (MWPCs) and drift chambers. The former consist of many anode wires lying between cathode pads, with the volume in between filled with gas and spanned by an electric field. A charged particle passing through the chamber causes ionization of the gas with the electric field being strong enough, near the wire, to cause rapid amplification of the initial ionization. The charge induced on the sense wire is *proportional* to the initial ionization. The signal on an individual wire, due to the avalanche around it, is not shared by other wires, which allows a position measurement to be made. The spatial resolution is limited by the wire spacing and more accurate measurements can be made using drift chambers. However the maximum drift distance in a MWPC is short, with the signal arriving a few nanoseconds after the particle traverses the chamber. For this reason they are used primarily for trigger information.

A drift chamber employs a set of alternate, widely spaced, anode and cathode sense wires strung between cathode plates, or a series of field shaping wires, which aim to create a uniform electric field between the sense wires. After a charged particle passes through the chamber and causes ionization in the gas, the resulting electrons move at near constant velocity towards the anode. If the drift velocity is known, the time taken for the signal to reach the wire can be used to determine the position of the initial ionization. In H1, the digitization of the signal induced on the sense wires is performed by Flash Analogue

to Digital Converters (FADCs), with sampling frequencies of 104 MHz. Hence resolutions are of the order of a few nanoseconds on the times of arrival of the pulses. The typical drift velocity is 50 μm ns^{-1} which means the distance in the drift direction is known to $100 - 200$ μm. Also, since the sub-detectors are given 24 bunch crossings (2.3 μs) to provide information to the central trigger, the maximum drift distance is restricted to be around 10 cm.

By constructing multiple layers of drift cells staggered relative to one another, detailed reconstruction of the trajectory of a charged particle, without an ambiguity as to which side of the sense wire the particle passed, is possible. The location of the hit in the direction of the sense wire can be inferred by charge division to $1-2$ % of the wire length, if it is read out at both ends. The momentum is measured from the curvature of the particle in the magnetic field, and particle identification can be performed from the loss of energy with distance travelled (dE/dx).

The tracking system of H1 is divided into three systems, shown in figure 1.2, providing charged track information in the pseudo-rapidity[6] range $-3 < \eta < 2.8$. The central tracking detector (CTD) covers the angular range of $15 < \theta < 165^{o}$, the forward tracking detector (FTD) the range $7 < \theta < 25^{o}$ and the backward drift chamber (BDC) covers the range $153 < \theta < 177.5^{o}$. The forward and central trackers use a combination of multi-wire proportional chambers (MWPCs) and drift chambers, for triggering and momentum measurement respectively.

1.4.1 The Central Tracking Detector

A cross-section of the Central Tracking Detector (CTD) in the $r - \phi$ plane is shown in figure 1.3. It consists of six chambers in total which are housed in an aluminium tank. These chambers are, from inside out, the Central Inner Proportional Chamber (CIP), the Central Inner z Chamber (CIZ), the inner Central Jet Chamber (CJC1), the Central Outer z Chamber (COZ), the Central Outer Proportional Chamber (COP), and the outer Central Jet Chamber (CJC2).

The main components are the largest two concentric drift chambers, CJC1 and CJC2 [5]. Their sense wires run parallel to the beam to give best measurement in the $r - \phi$ plane. CJC1 has 30 cells with 24 sense wires each, whilst CJC2 has 60 cells each containing 32 sense wires. Each cell is inclined by 30^{o} to the radial direction meaning that ionization electrons drift almost perpendicular to high momentum particles, tracks of all momenta

[6]Pseudo-rapidity is defined as $\eta = -\ln(\tan(\theta/2))$.

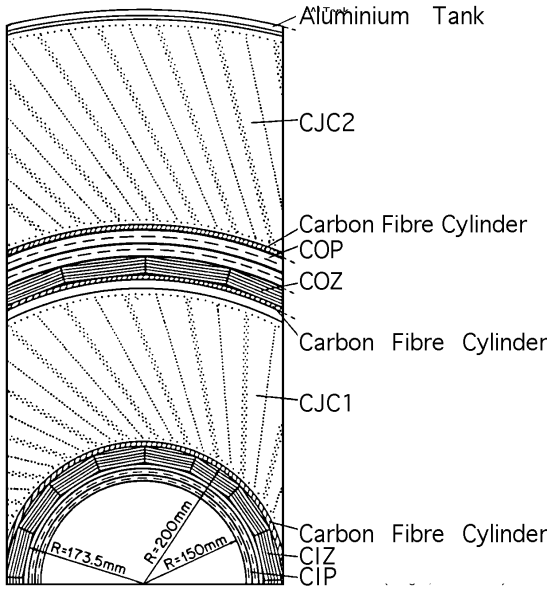

Figure 1.3: The Central Tracker. A view in the $r-\phi$ plane.

are sampled a number of times, and drift ambiguities are resolved. Drift time and charge division measurements achieve space-point resolutions in the the $r-\phi$ and z planes of 170 μm and 2.5 cm respectively.

The track recognition in the CJC is based mainly on the more precise $r-\phi$ information. The track parameters are constrained by imposing a common interaction vertex requirement. The tracks which fail this requirement are assigned either to secondary vertices (restricted to decays of neutral particles into a pair of oppositely charged particles) or to non-vertex fitted tracks which are attributed to cosmic muons or other sources of background. The z information of the tracks is greatly improved by the procedure of fitting all tracks to a common vertex and the resulting precision of the vertex determination in the z plane is around 1 cm. The CJC trigger is explained in section 1.11.3.

To obtain a better measurement in the z direction there are two sets of drift chambers, each with four layers of sense wires running perpendicular to the beam-pipe in the $r-\phi$ plane, such that the ionization drifts in the z direction. The Central Inner Z chamber (CIZ) and the Central Outer Z chamber (COZ) [6] cover the polar angular ranges $16 < \theta < 169^{\circ}$ and $25 < \theta < 156^{\circ}$ respectively. The z co-ordinate, calculated from drift time, has an internal hit resolution of $200-500$ μm. The vertex fitted tracks recognised in the CJC are supplied with information from the z chambers. As a result, the vertex resolution

is improved to 2 mm and the measurement of θ for individual tracks is improved from 20 mrad to 2 mrad. The combined track measurements of the four chambers give a design resolution on the momentum of charged tracks of $\Delta p/p^2 \sim 3 \times 10^{-3}$ GeV^{-1}, with a double track resolution of 2.5 mm.

The CTD also contains two MWPCs for triggering on tracks pointing to the nominal vertex region in the z plane. They are the Central Inner and Outer Proportional chambers (CIP and COP) [7]. The CIP is the innermost component of the central tracker whereas the COP is situated immediately inside CJC2. The CIP and COP both consist of double layers, with wires parallel to the z-axis. The angular coverage of the CIP is $9 < \theta < 171^o$ and is composed of 60 sectors of 36.5 mm in the z direction and 8 sectors in ϕ. The COP has an angular acceptance of $25 < \theta < 155^o$ and consists of 18 sectors of length 12.1 cm and 16 sectors in ϕ. They have no impact on the final track measurement but provide fast space-point information with a timing resolution better than the 96 ns between bunch crossings. The information from the CIP and COP is combined with that from a MWPC in the forward tracker to produce the z-vertex trigger (see section 1.11.2). The requirement of a vertex in the interaction region along the z axis can be a powerful way to reject background and is incorporated in the majority of physics triggers.

1.4.2 The Forward Tracker

The Forward Tracking Detector (FTD) [8], shown in figure 1.2, consists of three identical *supermodules* arranged along the z axis. Each supermodule consists, in increasing z, of twelve layers of planar drift chambers, a section of MWPCs, transition radiators and twelve layers of radial drift chambers.

The planar drift chambers, with wires in the $r-\phi$ plane, are offset from one another by 60^o in ϕ, so that a spatial measurement can be made. Each layer of the radial drift chambers consist of 48 radial sense wires, allowing an accurate measurement of the azimuthal angle, ϕ. A cruder measurement of the radial co-ordinate can be made from charge division, by reading out both ends.

1.4.3 Backward Drift Chamber

The Backward Drift Chamber (BDC) [9] is designed to provide an accurate measurement of the angle of the scattered electron in DIS processes with $Q^2 < 100$ GeV^2. It is mounted in front of the SPACAL calorimeter and has a similar angular acceptance $153 < \theta <$

177.5°. The BDC detector consists of four double-layer drift chambers mounted along the z direction, each of octagonal shape. The sense wires are strung along the octagonal shape, which produces an almost radial drift direction, such that the resolution in the polar angle θ is optimised. Each signal wire is contained in its own cathode cell. The wires in each double layer are shifted by half a cell width with respect to one another in order to resolve the left-right ambiguity of the drift origin. The double layers are rotated by 11.25° with respect to one another in order to obtain some measurement of the ϕ coordinate. The wire spacing decreases towards the inner region of the chambers in order to provide a uniform resolution in θ. The resolution of the BDC for the measurement of the scattering angle of the DIS electron, determined using the CJC as reference, is better than 1 mrad, with the systematic shift estimated to be below 0.5 mrad [10].

1.5 Calorimetry

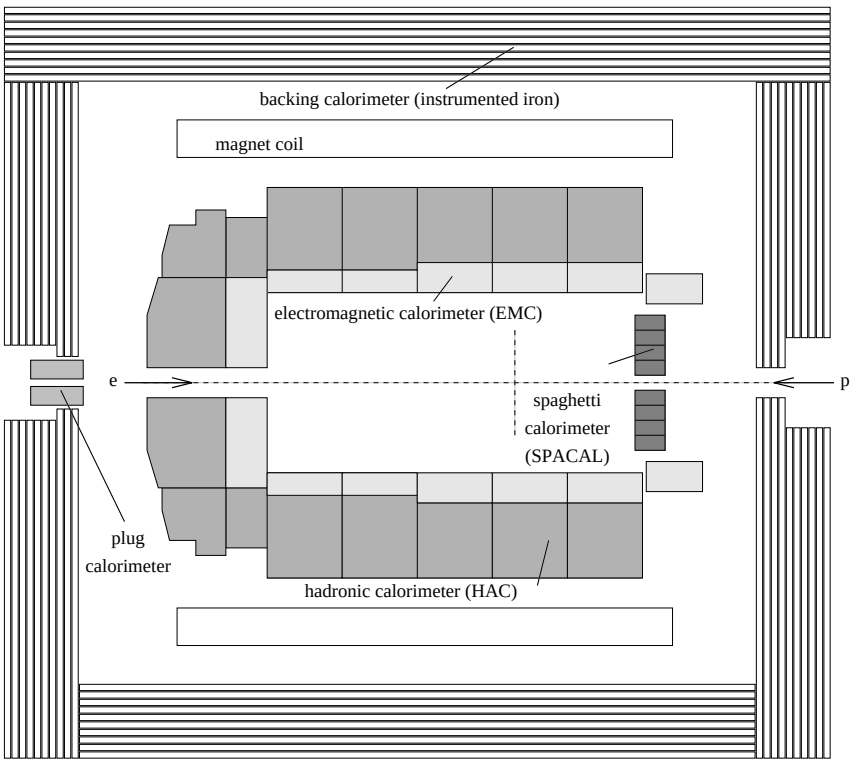

Figure 1.4: The H1 calorimetry system. It shows the LAr calorimeter, consisting of electromagnetic (EMC) and hadronic (HAC) parts, the backward electromagnetic and hadronic calorimeter SPACAL, the surrounding tail catcher (instrumented iron) and the plug calorimeter.

Figure 1.4 shows the layout of the four calorimetry units at H1. The combined coverage offered by the main two calorimeters, SPACAL and LAr, amounts to a laboratory pseudo-rapidity range of $-3.8 < \eta < 3.6$. The Plug calorimeter extends the acceptance in the

forward region and the instrumented iron, or tail catcher, measures energy leakage from the main calorimeters.

The measurement of energy in the calorimetry is achieved by layers of passive material (known as the absorber), where the incident particle loses energy by producing a cascade or 'shower' of other particles, interspersed with sample material where the energy deposition is measured. When an electromagnetic particle, that is an electron or photon, passes through an absorber, it rapidly loses energy through a combination of bremsstrahlung ($e \rightarrow e\gamma$) and pair production ($\gamma \rightarrow ee$) processes. The additional particles thus created undergo the same reactions, quickly generating a cascading shower of particles. The number of particles produced in the shower is proportional to the incident energy of the particle. Therefore, if the shower is fully contained within the calorimeter, a measurement of the total ionization reaching the sampling material will facilitate a measurement of the incident particle's energy. The characteristic length of the interaction of an electromagnetic particle and a material is given by the radiation length, X_0, which is the mean distance in which it loses all but $1/e$ of its initial energy in that material.

When a strongly interacting particle passes through matter, both elastic and inelastic scattering between the incident hadron and the nucleons occur. This results in secondary hadrons being produced which initiate a shower. The characteristic length assigned to this process, analogous to X_0, is the interaction length, λ, which is typically much larger than X_0 (for example, in lead $\lambda \sim 20\ X_0$). The less frequent sampling necessary for hadronic calorimeters degrades their resolution with respect to electromagnetic calorimeters.

The different shower developments for incident electromagnetic and hadronic particles results in different amounts of energy detected in the calorimeter relative to the energy of the incident particle. The calorimeter is said to be *non-compensating*. Typically, the energy response to hadronic particles is around 30% lower than that to electrons or photons. The majority of the energy in hadronic showers is lost through excitation or the break up of nucleons in the absorber. In addition, a hadronic shower typically contains both hadronic and electromagnetic components because any neutral pions produced in the shower decay into photons and initiate an electromagnetic shower as described above. Therefore, a correction has to be applied in the reconstruction of hadronic clusters.

1.5.1 The Liquid Argon Calorimeter

The study of the final state hadrons, and the measurement of scattered electrons in very high Q^2 (> 100 GeV^2) events is performed using the liquid argon (LAr) [11] calorimeter.

The calorimeter comprises electromagnetic (EMC) and hadronic parts (HAC), both using a single liquid argon cryostat. All of the LAr is situated within the solenoid magnet to reduce the amount of dead material encountered by particles before they reach the calorimeter. It is divided into 8 wheels in z, each of which is divided into, depending on ease of handling and accessibility, six to eight ϕ octants. The total range of angular coverage is $3 < \theta < 154^{o}$. The wheel situated at the most backward point is purely electromagnetic. All other wheels have hadronic and electromagnetic sections.

Liquid argon is used as the sampling material because of its high atomic density which results in large ionization. There is also the benefit that the probability for further inelastic collisions of the electrons and ions with the atoms of the liquid argon is reduced because argon is a noble gas. The lead absorption plates in the EMC are 2.4 mm thick, with comparable thickness for the LAr cells. The stainless steel absorption plates in the HAC are 16 mm thick with 5 mm of sampling material. The charge produced from the ionized atoms is collected on cathode pads resulting in around 45 000 read out channels. The granularity of the cells is designed to provide approximate uniformity in laboratory pseudo-rapidity. The thickness of the LAr varies due to the inherent asymmetry of the collisions at HERA, with the EMC varying between 30 and $20X_0$ in the forward and backward directions, and the combined HAC and EMC between 4.5λ and 8λ.

Tests of the energy resolution for single particles has been performed in test beam measurements. The energy resolution for electrons, in the EMC, is $\frac{\sigma(E)}{E} \sim \frac{0.12}{\sqrt{E}} \oplus 0.01$, with E in GeV, and that for hadrons, from both the EMC and HAC, is $\frac{\sigma(E)}{E} \sim \frac{0.50}{\sqrt{E}} \oplus 0.02$. By comparing the momentum measurement of electrons using the tracking chambers with the corresponding energy deposits in the LAr calorimeter in ep data, the electromagnetic scale is known to the level of 3%. The hadronic energy scale of the LAr calorimeter is determined with an uncertainty of 4% by studying the balance in transverse momentum ($p_{\perp}$) between the scattered electron and the hadronic particles in high Q^2 DIS events.

1.5.2 The Tail Catcher

The instrumented iron of the return yoke of the magnet is used to provide a coarse measurement of the energy of hadronic showers leaking out of the LAr. The instrumented iron is divided into three sections: the central barrel region, the forward and backward end caps. Each section has 16 layers of limited streamer tubes and 11 of these are used to detect ionization for the tail catcher. The energy resolution is 100% with a scale uncertainty, determined from cosmic muon data, of around 35%.

1.5.3 The Plug Calorimeter

The Plug Calorimeter closes the gap in acceptance between the LAr calorimeter ($\theta \sim 4^o$) and the beam-pipe ($\theta \sim 0.3^o$), see figure 1.4. The range in pseudo-rapidity covered is $3.5 < \eta < 5.0$. It comprises nine layers of copper with eight sampling sheets of silicon. The energy resolution is limited by the coarse sampling and the incomplete containment of showers, and is estimated to be $1.50/\sqrt{E\ (\mathrm{GeV})}$ [12].

1.5.4 SPACAL

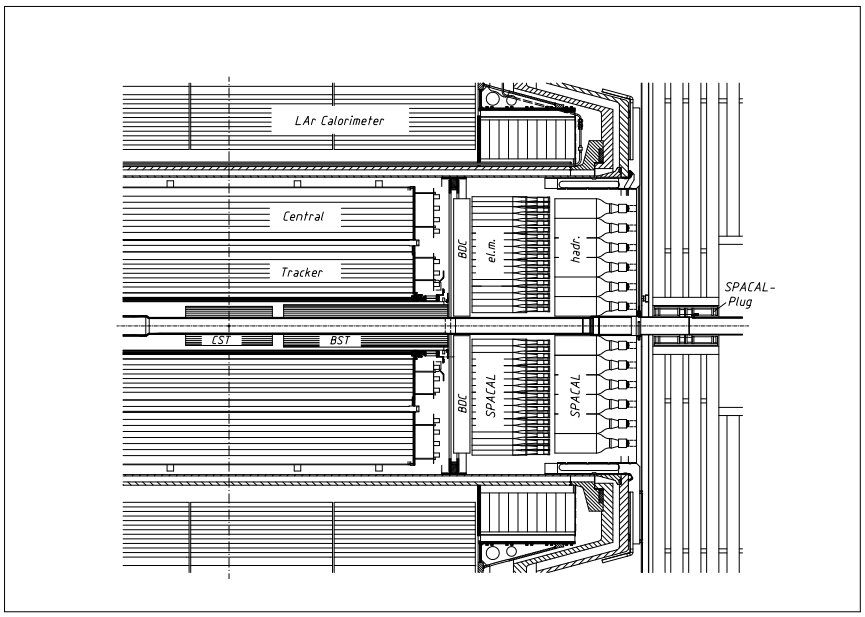

Figure 1.5: Side view of part of the H1 detector showing the location of the SPACAL sections.

The design of the SPACAL calorimeter [13], shown in figure 1.5, gives efficient electron identification and good measurement of the electron energy and angle. It also provides a measure of the hadronic energy in the backward direction and time-of-flight information in order to reject photoproduction, beam-gas and beam-wall backgrounds. The acceptance in the angle of the scattered electron in the SPACAL is $153 < \theta < 177.5^o$ corresponding to Q^2 values in the range $1 \lesssim Q^2 \lesssim 100$ GeV^2. The proximity of the calorimeter to the beam-pipe provides the possibility to measure very low x ($x \lesssim 10^{-5}$) events.

The active region of the SPACAL consists of lead sheets with grooves in which scintillating fibres are laid. The incident particles shower in the lead causing the fibres to scintillate. The light is collected at one end of the fibres by a photomultiplier tube. The electron identification is enhanced, and a measurement of the hadronic energy facilitated, by the

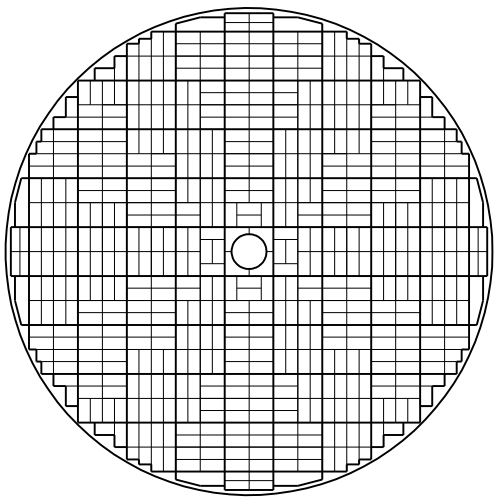

Figure 1.6: An $r-\phi$ sectional view of the electromagnetic part of the SPACAL calorimeter. The individual cells, each with their own photomultiplier, are joined together to form two-cell structures, shown by thin lines. These are then combined into the 16 cell modules, the thick lines mark the borders, which are mounted around the beam-pipe.

division of the calorimeter into two separate parts, electromagnetic (EM) and hadronic (HAD). The resulting probability of misidentifying an electron as a pion is less than 1 in 100 at energies of 5 GeV.

The electromagnetic section consists of 1192 cells of lateral dimension 40.5×40.5 mm^2. This is larger than the average radius of an electromagnetic shower in the material which is 25.5 mm. Each cell is constructed from 26 grooved lead plates interspersed with 2340 scintillating fibres 0.5 mm in diameter. Due to the small fibre size there is a high sampling frequency which leads to an energy resolution for the EM section of $\frac{0.07}{\sqrt{E(\mathrm{GeV})}} \oplus 0.01$ [14] as parameterised in test beam measurements. The spatial resolution of the calorimeter in the transverse plane was measured to be 3.4 mm. The region surrounding the beam-pipe is filled by an insert module with non-standard cell geometries and an 8 mm lead/fibre veto layer which allows identification of energy leakage from the insert cells into the beam-pipe.

The scintillation light of each cell is guided into its own photomultiplier tube (PMT) and converted into an electric pulse to be read out. The total of 1192 cells are combined into 16-cell modules, which are the building blocks for mounting around the beam-pipe, and this is shown in figure 1.6. The use of PMTs, combined with low noise in the electronics, permits a very low energy threshold for triggering and a reliable reconstruction of small energy deposits. The time resolution of the PMTs of around 1 ns allows the trigger to

veto non-ep background (see section 1.11.1). The cells are 250 mm deep with a lead/fibre ratio of 2.3:1, which corresponds to approximately 27 radiation lengths and 1 hadronic interaction length.

The hadronic section is based on a similar design to the EM section with lead scintillating fibres but with a larger diameter of 1 mm. There are 136 cells of typical dimension 119.3×119.3 mm^2 which reflects the greater lateral dimensions of hadronic showers. The ratio of lead:fibre is 3.4:1 and the hadronic section adds on another interaction length to the one interaction length provided by the electromagnetic section alone. The hadronic resolution of the combined HAD and EM calorimeter is $0.3/\sqrt{E(\mathrm{GeV})}$. The acceptance of the HAD section is increased to 178.7° by a backward plug section, comprising 12 cells, located around the beam-pipe in the return yoke.

1.5.5 Energy Calibration of the SPACAL

The SPACAL calorimeter is calibrated in order to determine the absolute energy scale, which is vital for the correct reconstruction of the event kinematics. The calibration is performed using the double angle (DA) kinematic reconstruction method [15] where the electron energy, E_{DA}, is determined from the polar scattering angle, θ_e, of the electron and the polar angle, γ_h, of the current jet. The advantage of the DA method is that, to first order, the reconstruction of the event kinematics is independent of the energy calibration of the detector. The calibration [16] consists of an iterative procedure in which the energy of each cell in an electron cluster is successively brought to convergence with that measured by the DA method. Additional corrections are necessary in the data and simulation to achieve homogeneity in the response of a given cell at the cell borders and cracks between the cell modules. The calibration is checked independently at large electron energies (to an accuracy of 0.5%) by analysis of the position and shape of the maximum in the measured electron energy spectrum, referred to as the 'kinematic peak' [10].

The linearity of the SPACAL calorimeter (i.e. the relationship between the energy deposited and the energy measured) is investigated using the double angle method for QED-Compton events ($ep \to ep\gamma$) [17]. The measurement of the azimuth and polar angles of the electron and photon are used to predict their energies. The difference between the data and the simulation is used to gauge the absolute uncertainty in the energy scale. It is found for the 1995 data to be 3% at 8 GeV and 1% at 27.5 GeV, with a linear interpolation between the minimum and maximum energies. The uncertainty reflects the known systematic uncertainties in the reconstruction of angles as well as the dead material before the calorimeter. Other methods employed for calibration include using cosmic

muons [18], proton beam-halo muons [19] as well as π^o decays [20].

The internal calibration of the cells of the hadronic SPACAL is performed using cosmic muon data [18]. The absolute scale is investigated by the energy response to individual hadronic particles whose momentum are measured in the CJC and by comparison of the data with the simulation for the global energy flow in an event [16].

1.6 Muon Detectors

1.6.1 Instrumented Iron

The instrumented iron of the return yoke of the magnet as used in the Tail Catcher is also used to detect muons. The reconstruction efficiency for muons, gauged from cosmic muon studies, is around 90% for momenta above 2 GeV. The central muon trigger [21] divides the system up into inner and outer, forward and backward endcap regions and forward and backward barrel regions. It uses coincidence information from 5 of the 16 layers in each of the six regions to search for track segments. It requires a signal in at least 3 of the 5 layers for all regions except the forward inner endcap, where the particle rate is highest, due to the proximity of the outgoing proton beam. In this case the requirement is that 4 out of 5 layers fire.

1.6.2 Forward Muon Detector

To aid the triggering and reconstruction of muons in the highly active forward region the Forward Muon Detector (FMD) [22] is situated beyond the return yoke and is shown in figure 1.7. It has an angular coverage of $3 < \theta < 17°$. It comprises six double layers of drift chambers, four with wires strung tangentially around the beam-pipe to measure θ and two with wires strung radially to give a ϕ measurement. Three double layers are situated either side of a toroidal magnet, designed to bend the muons to allow momentum measurement in the range $5 < p < 100$ GeV. The lower limit is set by multiple Coulomb scattering, where the fact that a muon loses on average 3 GeV of energy in the main body of the detector and 1.5 GeV in the toroid is taken into account. The upper bound is set by the degree to which a particle track can be bent in the magnetic field. The drift cells are 20 mm deep and 120 mm wide with the sense wire located in the middle. The spatial resolution of the drift cells is of the order ~ 250 μm from drift time and ~ 4 cm from drift charge division. By placing two layers of cells together, staggered from one another by half a cell, the efficiency compared to a single layer can be improved and the ambiguity

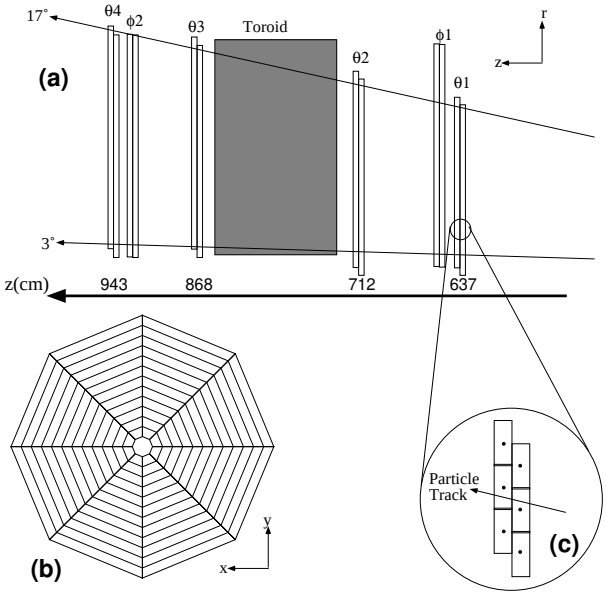

Figure 1.7: The Forward Muon Detector. (a) An $r-z$ projection showing the 6 pre and post toroid layers. (b) The $x-y$ projection of a theta layer. (c) An exploded view of the drift cells comprising two sub-layers.

as to which side of the sense wire a particle passed is eliminated. As shown in figure 1.7c, a charged particle leaves a pair of hits in the two layers of drift cells. The pairs of hits are linked to those in other layers on the same side of the toroid to form track segments. To produce full tracks the segments from before and after the toroid are linked.

The Forward Muon Trigger (FMT) [23] uses the theta layers of the FMD to provide a fast validation of any tracks passing through it. Only pairs of hits which can be extrapolated to the interaction vertex[7] are used to form pre and post toroid track segments.

1.7 Time-of-Flight Detectors

There are numerous simple, but essential, systems located in H1 which reject background events using time-of-flight (ToF) information. The ToF systems work on the principle that the time of arrival of particles from the interaction region, at a particular point in the detector, differs from that of particles from beam-induced processes. Therefore, the positioning of devices with good intrinsic timing resolution in the detector allows the discrimination of events coming from the interaction region from other backgrounds.

[7]Pairs of hits originating from non-vertex events will have a steeper slope in the $r-z$ plane.

The ToF systems, constructed from plastic scintillator, are located, near the beam-pipe, in the backward endcap of the return yoke (BToF), within the PLUG calorimeter (PToF) and near the FMD (FToF). In addition, the 'Veto Wall', a double set of scintillators positioned backward of the return yoke, detects particles from the proton beam-halo, which are mostly muons caused by inelastic collisions of the protons with the residual gas or the accelerator hardware well downstream of the detector. The time-of flight information from the SPACAL calorimeter, which is located close to the beam-pipe, is also used to reject background and is described in section 1.11.1.

1.8 The Luminosity System

The accurate determination of the luminosity is essential for the precise measurement of physics cross sections. The luminosity system [24], situated in the accelerator tunnel in the backward direction, provides this information. In addition to a luminosity measurement, the system detects and triggers on scattered electrons at very low Q^2 ($< 10^{-2}$ GeV^2), which are scattered through very small angles.

The luminosity system has two principal components; the Electron Tagger (ET), located at $z = -33.4$ m adjacent to the electron beam-pipe and the Photon Detector (PD) at $z = -102.9$ m adjacent to the proton beam-pipe. The luminosity is measured using the Bethe-Heitler process ($ep \rightarrow ep\gamma$) [25] for which the cross section is calculated precisely within QED. On-line, the luminosity measurement is made using a coincidence method, where the electron and photon are detected simultaneously, and in the limit $Q^2 \rightarrow 0$ the sum of the e and γ energies is constrained to equal the electron beam energy. The rate of Bethe-Heitler events is then corrected for background processes and the acceptance of the detector, to calculate the luminosity. The on-line luminosity measurement is used by the HERA operating crew to steer the beams for optimum luminosity at the start of each machine fill.

Off-line, the luminosity is derived from the measured rate of scattered photons only. A minimum photon energy of 8 GeV is required to remove both noise and trigger threshold effects. A contribution to the measured rate comes from proton satellite bunches, which appear at 5 ns intervals and arise from protons escaping into adjacent radio frequency 'buckets' during injection into HERA. The proton satellites can contribute up to 10% of the proton current and are subtracted from the luminosity calculation. The main source of background in the luminosity measurement is from bremsstrahlung radiation from electrons in the electromagnetic fields of the residual gas in the beam-pipe. This contribution is subtracted using the information from 'pilot' bunches. The final uncertainty of the

luminosity measurement is 1.5% for the data sample considered in this thesis.

1.9 The Very Forward Detectors

The very forward detectors are a series of detectors situated some way up-stream from the main detector, which are designed specifically to detect particles from the dissociated proton, and are used in the study of diffraction.

1.9.1 The Proton Remnant Tagger

The proton remnant tagger is situated 24 m from the nominal interaction point in the forward direction. It consists of of seven individual scintillators arranged around and between the electron and proton beam-pipes, as shown in figure 1.8. Each scintillator actually comprises two parallel sheets of plastic scintillator with separate photomultipliers and pulse-height discriminators. The pulses from the pair of channels are processed by a coincidence unit which only registers a signal if both pulses are coincident with the time expected for the particles from an ep interaction in the main detector to reach the tagger. The proton remnant tagger is sensitive to particles in the pseudo-rapidity range $6 \lesssim \eta \lesssim 8$ which are detected either directly, or indirectly via secondary scattering from the beam-pipe or other material in the forward region.

1.9.2 The Forward Proton Spectrometer

The Forward Proton Spectrometer (FPS) [26] is made of two up-stream stations at 81 m and 90 m and uses the HERA beam magnet as a spectrometer for measuring low angle intact final state protons which have escaped detection by remaining in the beam-pipe. For example, at the first station, a proton which is deflected at the interaction point by an angle of 0.5 mrad ($\eta \sim 12$) will have lost around 5% of its energy and appear at the FPS a distance of several millimeters from the nominal orbit. The detectors consist of layers of scintillating hodoscopes mounted in a vacuum which are lowered in to the beam-pipe when stable beam conditions are reached. There are also layers of trigger scintillator which provide trigger elements when protons leave a signal in both stations.

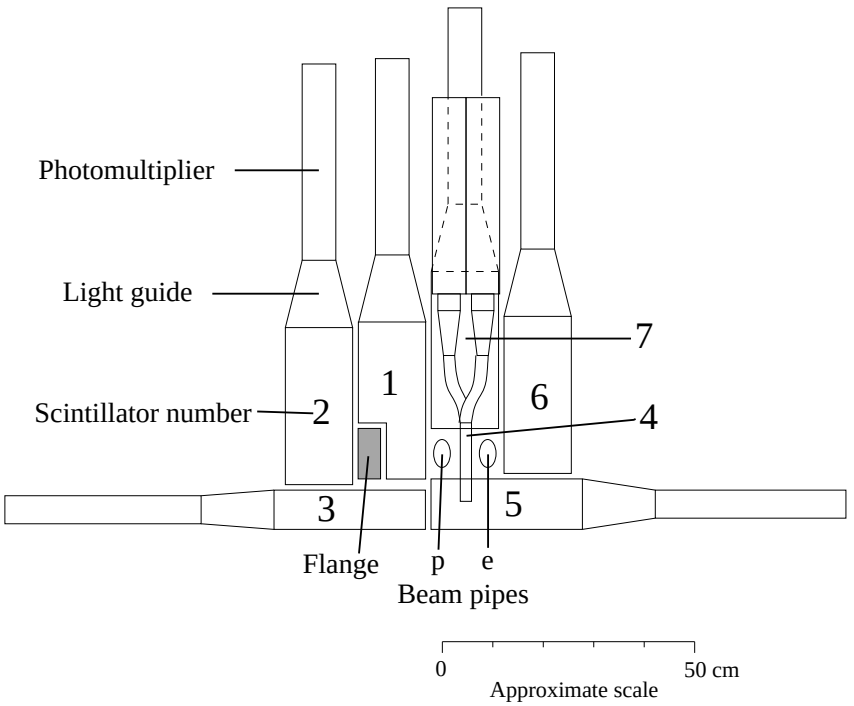

Figure 1.8: A schematic diagram of the proton remnant tagger, showing the seven double layers of scintillator. The diagram is drawn looking away from the interaction point, such that scintillators 1, 2 and 3 are on the inside of the HERA accelerator ring.

1.9.3 Forward Neutron Counter

At 106 m from the interaction point the Forward Neutron Counter (FNC) [27] detects neutral particles produced at angles of less than 0.8 mrad and energies greater than 300 GeV. The FNC is used to investigate events where high energy neutrons are the most forward particles [28].

1.10 Triggering and Data Acquisition

The high bunch crossing frequency and background rates at HERA coupled with the large number of channels (~270 000) to be read out per event provide a unique[8] and difficult challenge for the triggering and read-out system of the H1 experiment. The essence of the problem is the disparity between the bunch crossing interval (96 ns) and the response and read-out times of the detector components, meaning that the experiment could be 'dead' to events in the detector for a large fraction of the time if every event were processed in

[8]The triggering conditions at the LHC will be even more extreme, with an interval between bunch crossings of 25 ns.

full. The following solution to the problem is employed.

Almost every sub-detector, comprising the H1 experiment, has at least one trigger system. These send, at each bunch crossing, eight bits of information called *trigger elements* to the central trigger (CTL1) [29] which must arrive within 22 bunch crossings (2.1 μs) of the event. This delay is set by the response time of the slowest system which is the LAr calorimeter. The central trigger uses these trigger elements, of which at present there are 200, to make a decision on the quality of the event within 2 further bunch crossings. To avoid the problem of the detector being dead to further events for 24 bunch crossings the solution of *pipelining* is employed. The full detector information is stored in memory or pipelined, whilst the trigger information is being processed. If the central trigger accepts an event the pipelines are rewound, by the appropriate 24 bunch crossings, so that the information for the correct bunch crossing is read out. This makes the first trigger level dead-time free, because when an event is rejected by the central trigger the information for that bunch crossing simply falls off the end of the pipeline making room for the next event. Therefore it is critical that as much background rejection as possible is performed by CTL1.

The central trigger reaches a decision as to whether an event is a physics candidate by making logical combinations of the trigger elements to form *sub-triggers*, of which there are 128. If at least one sub-trigger is satisfied then the 'L1keep' signal is set. The sub-triggers mostly combine background rejection elements with physics selection elements. However, around half of the sub-triggers are used either to monitor specific background levels (e.g. cosmic muons), or to calculate trigger efficiencies. The latter are constructed from copies of sub-triggers with particular conditions missing to determine the efficiencies of the missing trigger elements. Obviously, it is not desirable for these triggers to occupy a large amount of the data bandwidth, because they have higher frequencies than the physics triggers, so *prescales* are applied. For example, a prescale factor of 10 will reduce the sub-trigger rate by a factor of ten by setting a 'L1keep' only for every tenth event that satisfies the sub-trigger condition.

When a 'L1Keep' signal is given the dead time for the experiment begins. This can be interrupted after 20 μs by a rejection from level 2 (L2) or after 210 μs by level 3[9], and the pipelines are re-enabled. The level 2 trigger is divided into two sections, the topological trigger (L2TT) [30] and the neural network (L2NN) [31]. They receive additional, more detailed, information from almost every trigger sub-system. This information allows the correlation of signals from *different* sub-detectors to reconstruct the paths of particles. The level 2 information, in effect, provides additional trigger elements for the level 1 sub-

[9]Level 3 is, as yet, not implemented.

triggers. Use of the additional L2 information allows prescale factors to be reduced for high rate L1 sub-triggers.

If an 'L2keep' signal is given, the full event information from all sub-detectors is sent to the level 4 (L4) trigger. When all the event information is read into the central event builder (CEB) of L4, the pipelines are re-enabled and dead-time ends. The triggering and reading of an event costs the experiment $1-2$ ms of dead time. The level 4 trigger processes asynchronously up to 30 events, in parallel, on a farm of microprocessors consisting of around 30 Power PC boards. A limited reconstruction is performed and fast, often complex, on-line software cuts are applied depending on the sub-triggers which fired the event. The Level 4 trigger rejects the bulk of the remaining beam-gas and cosmic induced background events, as well as those resulting from trigger noise. The rate of input to level 4 must not exceed ~ 50 Hz or dead time will accumulate from the reconstruction of events in the CEB. The total amount of dead time is kept to around 10% in normal running conditions. After passing the level 4 filter the data is written to tape, at a rate of ~ 10 Hz, and an average size of 130 KBytes per event. Approximately 1% of the events rejected at the level 4 stage are allowed through the filter, to monitor the effect of the cuts. Additionally separate streams of events are passed through L4 for the purposes of monitoring and calibration of certain sub-detectors. In the 1997 data running, physics processes with high rates, such as photoproduction and low Q^2 DIS, were downscaled at L4 in order to reduce the data volume. This required the introduction of 'finders' on L4 to avoid the random downscaling of priority events such as those with a 'hard' scale (e.g. high $p_\perp$ jets) or a particular final state such as a reconstructed D^* candidate.

Although all the data passing L4 is written to tape and permanently stored, further selection takes place to prepare the data sets for physics analysis and to remove the remaining background events. A full reconstruction and classification is done off-line and is referred to as level 5 (L5). This is performed by a dedicated workstation, typically within 24 hours of the time when the data was recorded at L4. The data is reconstructed in order to check the overall quality and to perform preliminary analyses. The data is reprocessed once more towards the end of the running when the final calorimeter energy scales and central tracking parameters have been established. On L5, after the reconstruction of the individual detectors, a detailed linking of charged track segments and energy clusters is performed to complete the overall description of the event. The fully reconstructed physics sub-triggers are subjected to cuts which requires them to be classified in at least one of the different physics classes (event classification), before being written to Production Output Tapes (POTs) and stored. The dynamic memory management system BOS [32] is used to format the events to allow convenient access. The output after reprocessing of the data is written to data summary tapes (DSTs) which contain compressed data that reflects

the characteristics of the event in a simple format useful for analysis, such as tracks and calorimeter clusters, rather than the raw sub-detector information. The typical size of an event on the DST is reduced to 10 kByte, thus allowing the events to be stored on disk, enabling easy and rapid access for analysis.

1.11 Trigger Sub-Systems

The trigger sub-systems which produce trigger elements used in this analysis are discussed in this section. The systems are the SPACAL trigger, the z vertex trigger and the central drift chamber trigger.

1.11.1 The SPACAL Trigger

The SPACAL trigger system performs two functions; a trigger for events containing DIS electron candidates and a veto of events originating from beam-induced background. To facilitate this dual requirement the trigger system comprises an Inclusive Electron Trigger (IET) for the EM section, ToF vetos for background rejection and total energy sums for both the EM and HAD sections.

The time-of-flight system in the SPACAL is sensitive to the difference in path length between particles from beam-gas and beam-wall backgrounds and those from the interaction region. The path length to the SPACAL is shorter for the background induced products than for particles from the interaction region, such that two distinct peaks are visible in the time distribution of the internal ToF system of the SPACAL. The early peak is due to background and the late peak due to physics interactions. The separation of the two peaks is around 10 ns which corresponds to the time taken for particles to travel the 1.5 m from the SPACAL to the interaction region and back again. The position of the interaction window is determined relative to the HERA clock and the in-time region is defined by a time window of typically ± 5 ns around the central value of 15 ns.

The IET is inclusive in that no additional criteria are required to provide the trigger decision other than an electromagnetic cluster. The basic unit of the IET is the in-time energy (ToF gated) analogue sum over a 4×4 cell configuration in which the majority of the energy deposited by the showering electron is likely to be contained. The energy sums are performed in overlapping sliding windows so that each sum overlaps the adjacent windows in both dimensions by two cells. This technique guarantees there is no trigger inefficiency arising from electrons with an impact point close to the edge of a group of

16 cells. Each sliding sum is compared to three programmable thresholds adjustable in the range 100 MeV to 20 GeV. These provide three trigger elements $SPACAL_{IET} > 0$, $SPACAL_{IET} > 1$ and $SPACAL_{IET} > 2$ and the typical thresholds are 0.5, 2 and 6 GeV respectively. Additionally, each IET threshold can be divided into 2 regions; the inner, which is centred on a 24 cm by 24 cm box region close to the beam-pipe in the approximate range $-17 < x < -9$ cm and $-9 < y < 17$ cm; and the outer region which encompasses the remainder of the SPACAL. The distinction between the two regions is made because the inner region of the SPACAL suffers a large counting rate due to an unknown beam background, referred to as the 'hot spot'.

1.11.2 The z-vertex Trigger

The majority of non-*ep* induced background can be eliminated by requiring a reconstructed vertex in the interaction region. The *z-vertex* trigger [33] accomplishes this on the first trigger level by using signals from the double MWPC layers of the CIP and COP combined with information from the double layer of the planar MWPC in the first supermodule of the forward tracker. The detector is divided into 16 segments in ϕ by the trigger logic. A *ray* is defined, for each segment, if there is a coincidence of hits which can be connected by a straight line in the rz plane in any two of the three chambers used. The usual requirement for coincidence is hits in four pads but this is relaxed to three in inefficient regions. All possible rays within each segment are extrapolated to $r = 0$ and a histogram is logically built in z consisting of 16 bins each of width 5.4 cm. The histograms from the 16 different ϕ segments are combined to form the *z vertex histogram*, where the bin with the largest number of entries, above the relatively flat background from wrongly identified rays, is expected to correspond to the interaction vertex of the *ep* collision.

The combined histogram is used in a fully programmable way to define L1 trigger elements with a large variety of peak significance and multiplicity conditions. The $zvtx - t0$ trigger element demands the existence of at least one ray. The $zvtx - t0$ bit is efficient at recognising any activity in the central region of the detector, and is used by most subtriggers for bunch crossing identification. Low multiplicity triggers are set in the case where there are few entries in the histogram, but they are all in the same bin. A high multiplicity trigger, $zvtx - sig$, is set when a large or significant peak above background is found in the interaction region. The trigger element $zvtx_{mul} < 7$ is applied in order to veto background events which have a large number of tracks in the detector; it requires less than 200 entries in the z vertex histogram.

1.11.3 The Central Drift Chamber Trigger

The CJC trigger [34] is responsible for triggering events containing high transverse momentum tracks. It employs 10 of the 56 wire layers in CJC1 and CJC2 and compares the digitized hits to a total of 10 000 predefined masks. The trigger accepts tracks whose distance of closest approach is calculated to be within 2 cm of the origin in the $r-\phi$ plane. The trigger elements are defined by the total number of tracks, the number of tracks of a particular charge and the number of tracks in the 'low' ($400 < p_\perp < 800$ MeV) and 'high' ($p_\perp > 800$ MeV) transverse momentum ranges. The trigger elements dependent on the low and high momentum thresholds are labelled $r\phi - T_{Low}$ and $r\phi - T_{High}$ respectively.

Chapter 2

HERA Physics

2.1 Introduction

Deep-Inelastic Scattering (DIS) has played a vital role in the understanding of the structure of matter. The structure of the proton and neutron can be investigated using lepton-nucleon scattering. The point-like lepton provides a probe of the the structure of an extended object, such as the proton. The final state is generally simpler to interpret than in proton-proton collisions, where both participating particles are extended objects.

This chapter gives an introduction to the physics of ep scattering and the main issues confronted in the new kinematical region made available at HERA. This will include an introduction to the general kinematics of Deep-Inelastic Scattering and a discussion of the structure of the proton in terms of the existing models and theories. In addition, a basic introduction to modelling the hadronic final state is given, including how the the measurement of forward energy flow can reveal the underlying dynamics of DIS, and how the production of open charm provides a direct measure of the gluon content of the proton.

2.2 DIS kinematics

The kinematics of a general DIS event, shown in figure 2.1a, are usually parameterised in terms of the Lorentz invariant quantities Q^2, x, y, W and s. According to the electroweak theory of the standard model, the electron[1] interacts with the proton via the exchange

[1] In this thesis references to the beam leptons as *electrons* should be considered as a generic term for *electrons* and *positrons* unless otherwise stated.

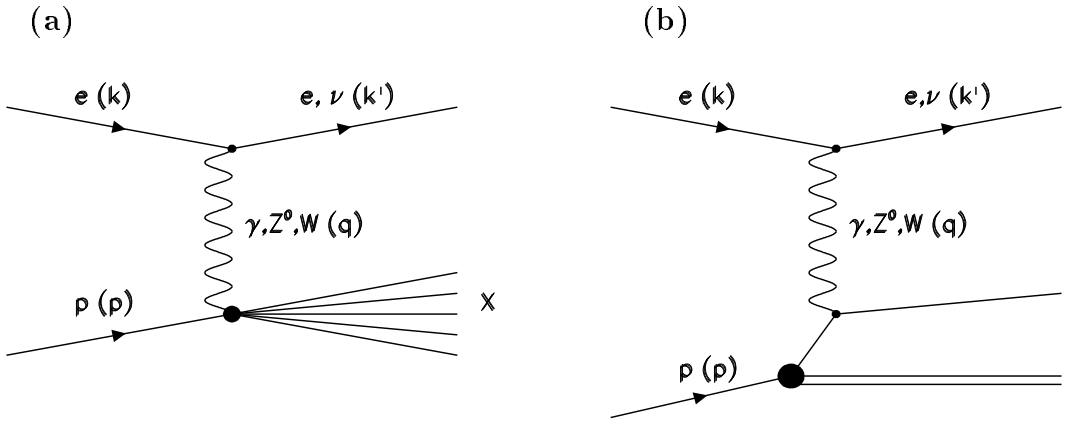

Figure 2.1: Schematic diagram of a deep-inelastic ep interaction (a) in general (b) in the quark parton model. The labels in brackets represent the four-momenta of the particles.

of an electroweak vector boson. In the case of a neutral current (NC) interaction, $ep \rightarrow eX$, a photon or Z^0 mediates the exchange, whereas in charged current (CC) scattering, $ep \rightarrow \nu_e X$, a $W^{\pm}$ is exchanged.

The negative four momentum transfer, Q^2, is defined as

$$Q^2 = -q^2 = -(k - k')^2 \tag{2.1}$$

and represents the virtuality of the exchanged boson. When the virtuality, Q^2, of the exchanged boson is large compared to m_p^2, where m_p is the mass of the proton, the proton is probed with high spatial resolution and the boson interacts with a constituent of the proton rather than with the whole. This is the regime of *Deep-Inelastic Scattering*.

Bjorken [35] demonstrated that DIS can be described by two dimensionless scaling variables, the first of which, x, is given by

$$x = \frac{Q^2}{2p.q} \tag{2.2}$$

In the infinite momentum frame of the proton, x is the fraction of the proton momentum carried by the struck parton. This interpretation can be extended to any other reference frame in which the proton has large momentum if the partons are assumed to be massless and have no momentum transverse to the proton direction.

The second dimensionless Bjorken scaling variable, y, is defined as

$$y = \frac{p.q}{p.k} \tag{2.3}$$

This is equivalent to, in the proton rest frame, the fractional energy loss of the lepton.

The squared invariant mass of the hadronic final state, which is equivalently the squared mass of the photon-proton system, is given simply by

$$W^2 = (q + p)^2 \tag{2.4}$$

This can be compared with the square of the centre of mass energy in the ep system,

$$s = (k + p)^2 \tag{2.5}$$

which, for the beam energies used in this analysis, has a value of 90 200 GeV^2.

Neglecting the azimuthal degree of freedom, the kinematics of the inclusive scattering process, at fixed s, can be completely described in terms of any two independent variables taken for example from x, y, W^2 and Q^2. They are related by

$$Q^2 \;=\; sxy \tag{2.6}$$

if the masses of the incoming particles are assumed to be small compared to the centre of mass energy. With this assumption, equation 2.4 can be expanded, using equations 2.6 and 2.3 and noting that $k.p = s/2$, to give

$$W^2 \;=\; Q^2 \left(\frac{1-x}{x}\right) \tag{2.7}$$

The exchange of a vector boson of mass M introduces a propagator term of the form

$$T \sim \frac{1}{Q^2 + M^2} \tag{2.8}$$

into the electroweak scattering amplitude. Therefore the cross section for ep scattering is dominated by low Q^2 photon exchange. The amplitude for the exchange of the Z^0 and $W^{\pm}$ is comparable with that for photon exchange only at Q^2 of the order $Q^2 \approx M_{Z^0}^2 \approx 10^4$ GeV^2.

In the NC process and neglecting Z^0 exchange, the interaction may be considered in terms of the factorised process,

$$\gamma^* p \rightarrow X \tag{2.9}$$

where the electron acts as a source of space-like[2] ($q^2 < 0$) photons. For small momentum transfers, $Q^2 \ll 1$ GeV^2, the photon is 'almost real' and its behaviour tends to that of a

[2]Particles with $q^2 > 0$ are said to be time-like.

real photon. Such low Q^2 interactions are referred to as *photoproduction* processes. As Q^2 increases, the wavelength of the virtual photon decreases until it is becomes smaller than the size of the proton ($Q^2 > 1$ GeV^2), and it is able to resolve the internal structure.

The 'Born' level diagram, shown in figure 2.1b, assumes that the interaction proceeds through the exchange of a single vector boson, which interacts with a point-like *parton* in the proton. For a NC photon exchange this is sufficient to describe the process since two photon exchange is suppressed by a factor $(1/\alpha_{em})^2$, where α_{em} is the electromagnetic coupling constant. The remainder of this thesis considers NC photon exchange only.

2.3 Proton Structure

The inclusive differential cross section for the inelastic collisions between electrons and protons[3] can be written, to lowest order in QED, as

$$\frac{d^2\sigma_{ep\to eX}}{dxdQ^2} = \frac{\alpha_{em}^2}{Q^4}\frac{E'}{E}L_{\mu\nu}W^{\mu\nu} \tag{2.10}$$

where E and E' are the incoming and outgoing electron energies in the laboratory frame, and $L_{\mu\nu}$ and $W^{\mu\nu}$ are the lepton and proton currents, of which the former is well known. Using the constraint of Lorentz current conservation the unknown structure of the proton can be parameterised in terms of two[4] independent *Structure Functions*, $F_1(x,Q^2)$ and $F_2(x,Q^2)$, to yield

$$\frac{d^2\sigma_{ep\to eX}}{dxdQ^2} = \frac{4\pi\alpha_{em}^2}{xQ^4}\left[xy^2F_1(x,Q^2) + (1-y)F_2(x,Q^2)\right] \tag{2.11}$$

The structure functions are interpreted as being related to the momentum distribution of the charged partons within the proton. A minimum of two structure functions are required because the photo-absorption cross section has two independent contributions, σ_T and σ_L, which arise from transversely and longitudinally polarised photons respectively. It is found that $2xF_1$ is proportional to σ_T and that F_2 is proportional to $\sigma_L + \sigma_T$. A longitudinal structure function, F_L, can be introduced which is proportional to σ_L and, hence, the three structure functions are related by,

$$F_2 = 2xF_1 + F_L \tag{2.12}$$

Equation 2.11 can be redefined in terms of one structure function as,

$$\frac{d^2\sigma_{ep\to eX}}{dxdQ^2} = \frac{4\pi\alpha_{em}^2}{xQ^4}\left(1 - y + \frac{y^2}{2\,[\,1 + R(x,Q^2)\,]}\right)F_2(x,Q^2) \tag{2.13}$$

[3] See [36] for a more detailed discussion.

[4] The presence of parity violation for W and Z^o exchange leads to the introduction of a third structure function $F_3(x,Q^2)$.

where the photo-absorption ratio, $R(x,Q^2)$, is defined by

$$R(x,Q^2) = \frac{\sigma_{_L}(x,Q^2)}{\sigma_{_T}(x,Q^2)} = \frac{F_{_L}(x,Q^2)}{F_2(x,Q^2) - F_{_L}(x,Q^2)} \tag{2.14}$$

The structure function $F_2(x,Q^2)$ is extracted from equation 2.13 by measuring the differential cross section $\frac{d^2\sigma_{ep\to eX}}{dxdQ^2}$, and estimating the contribution of F_L. For example, the most recent published measurement of the structure function F_2 at medium Q^2 by H1 [37] is shown in figure 2.2.

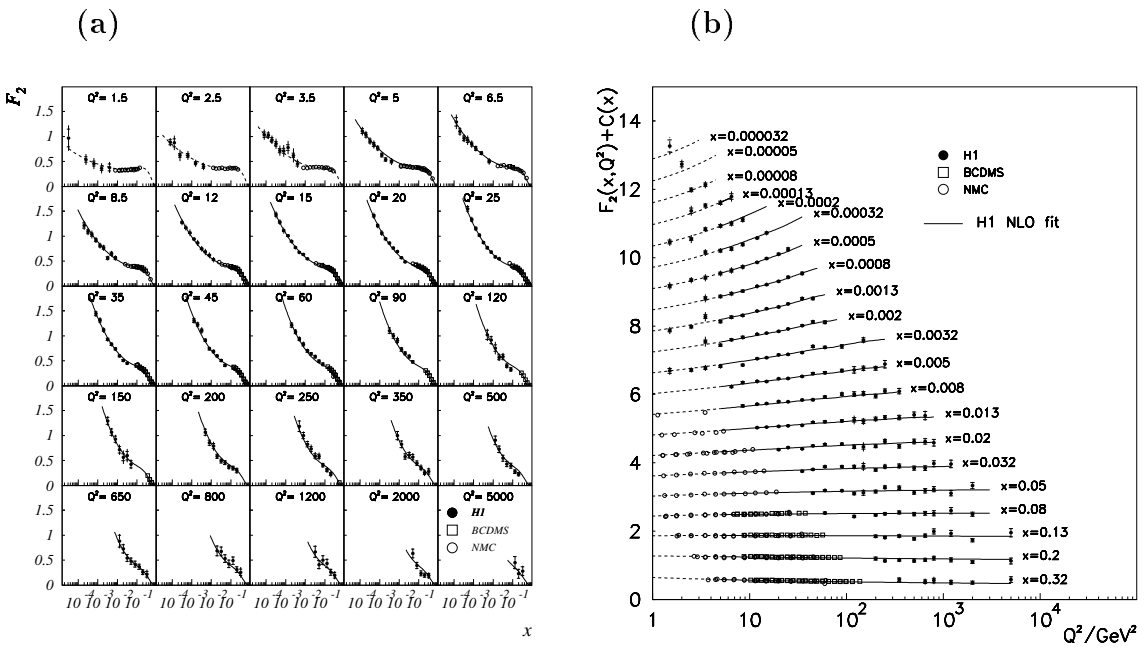

Figure 2.2: Measurement of the structure function F_2 by the H1 collaboration [37] as a function of (a) x for different values of Q^2, and (b) as a function of Q^2 for various values of x.

2.3.1 The Quark Parton Model

The Quark Parton Model (QPM) [35] was the first model used to explain the unexpected observation of *scale invariance* or *Bjorken scaling*, where $F_2(x,Q^2)$, at fixed x, shows little dependence on Q^2 over a wide kinematical range (see for example figure 2.2b). In this model, the proton is approximated as having a sub-structure of completely non-interacting point-like *partons*, namely quarks, off which the lepton undergoes elastic and incoherent scattering (see figure 2.1b). Therefore, equation 2.13 can be considered as the equation for point-like electron-parton scattering multiplied by the charge squared weighted momentum distribution of the partons, $F_2(x,Q^2)$. This leads to the introduction of a *parton density function*, $f_i(x,Q^2)$, for each parton family i, of charge e_i, which gives

a measure of the probability of finding a particular parton with a given fraction x of the proton's momentum. The structure functions may then be written as

$$F_1(x,Q^2) = \frac{1}{2}\sum_i e_i^2 \; f_i(x,Q^2) \tag{2.15}$$

$$F_2(x,Q^2) = x\sum_i e_i^2 \; f_i(x,Q^2) \tag{2.16}$$

It can be seen from these expressions that there exists a relationship between the two structure functions F_1 and F_2:

$$F_2(x,Q^2) = 2xF_1(x,Q^2) \tag{2.17}$$

This is known as the Callan-Gross [38] relationship and is a direct consequence of the spin-half nature of the quarks[5]. From equations 2.12 and 2.14, the Callan-Gross relationship implies that F_L and R are both zero. The experimental measurement of R close to zero [39], means that the Callan-Gross relationship holds approximately and supports the identification of the partons in the proton being spin-half fermions.

The proton is viewed as being constructed from a combination of three fractionally charged quarks with the wavefunction $|uud>$ where u and d represent the quark flavours up and down respectively. These quarks are referred to as the 'valence' quarks of the proton. The quantum numbers of the proton are determined by the valence quarks, but in addition any number of quark anti-quark pairs, $(q\bar{q})$, referred to as 'sea' quarks can be added to the valence quarks without affecting the proton quantum numbers.

When the structure function for F_2^{ep}, obtained from ep scattering, was compared to F_2^{en} from electron-neutron scattering[6], the separate sea and valence contributions could be extracted [40]. The result was found to be consistent with the valence quarks dominating at high x and the sea quarks at low x. Later measurements with neutrinos, which are only sensitive to partons of a particular charge due to the $W^{\pm}$ exchange, scattering off protons led to confirmation that the quarks had fractional charge and that there were indeed three valence quarks in the nucleon.

In the QPM, momentum conservation requires that the sum of the momenta of the quarks should equal that of the proton and this can be written as,

$$\sum_i \int_0^1 dx \; x \; f_i(x) = 1 \tag{2.18}$$

where the sum is over all quark flavours. Experimentally, this was found not to be the case [36]. Only half of the proton's momentum is in fact accounted for by the quarks alone.

[5] For spin-zero quarks the ratio $\frac{2xF_1}{F_2}$ would be zero.

[6] The neutron and proton form an isospin doublet, with the neutron wavefunction described by $|ddu>$.

2.3.2 Violation of Scaling and QCD Evolution

In addition to the 'missing' momentum in equation 2.18, there are a number of other problems with the parton model discussed so far. There is an apparent contradiction between the observed behaviour in DIS, which suggests that the quarks are non-interacting, and the non-observation of free quarks, suggesting strong inter-parton forces. Also, scale invariance is only observed to be completely true for x close to 0.15. Slight deviations, such that F_2 falls with Q^2 at high x and rises with Q^2 at low x are seen to occur (see figure 2.2b).

These observations can be explained by the introduction of *gluons*. The gluon is the gauge boson of the strong or *colour* force which is described by the theory of *quantum chromodynamics* (QCD). In QCD there is a *running* with Q^2 of the strong coupling constant α_s. As $Q^2 \to \infty$ then $\alpha_s(Q^2) \to 0$ which is referred to as *asymptotic freedom* and has the consequence that at sufficiently high values of Q^2 the quarks are quasi-free. This is the reason for the success of the 'naive' parton model. Conversely, when Q^2 is small, the coupling becomes large and the quarks are strongly bound together which is referred to as *infra-red slavery* or *confinement*. The QPM, in essence, is equivalent to zeroth order QCD. Higher order processes are described by a perturbative expansion in orders of α_s. When $\alpha_s(Q^2)$ is much less than unity, which is the case for $Q^2 > 1$ GeV^2, then a perturbative expansion converges rapidly. In this kinematic regime perturbative QCD (pQCD) is reliable.

The 'naive' parton model described thus far and QCD can be combined to give a consistent picture of proton structure. The proton consists of three valence quarks, a sea of quark anti-quark pairs at low x, and gluons, which are responsible for binding the quarks and generating the strong final state interactions that produce colourless hadrons. At HERA energies the quark sea includes the three light flavours up, down and strange (s) plus the two *heavy quarks* charm (c) and beauty (b). The distributions in x and Q^2 of the valence quarks, sea quarks and gluons are referred to as the *parton density functions*. In contrast to the 'naive' parton model the term parton now refers to valence quarks, sea quarks and gluons. The density functions for the three sets of partons are closely related due to QCD radiation. For example, the valence quarks may radiate gluons which in turn may produce sea quark pairs. Since α_s is a function of Q^2 it follows that these higher order effects produce an *evolution* of the proton structure with Q^2, and the violation of scale invariance may be explained within the framework of pQCD.

2.4 Low x Phenomenology

A striking feature of the DIS measurements at HERA is the substantial rise of F_2 with decreasing x at low x (see figure 2.2a). This section details briefly the two basic evolution schemes, which differ in the treatment of terms in the perturbative QCD expansion of F_2, that attempt to explain this rise. The expansion contains terms of the form $\alpha_s^n \ln^m Q^2$ and $\alpha_s^n \ln^m 1/x$ with $m \leq n$, which are expected to dominate in different regions of the $x - Q^2$ kinematic plane. The rise of F_2 is related to the increasing gluon density at low x which can be extracted within the framework of the evolution schemes and is detailed in section 2.4.3.

2.4.1 The DGLAP Evolution Formalism

The QCD prediction for the scaling violations was formalised in the set of equations developed by Dokshitzer, Gribov, Lipatov, Altarelli, and Parisi (DGLAP) [41] which predict the Q^2 evolution of the structure functions. In this approach the parton density functions are separated into parts representing the valence quark (flavour non-singlet), sea quark (flavour singlet) and gluon distributions. These non-perturbative functions are, as yet, incalculable within QCD[7] and have to be determined from the data at a starting scale, Q_0^2, above which a perturbative approach is valid, and then evolved to higher Q^2 using QCD. The assumption is made that below the starting value, Q_0^2, long distance physics applies for which perturbative techniques are not applicable but above Q_0^2 short distance physics, which can be described perturbatively, may be used. It will be seen that for a choice of $Q_0^2 \simeq 1$ GeV^2 this approach works well. The QCD evolution is determined by parton splitting processes, in which partons couple to others, as shown in figure 2.3. The radiation of particles is described in terms of *splitting functions* where, for example $P_{ab}(x/y)$, represents the probability of a parton a, with momentum fraction x, originating from a parton b with momentum fraction y.

The momentum fraction of the non-singlet valence quarks, which couple to the exchanged boson, is modified by the gluon Bremsstrahlung process ($q \rightarrow qg$). The singlet quark distribution is modified by gluon Bremsstrahlung and quark anti-quark pair production ($g \rightarrow q\bar{q}$). The gluon distribution originates from gluon Bremsstrahlung and gluon splitting ($g \rightarrow gg$).

The Q^2 evolution of the parton density functions for the non-singlet quark, $q^{NS}(x, Q^2)$,

[7] Lattice QCD [42] may offer the chance to calculate the non-perturbative input parton distributions and offer a direct prediction of the proton structure function.

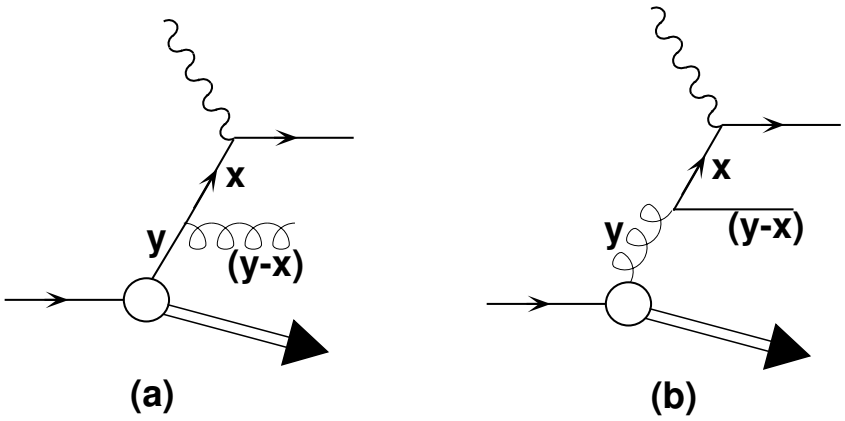

Figure 2.3: Diagram of the QCD splitting functions (a) $P_{qq}(x/y)$ and (b) $P_{qg}(x/y)$.

the singlet quark, $q^S(x,Q^2)$, and the gluon, $g(x,Q^2)$ are given by the following DGLAP equations:

$$\frac{dq^{NS}(x,Q^2)}{d\ln Q^2} = \frac{\alpha_s Q^2}{2\pi}\int_x^1 \frac{dy}{y}\left[q^{NS}(y,Q^2)P_{qq}\left(\frac{x}{y}\right)\right] \quad (2.19)$$

$$\frac{dq^{S}(x,Q^2)}{d\ln Q^2} = \frac{\alpha_s Q^2}{2\pi}\int_x^1 \frac{dy}{y}\left[q^{S}(y,Q^2)P_{qq}\left(\frac{x}{y}\right) + g(y,Q^2)P_{qg}\left(\frac{x}{y}\right)\right] \quad (2.20)$$

$$\frac{dg(x,Q^2)}{d\ln Q^2} = \frac{\alpha_s Q^2}{2\pi}\int_x^1 \frac{dy}{y}\left[q^{S}(y,Q^2)P_{gq}\left(\frac{x}{y}\right) + g(y,Q^2)P_{gg}\left(\frac{x}{y}\right)\right] \quad (2.21)$$

The splitting functions $P_{ab}(x/y)$ have been calculated in leading and next-to-leading order QCD. Solving these equations leads, via equation 2.16, to a logarithmic dependence of the structure function on Q^2, such that F_2 falls with Q^2 at high x and rises with Q^2 at low x. A physical interpretation of the Q^2 dependence is that as Q^2 increases the virtual photon resolves more partonic structure which results in a net migration of partons from high to low x. To calculate the evolution in full, an iteration of the lowest order splitting processes is performed which leads to the ladder of successive parton emissions as shown generically in figure 2.4a.

The method of summing the contributions of ladder diagrams is known as the Leading Logarithmic Approximation (LLA). The DGLAP evolution equations formally sum terms of the type $\alpha_s^n \ln^n Q^2$, where there are n rungs in the ladder, to all orders in perturbation theory (LLA(Q^2)). Therefore, they are applicable to a range where $\ln(1/x) \ll \ln(Q^2/Q_0^2)$, if terms in $\ln 1/x$ are to be safely neglected. The DGLAP formalism, therefore, should be valid in the region of large Q^2 and intermediate to large x. Furthermore, in the summation of the ladder, the largest contribution to the integral over the transverse momentum of the n^{th} parton, k_{Tn}, occurs when $k_{Tn}^2 \gg k_{Tn-1}^2$, and the partons follow a strong ordering

in transverse momenta

$$k_{Tn}^2 \gg k_{Tn-1}^2 \gg ... \gg k_{T1}^2 \tag{2.22}$$

There is only a soft ordering for the fractional longitudinal momenta

$$x_n < x_{n-1} < ... < x_1 \tag{2.23}$$

since the only restriction is that a daughter parton cannot possess a longitudinal momentum larger than its parent parton.

The DGLAP equations predict only the Q^2 evolution and not the x dependence of the structure functions. However, it has proved possible to extract parton distributions as a function of x from phenomenological DGLAP fits, using singlet and non-singlet quark plus gluon distributions, at some starting value Q_0^2 such that, when they are evolved to higher Q^2, they best reproduce the measured structure functions as a function of both x and Q^2. In spite of the kinematic restriction of applicability for the DGLAP formalism, parameterisations of F_2 based on DGLAP evolution have been successful in describing HERA data measured to date. The approach of Martin, Roberts and Stirling [43] has had notable success.

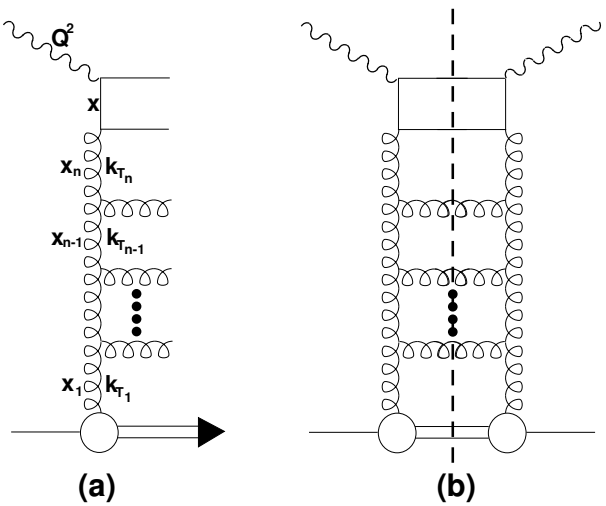

Figure 2.4: (a) A parton ladder diagram illustrating a contribution to $F_2(x,Q^2)$ at low x. In DGLAP evolution the partons are ordered in transverse momentum, k_T, whilst in BFKL evolution there is an ordering in x of the gluons. The equations are formed by summing squared amplitudes such as that in (b).

2.4.2 The BFKL Evolution Formalism

In the regime of very low x the terms in $\ln(1/x)$ cannot be neglected and, for a constant Q^2, another LLA this time expanding in terms of $1/x$ can be made. The requirement

is now that $\ln(Q^2/Q_0^2) \ll \ln(1/x)$. The perturbative equation describing this evolution in x was developed by Balitsky, Fadin, Kuraev and Lipatov (BFKL) [44]. They assume that at low x the parton distribution is dominated by gluon splitting ($g \to gg$) such that a gluon ladder (see figure 2.4a) can be constructed as the typical contribution to F_2. Squaring amplitudes, to obtain contributions such as that in figure 2.4b, for all possible gluon interactions, leads to the BFKL equation, written for simplicity as

$$x\frac{\partial f}{\partial x} \equiv K_{\mathcal{L}} \otimes f(x, k_T^2) \tag{2.24}$$

where $f(x, k_T^2)$ is the non-integrated gluon distribution and the symbol $\otimes$ implies integration over x and k_T. $K_{\mathcal{L}}$ is the *Lipatov kernel*, and represents the summation over the terms in $\alpha_s^n \ln(1/x)^n$. When the BFKL equation is solved analytically, at fixed Q^2, the variation of F_2 with x can be obtained. The result is $F_2 \sim x^{-\lambda}$, where $\lambda = \frac{12\alpha_s}{\pi} \ln 2$ and at HERA energy scales $\lambda \sim 0.5$[8]. The BFKL formalism therefore predicts the dependence on x of the structure function at low x, given the measured structure function at higher x and the same Q^2.

In the BFKL scheme, in contrast to the DGLAP formalism, the partons in the ladder follow a strong ordering in fractional longitudinal momentum

$$x_n \ll x_{n-1} \ll ... \ll x_1 \tag{2.25}$$

while there is no ordering in transverse momentum.

At the present level of accuracy achieved by the HERA experiments, the inclusive structure function measurements at low x are consistent with BFKL evolution, but are also sufficiently well described by parameterisations based on DGLAP evolution [37]. Further measurements of F_2 may allow regions of Q^2 and $1/x$ to be probed where the two predictions start to differ appreciably, in order to allow some discrimination. Measurements of the final state in DIS have also proven to be sensitive to the dynamics of the low x region and are discussed in section 2.7.

2.4.3 The Gluon distribution at Low x

At low x the parton distributions are dominated by the gluon distribution, and the rising structure function F_2 is caused by the increasing gluon density and the splitting process $g \to q\bar{q}$. Since the photon does not couple directly to gluons, the gluon density must be inferred from F_2 data. The gluon density can be extracted from F_2, in the DGLAP

[8]The BFKL equation has recently been solved in NLO [45]. The corrections to λ were found to be large. Work is in progress to try and understand this result.

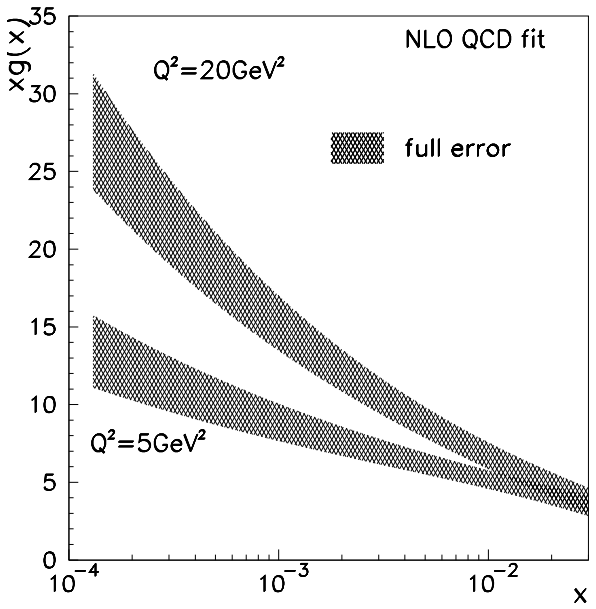

Figure 2.5: The gluon density $xg(x)$ extracted from H1 data [37] with a NLO QCD fit at $Q^2 = 5$ GeV^2 and $Q^2 = 20$ GeV^2.

formalism, if the approximation that the low x quark distribution coupling to photons is dominated by the splitting, $g \to q\bar{q}$.

H1 has extracted the gluon density, $xg(x)$, at two values of Q^2 (5 and 20 GeV^2) using a fit, involving the DGLAP evolution equations in the NLO approximation, to the structure function F_2 [37]. Functional forms for the singlet, non-singlet and gluon density distributions were assumed, and $xg(x)$ extracted from a χ^2 minimisation fit to the measured $F_2(x, Q^2)$, additionally constrained by measurements from fixed target experiments. The resulting NLO gluon density is shown in figure 2.5. The error bands are derived from separate consideration of the statistical and systematic errors. The expected rise at low x is observed, becoming more significant with increasing Q^2.

2.5 The Hadronic Final State

The structure functions reveal many details about the content of the proton and QCD dynamics. However, measurements of the hadronic final state can reveal the underlying QCD dynamics and test the models of fragmentation and hadronisation to which the structure functions are insensitive. The fragmentation and non-perturbative hadronisation phases in the production of the hadronic final state are so complex that Monte Carlo

generators must be used. The basic concepts of Monte Carlo programs are introduced in section 2.6.

At HERA it is possible to measure almost the entire hadronic final state, apart from low $p_\perp$ particles close to the beam axis, enabling detailed tests of the underlying QCD processes. The hadronic final state measurements made at HERA thus far include, amongst others, energy flow [46], jet production [47] and heavy flavour production [48]. In this thesis discussion is limited to the study of forward particle production (section 2.7) and open charm production (section 2.8). The measurement of forward particle production provides an example of how the final state may be used to reveal information about the underlying production mechanisms. Open charm production is examined in the context of the inclusive D^* cross section and the direct determination of the gluon density in the proton. The study of the hadronic final state in diffraction is discussed in chapter 3.

2.6 Monte Carlo Generators

All DIS Monte Carlo (MC) generators are based on a factorisation theorem in which an amplitude is obtained by convoluting the matrix elements of the underlying perturbative QCD parton process with the parton densities. The outgoing partons are evolved to final state hadrons through modelling the effects of higher order emissions and hadronisation. Therefore, the generation of simulated physics events is usually divided into a series of programs. In the first stage of the generation:

- the underlying parton calculation is performed to a certain order, usually leading order, in QED and QCD. These partonic cross sections are convoluted with parton distributions evolved with a hard scale, most commonly Q^2, from an input parameterisation defined at some starting scale Q_0^2.

The subsequent production of final state hadrons and leptons from the partons is usually divided into two distinct stages:

- **fragmentation** where the radiation of quarks and gluons from the outgoing partons from the hard subprocess simulates higher order perturbative effects.
- **hadronisation** where the partons emitted during the fragmentation develop non-perturbatively into hadrons.

There are two main methods used in the modelling of fragmentation for DIS events. One model uses leading logarithmic parton showers whereas the other treats the radiation in terms of colour dipoles. The hadronisation of the partons to hadrons is based on phenomenological models.

2.6.1 Fragmentation Models

Parton Showers

In DIS, the quark coupling to the photon can radiate quarks and gluons both before and after the interaction, giving rise to initial state and final state parton showers (PS). The evolution of these parton showers is based on the leading log Q^2 DGLAP equations introduced in section 2.4.1. The use of these splitting kernels allows arbitrarily high orders in α_s to be simulated without calculating the exact matrix element for each order.

The procedure adopted is as follows. A parton in the incoming nucleon can initiate a parton shower where, in each branching, one parton becomes increasingly off-shell with a space-like virtuality and the other has a time-like virtuality (see section 2.4.1). For the basic process of quark scattering, the initial state shower results in an incoming space-like quark which is struck by the boson and becomes either on-shell or time-like. This quark can itself radiate further, depending on how much it is off-shell, so giving rise to a final state time-like parton shower. This shower continues until all partons are almost on-shell. A cut-off of around 1 GeV is applied, below which DGLAP splitting is no longer used and non-perturbative hadronisation effects are applied.

The modelling of parton showers allows other QCD effects to be taken into account. For example, the coherence in soft gluon emission is taken into account through angular ordering by decreasing opening angles in subsequent branches. However, the parton shower approach has some shortcomings due to its approximate nature. The separation of initial and final state parton emission neglects interference terms between the two and is not gauge invariant. The PS model is implemented in the LEPTO [49] Monte Carlo program.

Colour Dipole Model

An alternative to the Parton Shower model is given by the Colour Dipole Model (CDM) [50]. The QCD radiation of gluons and quarks is treated as a chain of radiating colour dipoles. In the case of a $q\bar{q}$ pair radiating a gluon, the emitted gluon may be treated as radiation from the colour dipole formed between the q and the $\bar{q}$. The radiated gluon and the orig-

inal q and $\bar{q}$ are then treated as two independent colour dipoles, one between the gluon and the quark and the other between the gluon and the anti-quark, each of which can radiate further gluons. The gluon emission, ordered in decreasing transverse momentum of the emitted gluon, results in a chain of independent radiating dipoles connected via the gluons. The strong ordering in transverse momentum places kinematical constraints on the allowed rapidity of an emitted gluon, which produces angular ordering in the cascade, such that most QCD coherence effects are accounted for in a natural way.

This model has had considerable success in describing data from e^+e^- experiments. However, in order to describe DIS data two important modifications are implemented. Firstly, in e^+e^- both the q and $\bar{q}$ can be considered point-like, but for DIS this applies only to the struck quark. The hadron remnant is an extended object and, therefore, wavelengths shorter than the size of the emitting dipole are suppressed. Secondly, because the gluon radiation is assumed to come from the dipole formed by the struck quark and the proton remnant only, the boson-gluon fusion process ($\gamma g \rightarrow q\bar{q}$) has to be added and is taken from the QCD matrix element. The CDM is implemented in the ARIADNE [51] Monte Carlo program.

2.6.2 Hadronisation

Hadronisation is the process by which partons 'dress' themselves and become hadrons. The most commonly used phenomenological model for this process is the Lund string model. The model forms a narrow colour flux or 'string' between two colour charges. As the particles move the string is stretched such that the energy density in the string is increased. When the energy in the string is high enough a $q\bar{q}$ pair is produced from the vacuum, breaking the string into shorter strings which continue to separate. If there is insufficient energy to form a $q\bar{q}$ pair the shorter colour string pieces form conventional on-shell hadrons. The model is implemented in the JETSET [52] Monte Carlo program.

2.7 Forward Energy Flow

The measurement of the hadronic final state between the proton remnant and the struck quark is a powerful technique for studying the underlying dynamics of the QCD cascade at low x. The difference between the leading log DGLAP and BFKL schemes for the ordering of the transverse and longitudinal momenta detailed in section 2.4 leads to significantly larger amounts of perturbative radiation in the forward region (i.e. close to the proton fragmentation region) for the BFKL than the DGLAP evolution scheme. Using

the hadronic final state to detect the difference between the two schemes, as opposed to the inclusive measurement, introduces additional complications due to soft hadronisation processes. These may be reduced by studying 'hard' processes. For example, the H1 experiment have studied the complementary processes of high $p_\perp$ ($p_\perp > 1$ GeV) single particle production and high $p_\perp$ ($p_{\perp jet} > 3.5$ GeV) jet production in the approximate angular range $5^o < \theta < 25^o$, and covering a range in Bjorken x of $0.0001 < x < 0.004$ [53]. The forward jet cross section as a function of Bjorken x for two $p_{\perp jet}$ cuts is shown in figure 2.6. The data rise at low x except in the lowest x bin where the rise is suppressed due to the kinematic cuts. In figures 2.6a and 2.6c the data are compared to Monte Carlo programs based on QCD phenomenology. The data rise faster with decreasing x than is predicted by the LEPTO program which, as discussed in section 2.6.1, is based on LO DGLAP dynamics. However, the data can be described by a program based on DGLAP evolution if a 'resolved' photon contribution is added. This is implemented in the RAPGAP [54] Monte Carlo program and works on the principle that in the kinematic range $E^2_{\perp jet} \geq Q^2$ the parton from the proton is able to probe the internal partonic structure of the photon. This is realised by assigning a structure function to the photon [55] and DGLAP evolution is allowed to take place from partons in both the proton and photon. The ladder diagram shown in figure 2.4 then consists of two smaller ladders, one between the hard scattering and the photon and the other between the hard scattering and the proton. As a result there is no longer a strong ordering in k_T from the photon to the proton vertex.

The ARIADNE Monte Carlo program predicts the rise of the jet cross section at low x. This program is based on the Colour Dipole Model, described in section 2.6.1, and unlike LEPTO does not have a cascade ordered in k_T. Therefore, at a first approximation, the prediction of this model may be thought of as being similar to BFKL evolution [56].

The data is also compared to the LDCMC [57] Monte Carlo program which is based on the linked dipole chain (LDC) model [58] that is a reformulation of the CCFM (Ciafaloni, Catani, Fiorani, Marchesini) [59] evolution equation. The CCFM equation forms a bridge between the BFKL and DGLAP approaches by imposing angular ordering of the partons in the QCD cascade. The prediction of the model gives a poor description of the forward jet distribution despite the fact that it should provide a smooth interpolation between the BFKL and DGLAP regimes.

The data are compared in figures 2.6b and 2.6d with analytical calculations, performed without hadronisation corrections, based on the LO BFKL calculation [60] and with a NLO DGLAP calculation for a direct interaction of the photon with the proton [61]. The calculation based on the LO BFKL equation describes the shape but not the normalisation

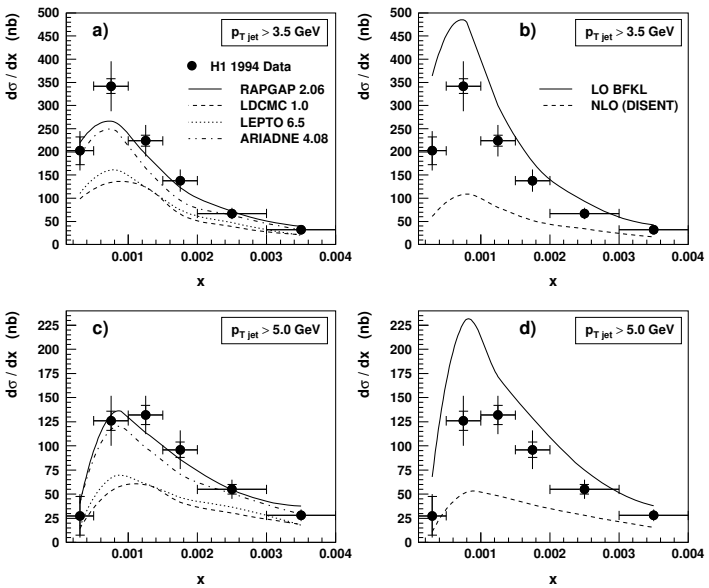

Figure 2.6: The forward jet cross section, as measured by the H1 experiment [53], defined in the kinematic range $x_{jet} = E_{jet}/E_p > 0.035$, $0.5 < p^2_{\perp jet}/Q^2 < 2$, $7^o < \theta_{jet} < 20^o$ as a function of x for two $p_{\perp jet}$ cuts: 3.5 GeV and 5 GeV. In (a) and (c) the data is compared with the Monte Carlo calculations: RAPGAP (full line), LDCMC (dashed line), LEPTO (dotted line) and ARIADNE (dashed dotted line). In (b) and (d) the same data is compared with LO BFKL calculations at the parton level (full line) and NLO calculations for a direct photon interaction (dashed line).

of the data. The effects on the BFKL prediction of the forward jet cross section due to hadronisation effects and NLO corrections, which have recently been calculated for the inclusive cross section [45], have yet to be calculated for hadronic final state observables but they are expected to be large. Until these calculations are performed the interpretation of the forward jet cross section in terms of BFKL dynamics is difficult. The NLO calculation, based on the direct interaction of the photon with the proton, has a similar shape and normalisation to the LEPTO prediction and, even allowing for hadronisation corrections, grossly underestimates the forward jet cross section. Similar conclusions concerning the comparison of the data with the Monte Carlo models and QCD calculations are obtained from the analysis of high transverse momenta single forward particle production.

2.8 Charm Production

Charm events, in which a $c\bar{c}$ pair is produced, may be divided into *open-charm* and *hidden charm* events. In the production of open charm, there is a large momentum difference between the quark and anti-quark, which fragment independently - typically into a D and $\bar{D}$ meson. If the quark and anti-quark are close together in momentum space, they may form a bound state - a J/ψ or one of its excited states, which has a net charm content of zero, and the charm is 'hidden'. This thesis will discuss the production of open charm only. The tagging of open charm events is usually performed by the reconstruction of D^0 and/or D^* mesons[9]. The study of charm production in DIS ep scattering provides important information about charm quark production mechanisms in the hadronic final state and this is discussed in section 2.8.1. The advent of HERA, which probes structure functions at far lower values of x than any previous experiment, allows the detailed measurement of the charm contribution, $F_2^{c\bar{c}}$, to the structure function. The definition, measurement and comparison to theoretical calculations of $F_2^{c\bar{c}}$ is given in section 2.8.2. The production rate for charm is sensitive to the gluon density of the proton which allows a direct measurement of $xg(x)$. The method and results of the measurement of the gluon density using open charm events are explained in section 2.8.3.

2.8.1 Charm Production Mechanisms

At the low values of x covered at HERA, the boson-gluon fusion process (BGF), shown in figure 2.7, is expected to be the dominant mechanism for the production of charm quarks. This production mechanism is referred to as *extrinsic charm* production because

[9]See chapter 5 for the description of a method for reconstructing D^* mesons.

the charm quark appears only in the final state and is not directly associated with proton structure. The alternative production mechanism is *intrinsic charm* production [62] which was introduced to explain some of the features of charm production at large x in hadroproduction data which cannot be described by pQCD. The intrinsic charm hypothesis assumes the existence of a $c\bar{c}$ pair as a non-perturbative component in the bound state nucleon. Therefore, the Fock-state decomposition of the proton wave function contains a small, but finite, probability for a quantum fluctuation to produce a charm quark pair i.e. the state $|uudc\bar{c}>$. The analysis of $F_2^{c\bar{c}}$ from fixed target data at high x estimates an intrinsic charm contribution of $0.9 \pm 0.6\%$ [63]. In contrast to boson-gluon fusion, where the charm and the anti-charm quark appear back-to-back in the hadronic final state, the transverse momentum of the charm or anti-charm quark arising from intrinsic charm in the proton is not balanced by that of its anti-particle. The production process is therefore similar to that for the scattering process in the quark parton model shown in figure 2.1b. Figure 2.8 shows the differential cross section for open charm production as a function of x_D, where $x_D = 2|\vec{p}^*_{D^0}|/W$ and $\vec{p}^*_{D^0}$ is the three momentum of the D^0 meson in the hadronic centre of mass frame, as measured by H1, in the range $10 < Q^2 < 100$ GeV^2 and $< W > \simeq 125$ GeV [64]. The data are compared with:

- A LO Monte Carlo prediction based on the BGF mechanism.
- A Monte Carlo prediction where intrinsic charm sea quarks only are generated.
- An extrapolation from measurements of fixed target $\bar{\nu}N$ scattering where charm production proceeds mainly via $W^{\pm}$ scattering off the strange quark sea in the proton. The results are evolved to the larger hadronic centre of mass energy at HERA using QCD. The shape of the distribution agrees with the intrinsic charm Monte Carlo prediction which confirms the assumption that in $\bar{\nu}N$ scattering the charm quarks are produced by the quark parton model.

The data are consistent with the boson-gluon fusion model, with an upper limit of a 5% contribution from intrinsic charm, confirming boson-gluon fusion as the dominant charm production process in DIS at HERA.

2.8.2 The Charm Structure Function

The charm structure function, $F_2^{c\bar{c}}(x, Q^2)$, is defined by analogy with F_2, as

$$\frac{d^2\sigma^{c\bar{c}}}{dxdQ^2} = \frac{2\pi\alpha_{em}^2}{Q^4 x}\ (1 + (1-y)^2)\ F_2^{c\bar{c}}(x, Q^2) \tag{2.26}$$

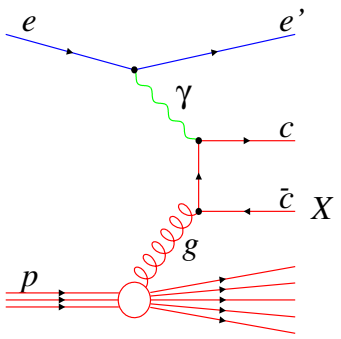

Figure 2.7: The Feynman diagram for the production of $c\bar{c}$ pairs via boson-gluon fusion.

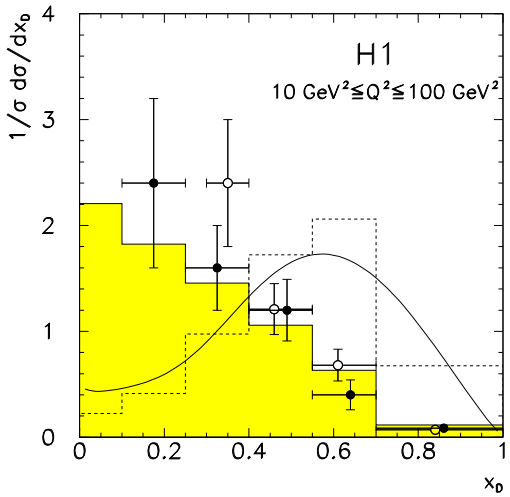

Figure 2.8: The normalised x_D distribution in DIS, measured by the H1 collaboration [64], at $< W > \simeq$ 125 GeV for D^0 (open points) and D^* (closed points). The shaded histogram represents the prediction for the BGF process, the dashed histogram the intrinsic charm sea contribution according to the LEPTO Monte Carlo program [49], and the full line the QCD evolution of $\bar{\nu}N$ data [65].

where $\sigma^{c\bar{c}}$ is the measured cross section for charm quark anti-quark production ($ep \rightarrow ec\bar{c}X$). In equation 2.26 the simplification is made that the Callan-Gross relation holds, i.e. R=0. According to NLO QCD calculations an increase in $F_2^{c\bar{c}}(x,Q^2)$ of at most 2%, at small x, is expected if R is unity.

The cross section $\frac{d^2\sigma^{c\bar{c}}}{dxdQ^2}$ is determined from the cross section for D mesons ($ep \rightarrow DX$), measured in bins of x and Q^2. The D meson cross section, due to detector acceptance, is measured in a limited range of $p_\perp$ and η of the D meson and an extrapolation to the full phase space is made using a Monte Carlo generator. The D meson cross section is then converted into the $c\bar{c}$ cross section ($ep \rightarrow ec\bar{c}X$) using the probability for a charm quark to fragment and hadronise into a D meson (~ 0.27) as measured in e^+e^- experiments [66].

The H1 collaboration have found the contribution of $F_2^{c\bar{c}}$ to the inclusive structure function to be 0.237 ± 0.021 [64] and the corresponding structure function is shown in figure 2.9. The contribution of charm to the proton structure function is far greater at HERA than that for lower energy fixed target experiments which probe higher values of x. This is expected since the gluon density of the proton is observed to rise sharply at low x.

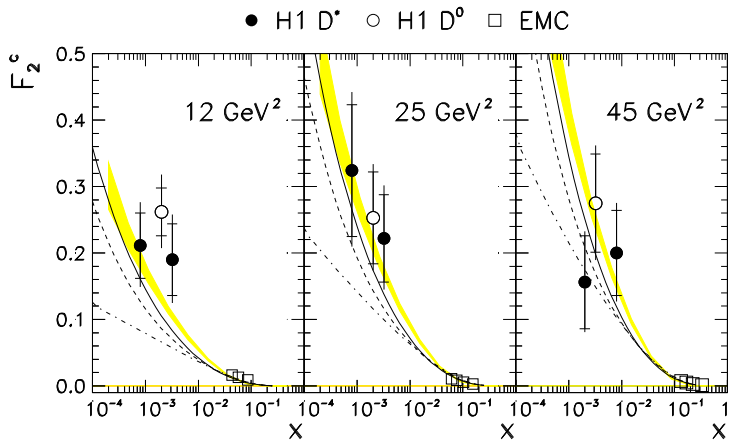

Figure 2.9: $F_2^{c\bar{c}}$ measurements from H1 [64] D^0 (full circles), H1 D^* (open circles) and EMC (squares) analyses. The data are compared with massive NLO calculations [67] based on proton parton distributions taken from GRV-HO [68] (full line), MRSH [69] (dashed line) and MRSD0' [70] (dash-dotted line). The contribution of $F_2^{c\bar{c}}$ as calculated from a QCD analysis of H1 F_2 measurements is also shown (shaded stripe).

Two different theoretical prescriptions for the charm structure function exist. The first model treats the charm quark as a massive quark and its contribution to the structure function is given by fixed order perturbation theory. This involves the computation of the boson-gluon fusion process and its higher order corrections. The approach is usually known as the fixed flavour number scheme (FFNS) [71]. This model provides the most

appropriate way to calculate the charm structure function at low Q^2 because it describes the threshold behaviour correctly (i.e. the structure function vanishes above $x = \frac{Q^2}{Q^2+m_c^2}$). However, it does have one major shortcoming. When Q^2 increases so that $Q^2 \gg m_c^2$, terms involving large logarithms in Q^2/m_c^2 become important and these are not accounted for.

The simplest way to sum terms containing large logarithms in Q^2/m_c^2 is to treat the charm quark as a massless parton and require that its distribution function satisfies the same DGLAP equations as do the light partons. For example, an approach which incorporates this idea is the zero-mass variable flavour number scheme (ZM-VFNS) [72]. This treats the charm quark as being infinitely massive below some threshold, and massless above the threshold for which the evolution of the charm quark begins. At first sight, the massless charm quark model looks similar to intrinsic charm production. The distinction is that in the ZM-VFNS model there is a charm density of zero at the starting scale, Q_0^2, of the evolution. It is claimed [73] that there exists a relationship between the parton density of the charm quarks and the gluon density originally appearing in the boson-gluon fusion mechanism. These conditions do not exist in the intrinsic charm approach and the ZM-VFNS is labelled an extrinsic charm process[10]. However, it is clear from the construction of the ZM-VFNS that it will not suffice as a good description of charm production in the region of the charm threshold. Hence, a modern approach is to extrapolate smoothly from the FFNS at low Q^2 to the ZM-VFNS at high Q^2 in order to produce a good description of the effect of charm quarks on structure functions over the whole range of Q^2. This may be done on the basis of phenomenological arguments [73] or using a more ambitious scheme of matching the coefficients of the two processes at all orders [75]. The scheme is referred to as the variable flavour number scheme (VFNS). In figure 2.10, a VFNS prediction for $F_2^{c\bar{c}}$ is seen to smoothly interpolate from the FFNS at low Q^2 to the ZM-VFNS at larger Q^2. The measurements of the charm structure function at HERA, performed in the range $Q^2 \geq 10$ GeV^2, do not, as yet, allow a distinction between the different schemes to be made.

2.8.3 Determination of the Gluon Density

The boson-gluon fusion mechanism has been shown to be the principal mechanism for the production of heavy quarks at HERA. The production rate is thus sensitive to the size of the gluon content in the proton. Therefore a complementary extraction of the gluon density, to the one obtained from the analysis of the scaling violations of F_2, can be made

[10]The experimental observation of the BGF process at values of Q^2 where the massless approach gives the correct description of the inclusive structure function ($Q^2 \gtrsim 30$ GeV^2), highlight the importance of large scales in the calculation of final state differential distributions [74].

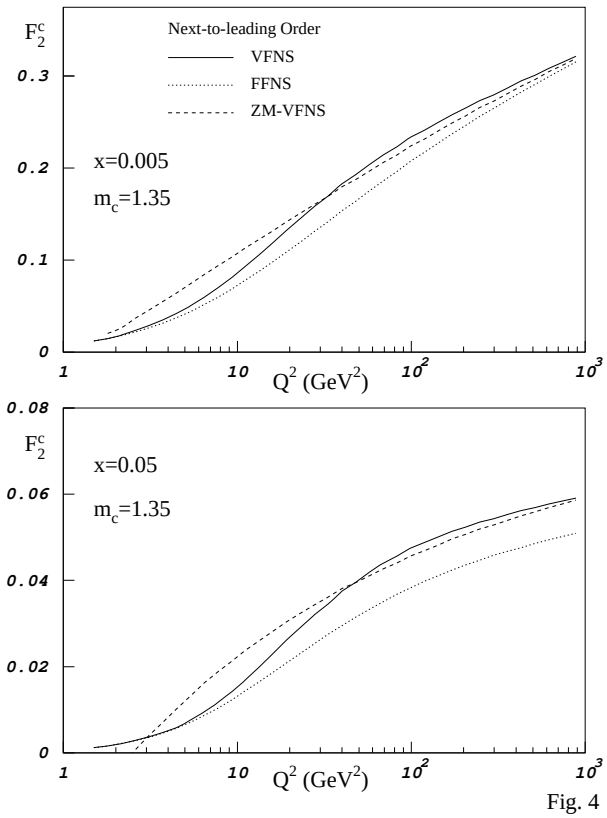

Figure 2.10: Example NLO predictions for $F_2^{c\bar{c}}$ as a function of Q^2 at (upper) $x = 0.005$ and (lower) $x = 0.05$. The variable flavour number scheme (VFNS) [75] is seen to smoothly continue from the FFNS at low Q^2 to the ZM-VFNS at higher Q^2.

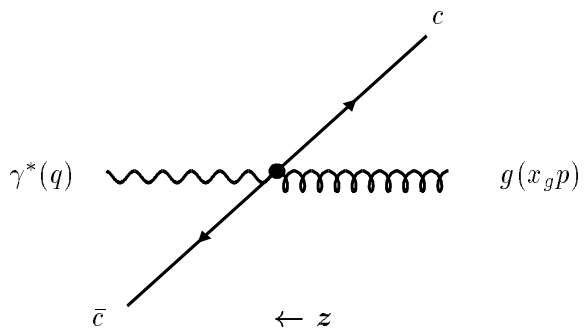

Figure 2.11: Diagram of the "$2 \rightarrow 2$ *parton*" boson-gluon fusion ($\gamma^* g \rightarrow c\bar{c}$) interaction in the hadronic centre of mass frame. The incoming gluon, g, in the limit of having zero transverse momentum, is collinear with the proton which defines the positive z axis. The virtual photon γ^* and the gluon have four-momenta q and $x_g p$ respectively.

by the measurement of the charm yield in the hadronic final state. Well defined hadron level variables may be constructed which are sensitive to the kinematics of the interacting partons, and therefore to the momentum distribution of the gluon. The measurement is referred to as direct since it is more sensitive, although statistically limited, to the local variations in the gluon density than the indirect method using scaling violations. In addition, the latter method assumes a parameterisation of the x dependence for the gluon distribution. The procedure employed by the H1 collaboration [48], which uses the measurement of the D^* meson cross section, is outlined below.

With the assumption that the charm quarks are produced by the boson-gluon fusion process, such that a "$2 \rightarrow 2$ *parton*" interaction occurs, then the kinematics are completely determined if the momentum of one ingoing and one outgoing particle, in this case the photon and either the charm quark or the charm anti-quark, are known. If the photon and the gluon entering the hard scattering have 4-momenta q and $x_g.p$ respectively (see figure 2.11), where p is the 4-momenta of the initial state proton, the outgoing di-quark system has squared invariant mass

$$\hat{s} = (x_g.p + q)^2 \tag{2.27}$$

With the assumption $m_p^2 = 0$, the fraction of the proton's momentum carried by the gluon involved in the hard interaction may be calculated as

$$x_g = x_{BJ}\left(1 + \frac{\hat{s}}{Q^2}\right) \tag{2.28}$$

where x_{BJ} is defined in equation 2.2.

In order to reconstruct $\hat{s}$ it is first necessary to define a Lorentz invariant quantity, z_c,

known as the elasticity, and which is given by

$$z_c = \frac{p.c}{p.q} \tag{2.29}$$

where c is the 4-momentum of the final state charm quark.

In the hadronic centre of mass and the laboratory reference frames, with the incoming proton defining the $+z$ direction, z_c may be written

$$z_c = \frac{(E^* - p_z^*)_c}{(E^* - p_z^*)_\gamma} = \frac{(E - p_z)_c}{(E - p_z)_\gamma} \tag{2.30}$$

where the subscripts c and γ refer to the charm quark and photon respectively and the superscript $*$ denotes the hadronic centre of mass quantites. In the hadronic centre of mass frame the $E - p_z$ of the gluon is zero, i.e. $(E^* - p_z^*)_g = 0$. Therefore, the conservation of $E - p_z$ in this frame results in the following relationships:

$$(E^* - p_z^*)_\gamma = (E^* - p_z^*)_{c\bar{c}} = (E^* - p_z^*)_{g\gamma} \tag{2.31}$$

$$(E^* - p_z^*)_{c\bar{c}} = (E^* - p_z^*)_c + (E^* - p_z^*)_{\bar{c}} \tag{2.32}$$

where the subscripts $c\bar{c}$ and $g\gamma$ refer to the charm quark anti-quark pair and the gluon-photon system respectively. Using these relations, an expression for $z_c(1 - z_c)$ can be calculated as

$$z_c(1 - z_c) = \frac{(E^* - p_z^*)_c (E^* - p_z^*)_{\bar{c}}}{(E^* - p_z^*)_\gamma^2} \tag{2.33}$$

Using the fact that $(p_z^*)_\gamma = (-p_z^*)_g$, the denominator of equation 2.33 can be written as

$$(E^* - p_z^*)_\gamma^2 = (E_\gamma^* + E_g^*)^2 = \hat{s} \tag{2.34}$$

In the centre of mass frame the charm quark and charm anti-quark have the same energy and their longitudinal momenta balance, i.e. $E_c^* = E_{\bar{c}}^*$ and $(p_z^*)_c = -(p_z^*)_{\bar{c}}$, so that

$$(E^* - p_z^*)_{\bar{c}} = (E^* + p_z^*)_c \tag{2.35}$$

Substituting the results of equations 2.34 and 2.35 into equation 2.33 gives

$$z_c(1 - z_c) = \frac{(E^{*2} - p_z^{*2})_c}{\hat{s}} = \frac{m_c^2 + p_{\perp c}^{*2}}{\hat{s}} \tag{2.36}$$

which can be re-arranged to give an expression for $\hat{s}$ which depends on the properties of the charm quarks in the hadronic centre of mass frame and z_c:

$$\hat{s} = \frac{m_c^2 + p_{\perp c}^{*2}}{z_c(1 - z_c)} \tag{2.37}$$

Experimentally, since z_c is a Lorentz invariant it is most easily evaluated in the laboratory frame as

$$z_c = \frac{(E - p_z)_c^{LAB}}{2yE_e} \tag{2.38}$$

where the relation $(E - p_z)_\gamma = 2yE_e$, which follows from equation 2.3, has been used.

In the presence of gluon radiation ($\gamma g \to c\bar{c}g$) (or similarly an intrinsic gluon transverse momentum) equation 2.28 holds only approximately. Also, in the hadronic final state the properties of the charm quark cannot be reconstructed directly and must be inferred from the measured D^* meson which carries only a fraction of the initial charm quark momentum. However, a hadronic observable, x_g^{obs}, which is well correlated with the true x_g in equation 2.28, may be constructed by replacing in equations 2.37 and 2.38,

$$p^*_{\perp c} \to 1.2\ p^*_{\perp D^*},\ (E - p_z)_c \to (E - p_z)_{D^*} \tag{2.39}$$

The factor 1.2 compensates for the average reduction in momentum of the D^* meson compared to the c quark. The definition of the observable x_g^{obs} is:

$$x_g^{obs} = x_{BJ}\left(1 + \frac{\hat{s}^{obs}}{Q^2}\right) \tag{2.40}$$

where

$$\hat{s}^{obs} = \frac{m_c^2 + (1.2\ p^*_{\perp D^*})^2}{z_{D^*}(1 - z_{D^*})} \tag{2.41}$$

and

$$z_{D^*} = \frac{(E - p_z)_{D^*}^{LAB}}{2yE_e} \tag{2.42}$$

In the H1 publication the cross section for D^* meson production was measured differentially as a function of the variable x_g^{obs}. The distribution in x_g^{obs} was then unfolded to the partonic variable x_g and the gluon density $x_g(x_g, \mu^2)$ extracted, where μ^2 is the factorisation scale and was chosen to be $\mu^2 = 4m_c^2 + Q^2$. The unfolding was done using a program [76] which involves a next-to-leading-order QCD calculation of the D^* cross section in the fixed flavour number scheme. The program is found to give a good description of all the differential D^* cross sections including x_g^{obs} and therefore may be reliably used for the extraction of the gluon density. The non-perturbative hadronisation of the charm quark into a D^* meson was modelled by convoluting the charm quark cross section with the Peterson fragmentation function [77] determined from e^+e^- annihilation data. The program therefore estimates the correlations between the hadronic and partonic quantities, x_g^{obs} and x_g, taking into account gluon radiation and hadronisation. The correlation

between x_g^{obs} and x_g is shown in figure 2.12a. The gluon density, extracted at an average scale $\mu^2 = 25$ GeV^2 is shown in figure 2.12b. The result for $x_g g(x_g)$ obtained from the scaling violations of F_2 measured by H1, at the same scale, is overlaid. A reasonable agreement is observed although, particularly at low x_g, the statistical uncertainty from the D^* method is very large. A similar extraction is performed in photoproduction and the resulting gluon density is in good agreement with that extracted in DIS, confirming the applicability of the QCD concepts employed and demonstrating the universality of the gluon distribution.

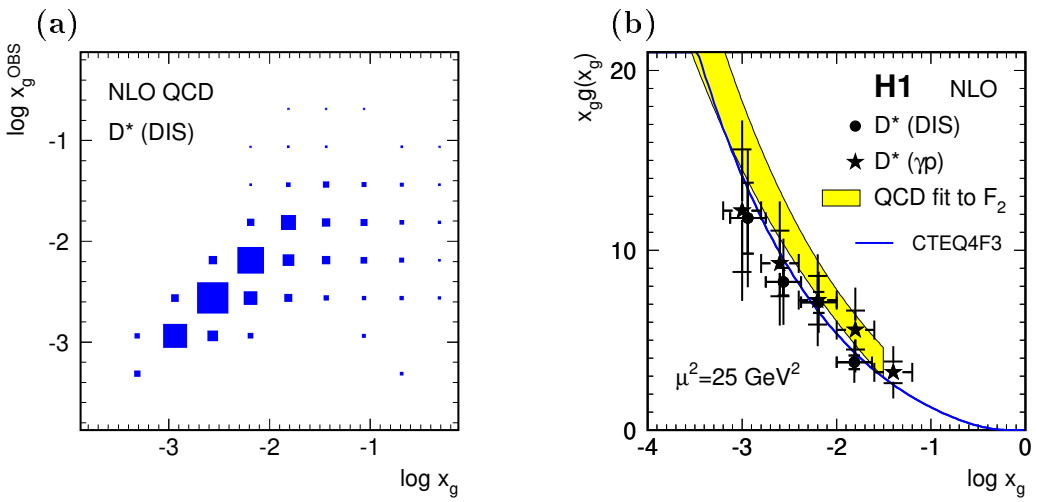

Figure 2.12: (a) The correlation between x_g^{OBS} as calculated from the D^* and electron momenta, and true momentum fraction x_g using a NLO calculation with the Peterson fragmentation function as implemented in the HVQDIS program [76]. (b) The gluon density of the proton determined at the scale $\mu^2 = 25$ GeV^2 from measurement of the D^* cross section in DIS and photoproduction [48]. The data are compared to the result of the H1 QCD analysis of F_2 (shaded band) and the CTEQ4F3 [78] parameterisation.

2.9 Summary

The measurement of the proton structure function at HERA provides a detailed testing ground for QCD. The rise of the structure function $F_2(x, Q^2)$ at low x is related to the rising gluon density in the proton, which can be extracted from the scaling violations of F_2. Inclusive data are described equally well, in the regions of their validity, by the DGLAP mechanism or by a mixture of BFKL and DGLAP evolution. The analysis of final states produced in DIS is also sensitive to the dynamics at low x. For example, the measurement of high transverse momentum single particle and jet rates in the forward direction at low x eliminates any model based on DGLAP evolution which does not contain a contribution from the internal structure of the photon. The low x region accessed by HERA allows the measurement of the charm structure function $F_2^{c\bar{c}}$. The contribution of charm to the total

structure function is found to rise with decreasing x. The production of charm is seen to be dominated by the boson-gluon fusion mechanism. A variable which is dependent on the momentum of the gluon entering the hard sub-process can be reconstructed using the measured momentum of the D^* mesons and the scattered electron. This allows the direct measurement of the gluon density, and the result is found to be consistent with the indirect value extracted from F_2.

The next chapter discusses the contribution of diffractive events to the proton structure function. As with the inclusive structure function, the production of charm in diffractive events is shown to be sensitive to the gluon content of the diffractive exchange.

Chapter 3

Diffraction

3.1 Introduction

In order to fully comprehend the strong interaction it is necessary not only to survey short range, hard partonic interactions, but also the long range, soft, interactions that constitute the bulk of hadron-hadron and hadron-photon cross sections at high energy. The soft hadronic physics interactions are characterised by low momentum transfer with the particles remaining intact or in very low mass excited states. This long range force is non-perturbative and only qualitatively understood within QCD.

The best description of soft hadronic interactions, developed before the advent of QCD, is given by the Regge phenomenological model [3], in which the scattering process is described by the t-channel exchange of mesons. In Regge models, to explain the slow rise of the total cross section at high energy a *diffractive* exchange is introduced, called the *pomeron*, to which no known meson can be firmly linked. Regge exchange processes are characterised by *rapidity gaps*, that is to say large regions of rapidity which contain no final state hadrons.

Large rapidity gap events observed at HERA constitute approximately 20% [79] of the cross section in photoproduction and 10% [80] in DIS and are attributed predominantly to pomeron exchange. If one can assume diffractive factorisation (see equations 3.21 and 3.22) the probe of the virtual photon in DIS may be able to shed light on the partonic structure of the pomeron. Perturbative QCD may be applicable to the exchange process. This provides the possibility of gaining an understanding of diffraction and the pomeron at the level of parton dynamics and of studying the transition between perturbative and non-perturbative QCD processes.

In section 3.2, a brief introduction to Regge theory is given. In section 3.3 the measurement of the diffractive structure $F_2^{D(3)}$ by the H1 experiment is described. In this section, the H1 data is confronted with a model based on Regge theory and QCD. Alternative models which also describe the diffractive structure function are discussed in sections 3.4 and 3.5. The different models of diffraction may be tested, in detail, by studies of the hadronic final state. A brief summary of the measurements performed thus far is presented in section 3.6. Finally, the models relevant to the production of open charm in diffraction are discussed in section 3.7.

3.2 Regge Theory

The general two-body scattering process, $AB \to CD$, where A, B, C and D denote the 4-vectors of the initial and final state hadrons, may be described in terms of two independent Mandelstam variables s and t, defined by

$$s = (A + B)^2 = (C + D)^2 \tag{3.1}$$

$$t = (A - C)^2 = (B - D)^2 \tag{3.2}$$

The variable s is the square of the centre of mass energy of the reaction. The variable t is the square of the 4-momentum transferred between the particles A and B, and is negative.

In field theories, interactions are described in terms of intermediate states that occur in the s-channel, as resonances, and in the t-channel, as exchanges. The exchanged objects in long range interactions are not viewed in terms of single gauge boson exchange but as being due to the exchange of virtual 'hadrons' that are net colour singlets. The generalised s and t-channel processes, as defined in this discussion, are shown in figure 3.1. The scattering amplitude in the t-channel is described by analytically continuing the amplitude for the resonance reaction in the crossed s-channel.

The simplest scattering amplitude to consider is that for the exchange of the lightest meson. For example, in the One Particle Exchange model [81] the amplitude for single π exchange contains a propagator of the form

$$T(s,t) \sim \frac{1}{m_\pi^2 - t} \tag{3.3}$$

and since t is negative for an exchange particle there is a singularity or *pole* in the unphysical, $t > 0$, region of the t-channel diagram, where $t = m_\pi^2$, which corresponds to the s-channel resonance.

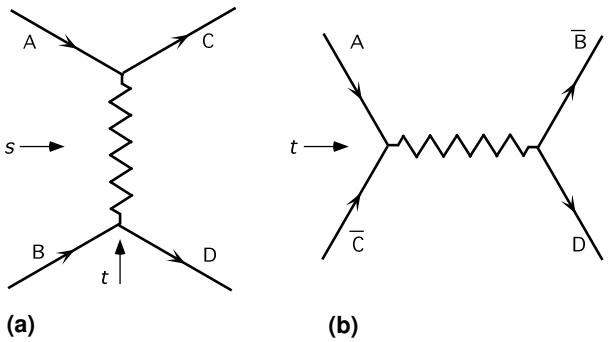

Figure 3.1: An illustration of the relationship between (a) the t-channel process $AB \to CD$ and (b) the corresponding crossed s-channel process $A\bar{C} \to \bar{B}D$.

For a more accurate and complete description of hadronic cross section amplitudes it is necessary to sum contributions from all possible exchanges with the appropriate quantum numbers, and this is done within the framework of Regge theory. The angular momentum and mass-squared of contributing exchange particles are simply related by a *Regge Trajectory*. For example, when the s-channel resonances (or bound states) are assembled in groups with identical quantum numbers (other than spin) and the spin is plotted against the square of the mass, the resonances are found to lie on approximately straight lines[1] as shown in figure 3.2. The trajectory in the s-channel, or at small $|t|$ in the t-channel, may be written in the linear form

$$\alpha(t) = \alpha(0) + \alpha' t \tag{3.4}$$

In the asymptotic limit ($s \to \infty$, $t/s \to 0$) the leading contribution to the scattering amplitude, $A(s,t)$, from a trajectory $\alpha(t)$, is given by:

$$A(s,t) \sim \beta(t) \left(\frac{s}{s_0}\right)^{\alpha(t)} \tag{3.5}$$

where $\beta(t)$ describes the coupling of the exchange to the external particles and s_0 defines the scale relative to which s must be large (usually ~ 1 GeV^2). The differential cross section for the t-channel scattering process is calculated as

$$\frac{d\sigma}{dt} \sim \frac{1}{s^2}|A(s,t)|^2 \tag{3.6}$$

$$\frac{d\sigma}{dt} \sim f(t) \left(\frac{s}{s_0}\right)^{2\alpha(t)-2} \tag{3.7}$$

[1]This linearity is understood within a QCD inspired model, if the meson consists of a quark anti-quark pair connected by a gluon flux string with energy proportional to its length [82].

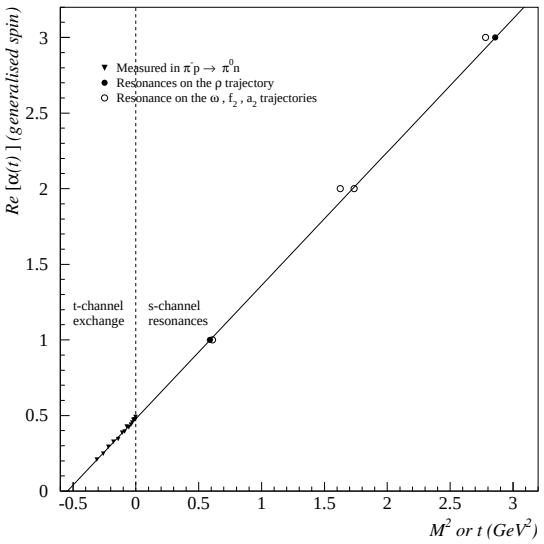

Figure 3.2: The exchange-degenerate leading meson trajectory, the Reggeon, $\alpha_{\mathrm{IR}}(t)$, containing the ρ, f, a and ω trajectories. An extrapolation of the trajectory at positive $M^2 \equiv t$ fits well through the points at negative t. The data shown with triangles at negative t are measured in the charge exchange reaction, $\pi^- p \to \pi^0 n$, and are taken from [83].

The *Optical Theorem* relates the elastic amplitude, $AB \to AB$, to the total cross section, $AB \to X$, by:

$$\sigma_{tot} \sim \frac{1}{s}\mathcal{I}m(A^{AB\to AB})_{t=0} \tag{3.8}$$

$$\sim s^{\alpha(0)-1} \tag{3.9}$$

where the second equality follows from equation 3.7 and from the fact that the elastic amplitude is almost pure imaginary.

All known meson trajectories have intercepts $\alpha(0)$ less than 0.6 and therefore, from equation 3.9, give contributions to the elastic and total cross sections that decrease with increasing centre of mass energy $\sqrt{s}$. Experimentally, total and elastic hadron cross sections decrease with $\sqrt{s}$ at low energy ($\sqrt{s} < 10$ GeV), but at high energy a slow increase with $\sqrt{s}$ is seen [84]. It was this fact which caused the Pomeranchuk trajectory, also known as the pomeron ($\mathbb{P}$), to be postulated [85]. The pomeron has the quantum numbers of the vacuum since it mediates elastic scattering. The pomeron trajectory [86] obtained from the measurement of total and elastic scattering cross sections at hadron-hadron experiments, is

$$\alpha_{\mathbb{P}}(t) = 1.08 + 0.25t \tag{3.10}$$

The processes which involve pomeron exchange are referred to as *diffractive*. The t dependence of the elastic process at fixed s looks similar to the classical diffraction pattern from the scattering of light from an opaque sphere.

Using the low $|t|$ parameterisation of equation 3.4, the t-channel elastic differential cross section may be written as

$$\frac{d\sigma}{dt} \sim f(t)\left(\frac{s}{s_0}\right)^{2\alpha(0)-2} e^{2\alpha' ln\left(\frac{s}{s_0}\right)t} \tag{3.11}$$

$$\sim \left(\frac{d\sigma}{dt}\right)_{t=0} e^{bt} \tag{3.12}$$

where b is known as the *slope parameter*

$$b \sim b_0 + 2\alpha' \ln\left(\frac{s}{s_0}\right) \tag{3.13}$$

and describes a logarithmic *shrinkage* of the forward ($t = 0$) peak for a process with centre of mass energy $\sqrt{s}$. The constant b_0 arises from the t dependence of $f(t)$ which is determined experimentally to be approximately exponential and is related to the hadron form factor. The slope parameter has a value in the range $5 - 10$ GeV^2 in elastic hadronic interactions. Despite being a phenomenological model, with as yet no solid basis in QCD, Regge theory is able to provide accurate predictions for the s and t dependencies of a wide range of hadronic interactions at low momentum transfer, over many orders of magnitude in s.

As well as being relevant to the elastic and total cross sections, diffraction also exists in inelastic processes, in which one or both of the interacting hadrons *dissociates* to an unbound state in a high mass continuum. Considering γp interactions and diffractive exchange, the dissociated state must still have identical quantum numbers to the incident photon or proton. In the case of *single photon dissociation* the photon dissociates into a system, X, of mass M_X, and the proton remains intact. Conversely, in *single proton dissociation* the proton dissociates into a system Y, of mass M_Y, and the system X is predominantly a vector meson with the quantum numbers of the photon ($J^{PC} = 1^{--}$). In *double dissociation* both incoming particles dissociate.

Regge theory provides predictions, based on the exchange trajectories, for the dynamics of inclusive hadronic processes involving dissociation. The region of phase space where $s \gg M^2 \gg t$, where M is the mass of the dissociating system, is referred to as the triple Regge region. In this region, as in the elastic case, diffractive exchange should be the dominant exchange. Triple Regge theory predicts that the masses of the dissociating systems, X and Y, exhibit an approximate $d\sigma/dM^2 \sim 1/M^2$ dependence at fixed s and that there is shrinkage of the slope parameter. The mass dependence of the dissociating

system has been demonstrated experimentally for hadron-hadron [87] and photoproduction [88] interactions. Shrinkage in diffractive dissociation has been demonstrated in $p\bar{p}$ data [89]. The slope parameter is observed to fall to approximately half of its elastic value by the triple Regge region [90]. Regge theory has also been successful in describing photoproduction data at HERA [79].

3.3 Structure of the Pomeron

3.3.1 Diffractive DIS Kinematics

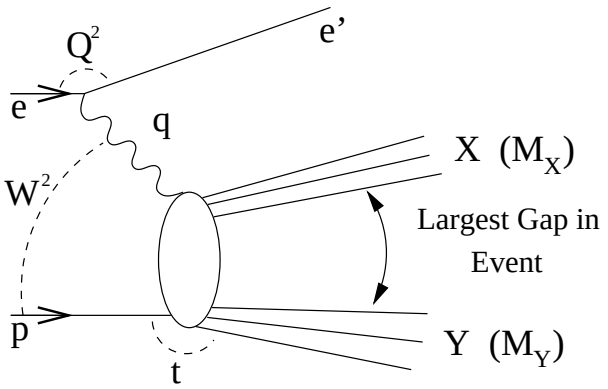

Figure 3.3: Diagram representing the Inclusive Deep-Inelastic Diffractive Scattering process. The process is described by the 4-vectors of the system X (X), the system Y (Y), the exchanged photon (q), the incoming proton (p), and the squared four-momentum transfer at the proton vertex (t).

The observation at HERA [91] of DIS events containing a large rapidity gap, between the proton system and the remainder of the hadronic final state, is suggestive of pomeron exchange. These events may be interpreted within the joint frameworks of Regge theory, QED and QCD as a highly virtual photon effectively probing the structure of the diffractive exchange. In diffractive DIS the same conventional kinematics introduced to describe DIS events in section 2.2 apply, but additional invariants are defined, in terms of the 4-vectors of figure 3.3, as follows:

$$M_Y^2 = Y.Y \tag{3.14}$$

$$M_X^2 = X.X \tag{3.15}$$

$$t = (p - Y)^2 \tag{3.16}$$

$$= (q - X)^2 \tag{3.17}$$

$$x_{I\!P} = \frac{q.(p-Y)}{q.p} \sim \frac{Q^2 + M_X^2}{Q^2 + W^2} \tag{3.18}$$

$$\beta = \frac{Q^2}{2q.(p-Y)} \sim \frac{Q^2}{Q^2+M_X^2} \tag{3.19}$$

The approximation made is that t, and the mass of the proton and electron are small compared to the centre-of-mass energy. Like x for the proton, β is the fraction of the momentum of the pomeron interacting with the photon. In the limit $t \to 0$, $x_{I\!P}$ is the fraction of the momentum of the proton carried by the pomeron. It is useful to note that $x = x_{I\!P}\beta$.

3.3.2 Diffractive Structure Function

By analogy with the total proton structure function F_2, a diffractive structure function may be completely defined with five degrees of freedom,

$$\frac{d^5\sigma_{ep\to eXY}}{d\beta\ dQ^2\ dx_{I\!P}\ dt\ dM_Y} = \frac{4\pi\alpha_{em}^2}{\beta Q^4}\left(1-y+\frac{y^2}{2}\right)F_2^{D(5)}(\beta,Q^2,x_{I\!P},t,M_Y) \tag{3.20}$$

where the photo-absorption ratio for diffraction, $R^{D(5)}$, is set to zero.

The variables β, Q^2 and $x_{I\!P}$ are reconstructed from the scattered electron and/or the diffracted hadronic final state. The system Y is usually not measured directly and the resolution in t, which may be reconstructed from the transverse momentum of the system X, is very poor. Therefore, an integration is performed over the two unmeasured quantities in the range $M_Y < 1.6$ GeV and $|t| < 1$ GeV^2 to produce measurements of $F_2^{D(3)}(\beta,Q^2,x_{I\!P})$. For most measurements $x_{I\!P}$ is required to be less than 0.05, so that Y takes at least 95% of the momentum carried by the initial state proton. In this kinematic region non-zero isospin exchanges (e.g. π exchange) are suppressed and the cross section is dominated by single photon dissociation processes $\gamma^* p \to Xp$.

It should be noted that the diffractive structure function F_2^D defined in equation 3.20 is the proton structure function F_2 integrated over a limited phase space defined by 5 variables. Therefore, no subtraction of background processes is performed to obtain the true 'diffractive' (i.e. pomeron) contribution. This has the advantage that the measured cross section is well defined at the hadron level and no assumption about the nature of the interaction is made.

It has been suggested [92] that the diffractive structure function given by equation 3.20 is dominated by pomeron exchange so that it may be factorised into two independent terms;

$$F_2^{D(3)}(\beta,Q^2,x_{I\!P}) = f_{I\!P/p}(x_{I\!P})\ F_2^{I\!P}(\beta,Q^2) \tag{3.21}$$

where $f_{I\!P/p}(x_{I\!P})$ is the t-integrated pomeron flux associated with the proton and $F_2^{I\!P}(\beta,Q^2)$ is the pomeron structure function which is sensitive to the parton distributions of the

pomeron. Regge theory describes the presumed flux factor in terms of soft dynamics by,

$$f_{I\!P/p}(x_{I\!P}, t) \sim f(t) \left(\frac{1}{x_{I\!P}} \right)^{2\alpha(t)-1} \tag{3.22}$$

where $\alpha(t)$ is the pomeron trajectory.

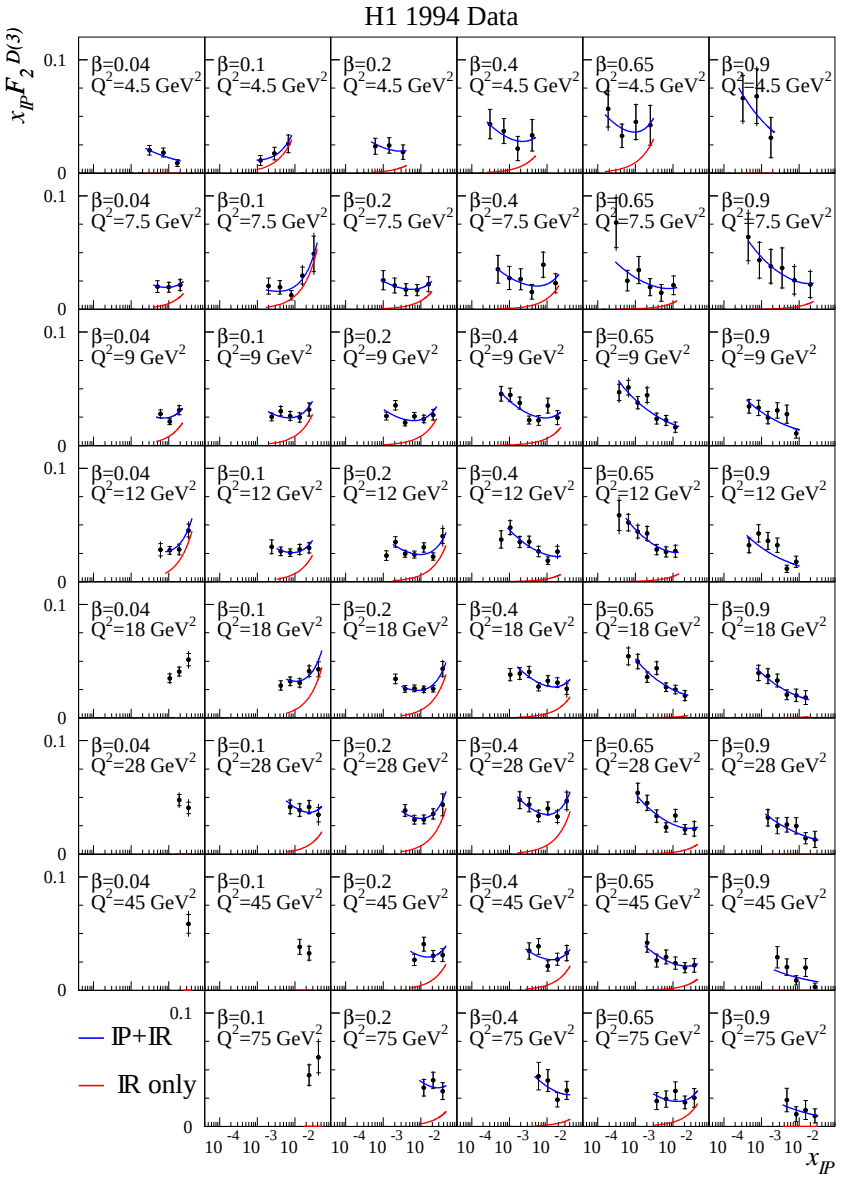

Figure 3.4: The diffractive structure function, as measured by H1 [4], plotted as $x_{I\!P} F_2^{D(3)}(x_{I\!P}, \beta, Q^2)$ against $x_{I\!P}$ for different β and Q^2 values. The curves show the result of a Regge parameterisation with the reggeon contribution (lower line), and the total pomeron plus meson contribution (upper line).

The latest measurement of $F_2^{D(3)}$ by H1 [4] shows a $1/x_{I\!P}$ dependence, very different to that expected for a leading meson trajectory, but consistent with the exchange being

dominated by the pomeron. However, the data prove to be inconsistent with the assumption of pomeron dominance across the whole kinematic range, because the $x_{I\!P}$ dependence changes at large $x_{I\!P}$ in some β and Q^2 ranges as shown in figure 3.4. A natural explanation for this feature is that there is a contribution from the exchange of the set of mesons which lie on the approximately degenerate reggeon trajectory $\alpha_{I\!R}(t) \simeq 0.55 + 0.9t$ that contains the ρ, ω, a and f mesons. The reggeon trajectory has the highest intercept of all meson trajectories and therefore its contribution survives to higher centre of mass energies. The measured diffractive structure function can be parameterised in the following form which retains factorisation individually for both pomeron and reggeon exchange:

$$F_2^{D(3)} = f_{I\!P/\mathrm{p}}(x_{I\!P}) F_2^{I\!P}(\beta, Q^2) + f_{I\!R/\mathrm{p}}(x_{I\!R}) F_2^{I\!R}(\beta, Q^2) \tag{3.23}$$

where now $f_{I\!R/\mathrm{p}}(x_{I\!R})$ is the reggeon flux and $F_2^{I\!R}(\beta, Q^2)$ the reggeon structure function. A fit to the H1 data, with this Regge parameterisation, produces a consistent meson intercept and for the pomeron an intercept of

$$\alpha_{I\!P}(0) = 1.203 \pm 0.020(stat.) \pm 0.013(sys.)^{+0.030}_{-0.035}(model) \tag{3.24}$$

The t dependence of the trajectories cannot be constrained by the data and so are assumed to be the same as those obtained from analyses of hadron-hadron data. The value of $\alpha_{I\!P}(0)$ measured in equation 3.24 is significantly larger than the value measured in hadron-hadron experiments and displayed in equation 3.10. It also exceeds appreciably the value $\alpha_{I\!P}(0) = 1.068 \pm 0.016(stat.) \pm 0.022(sys.) \pm 0.041(model)$ which was obtained from an H1 analysis of the photon diffractive dissociation cross section in photoproduction [79].

If the factorisation hypothesis of equation 3.23 is correct then the structure functions $F_2^{I\!P}(\beta, Q^2)$ and $F_2^{I\!R}(\beta, Q^2)$ describe the deep-inelastic structure of the pomeron and meson exchanges respectively. The pomeron structure function term $F_2^{I\!P}(\beta, Q^2)$ can then be expressed in terms of quark distributions in the same way as the proton structure function F_2:

$$F_2^{I\!P}(\beta, Q^2) = \beta \sum_i e_i^2 f_i(x, Q^2) \tag{3.25}$$

where $f_i(x, Q^2)$ is the parton density function for each parton family i, of charge e_i, within the pomeron. In this picture, the pomeron structure function is understood in terms of parton dynamics and its evolution therefore ought to be calculable using perturbative QCD. Models which treat the pomeron as though it were a hadron composed of partons are referred to as *resolved* or *factorisable* pomeron models. H1 has extended the phenomenological model discussed above and assigned parton distributions to the pomeron and meson [4]. The non-perturbative pomeron and meson parton distributions are parameterised at a starting scale $Q_0^2 = 3$ GeV^2 and the distributions evolved, with

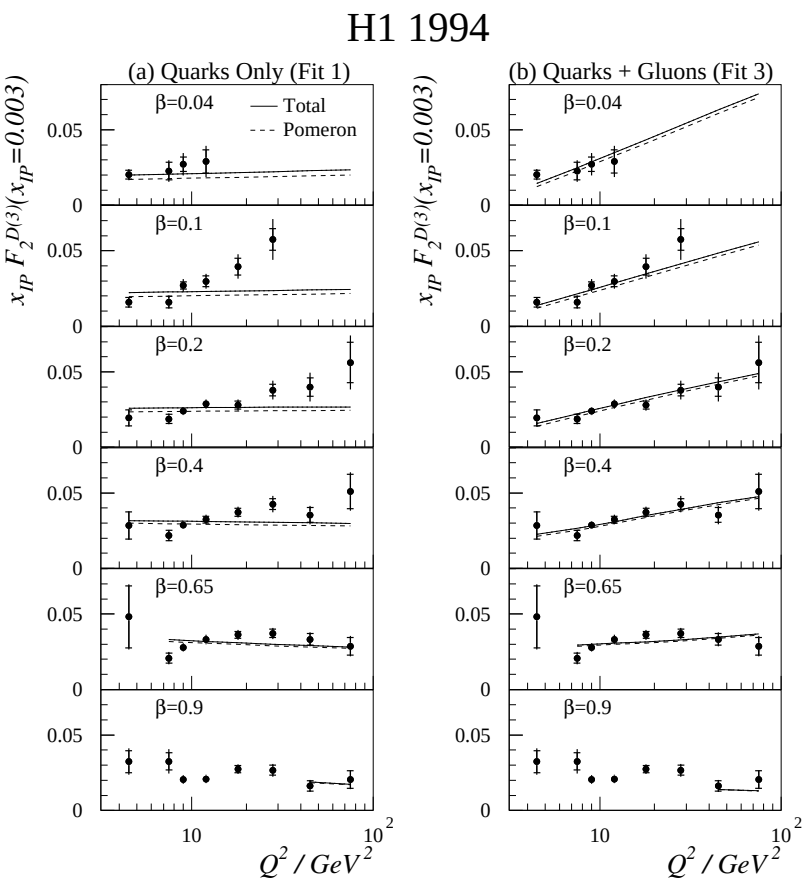

Figure 3.5: The value of $x_{I\!P} F_2^{D(3)}(x_{I\!P}, \beta, Q^2)$ at $x_{I\!P} = 0.003$ as a function of Q^2 for different values of β. In both (a) and (b) the solid points show the data. The results of QCD fits are superimposed by the full line with the pomeron contribution in the fit shown by a dashed line. (a) the result of QCD fit 1 (only quarks contribute to pomeron structure at $Q^2 = 3$ GeV^2) (b) QCD fit 3 (both quarks and gluons contribute).

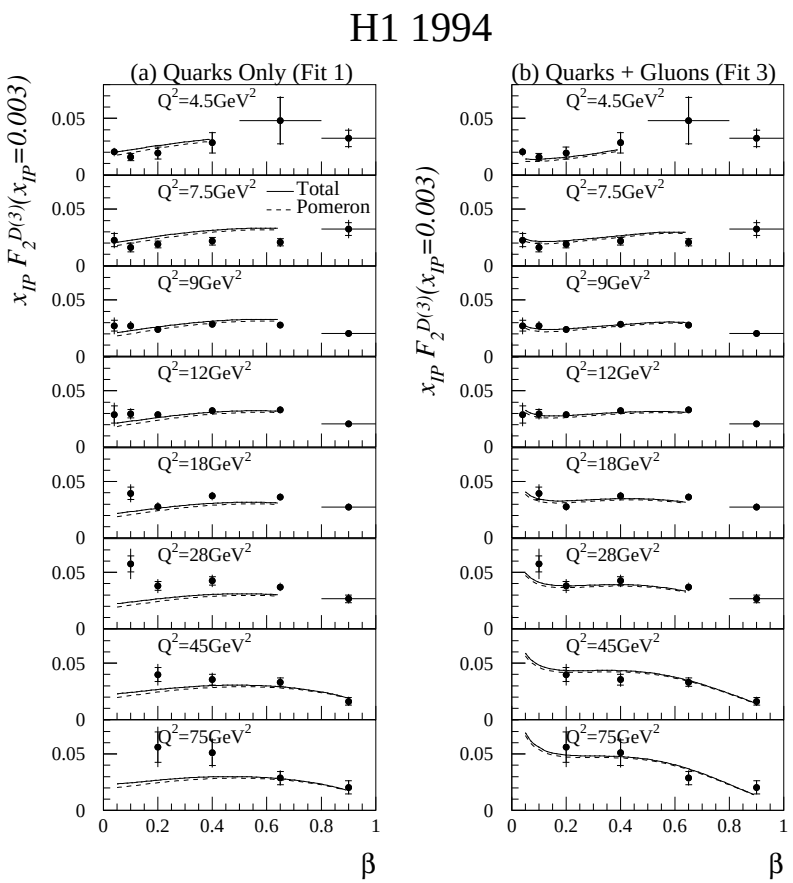

Figure 3.6: The value of $x_{I\!P} F_2^{D(3)}(x_{I\!P}, \beta, Q^2)$ at $x_{I\!P} = 0.003$ as a function of β for different values of Q^2. In both (a) and (b) the solid points show the data. The results of QCD fits are superimposed by the full line with the pomeron contribution in the fit shown by a dashed line. (a) the result of QCD fit 1 (only quarks contribute to pomeron structure at $Q^2 = 3$ GeV^2) (b) QCD fit 3 (both quarks and gluons contribute).

increasing Q^2 according to the DGLAP equations presented in section 2.4.1. For the pomeron, the input distributions are parameterised using a quark flavour singlet distribution ($z\mathcal{F}_q(z,Q^2) = u + \bar{u} + d + \bar{d} + s + \bar{s}$) and a gluon distribution ($z\mathcal{F}_g(z,Q^2)$), where z is the fractional momentum of the pomeron carried by the struck parton. If the photon couples directly to a quark intrinsic to the pomeron structure then $z = \beta$, whereas if the photon interacts via boson-gluon fusion with a gluon from the pomeron structure then the relation $0 < \beta < z$ holds. The QCD fits are confined to the region $y > 0.45$, just as for the phenomenological Regge fits, in order to limit the uncertainty introduced by the lack of knowledge of $R^{D(5)}$. Data points with values of M_X less than 2 GeV are also omitted in order to exclude the large contribution of higher twist processes in this region, including the production of resonant vector mesons.

The data are confronted with three different starting parameterisations for the pomeron parton distributions. In fit 1 only quarks are assumed to contribute at the starting scale. The resulting parameterisation of $F_2^{D(3)}$ is shown at a fixed value of $x_{I\!P} = 0.003$, where pomeron exchange is expected to dominate, as a function of Q^2 for different values of β in figure 3.5a, and as a function of β for different values of Q^2 in figure 3.6a. The parameterisation clearly fails to describe the scaling violations of $F_2^{D(3)}$. In fit 2 a contribution from gluons is introduced at the starting scale and this significantly improves the quality of the fit. In fit 3 two further terms in a polynomial expansion are introduced for the gluon distribution and this improves slightly the description of the data. Fit 3 is shown in figures 3.5b and 3.6b, and can be seen to reproduce the scaling violations of $F_2^{D(3)}$ in Q^2 and the dependence on β. The introduction of further degrees of freedom in the shape of the gluon distribution beyond those allowed in fit 3 does not improve the quality of the fit.

The resulting parton distributions for fit 2 and fit 3 are shown in figure 3.7 for three different values of Q^2. For both fits, a large fraction of the pomeron momentum is carried by the gluons. This contribution decreases with increasing Q^2 from $\sim 90\%$ at $Q^2 = 4.5$ GeV^2 to $\sim 80\%$ at $Q^2 = 75$ GeV^2. The fit to the data is better for fit 3 with a gluon distribution that is concentrated at high z; so that at low values of Q^2 the majority of the pomeron momentum is carried by a single gluon. These two features support models of diffractive DIS in which the dominant mechanism is boson-gluon fusion with the incoming gluon carrying a large fraction of the momentum of the pomeron. The gluonic nature of the exchanged object can be inferred by direct comparison of the scaling violations of $F_2^{D(3)}$ and F_2. The diffractive structure function rises with $\ln Q^2$ at fixed β, as with F_2 at low x, but this behaviour persists to values of β as high as 0.65.

The analysis of the diffractive structure function thus far has been performed within the

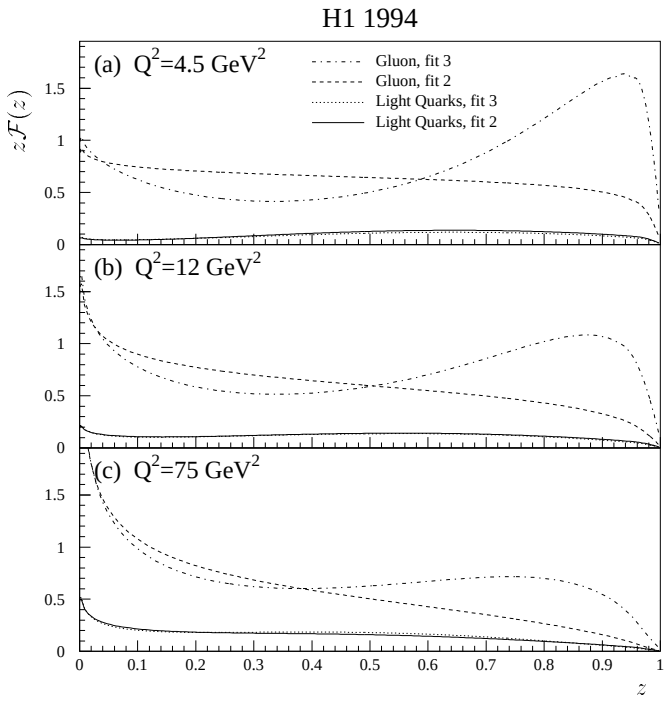

Figure 3.7: The contribution of the light quark and gluon distributions to $z\mathcal{F}(z)$ for QCD fits 2 and 3 at (a) $Q^2 = 4.5$ GeV^2, (b) $Q^2 = 12$ GeV^2 and (c) $Q^2 = 75$ GeV^2.

framework of a model in which the pomeron can be factorised. The majority of diffractive DIS models available assume factorisation. The cross section for diffractive scattering is treated as the product of a non-perturbative (soft) flux factor, $f_{\mathbb{P}/\mathrm{p}}(x_{I\!P}, t)$, taken from Regge fits to previous γp or pp data, and a perturbative factor describing the hard interaction between the virtual photon and a parton from the pomeron. The parton densities obtained from DGLAP QCD fits of the structure function may then be used to make predictions of diffractive final state properties in both ep and pp scattering which are expected to be highly sensitive to the difference between q and g dominated exchanges [93]. The H1 parton distributions from fits 1 to 3 described above are implemented in a factorisable pomeron model within the RAPGAP Monte Carlo program [54].

3.4 Dipole Models

It is informative to treat diffractive $\gamma^\star p$ scattering as partonic fluctuations of the photon scattering elastically from the proton. At high energy, in the proton rest frame, the photon fluctuates into partons long before the interaction with the proton occurs. The simplest fluctuation or lowest Fock state of the photon is the formation of a $q\bar{q}$ pair. The

$q\bar{q}$ pair may radiate additional gluons, the next state being $q\bar{q}g$, before it interacts with the proton.

The attractive feature of this approach is that the $q\bar{q}$ splitting of the photon is calculable using only QED. The $q\bar{q}g$ wavefunction of the photon is not yet fully calculated, although it can be approximated by a dipole consisting of a $q\bar{q}$ colour octet and a gluon [94]. Many properties of the final state, in particular the β distribution, can be derived from the partonic wavefunctions of the photon alone. The dipole based approach allows separate consideration of longitudinal and transverse photon contributions. It can also account for higher twist contributions such as the elastic production of vector mesons.

3.4.1 A Two Gluon Exchange Model

The simplest realisation of the pomeron in perturbative QCD is as two gluons in a net colour singlet state. A parameterisation [94] in terms of leading and higher twist contributions from transverse and longitudinal polarised photons for two gluon exchange can give a reasonable description of $F_2^{D(3)}$ data. The parameterisation, proposed by Bartels, Ellis, Kowalski and Wüsthoff (BEKW), derives β and Q^2 dependences from the $q\bar{q}$ and $q\bar{q}g$ wavefunctions of the photon and the two gluon exchange to the proton. The energy dependence of the gluon pair is not predicted and thus the $x_{I\!P}$ dependence is parameterised in a form similar to the asymptotic limit in Regge theory.

The contributions of the various polarised Fock states, resulting from the parameterisation of H1 data, are shown in figure 3.8. The parameterisation reveals different contributions in three distinct regions of β. The low β region ($\beta \lesssim 0.3$) is dominated by $q\bar{q}g$ produced from transversely polarised photons, the medium β region by $q\bar{q}$ pairs arising from transversely polarised photons, and the large β ($\beta \gtrsim 0.9$) region by longitudinally polarised $q\bar{q}$ states. The longitudinal contribution is suppressed by $1/Q^2$ since it represents the higher twist region which was excluded from the QCD fits discussed in section 3.3.2. When added together the different contributions produce a relatively flat dependence on β at low Q^2.

3.4.2 A Semi-Classical Model

Fluctuations of the photon are also considered in the semi-classical model of Hebecker, Gehrmann and Buchmüller [95]. In this picture, the interaction of the partons from the photon with the proton is described by the superposition of colour fields of the proton according to a simple non-perturbative model that averages over all colour field configura-

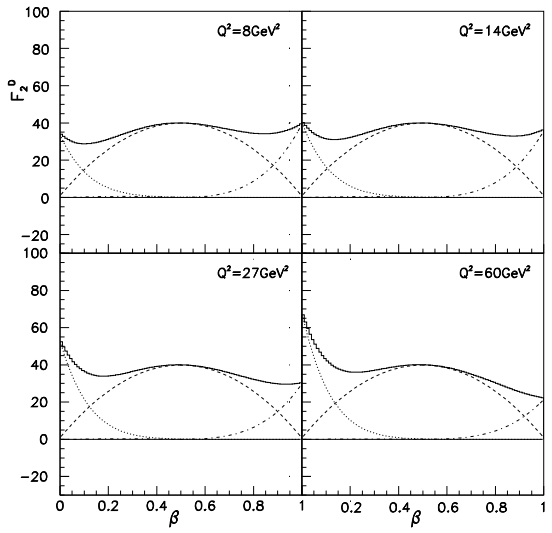

Figure 3.8: The β dependence of $F_2^{D(3)}$ at a constant value of $x_{I\!P} = 0.001$ in a parameterisation of the H1 $F_2^{D(3)}$ data using the model of BEKW [94]. The dotted line shows the contribution of $q\bar{q}g$ Fock states arising from transversely polarised photons, the dashed line the contribution of $q\bar{q}$ Fock states also arising from transversely polarised photons, the dashed-dotted line the contribution of $q\bar{q}$ pairs from longitudinally polarised photons, and the full line the total sum.

tions. The diffractive cross section can be re-expressed as a more conventional convolution of parton distributions with parton cross sections. The higher order corrections are equivalent to the logarithmic corrections in the conventional parton approach, such that the usual DGLAP evolution equations can be used where β and Q^2 are the relevant variables for evolution. A fit is performed to F_2^D to obtain initial diffractive parton distributions at some low scale Q_0^2 which, when evolved to higher Q^2 using the DGLAP equations, give a reasonable description of the data. At the starting scale ($Q_0^2 = 1.2$ GeV^2) the contribution of gluons to the parton distribution function is approximately three times as large as the contribution from quarks. The quark distribution is peaked at $\beta \approx 0.65$ at the starting scale, whereas the gluon distribution dominates the lower β region ($\beta \approx 0.4$).

At sufficiently small x in this model, the energy dependence of F_2^D factorises from the dependence on β and Q^2. The rise of F_2^D at low x is due to the non-perturbative energy dependence of the averaging of the soft colour configurations in the proton. The results from the best fit are compared to H1 data in figure 3.9. The description of the data is reasonable except in the region which is excluded from the fit due to the contribution of higher twist effects.

When the fluctuations of the photon into either a $q\bar{q}$ or $q\bar{q}g$ state, as viewed in the proton

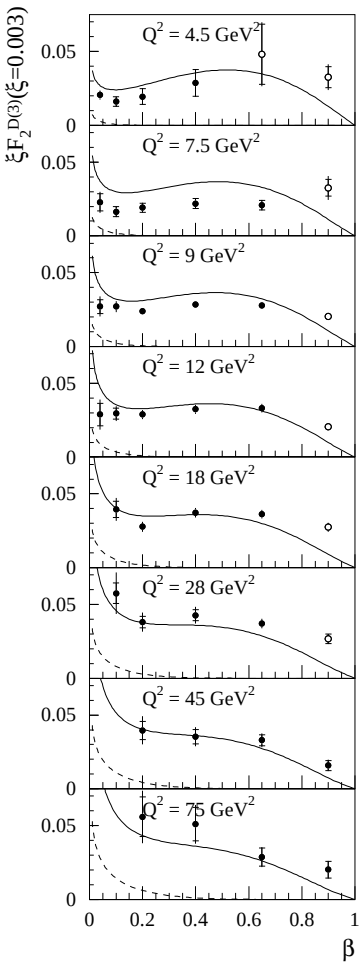

Figure 3.9: The dependence of the diffractive structure function $F_2^{D(3)}$ on β and Q^2 at fixed $x_{I\!P} = \xi = 0.003$ in the semi-classical model [95], compared to H1 data [4]. The open points correspond to $M_X^2 \leq 4\ \mathrm{GeV}^2$ where higher twist effects are likely to be important. They are excluded from the fit. The charm content of the structure function, which is produced in the massive scheme via boson-gluon fusion, is indicated as a dashed line.

rest frame, are boosted into the Breit frame (see figure 3.10) the production processes are quark scattering and boson-gluon fusion respectively. In the case of $q\bar{q}g$ fluctuations the gluon emitted by the photon appears in the final state system X in the Breit frame. The direct analogy between the factorisable pomeron picture, where there is a 'soft' pomeron remnant, and the fluctuations of the photon, where the non-perturbative aspects of the problem are treated in the density or colour field of the proton is non-trivial. However, in processes which are perturbatively calculable (such as high $p_\perp$ jets and charm production) the measurement of the hadronic final state is a powerful test of the contribution of the various Fock states of the photon to the system X.

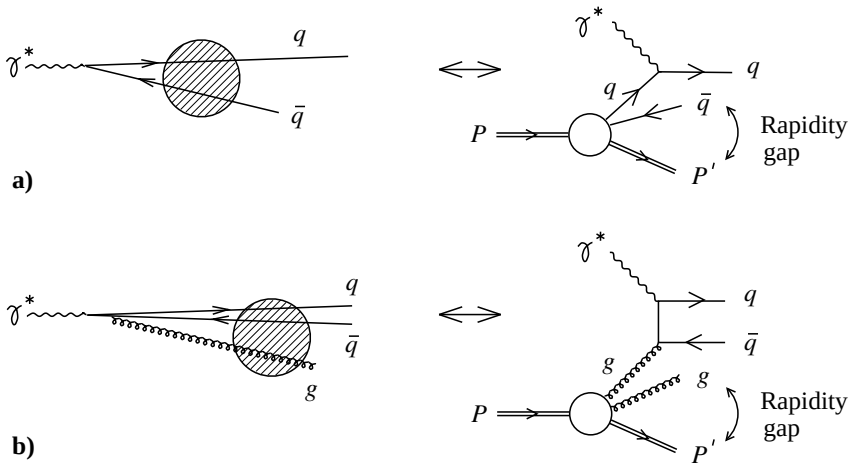

Figure 3.10: Diffractive DIS as modelled by photon fluctuations interacting with the colour field of the proton; in the proton rest frame (left) and the Breit frame (right). (a) $q\bar{q}$ fluctuations correspond to quark scattering, (b) $q\bar{q}g$ fluctuations correspond to diffractive boson-gluon fusion.

3.5 Soft Colour Interactions

The second alternative model to the resolved pomeron model considered here is the mechanism of *soft colour interactions* (SCI) proposed by Edin, Ingelman and Rathsman [96]. This assumes that the underlying hard interaction is the same in all DIS processes (diffractive and non-diffractive), and it is subsequent soft interactions that lead to a colour-singlet current system in some events. In the model proposed in [96], each pair of coloured partons in the partonic state emerging from the hard interaction may interact, exchanging low momenta partons, such that colour but not momentum is exchanged. The probability of SCI taking place is described using a single adjustable parameter. The model is implemented in the Monte Carlo generator LEPTO 6.5 which enables detailed comparisons with diffractive hadronic final state data. In the description of $F_2^{D(3)}$, the model describes adequately the shape of the $x_{I\!P}$ distribution although the evolution in Q^2 is not as well described as in the models discussed previously, although there are considerably fewer parameters in the SCI model.

3.6 The Hadronic Final State in Diffraction

The study of the hadronic final state in diffraction plays a vital role in understanding the underlying parton dynamics of large rapidity gap events. In the factorisable pomeron model, the properties of the hadronic final state are sensitive to the partonic composition

of the pomeron and reveal whether the pomeron is a quark or gluon dominated object. In models which treat diffraction as the scattering of partonic fluctuations of the photon from the proton, the hadronic final state is sensitive to the relative contributions of $q\bar{q}$ and $q\bar{q}g$ states.

The parton distributions extracted from the H1 QCD analysis of $F_2^{D(3)}$ when implemented in the RAPGAP Monte Carlo program are able to describe measurements of event thrust [97], energy flow, charged particle spectra [98], and charged particle multiplicities and their correlations [99] in diffractive DIS. This confirms the picture that the pomeron is a gluon dominated object and therefore the dominant production mechanism is boson-gluon fusion from the gluon distribution of the pomeron.

The study of high $p_\perp$ diffractive dijets [100] [101] has been, to date, the most powerful test of the shape, and in contrast to the analyses above, the normalisation of both the quark (e.g. via $\gamma q \rightarrow qg$) and gluon (e.g. via $\gamma g \rightarrow q\bar{q}$) densities in the pomeron. The normalisation and shape of the dijet measurements are best described by models containing parton distributions dominated by hard gluons at the starting scale. For comparison, quark dominated diffractive parton densities result in dijet rates that are significantly smaller than those measured. The parton distributions with a large gluon content at the starting scale are also found to be valid when they are compared to the cross section measurements of photoproduction of dijets. The $p_\perp$ of the jets provides a 'hard' factorisation scale for evolving the parton distributions.

The final state dijets can be used to construct hadronic variables that are sensitive to the fraction of the photon and pomeron momentum carried by the partons entering the hard scattering. For example, a hadronic estimate of $z_{I\!P}$, labelled $z_{I\!P}^{jets}$, can be made and is shown in figure 3.11 for the measurement of dijets in DIS by H1 [100]. The QCD fits 2 and 3 which contain a large fraction of gluons at the starting scale are seen to give a good description of the shape and normalisation of the cross section differential in $z_{I\!P}^{jets}$. The soft colour interaction mechanism, as implemented in the LEPTO 6.5 Monte Carlo model, also gives an acceptable description of the diffractive dijet measurements. In fact, agreement is found between the SCI model and all the other diffractive DIS final state measurements discussed so far. When the $z_{I\!P}^{jets}$ distribution is compared to a model based on the scattering of partonic fluctuations of the virtual photon [102], the measured rate cannot be described by a simulation based on the $q\bar{q}$ Fock state of the transverse photon alone. Fluctuations to states containing one or more gluons are therefore expected to be dominant in the high $p_\perp$ and high M_X region probed in dijet production.

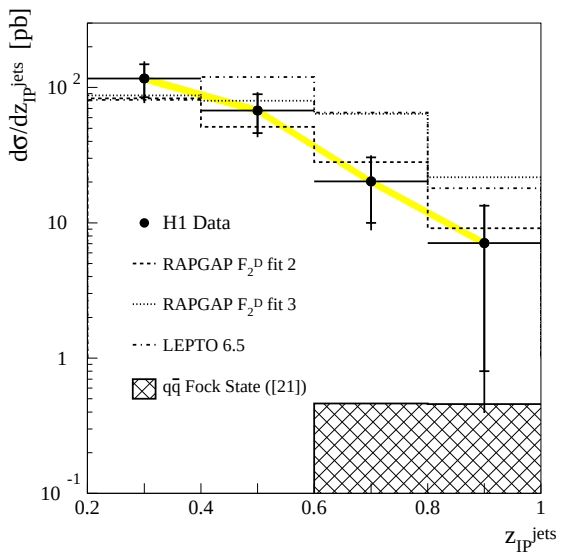

Figure 3.11: The differential cross section in $z_{I\!P}^{jets}$ for diffractive dijets in DIS as measured by H1 [100]. The data are compared to Monte Carlo models with parton densities corresponding to $F_2^{D(3)}$ fit 2 and $F_2^{D(3)}$ fit 3. Also shown is the prediction of the SCI model implemented in the LEPTO 6.5 Monte Carlo program, and a prediction [102] based on the diffractive scattering of the $q\bar{q}$ Fock state of the transversely polarised photon.

3.7 Diffractive Charm Production Models

In section 2.8 it was shown that the principalproduction mechanism for charm at HERA is the boson-gluon fusion mechanism. The parton distributions obtained from DGLAP QCD fits to $F_2^{D(3)}$ indicate a large hard gluon content to the pomeron. Therefore, in the factorisable pomeron approach the measurement of charm in diffraction provides a powerful and direct test of the gluon content of the diffractive exchange. It is useful to note that the error on the gluon content of the pomeron from DGLAP QCD fits to F_2^D is of the order of 50% at high z.

The predictions of diffractive charm production models that are relevant to the comparisons with the data studied in this thesis are discussed in this section. The predictions of three models are treated in turn. These are the factorisable pomeron model, the model of soft colour interactions and the model of perturbative two gluon exchange. First it will be necessary to introduce two further variables which are needed to describe the kinematics of the charm quarks and whose distributions are sensitive to the underlying production process.

3.7.1 Definition of Variables

The kinematic variables describing the charm quarks in the laboratory frame will be distinguished from those in the centre of mass by the use of a superscript $*$ in the centre of mass system. The definition of the co-ordinate system, adopted in this thesis, is that the plane of the outgoing electron defines the positive x axis in the hadronic centre of mass frame. The azimuthal difference between the scattered electron plane and the charm quark anti-quark plane is labelled by the angle ϕ^* as in diagram 3.12.

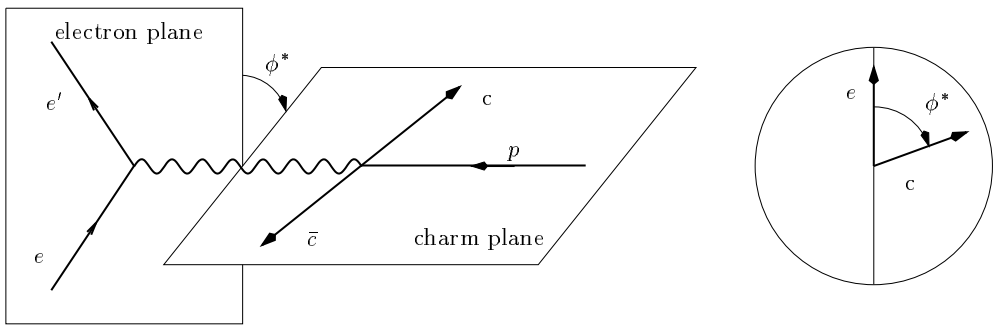

Figure 3.12: Definition of the azimuthal angle ϕ^* in the centre of mass system.

The fraction of the pomeron momentum carried by the parton entering the hard scattering, $z_{I\!P}$, was introduced in section 3.3.2 in relation to the pomeron parton distributions and referred to again in section 3.6 in relation to dijet production. In the case of charm production, $z_{I\!P}$ may be written as

$$z_{I\!P} = \beta \left(1 + \frac{\hat{s}}{Q^2}\right) \tag{3.26}$$

$$\simeq \frac{Q^2 + \hat{s}}{Q^2 + M_X^2} \tag{3.27}$$

Noting that $\beta = x_{BJ}/x_{I\!P}$ and with reference to the definition for x_g, given by equation 2.28, $z_{I\!P}$ may be stated simply as

$$z_{I\!P} = \frac{x_g}{x_{I\!P}} \tag{3.28}$$

The parton level predictions for diffractive charm production, of the three models considered, for $x_{I\!P}$, β, $z_{I\!P}$ and $|\phi^*|$ are collected together for comparison in figure 3.13.

3.7.2 Factorisable Pomeron Predictions

Parton distributions extracted from QCD fits to the diffractive structure function $F_2^{D(3)}$ may be used as input for calculating the production of charm in diffraction [103]. In this

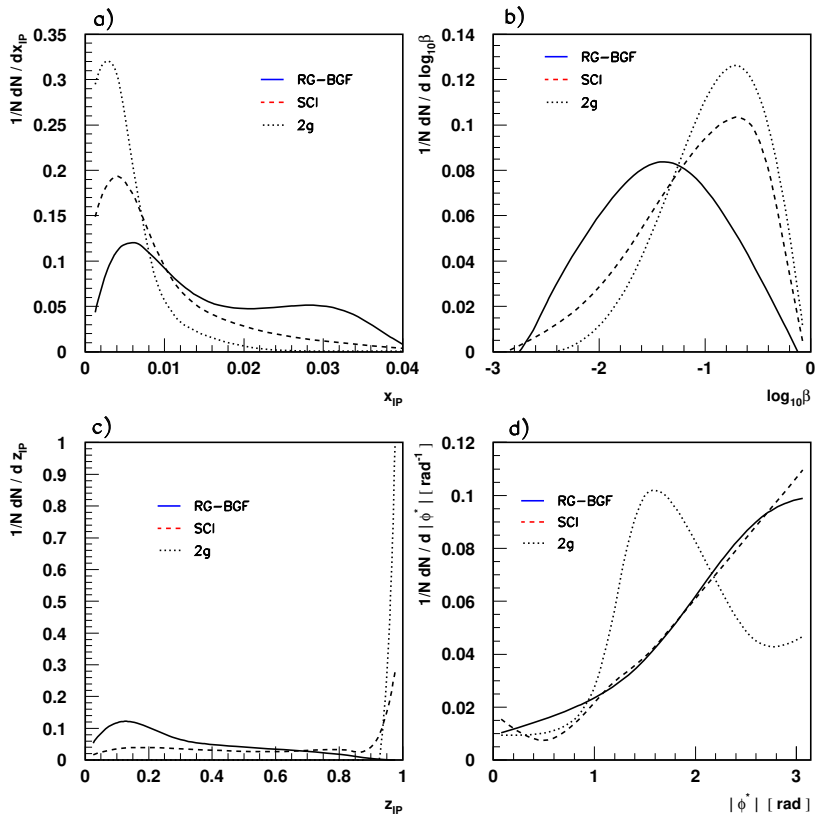

Figure 3.13: The parton level prediction for diffractive $c\bar{c}$ production in DIS for the factorisable pomeron model (RAPGAP-BGF) (full line), the SCI model (dashed line), and the 2 gluon model (dotted line). Distributions are shown for (a) $x_{I\!P}$ (b) β (c) $z_{I\!P}$ and (d) $|\phi^*|$. The $|\phi^*|$ distribution is shown for the charm quark which has the largest transverse momentum in the laboratory frame. The predictions are normalised to the number of events in each generated sample, N.

thesis predictions are made using the parton distributions obtained by H1 [4] and the RAPGAP Monte Carlo program (see section 7.2 for more details). The charm quarks are produced only from the gluon distribution of the pomeron in $c\bar{c}$ pairs via the boson-gluon fusion mechanism as shown in figure 3.14a. The parton distributions are evolved with a factorisation scale usually involving the charm quark mass, for example $Q^2 + 4m_c^2$, and therefore are applicable for Q^2 values lower than that for which the original QCD analysis was performed.

The $x_{I\!P}$ distribution in RAPGAP (see figure 3.13a) is peaked towards lower values; which is due to the fact that pomeron exchange contributes 90% of the cross section. The 10% contribution from reggeon exchange is restricted to larger values of $x_{I\!P}$. The mass of the diffractive system, M_X, covers a wide range, starting from the threshold for two charm

quarks at ~ 3 GeV, extending up to ~ 100 GeV. The largest masses are achieved because both the charm quark pair and the pomeron remnant are produced in the system X. The large available mass of the diffractive system implies that there are significant contributions in the low β ($\beta < 0.1$) region (figure 3.13b). Similarly, the momentum fraction of the pomeron carried by the gluon entering the hard sub-process, $z_{\mathbb{P}}$, is dominated by low values (figure 3.13c).

The kinematic distributions of the charm quarks in factorisable models are characteristic of the boson-gluon fusion mechanism. For example, the transverse momentum distribution in the hadronic centre of mass system is relatively hard. Also, in the hadronic centre of mass, the plane in which the charm quark pair are produced is dominantly coplanar with the plane of the scattered electron (i.e. $|\phi^*| = \pi$) (see figure 3.13d).

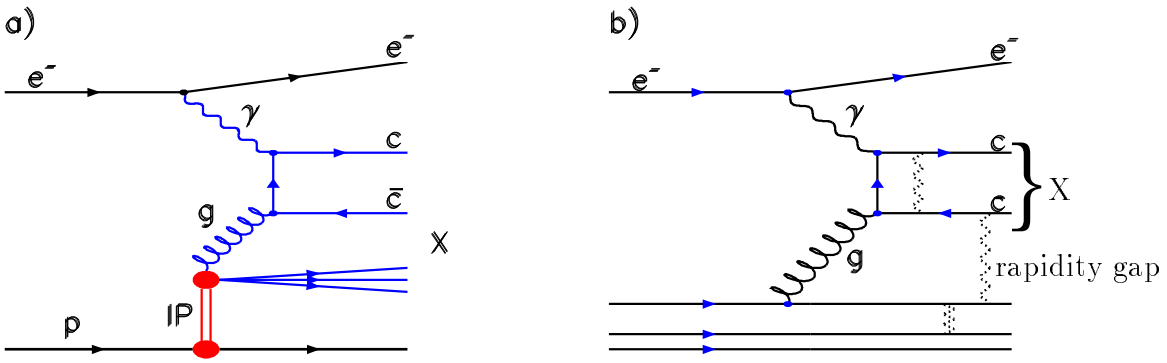

Figure 3.14: The production of diffractive open charm in DIS. (a) The factorisable pomeron model. The $c\bar{c}$ and the pomeron remnant are produced in the system X. (b) Soft colour interactions. The underlying process is BGF. Soft colour exchanges produce large rapidity gap events.

3.7.3 SCI Predictions

The soft colour interaction mechanism described in section 3.5, is implemented for charm production in the AROMA [112] Monte Carlo model. The model produces charm via the leading order boson-gluon fusion matrix element from the gluon distribution of the proton, as shown in figure 3.14b. Therefore, the transverse momentum $p_\perp$ and the azimuthal angle ϕ^* distributions (figure 3.13d) are similar to those in the factorisable pomeron model. The mass of the diffractive system, M_X, in the SCI model is determined by the radiation of gluons from the final state $c\bar{c}$ pair. In contrast to the production of light quarks, the gluon radiation from the quark anti-quark pair is suppressed by the large mass of the charm

quark. Therefore the mass of the diffractive system M_X and hence $x_{I\!P}$ is relatively small (figure 3.13a) and β is predominately large (figure 3.13b).

3.7.4 Perturbative Two Gluon Exchange Predictions

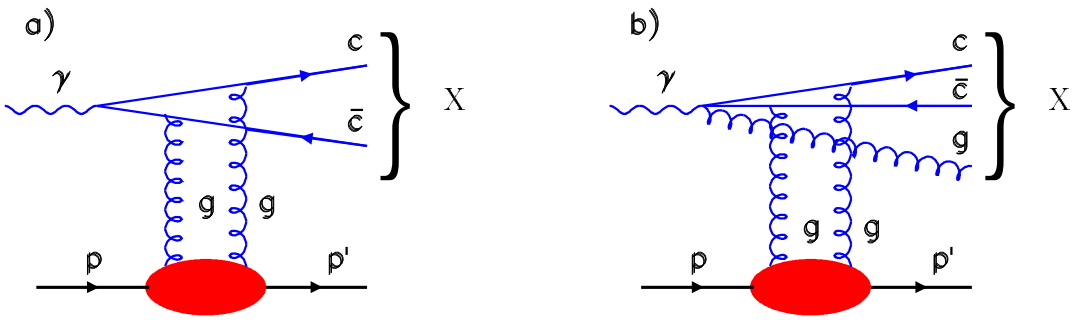

Figure 3.15: The production of diffractive open charm in the perturbative two gluon exchange model. (a) For the photon Fock state $c\bar{c}$ (b) For the higher order Fock state $c\bar{c}g$.

The production of charm in diffraction via partonic fluctuations of the photon into a $c\bar{c}$ pair which then interacts with two perturbative gluons from the proton have been investigated by Bartels et al [102]. The cross section formula has been calculated explicitly for the fluctuation of the photon into a $c\bar{c}$ pair, as shown in figure 3.15a. The calculation is implemented within the RAPGAP Monte Carlo program. Estimates of the higher order effects due to gluon emission have also been made [104] (see figure 3.15b), although the full calculation has not yet been performed. For the simplest $c\bar{c}$ state, the colour transparency mechanism suppresses the cross section when the transverse separation of the two partons is small [105]. Colour transparency occurs when the colour fields of the charm quark and anti-charm quark, which have opposite colour, overlap and effectively cancel one another so that their colour field is not 'visible' to the proton. The transverse separation of the two partons is inversely proportional to their transverse momenta in the centre of mass frame of the hard interaction. Therefore, the cross section for $c\bar{c}$ states is expected to be significant only for comparatively small transverse momenta of the outgoing partons in the centre of mass frame. The $x_{I\!P}$ distribution (see figure 3.13a) rises at low $x_{I\!P}$ which is related to the rise in the gluon density of the proton at low x. The entire diffractive mass is shared by the quark anti-quark pair. Therefore, the fluctuation of the photon into a $c\bar{c}$ pair is restricted to the high β region, and $z_{I\!P}$ is effectively one (see figures 3.13b and 3.13c). The M_X spectrum extends from threshold to around 20 GeV.

In direct contrast to the boson-gluon fusion mechanism, the azimuthal angle between the

electron scattering plane and the charm quark anti-quark scattering plane in the hadronic centre of mass frame, is peaked at $|\phi^*| = \pi/2$ (see figure 3.13d). In principle this should allow a clear distinction between the two processes to be made. Experimentally, however, the presence of any higher fluctuations of the photon (which are analogous to boson-gluon fusion in the Breit frame) will reduce the difference in the ϕ^* distributions.

3.8 Summary

The phenomenological model of Regge theory successfully describes the vast majority of total, elastic and dissociative cross sections in hadron-hadron and photoproduction (including HERA) interactions at high energy. The observation of diffractive events in DIS at HERA allows the partonic structure of the pomeron to be probed using a hard virtual photon. When the measured diffractive structure function $F_2^{D(3)}$ is confronted with a model in which the pomeron flux is based on Regge phenomenology, and perturbative QCD describes the β and Q^2 evolution of the partons within the pomeron, a large gluon content to the pomeron is revealed. When these parton distributions are used as input to describe the diffractive hadronic final state they are found to give an excellent description of the shape and normalisation of the data. Within this resolved pomeron model, the large gluon content to the pomeron suggests a large rate for charm production via the boson-gluon fusion mechanism. The prediction for charm production of the soft colour interactions model, which also gives a good description of all the diffractive final state data, is seen to differ from the partonic pomeron model, allowing the possibility that the processes may be distinguished on the basis of charm measurements. When viewed in the proton rest frame, the measurement of charm in diffraction is sensitive to the relative contribution of different fluctuations of the photon to the diffractive system.

Chapter 4

Event Selection and Kinematic Reconstruction of DIS Events

4.1 Introduction

This chapter lays the foundation for the selection of DIS data for the measurement of both the inclusive D^* cross section in chapter 6 and the diffractive D^* cross section in chapter 8. The selection of events to be analysed aims for a balance between loose cuts, which gain the highest statistical significance of the measurement and tighter cuts that achieve the lowest background contamination. The criteria applied to the quality of the data in this analysis are introduced in section 4.2.

The steady increase in luminosity at HERA has meant that H1 has had to be increasingly selective in the data written to tape. The major consequence for this analysis is the downscaling of low Q^2 DIS events on-line at the level 4 trigger. The data is then reconstructed off-line (level 5) and the events classified into physics sub-classes. In order to minimise any systematic bias in the calculation of the event efficiency in the analysis, a level 5 event class that combines a high and easily understood efficiency with a minimum amount of level 4 downscaling is chosen. The pre-selection performed in this 'Inclusive Final State' event class is discussed in section 4.3.

The DIS events used in this analysis are triggered by a level 1 trigger based on the identification of an electron candidate in the backward calorimeter, the SPACAL, and a significant number of tracks associated with the event vertex in the central tracking detector; at least one of which has high transverse momentum. The details of the analysis sub-trigger are given in section 4.4. The method of reconstructing the parameters of the electron cluster and its associated track, and further cuts to reduce the background from

sources such as interactions of the beams with the beam-pipe walls or residual gas particles in the beam-pipe, and photoproduction are discussed in section 4.5. The experimental method of reconstructing the kinematical variables x, y and Q^2 is described in section 4.6.

4.2 Selection of Quality Data

The data used in this analysis were collected during the 1995, 1996 and 1997 running periods when HERA collided 27.5 GeV positrons with 820 GeV protons. The following selections on the quality of the data taken during this period are imposed:

- Detector High Voltages and Read-out:
  Only data recorded during periods when the sub-detectors essential to the analysis had fully operational read-out and high voltage systems are used. The relevant components are the CJC2, the inner tracking chambers CJC1 and CIZ, the BDC, the liquid argon and SPACAL calorimeters, the time-of-flight scintillators and the luminosity system.

- Trigger Phase:
  There are four different trigger phases during a luminosity fill. Each phase has a set of prescale factors for the sub-triggers, which are formulated to provide a tolerable input rate to the level 4 processing farm for the varying beam conditions of a luminosity fill. Phase 1 is activated at the start of the fill when HERA declares luminosity and the beam currents and backgrounds are correspondingly high. All sub-triggers, apart from those responsible for triggering the largest Q^2 events, are heavily prescaled in this difficult period as the sub-systems of the detector are turned on. Once all the detectors are on and the beam currents have decreased, such that the input to the level 4 farm also decreases, then the next phase can be entered and the prescales of the sub-triggers can be reduced. The four trigger phases have successively lower prescales for the high rate triggers. For example, when phase 4 is reached the electron beam current is typically one half its original value, allowing the majority of the SPACAL sub-triggers to operate without a prescale. Runs recorded in phase 1 are excluded in this analysis because the SPACAL triggers are highly prescaled and the high-voltages of the tracking detectors are being ramped up for the majority of the phase. All data from phases $2-4$ are, however, included in the analysis.

- Additional Requirements for 1995 data;
  The 1995 data were the first to be taken with the newly commissioned components,

the BDC and the SPACAL. There were various hardware problems associated with their installation. To ensure that these problematic periods were excluded, a more detailed run selection is used [106], which ensures that there is a working SPACAL trigger and a reliable energy calibration.

The effect of the run selection, trigger phase, detector and read-out requirements on the luminosity, for each of the three years, is shown in table 4.1. Since the main aim of this thesis is the measurement of the diffractive D^* cross section, the high voltage and readout of the Forward Muon Detector is also required to be operational. The major effect of this extra condition is the exclusion of a period of luminosity at the start of the 1997 running period, the effect of which is shown in the row labelled 'Additional Run Selection' in table 4.1. The effect of an inoperational Forward Muon Detector in the remaining run range is small and produces a reduction in the luminosity of around 5%. Further details about the high-voltage and read-out requirement on the Forward Muon Detector are given in section 7.4.1. The effect of the extra conditions applied in the run selection for the 1995 data is also shown in the 'Additional Run Selection' row of table 4.1.

The exclusion of phase 1 runs has a large effect on the luminosity from the 1997 running period because of problems with changing phase at the central trigger. The correction due to satellite bunches (see section 1.8) is calculated for the condition that the vertex lies within 40 cm of the run averaged z vertex. The requirement of an operational detector read-out produces a small, though important, correction. After these corrections, the combined luminosity of the three data samples is 23.32 pb^{-1}.

Condition	$\int \mathcal{L}\, dt$ (pb^{-1})			
	1995	1996	1997	sum
All Runs	5.465	9.356	21.570	36.391
Additional Run Selection	2.981	9.356	18.854	31.191
Trigger Phase 2-4	2.981	8.984	15.243	27.208
Satellite Correction	2.895	8.314	14.198	25.407
HV status OK	2.696	7.476	13.624	23.796
All Systems in Readout	2.442	7.425	13.452	23.319
Average prescale	1.225	1.028	1.157	

Table 4.1: The effect of increasing the quality criteria on the data selection for each of the three samples 1995,1996,1997 and their total. Starting from the total luminosity for all reprocessed runs and demanding that; any additional run selection is made (see text for details), the trigger phase is in the range 2-4, satellite bunches greater than 40 cm in z from the nominal run vertex are removed, the detector high-voltage (including the Forward Muon Detector) is operational, and the readout systems are operational. The luminosity weighted average of the prescale applied to the sub-trigger used in the analysis is shown in the last row.

4.3 The Event Classification

4.3.1 Level 4 Downscaling

The on-line level 4[1] trigger subjects all photoproduction and low Q^2 ($Q^2 < 6$ GeV^2) DIS events to a series of algorithms called 'finders' which search for a particular hadronic final state of interest, such as a reconstructed heavy flavour meson or baryon, or a high $p_\perp$ jet. If no topology of particular interest is found in the hadronic final state, the event is rejected in photoproduction and downscaled in DIS. The downscaled DIS events are given an *L4 weight*, increasing with decreasing Q^2, and from this weight a statistically accurate representation of the original distribution can be obtained.

The most obvious L4 'finder' available for the measurement of the D^* cross sections in this thesis searches for the decay $D^* \to K\pi\pi_{slow}$ (see section 5.6) using tracks reconstructed in the central tracking detector. The 'finder' uses information from the CJC, determined with the on-line calibration, to reconstruct the D^* candidate. When the same data is reprocessed off-line, with improved calibration constants and the z chamber information added where available, differences as large as 10% in the number of tracks passing the selection occur. To reduce this effect in the final off-line analysis, the already quite severe track cuts would need to be tightened once more, which leads to a further reduction in the efficiency for D^* reconstruction[2]. This problem, combined with the fact that the overall event efficiency is already complicated by the track conditions imposed by the level 1 sub-trigger (see section 4.4), means that an alternative solution for selecting the data needs to be sought.

4.3.2 The 'Inclusive Final State' Event Class

The 'Inclusive Final State' event class, formulated in the level 5 off-line selection, provides an inclusive low Q^2 event sample with a tolerable data volume by introducing a number of kinematic cuts to reduce the amount of background contamination. A small area of the kinematic range at low y, associated with high background rates from beam-gas and beam-pipe interactions, is sacrificed. There is no corresponding level 4 'finder' for this

[1]The downscaling of data by the level 4 trigger occurred only for the 1997 data. However, the 1996 data is subjected to a similar downscaling at level 5, such that the same principles of the discussion are applicable to this data set. For the 1995 data there was no downscaling of events at either level 4 or level 5 and the event class used is 100% efficient. See sections 1.10 for a discussion of the on-line level 4 trigger and the off-line reconstruction (level 5).

[2]The track cuts of the L4 'finder' are around 10% less efficient than those used in this analysis. The efficiency of the analysis track cuts is evaluated in section 6.5.

event class. The 'Inclusive Final State' class therefore contains a fraction of events that were downscaled by the level 4 trigger. However, the majority of the events selected in this analysis are saved at level 4, either by the high $p_\perp$ jet 'finder' or another heavy flavour meson 'finder'. The average L4 weight for the final event sample in the kinematic region ($Q^2 < 6$ GeV^2) is 1.0012, such that the precise origin of the level 4 downscaling, including the fluctuations due to different detector calibrations, does not have to be understood in detail. In the case of diffraction, studied in chapter 8, the amount of downscaling is further reduced by the operation of a diffractive 'finder'.

To be classified as an 'Inclusive Final State' event, for the data recorded in 1996, the full set of selection criteria is as follows:

- there must be an electromagnetic cluster reconstructed in the SPACAL with energy > 9 GeV;
- the radial position of the centre of gravity of the SPACAL cluster must be > 8 cm;
- the average time of signals from the cells within the electromagnetic cluster, $\hat{t}_{cell}$, is required, if defined, to be in the range expected for ep interactions, $7 < \hat{t}_{cell} < 20$ ns;
- The $\sum(E - p_z)$ of the hadronic final state, where the sum is over all calorimeter clusters including the scattered electron, is required to be in the range $25 < \sum(E - p_z) < 70$ GeV;
- there must be a fitted primary vertex within 50 cm, along the z axis, of the average vertex for the run;
- there must be at least one track reconstructed in the Central Tracking Detector in the angular region $22^o < \theta < 150^o$ which has a transverse momentum $p_\perp > 150$ MeV with at least 10 wire hits.

additionally for the 1997 data set the following conditions are implemented

- the minimum radial position of the centre of gravity of the SPACAL cluster is reduced to > 7.5 cm;
- phase 1 trigger runs are excluded;
- the value of y, reconstructed using the electron method (see section 4.6) with the electron parameters obtained from the SPACAL cluster, is required to be $y > 0.05$.

In formulating the final analysis selection it is usually pertinent to perform tighter cuts than those in the event classification. The event classification is not performed on the final energy scale and small fluctuations occur in the reconstruction of event kinematics after the final calibration or due to alternative reconstruction techniques. The analysis cuts described in section 4.5, except those in the electron energy and y, are tighter than those in the event classification. The differences in the measurement of the electron energy and angle (and hence in y) between the event classification and final analysis are small (of the order of 0.5%) and are well described by the detector simulation. This allows the final analysis cuts in these variables to be made at the same values as those used in the event classification.

From detector simulations, the loose track requirement in the 'Inclusive Final State' class is found to be 100% efficient for the cuts on the D^* used in this analysis. The imposition of only a loose track requirement in the event class means that the efficiency of the track cuts made in the analysis can be studied using the data.

4.4 The Analysis Sub-Trigger

The majority of the data were collected with a sub-trigger operating at level 1 only, which demanded a signal from the SPACAL IET-trigger (see section 1.11.1), in coincidence with a charged track signal from both the $zvtx$ trigger (see section 1.11.2) and the $r-\phi$ trigger (see section 1.11.3). The precise definition of the sub-trigger arrangement changed several times during the data taking periods of 1996 and 1997[3]. The changes were necessary to reduce the background rate, which varied with the beam conditions, in order to keep the amount of prescaling to a minimum. The basic definition of the sub-trigger is as follows:

- The entire acceptance of the SPACAL is used by combining IET trigger elements in the central and outer regions. The energy threshold of the trigger for an electromagnetic cluster is uniform across the surface of the SPACAL and is either, approximately, 2 or 6 GeV depending on the run range.

The large background rate for this sub-trigger, particularly in the case of the very lowest electron energy threshold, is suppressed by the following tight track requirements

- A significant peak in the z-vertex histogram given by the $zvtx-sig$ trigger element.

[3]For the 1995 data sample the trigger efficiency is close to 100%, and the systematic error is taken from [107].

- The $r\phi - T_{high}$ trigger element is required so that at least one track above a threshold of $p_\perp > 800$ MeV is reconstructed in the central jet chamber.

In addition, conditions are applied to reject out-of-time background

- An absence of activity outside the window expected for ep interactions is demanded in the time-of-flight detectors of the hadronic and electromagnetic sections of the SPACAL, the FToF scintillators and the BToF scintillators.

4.5 Selection of DIS Events

Events triggered by the analysis sub-trigger which pass the 'Inclusive Final State' event class criteria form the basis of the event selection. This section describes the final cuts, in the selection of DIS events, which are made on the electron candidate in the SPACAL (section 4.5.1), on the $\sum(E - p_z)$ of the final state (section 4.5.2) and on the event vertex (section 4.5.3). The cuts are summarised in table 4.2.

4.5.1 The Electron Candidate

The energy deposits in each neighbouring cell of the SPACAL are combined into clusters. The cluster energy, E_{clus}, is formed by summing the single cell energy E_i of the ith cell of the n cells assigned to the cluster. The centre of gravity of the cluster, $\mathbf{r}_{clus}$, is determined from cells which have energy greater than 0.01 GeV using the following formulae,

$$\mathbf{r}_{clus} = \frac{\sum_{i=1}^{n} w(E_i)\mathbf{r}_i}{\sum_{i=1}^{n} w(E_i)} \quad ; \quad w = \sqrt{E_i} \tag{4.1}$$

where $\mathbf{r}_i$ is the centre of gravity of the ith cell. This 'square root' weighting enhances the contribution of cells near to the cluster centre, which improves the impact point determination [16]. The centre of gravity of a cell, $\mathbf{r}_i$, is taken as the geometric centre of a cell. A special weighting is used to take into account the effect of energy loss in the cells of the SPACAL insert [108].

The longitudinal position of the cluster, z_{clus}, is obtained from a parameterisation of the longitudinal component of the electromagnetic shower development, implemented in the detector simulation [109], which is dependent on the cluster energy, E_{clus}, and given by

$$z_{clus} = aE_{clus} + b\log(cE_{clus}) \tag{4.2}$$

where a, b and c are constants.

The largest source of background clusters in the SPACAL is that from photoproduction events ($Q^2 \sim 0$), since the cross section is approximately two orders of magnitude higher than that for the low Q^2 DIS range measured in this analysis. In photoproduction, the final state electron is almost undeflected and travels down the beam-pipe. However, for a fraction of the photoproduction events an electron signature is faked in the SPACAL by particles from the hadronic final state. Typically, the fake electron candidates in the SPACAL stem from photon conversions ($\gamma \to e^+e^-$) from showering in the dead material before the calorimeter. The photons are usually produced from the abundant flux of π^0 mesons via the decay $\pi^0 \to \gamma\gamma$. Furthermore, the overlap of charged hadrons with photons, for example a $\pi^\pm$ and γ, can produce a charged track in the tracking detector and an electromagnetic cluster in the calorimeter. Also, purely hadronic showers can be classified as electromagnetic due to statistical fluctuations in the shower development.

In order to reject photoproduction background and beam-gas interactions the cluster with the highest energy that passes the following criteria is selected as the electron candidate:

- **Energy of the cluster - E_{clus}**
  As a cut against hadrons faking an electron candidate, the centre of gravity of the reconstructed cluster and 90% of the cluster energy must lie within the electromagnetic part of the SPACAL. The energy of the electron cluster, E_{clus}, must be larger than 9 GeV.

- **Timing of the Cluster - t_{hot}**
  To reject out-of-time proton beam induced background which, due to different path lengths, arrives early in the SPACAL, the time-of-flight of the cell with the largest energy within the cluster, t_{hot}, must lie in the interaction window for ep interactions $7 < t_{hot} < 20$ ns.

- **Size of the cluster - R_{clus}**
  The lateral size of the electromagnetic cluster in the SPACAL can be used to discriminate against background from pions. A hadronic shower will tend to be broader than a more localised electromagnetic deposit. The energy weighted cluster radius, R_{clus}, is defined as:

$$R_{clus} = \frac{1}{E_{clus}} \sum_{i=1}^{n} E_i . |\mathbf{r}_i - \mathbf{r}_{clus}| \tag{4.3}$$

  where E_{clus} and $\mathbf{r}_{clus}$ are the energy and centre of gravity of the cluster, and E_i and $\mathbf{r}_i$ are the energy and centre of gravity of the ith cell of the n cells forming the cluster. The radius is required to be $R_{clus} < 3.5$ cm [106].

- **Associated Hit in the BDC - ΔR_{BDC}**
  There must be a track segment reconstructed in the BDC which, when extrapolated to the SPACAL, lies within 2.5 cm of the centre of gravity of the SPACAL cluster. This reduces the background from photons which leave an energy deposit in the SPACAL but usually no charged track in the BDC.

  The polar angle of the scattered electron, θ', used in the reconstruction of the event kinematics, is calculated from the track segment in the BDC in preference to that calculated from the cluster in the SPACAL because of the superior resolution (see section 1.4.3). The effect of the inclination of the beam axis with respect to the H1 co-ordinate system on the angle of the scattered electron is corrected for. The tilt in x and y, as well as the beam co-ordinates, are calculated for each data run using the distribution of event vertices measured by the CJC.

- **Radial Position of the Cluster - R_{SPACAL}**
  The radial position of the cluster, R_{SPACAL}, is calculated from the angle of the BDC track, θ', and the position in z of the SPACAL cluster. The measured radius is required to be greater than 8.7 cm. This cut removes an area close to the beam-pipe which suffers from a large background rate and also limits the electron to an area of high acceptance in the SPACAL, since the shower is well contained and there is little energy loss.

4.5.2 The $\sum(E - p_z)$ of the Final State

The $\sum(E - p_z)$ denotes the difference between the energy and z component of the momentum summed over all particles in the event. The $\sum(E - p_z)$ of the whole final state is calculated from a combination of track and calorimeter information, avoiding double counting. A full description of the hadronic final state reconstruction algorithm is given in section 7.7. The value of $\sum(E - p_z)$ is required to be larger than 35 GeV and less than 65 GeV. The lower cut on the $\sum(E - p_z)$ of the final state reduces contamination from photoproduction events. In a fully contained event the value of $\sum(E - p_z)$ should be equal to twice the sum of the incident electron beam energy. In a photoproduction background event the final state electron disappears undetected into the backward beam-pipe and the $\sum(E - p_z)$ of the event is peaked towards lower values. The lower cut in $\sum(E - p_z)$ also reduces the contribution of events with significant bremsstrahlung radiation from the initial state electron (see section 4.6) which affect the determination of the kinematical variables x, y and Q^2. The upper cut in $\sum(E - p_z)$ rejects poorly reconstructed events.

4.5.3 The Event Vertex

The rate of background from interactions between the proton beam and the residual molecules of gas in the beam-pipe, or with the walls of the beam-pipe upstream is high. Most of the resulting background events have a large number of tracks that do not point to a vertex near the nominal interaction point. To reduce this background the events are required to have a reconstructed vertex within 40 cm, along the z axis, of the mean vertex position for the running period, $\bar{z}$, which averaged over the whole sample, is around -1 cm in standard H1 co-ordinates.

$E_{clus} > 9$ GeV
$7 < t_{hot} < 20$ ns
$R_{clus} < 3.5$ cm
$\Delta R_{BDC} < 2.5$ cm
$R_{SPACAL} > 8.7$ cm
35 GeV $< \sum(E - p_z) <$ 65 GeV
$\lvert z_{vtx} - \bar{z} \rvert < 40$ cm

Table 4.2: A summary of the cuts applied to select a sample of DIS events. The parameters are defined in the text.

4.6 Kinematic Reconstruction

The kinematic quantities y, Q^2 and x can be reconstructed using various methods which have different sensitivity to QED radiation, to the accuracy of the energy scales of the hadronic and electromagnetic calorimeters of the detector, and to the determination of electron and hadron polar angles. The two main methods for reconstruction of the event kinematics are described below.

- The **Electron Method** uses the information of the energy, E'_e, and polar angle, θ'_e, of the scattered electron to calculate y, Q^2 and x using the following formulae:

$$y_e = 1 - \frac{E'_e}{E_e} \sin^2 \frac{\theta'_e}{2} \tag{4.4}$$

$$Q^2_e = 4\ E'_e\ E\ \cos^2 \frac{\theta'_e}{2} \tag{4.5}$$

$$x_e = \frac{Q^2_e}{s\ y_e} \tag{4.6}$$

At high y, this method of reconstruction has superior resolution compared to all other methods. The resolution degrades towards lower y as $1/y$ and accurate calibration of the electromagnetic energy scale becomes essential. The resolution in Q^2, at the low values of Q^2 used in this analysis, is dominated by the precision in the polar scattering angle θ'_e. The kinematics of the electron method are sensitive to QED radiation off the incident electron, which cause migrations in the kinematic variables.

- The **Σ Method** makes efficient use of the redundancy in the measurement of the kinematical variables by utilising information from both the scattered electron and the final state hadrons to achieve a good resolution over a wide kinematic range. The formulae used are as follows:

$$\Sigma = \sum (E_h - p_{z,h}) \tag{4.7}$$

$$y_\Sigma = \frac{\Sigma}{\Sigma + E_e\ (1 - \cos\theta'_e)} \tag{4.8}$$

$$Q^2_\Sigma = \frac{E'^2_e\ \sin^2\theta'_e}{1 - y_\Sigma} \tag{4.9}$$

$$x_\Sigma = \frac{Q^2_\Sigma}{s\ y_\Sigma} \tag{4.10}$$

where the sum in the calculation of Σ runs over the final state hadrons only. The main advantage of the Σ method is that it is less sensitive to QED initial state radiation than the electron method. For this reason the Σ method is chosen to reconstruct the kinematic variables in this analysis. The value of Σ is determined using the final state algorithm described in section 7.7.

4.6.1 The DIS Kinematic Range

The DIS kinematic range of the measurement is confined to a region in which the geometric acceptance and reconstruction efficiency are high. The defined kinematic range in terms of Q^2 and y, for all the measurements in this thesis, is:

$$2\ \text{GeV}^2 < Q^2 < 100\ \text{GeV}^2 \tag{4.11}$$

$$0.05 < y < 0.70 \tag{4.12}$$

The range in Q^2 is determined by the geometrical acceptance of the scattered electron in the SPACAL. The cuts to remove background in section 4.5 limit the acceptance at the very lowest Q^2 such that any measurement below $Q^2 \sim 2$ GeV^2 is sensitive to the Q^2 dependence in the Monte Carlo model used in the simulation. For Q^2 values larger than around 100 GeV^2 the electron is scattered into the liquid argon calorimeter.

The measurement of the cross section in the region $y < 0.05$ is precluded for many reasons. The 'Inclusive Final State' event class used to select the data sample excludes this region due to high beam-gas backgrounds. In addition, the sub-trigger used in this analysis has hard central tracker requirements, to reduce the background rate, which mean that the trigger efficiency falls towards lower y (see section 6.7). The upper limit in y is a result of the cut of 9 GeV on the scattered electron energy.

Chapter 5

The Reconstruction of D^* Mesons

5.1 Introduction

This chapter serves as an introduction to the method of reconstruction and signal extraction of D^* mesons used in the calculation of the cross sections presented in chapter 6 and chapter 8. In section 5.2, the advantages of the D^* decay mode used in this thesis are explained. In section 5.3, the kinematic range of the cross section is fully defined in terms of the rapidity and transverse momentum of the final state D^* meson. An introduction to the Monte Carlo programs for inclusive charm production which are used in chapter 6 for the determination of acceptances and for model comparisons is given in section 5.4. The Monte Carlo programs are used in this chapter, in section 5.5, to investigate the kinematics of the D^* meson in the hadronic final state. The method of mass reconstruction, including the track cuts applied to the decay particles, and the extraction of the number of events in the signal are described in sections 5.6 and 5.7 respectively.

5.2 The D^* Decay Mode

The D^{*+} meson[1] is reconstructed using the exclusive decay channel

$$D^{*+} \rightarrow D^0 \, \pi^+_{slow} \rightarrow (K^- \, \pi^+) \, \pi^+_{slow} \tag{5.1}$$

The branching fractions and particle masses relevant to the decay mode are listed in table 5.1. The mass difference between the D^{*+} meson and the D^0 meson of 145.4 MeV is only slightly larger than the π^+ mass. Therefore the available energy, or Q-value,

[1] The charge conjugate state is always implied.

for the decay products is small and the π^+ and D^0 meson are produced with a very low momentum of 39 MeV each in the rest frame of the D^{*+}. When boosting to the laboratory frame the momenta of the π^+ and D^0 meson are highly correlated $p_\pi \sim \frac{M_{\pi^+}}{M_{D^0}} p_{D^0}$. The low momentum of the pion in the laboratory leads to it being referred to as the *soft* or *slow* pion. This tight kinematic constraint implies a strong correlation between the reconstructed invariant masses of the D^0 and D^{*+} so that the mass difference

$$\Delta M = M_{D^{*+}} - M_{D^0} \tag{5.2}$$

is better resolved than the individual masses by a factor of approximately 25 [110]. Additionally, the phase space for combinatorial background, namely fake D^{*+} candidates made from unrelated particles, increases with ΔM, and is therefore suppressed by the small mass difference. The decay channel $D^0 \to K^-\pi^+$, although having a small branching fraction, is chosen so that the final D^{*+} decay products are all charged particles with a low multiplicity of only three hadrons. This ensures that the combinatorial background will be low and that both the correction to the cross section and the systematic error introduced due to the inefficiency of the track reconstruction will be small.

Branching Fraction		Invariant Masses	
$D^{*+} \to D^0\pi^+$	$68.3 \pm 1.4\%$	D^0	1864.6 ± 0.5 MeV
$D^0 \to K^-\pi^+$	$3.85 \pm 0.09\%$	D^{*+}	2010.0 ± 0.5 MeV
$D^{*+} \to K^-\pi^+\pi^+$	$2.63 \pm 0.08\%$	ΔM	145.397 ± 0.030 MeV

Table 5.1: The branching fractions and invariant masses relevant to the decay mode used in this thesis. All the values are taken from [111].

5.3 The Kinematic Range for D^* Cross Section Measurements

The cross sections presented in this thesis are fully defined in terms of the D^* meson by the range in transverse momentum, $p_\perp(D^*)$, and pseudo-rapidity, $\eta(D^*)$, in the laboratory frame. The cross section measurements are restricted to the region of high acceptance in these variables and no extrapolation to a larger phase space is performed. Therefore the geometric acceptance and reconstruction efficiency of the H1 tracking detector constrains the kinematic region of the D^* to within the following limits

- The pseudo-rapidity of the D^* meson, $\eta(D^*)$, is required to be in the range $-1.5 < \eta(D^*) < 1.5$ such that the reconstructed D^* meson and its decay products lie in an area of good angular acceptance in the central tracking detector.

- The transverse momentum of the D^*, $p_\perp(D^*)$, must be larger than 2 GeV. This cut suppresses combinatorial background from low $p_\perp$ tracks and the daughter particles are confined to a momentum range where the central tracking detector has high, and well understood, reconstruction efficiency.

5.4 Monte Carlo Models for Charm Production

5.4.1 AROMA

The AROMA [112] program generates the process $ep \to ec\bar{c}X$ via the boson-gluon fusion mechanism ($\gamma g \to c\bar{c}$). In the calculation of the parton level cross section the following equation is used

$$\sigma(ep \to ec\bar{c}X) = \int dy \int dQ^2 \int dx_g \int dz \int d\phi^* \; g(x_g, \mu^2)\mathcal{F}(y, Q^2, x_g, z, \phi^*) \qquad (5.3)$$

where $g(x_g, \mu^2)$ is the gluon density of the proton sampled at a factorisation scale μ^2, and $\mathcal{F}(y, Q^2, x_g, z, \phi^*)$[2] is the leading order matrix element for boson-gluon fusion. The boson-gluon fusion matrix element has been calculated in [113] taking proper account of the charm quark mass. The factorisation scale, μ^2, for the gluon density is taken to be the centre of mass energy for the partonic interaction $\sqrt{\hat{s}}$.

Higher order QCD corrections in AROMA are treated using initial and final state parton showers similar to those in the LEPTO program. In the treatment of final state gluon radiation from the charm quark and anti-quark pair, the maximum virtuality that may initiate the shower is chosen to be equal to the transverse mass of the pair. The final state partons then undergo soft colour interactions which lead to the production of large rapidity gap events for approximately 10% of the events. The hadronisation is performed using the Lund string model as implemented in JETSET.

5.4.2 RAPGAP

The RAPGAP Monte Carlo program, as with the AROMA program, generates charm quarks via the convolution of the leading order boson-gluon fusion matrix element and the gluon density of the proton as given in equation 5.3. The main differences with AROMA occur in the implementation of the subsequent fragmentation. In particular, the production of large rapidity gap events is provided by the factorisable pomeron approach, as opposed to the model of soft colour interactions.

[2] z and ϕ^* are defined in equation 2.29 and figure 3.12 respectively.

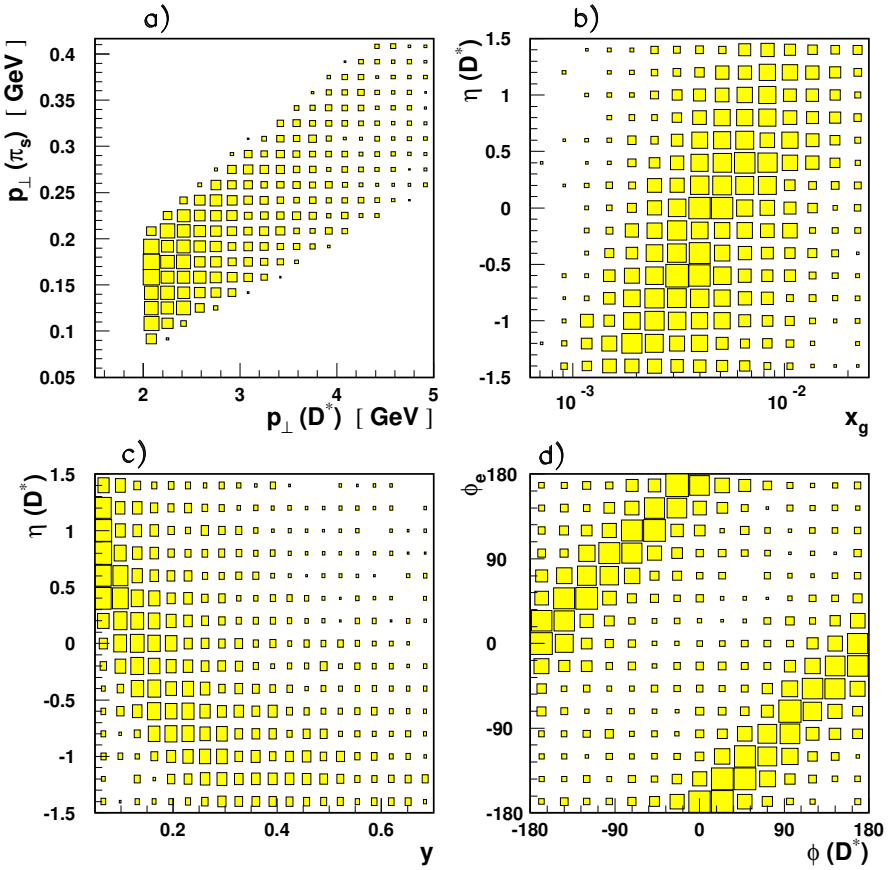

Figure 5.1: The correlation of kinematical quantities, for inclusive D^* production, calculated using the AROMA simulation program. (a) The strong correlation between $p_\perp(D^*)$ and $p_\perp(\pi_{slow})$. The correlation of $\eta(D^*)$ with (b) x_g and (c) y. (d) The correlation in the laboratory frame of the azimuthal angle of the electron, ϕ_e, and the azimuthal angle of the D^* meson, $\phi(D^*)$.

5.5 The Kinematics of the D^* in the Final State

The correlation for different kinematical quantities, calculated using the AROMA simulation program, for inclusive D^* production are shown in figure 5.1. The generated D^* mesons are produced in the kinematic range defined for the cross section measurements. The strong kinematic relationship between the π_{slow} and the D^* meson is clearly evident in figure 5.1a. The π_{slow} carries less than 10% of the D^* transverse momentum. The D^* meson follows the behaviour typical of the hadronic final state in DIS, namely increasing x_g boosts the centre of mass system, and hence the produced D^*, towards the forward direction (figure 5.1b). In contrast, increasing y, such that the photon carries more longitudinal momentum into the hard interaction, means that the D^* is produced

increasingly in the backward direction (figure 5.1c). In the laboratory frame, the transverse momentum of the electron is balanced by the transverse momentum of the hadronic jets produced from the hadronisation of the charm quark anti-quark pair. Therefore the electron is produced approximately back-to-back with the D^* meson (figure 5.1d).

5.6 Reconstruction of D^* Decays in the Central Tracking Detector

The decay products of the D^* are detected in the Central Tracking Detector only. To ensure good detection efficiency and to reduce the combinatorial background, the tracks are required to pass the following quality conditions before they are considered as either π, K or π_{slow} candidates.

- The tracks must be fitted to the primary vertex and have a distance of closest approach (DCA) to this vertex, in the $r-\phi$ plane, of less than 2 cm.
- The tracks are required to have a θ and $p_\perp$ in an efficient region of the CJC. All daughter candidates must lie in the angular range $20^o < \theta < 160^o$ and the momentum of the particles are required to be $p_\perp(K,\pi) > 250$ MeV or $p_\perp(\pi_{slow}) > 140$ MeV. The transverse momentum cut on the slow pion is a compromise between remaining in an efficient region of the CJC (the track reaches the outer CJC which improves the reliability of the track reconstruction) and increasing the efficiency for D^* detection, since the transverse momentum of the slow pion is strongly related to that of the D^* as can be seen in figure 5.1a. The higher transverse momentum cut on the K and π candidates is used to reject combinatorial background from low momentum, mainly light quark induced, tracks.
- To protect further against badly reconstructed tracks, each track is required to have a radial length (measured in the $r-\phi$ plane) of at least 10 cm. The tracks are also required to start inside CJC1 by demanding that the radial distance of the first wire hit of the track is less than 35(50) cm from the z-axis for the 1995 and 1996(1997) data samples.

No initial particle identification is made, and all accepted tracks with $p_\perp > 250$ MeV are combined in oppositely charged pairs under the hypothesis that each track is a π or a K. If the invariant mass of the hypothesised pair is within 80 MeV of the nominal D^0 mass it is counted as a D^0 candidate. Each D^0 candidate is then combined in turn with all

remaining tracks with $p_\perp > 140$ MeV and a charge opposite to that of the K candidate which is appropriate for the D^* decay considered. Before the final mass difference is formed the final cuts are made on the transverse momentum ($p_\perp(D^*) > 2$ GeV) and direction ($|\eta(D^*)| < 1.5$) of the D^*, whose 4-momentum is reconstructed from the three candidate particles. The low momentum combinatorial background is further suppressed by demanding $z(D^*) > 0.2$[3] for $p_\perp(D^*) < 3$ GeV.

The resulting mass difference ΔM formed between the invariant masses is plotted for the inclusive D^* sample individually for the three years' data and also for all years combined in figure 5.2. A clear signal above background is observed in all plots around the expected mass difference.

5.7 Determination of the Number of D^* Mesons

The number of D^{*+} mesons observed is estimated by fitting the ΔM distribution with a Gaussian for the signal and approximating the background with a function of the form

$$a(\Delta M - m_\pi)^b \tag{5.4}$$

The background form chosen is typical of the phase space volume available at threshold. The approximation holds best near to threshold, so the ΔM distribution is fitted only up to values of $\Delta M = 170$ MeV. The fitting package MINUIT [114] is used to perform the fit using a maximum likelihood method. The area, mean and width of the Gaussian and the parameters a and b are allowed to vary. For each of the data samples, the values of the mean of the Gaussian obtained are consistent with those from MC simulations and are shown in table 5.2. The width of the Gaussians tend to be significantly larger in the data than in the simulation. This inconsistency is due to the imperfect simulation of the properties of the central tracker (see section 6.4.2).

The area of the Gaussian peak, N_{obs}, from free fits to the ΔM distributions of the data samples can be seen in figure 5.2. For example, in the combined data sample $N_{obs} = 1076 \pm 58$. The statistical error, as calculated by MINUIT, is larger than $\sqrt{N_{obs}}$ since the error effectively contains a contribution from the uncertainty in the background shape and normalisation, in addition to the uncertainty in the mean and width of the Gaussian. The value of the exponent b of the background function varies typically from around 0.3 to 0.4 as can also be seen in the figure.

The form of the background function given by equation 5.4 may be studied by considering

[3] See section 2.8.3 for a definition of $z(D^*)$.

		data sample			
		1995	1996	1997	1995-1997
mean (MeV)	data	145.61 ± 0.16	145.56 ± 0.10	145.64 ± 0.08	145.58 ± 0.06
	simulation	145.65 ± 0.03	145.64 ± 0.02	145.68 ± 0.02	145.66 ± 0.03
width (MeV)	data	1.17 ± 0.19	0.98 ± 0.09	1.21 ± 0.09	1.11 ± 0.07
	simulation	0.88 ± 0.02	0.89 ± 0.02	0.91 ± 0.02	0.90 ± 0.02

Table 5.2: A comparison of the mean and the width of the signal Gaussian from a free fit, of the form described in the text, to the ΔM distribution for data and MC simulations.

combinations in the same $M(K\pi)$ range, in which both tracks forming the D^0 candidate have the same charge, with the π_{slow} having the opposite charge. These are referred to as wrong charge combinations. The ΔM distribution from such wrong charge combinations is shown for the 1997 data sample in figure 5.3a. The agreement in shape between the wrong charge and right charge combinations justifies the functional form chosen for the determination of the background.

In figure 5.3b the $M(K\pi)$ distribution from candidates having a mass difference within the range $143.6 < \Delta M < 147.6$ MeV (i.e. within 2 MeV of the mean position of the signal Gaussian) is shown for the 1997 data sample. A clear D^0 peak is observed. A fit to the $M(K\pi)$ distribution of two Gaussians plus an exponential falling background gives a peak for the D^0 at $M(K\pi) = 1860 \pm 3$ MeV with a width of 26 ± 3 MeV. The mass value found for the D^0 is consistent with the PDG [111] value given in table 5.1. The cut of 80 MeV around the $M(K\pi)$ mass applied in the reconstruction of the D^* (see section 5.6) is therefore approximately 3σ away from the nominal D^0 mass. In figure 5.3b the dashed histogram shows the wrong charge combinations defined above. The second Gaussian around 1.6 GeV and the excess of events with respect to the wrong charge distribution in this region originate primarily from D^0 decays to $K^-\pi^+\pi^0$ where the neutral π^0 is not reconstructed.

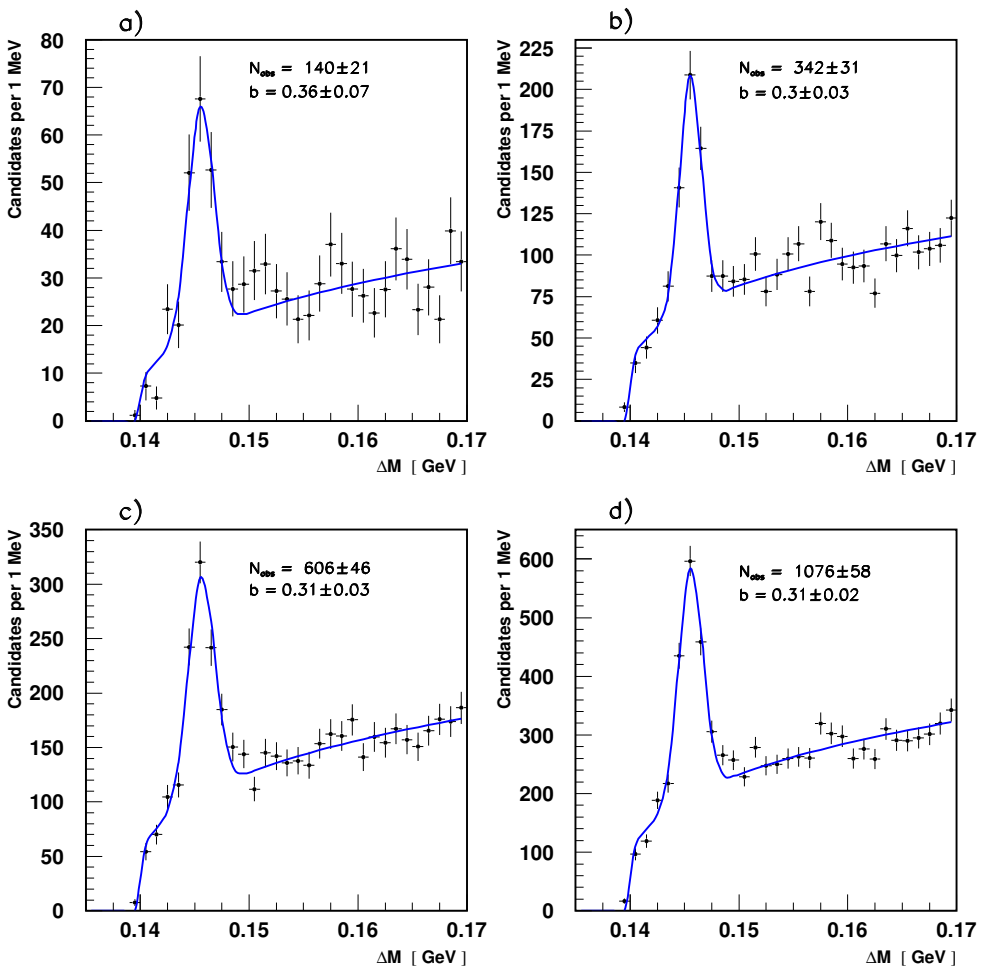

Figure 5.2: The ΔM distributions for the data samples (a) 1995, (b) 1996, (c) 1997 and (d) 1995-1997 combined. The number of D^* mesons obtained from the fit (see section 5.7) , N_{obs}, and the exponent of the background function, b, are shown together with their statistical errors.

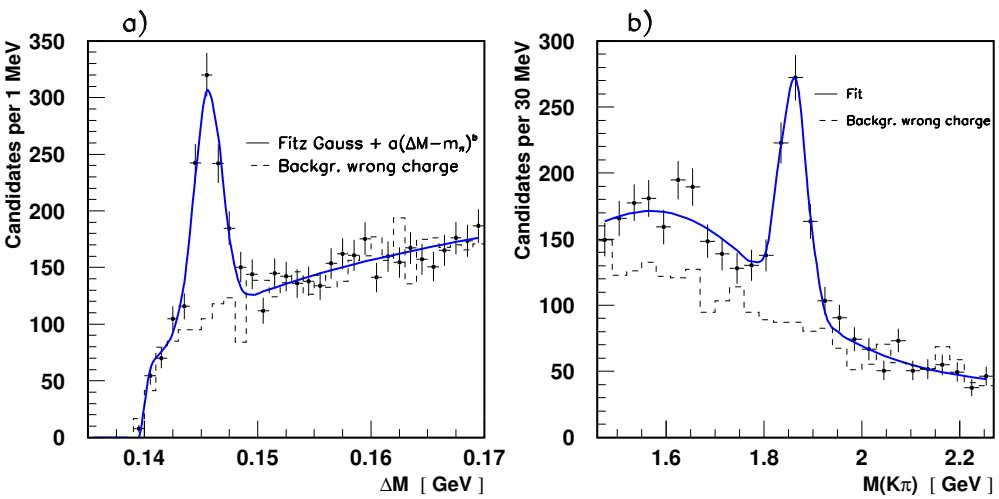

Figure 5.3: (a) The ΔM distribution for the 1997 data sample showing the result of the fit to the sum of a Gaussian and the functional form $a(\Delta M - m_\pi)^b$. The dashed histogram is the result of wrong charge combinations from the D^0 signal region. The wrong charge distribution is normalised to the right charge distribution in the range $150 < \Delta M < 170$ MeV. (b) The $M(K\pi)$ distribution from combinations having ΔM values within 2 MeV of the mean position of the signal Gaussian. The solid line shows the result of the fit described in the text and the dashed line the result of wrong charge combinations.

Chapter 6

Measurement of the Inclusive D^* Cross Section

6.1 Introduction

This chapter contains the measurement of the total cross section $\sigma(ep \to eD^{*\pm}X)$, which is presented differentially as a function of various kinematic variables. In this thesis, the measurement of the inclusive differential cross section provides both a test of LO QCD in its own right and a 'quality' check for the diffractive measurement. The large statistics allow the method of D^* and kinematic reconstruction to be investigated, as well as the ability of the simulation to describe the response of the central tracking detector and its associated triggers.

6.2 Calculation of the Cross Section ($ep \to eD^*X$)

The ep cross section ($ep \to eD^{*\pm}X$) is defined as

$$\sigma(ep \to eD^{*\pm}X) = \frac{1}{\mathcal{L}} \frac{dN_{D^*}}{dt} \tag{6.1}$$

where $\frac{dN_{D^*}}{dt}$ is the mean rate of production of $D^{*\pm}$ mesons in the given kinematic range and $\mathcal{L}$ is the instantaneous luminosity. In practice, the following equation is used;

$$\sigma(ep \to eD^{*\pm}X) = \frac{N_{obs}\ (1-r)}{(\int \mathcal{L}\ dt)\ B\ A_{tot}} \tag{6.2}$$

where

- N_{obs} is the number of D^* mesons obtained from fits to the ΔM distribution (see section 5.7);
- r is the fraction of the D^* mesons in the peak due to other decay modes, called reflections, which are not included in the simulation;
- $\int \mathcal{L}\, dt$ is the integrated luminosity (see section 4.2);
- A_{tot} is the 'smeared' acceptance, which corrects for geometric and detector effects (including the trigger efficiency) and for smearing of kinematic variables due to the finite resolution of the detector. A_{tot} is estimated using Monte Carlo simulations of the decay $D^{*+} \rightarrow (K^-\pi^+)\pi^+_{slow}$.
- B is the branching fraction for the decay $D^{*+} \rightarrow (K^-\pi^+)\pi^+_{slow}$ (see section 5.2);

The extension from the total cross section to the measurement of single differential cross sections, for example $\frac{d\sigma}{dp_\perp(D^*)}$, is straightforward. The number of D^* mesons in each bin is obtained from the ΔM distribution formed within the kinematic limits of that bin. The detector acceptance is calculated as a function of the differential variable. Finally, the cross section in each bin is divided by the width of the bin. The measured differential cross section is an average over the whole of each bin and no correction is applied to account for the cross section behaviour within the particular bin.

In the following sections the two remaining variables to be evaluated in the calculation of the cross section from equation 6.2, namely A_{tot} and r, are discussed.

6.3 Calculation of the 'Smeared' Acceptance - A_{tot}

The decay channel $D^{*+} \rightarrow D^0\ \pi^+_{slow}$ is selected from a sample of $c\bar{c}$ events produced by the AROMA Monte Carlo generator (see section 5.4) so that only the signal, and not the background from other decay channels or processes, is modelled. The generated sample is then passed through the H1 detector simulation program H1SIM [115], and undergoes the same reconstruction and analysis chain as the data. The reconstructed ΔM distribution for the simulated events and, for comparison, the inclusive ΔM distribution from data are shown in figure 6.1. The combinatorial background is extremely low in the simulation as compared with the data.

The 'smeared' acceptance is given by the ratio of the number of D^* mesons reconstructed in the defined kinematic region after all detector cuts and trigger selections (regardless

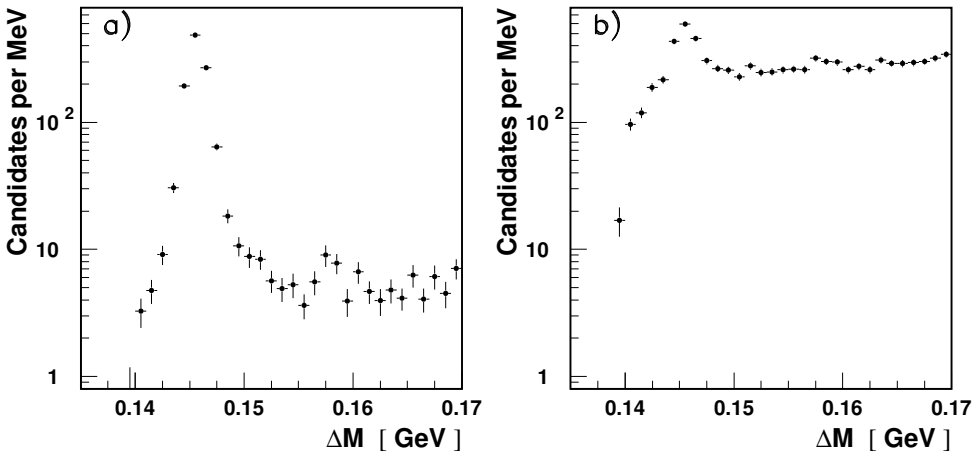

Figure 6.1: The ΔM distribution reconstructed from a sample of (a) simulated Monte Carlo events (b) data. The distribution for the simulated events is normalised to the data by the number of D^* mesons obtained in the fitting procedure. Only the signal decay $D^{*+} \to D^0\ \pi^+_{slow}$ is simulated, which explains the extremely low level of combinatorial background when compared with the data.

of their generated kinematic value), N_{rec}, to the number of D^* mesons generated in the measured kinematic range, N_{gen}. The calculation of the acceptance using a full detector simulation takes into account the most important geometrical and detector effects:

- the fraction of generated D^* mesons for which all the decay products are reconstructed in the central tracker giving a D^* meson in the required range of η and $p_\perp$.
- the fraction of the reconstructed D^* mesons which satisfy the trigger requirements of the track based trigger used in the analysis.
- the fraction of events in which the scattered electron is detected in the SPACAL calorimeter within the required ranges in energy and spatial position.
- the smearing in energy, momentum and angles due to the resolution of the various components of the detector and the finite resolution of the reconstruction procedure.

To illustrate that this method takes into account both the efficiency and bin smearing due to the resolution of the various components of the detector, it is instructive to define the following variables:

- N_{stay}: the number of D^* mesons successfully reconstructed in the kinematic range that were also generated within the kinematic range.
- N_{leave}: the number of D^* mesons generated in the kinematic range which were either not reconstructed or were reconstructed outside the required kinematic range.
- N_{come}: the number of D^* mesons reconstructed in the required kinematic range that were generated outside the kinematic range.

The 'smeared' acceptance is then given by

$$A_{tot} = \frac{N_{rec}}{N_{gen}} = \frac{N_{stay} + N_{come}}{N_{stay} + N_{leave}} \tag{6.3}$$

The migration of events between bins is sometimes quantified by the 'purity', defined in this analysis as

$$P = \frac{N_{stay}}{N_{rec}} \tag{6.4}$$

In order to illustrate further the composition of the 'smeared' acceptance, it may be factorised into three components

$$A_{tot} = \frac{N_{gen}(\text{all cuts})}{N_{gen}} \times \frac{N_{rec}(\text{no trigger})}{N_{gen}(\text{all cuts})} \times \frac{N_{rec}}{N_{rec}(\text{no trigger})} \tag{6.5}$$

$$A_{tot} = A_{kin} \times \epsilon_{rec} \times \epsilon_{trig} \tag{6.6}$$

where N_{gen}(all cuts) is the number of D^* mesons generated in the required kinematic range which, in addition, have generated decay particles that lie in their corresponding reconstructed angular and momentum ranges (i.e. $p_\perp(K,\pi) > 250$ MeV, $p_\perp(\pi_{slow}) > 140$ MeV and $20^o < \theta(K,\pi,\pi_{slow}) < 160^o$). The cut in $z(D^*)$ at low momentum is also applied to the generated D^* meson in the calculation of N_{gen}(all cuts). N_{rec}(no trigger) is the number of reconstructed D^* mesons after all detector cuts but without requiring the analysis trigger elements to have fired.

According to equation 6.6 the 'smeared' acceptance comprises the kinematic acceptance, A_{kin}, which depends on the generated kinematical distributions and D^* decay distributions of the generator program, the reconstruction efficiency, ϵ_{rec}, which accounts for the losses and smearing introduced by the reconstruction of the event and D^* kinematics, and the trigger efficiency, ϵ_{trig}, which depends on the simulation of the trigger elements of the analysis sub-trigger.

The 'smeared' acceptance, calculated using the AROMA program after simulation of the detector for 1995, 1996 and 1997 running conditions, is shown as a function of all the kinematic quantities for which the cross section is measured, with the same binning, in figures 6.11 and 6.12. The dashed line indicates the kinematic acceptance, A_{kin}, the solid line the reconstruction efficiency, ϵ_{rec}, the dotted line the trigger efficiency, ϵ_{trig}, and the 'smeared' acceptance is shown by the points marked with error bars.

From inspection of figures 6.11 and 6.12, the following may be deduced about each component of the 'smeared' acceptance.

- A_{kin}
  The total kinematic acceptance for the generated particles, A_{kin}, is 70%. The kinematic acceptance is lowest in the bin $0 < z(D^*) < 0.2$ which is due to the cut in this range for low $p_\perp(D^*)$. Similarly, a reduction in the acceptance at low $p_\perp(D^*)$ and high y is caused by the application of the cut in $z(D^*)$. For example, removing the z cut increases the kinematic acceptance in the lowest $p_\perp(D^*)$ bin by 10%. However, even after the removal of the cut in $z(D^*)$, the kinematic acceptance varies most strongly with $p_\perp(D^*)$, which is a consequence of the kinematic correlation between the D^* and the π_{slow}.

- ϵ_{rec}
  The reconstruction efficiency, ϵ_{rec}, is 67% when averaged over all bins, and is reasonably flat for all distributions. Therefore, when combined with A_{kin} the overall acceptance for D^* reconstruction, without including the trigger efficiency, is 47%. In order to understand the reconstruction efficiency further, it may be factorised into the components

$$\epsilon_{rec} = \frac{N_{rec}(\text{no trigger})}{N_{rec}(\text{no track cuts})} \times \frac{N_{rec}(\text{no track cuts})}{N_{gen}(\text{all cuts})} \tag{6.7}$$

$$\epsilon_{rec} = \epsilon_{\text{track cuts}} \times \epsilon_{rec}(\text{no track cuts}) \tag{6.8}$$

  where $N_{rec}(\text{no track cuts})$ refers to the number of D^* mesons reconstructed without applying the track cuts in the DCA, minimum radial track length and maximum radius of the track start. Equation 6.8 illustrates that the reconstruction efficiency may be decomposed into an efficiency for applying the track cuts, $\epsilon_{\text{track cuts}}$, which is determined from the fraction of D^* mesons reconstructed with and without the track cuts applied and a 'track' reconstruction efficiency, $\epsilon_{rec}(\text{no track cuts})$, which accounts for the kinematic smearing and the remaining track and electron reconstruction inefficiency.

  The track cut efficiency, $\epsilon_{\text{track cuts}}$, and the 'track' reconstruction efficiency,

ϵ_{rec}(no track cuts), are shown, for example, in table 6.1 as a function of $p_\perp(D^*)$ for the 1996 and 1997 detector simulations[1].

$p_\perp(D^*)$	1996		1997	
	$\epsilon_{\text{track cuts}}$	ϵ_{rec}(no track cuts)	$\epsilon_{\text{track cuts}}$	ϵ_{rec}(no track cuts)
$2.0 < p_\perp(D^*) < 2.5$ GeV	94.6 ± 1.3	77.6 ± 1.3	91.4 ± 1.1	60.8 ± 1.2
$2.5 < p_\perp(D^*) < 3.5$ GeV	94.4 ± 0.9	81.8 ± 0.9	90.7 ± 0.9	68.6 ± 0.9
$3.5 < p_\perp(D^*) < 5.0$ GeV	95.9 ± 1.1	82.2 ± 1.1	95.3 ± 1.1	69.7 ± 1.1
$5.0 < p_\perp(D^*) < 10.0$ GeV	97.1 ± 1.5	75.1 ± 1.5	97.7 ± 1.2	52.7 ± 1.2

Table 6.1: The reconstruction efficiency, ϵ_{rec}, as a function of $p_\perp(D^*)$ factorised into the track cut efficiency, $\epsilon_{\text{track cuts}}$, and the 'track' reconstruction efficiency, ϵ_{rec}(no track cuts), for the 1996 and 1997 detector simulations.

For both data sets the 'track' reconstruction efficiency, ϵ_{rec}(no track cuts), is the dominant source of inefficiency in ϵ_{rec}, whereas the loose track cuts applied in section 5.6 are, when averaged over the two years, only 7% inefficient.

The losses in the 'track' reconstruction efficiency, ϵ_{rec}(no track cuts), are dominated by the inefficiency in reconstructing three tracks in the central tracking detector; and the effects of the event reconstruction inefficiency and the kinematic smearing are small. To illustrate this, a 'true' efficiency for track reconstruction may be defined by recalculating ϵ_{rec}(no track cuts) but this time allowing no D^* mesons to enter the sample which were generated outside the kinematic range, such that the purity of the sample is one. In addition, the reconstructed decay candidates are traced through the detector simulation and linked to their corresponding generated particles so that no misidentified tracks enter into the calculation of the 'true' efficiency. The 'true' efficiency for the reconstruction of the three decay tracks is found to be 80% for the 1996 simulation and 65% in 1997; indicating that the 'true' efficiency for reconstructing a single track in 1996 is 93%, which falls to 87% in the 1997 simulation. The significant drop in efficiency between the two years is due to a degradation in response of the CJC.

The 'smearing' of events across the boundary of the kinematical range of the cross section measurement is small and the purity of the whole sample is 93%. The binning for the measurement of the differential cross sections is chosen so that the bin size is much larger than the detector resolution and, hence, the purity for each bin remains high.

- ϵ_{trig}

  The trigger efficiency is 86%, and this reduces the overall 'smeared' acceptance to

[1] The results of the 1995 detector simulation are similar to those for the 1996 simulation.

40%. The trigger inefficiency is dominated by the hard track conditions applied to the level 1 trigger used in the analysis of the 1996 and 1997 data. The trigger efficiency varies strongly as a function of y, with the efficiency decreasing with decreasing y. In events with low y, the D^* meson and the remainder of the hadronic final state are produced preferentially in the forward direction (see section 5.5). This increases the likelihood that a decay particle from the D^* meson lies in a region of low acceptance for the $z - vtx$ trigger, i.e. at a low scattering angle.

The decomposition of A_{tot}, although complicated, has identified those aspects of the simulation which have the largest effect on the cross section measurement. The most important contribution to acceptance loss is the inefficiency in the reconstruction of three tracks in the central tracking detector. The second most important source of acceptance loss is the inefficiency of the hard track trigger conditions. The contribution to acceptance losses due to the reconstruction of the electron and the 'smearing' in the reconstruction of the event kinematics are smaller although still important. The acceptance, as determined using the simulation, is also particularly sensitive to the generated input kinematical distributions. In order to maintain small systematic errors on the measurement, the accuracy of the simulation in describing all these aspects of the data is investigated as follows:

- The systematic error in the track reconstruction efficiency is inferred from the ability of the simulation to describe various distributions in the central tracking detector. The number of hits per track and the width of the signal in the ΔM distribution are investigated in the data and simulation in section 6.4. The efficiency of the track cuts, $\epsilon_{\text{track cuts}}$, is measured directly in the data and compared with the simulation in section 6.5. Further information is obtained from other detailed studies of the simulation which are discussed in section 6.6.

- The ability of the simulation to describe the inefficiency of the hard track conditions applied to the level 1 trigger is investigated by the evaluation of the trigger efficiency, ϵ_{trig}, directly in the data in section 6.7.

- To ensure that the reconstruction of the DIS electron and the event kinematics are well modelled, the data and simulation are compared in section 6.8.

- The uncertainty in the underlying distributions is estimated by using different physics models in section 6.11.

6.4 Simulation of the Central Tracking Detector

6.4.1 Hit Multiplicities Per Track

Due to various hardware problems it may occur that some drift wires or drift cells are inoperational for certain periods of the running. To monitor this, calibration data used to determine the efficiency of each hit wire in a drift cell is taken periodically during the running period and the results implemented into the detector simulation. The number of hits per track in the data and simulation are compared for all π and K candidates in the ΔM distribution for CJC1 and CJC2 for each years' data in figure 6.2. The figure shows very good agreement between data and the simulation considering that the data contains a large fraction of combinatorial background that is not present in the simulation[2]. There is evidence for too high an efficiency for the CJC2 in the 1995 simulation. In the 1997 running there were problems with both 'dead' drift cells in CJC1 and reduced efficiency in CJC2, which can be seen clearly from the severely depleted number of hits per track in the lower half ($\phi < 0^{\circ}$) of the CJC in figures 6.2e and figure 6.2f. This led to the central jet chambers being completely re-wired during the shutdown between the 1997 and 1998 running periods. The worsening performance of the CJC makes it important to study other aspects of the simulation to see that it continues to provide a reasonable description. The hit wire multiplicity distribution, although sensitive to inefficient regions in the CJC, is not the most sensitive probe of the tracker performance since the momentum resolution is only inversely proportional to the square root of the number of hits whereas it is proportional to the square of the track length.

6.4.2 Asymmetry in the Width of the ΔM Distribution as a function of ϕ

It was noted in section 5.7 that the width of the signal in the ΔM distribution in the simulation is narrower than that obtained from the data. The width in the data and simulation are investigated, from free fits to the ΔM distributions, as a function of the azimuthal angle, $\phi(D^*)$, of the D^* meson in table 6.2. The binning in ϕ is chosen so that inefficient regions of the CJC are contained within a single bin, as can be observed from figure 6.2. The value of the width of the signal region in the simulation remains constant between different years of the simulation, and the average is shown in table 6.2. For the 1996 data sample, the discrepancy in the width between the data and simulation

[2]See figure 6.1 for a comparison of the increased combinatorial background in the ΔM distributions for the data when compared with the simulation.

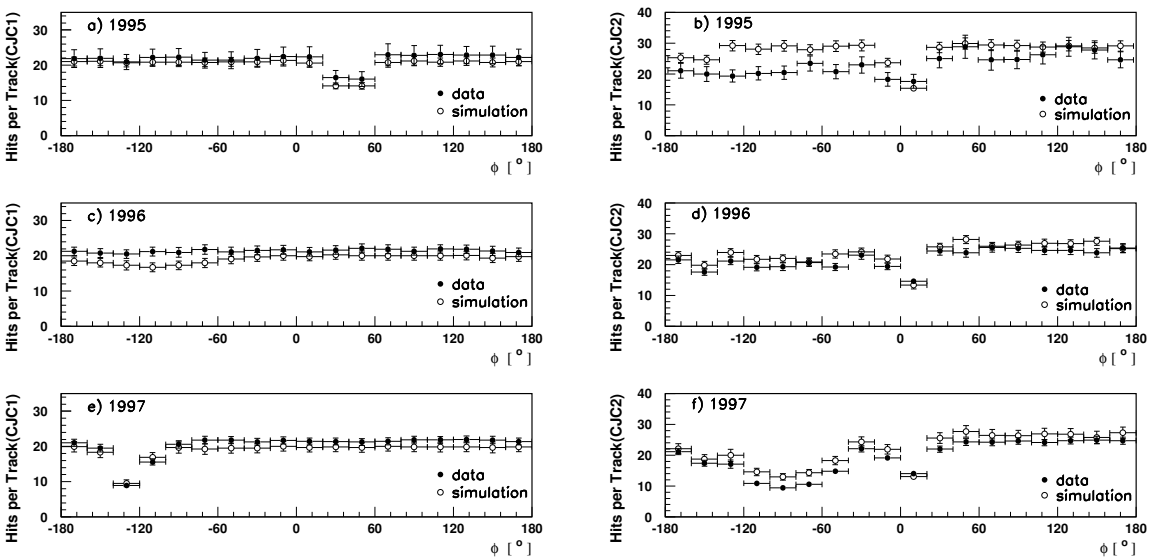

Figure 6.2: The number of hits in CJC1 [CJC2] per track for the K and π candidates within the ΔM distribution for (a)[(b)] 1995 (c)[(d)] 1996 and (e)[(f)] 1997 data samples. The data is shown by the filled circles and the simulation by the open circles.

is attributed to the region $-180^o < \phi(D^*) < -60^o$. A similar conclusion may be drawn for the 1995 data, although the low statistics in the central ϕ bin, due to an inefficient region in CJC1, mean that a free fit to the ΔM distribution cannot be performed. The ΔM distributions for the ϕ bins are shown for the 1996 and 1997 data in figure 6.3. The reduction in efficiency in the 1997 data for the lower half of the CJC is clearly seen in the yield of events. The width for the other ϕ regions also increases for the 1997 data. The difference between the number of events obtained from the fit with a free width and when fixing the width of the Gaussian to that obtained from all D^* events is, on average, 7% for the three ϕ bins shown.

	simulation	data		
ϕ range		1995	1996	1997
$-180^o < \phi(D^*) < -60^o$	0.89 ± 0.05	1.14 ± 0.25	1.13 ± 0.17	1.27 ± 0.39
$-60^o < \phi(D^*) < 60^o$	0.89 ± 0.04	–	0.78 ± 0.16	0.96 ± 0.11
$60^o < \phi(D^*) < 180^o$	0.93 ± 0.05	0.74 ± 0.12	0.92 ± 0.11	1.39 ± 0.15

Table 6.2: The width of the Gaussian obtained from free fits to the ΔM distribution in both the simulation and for the 1995, 1996 and 1997 data samples as a function of the azimuthal angle, ϕ, of the D^*. All values shown are in MeV.

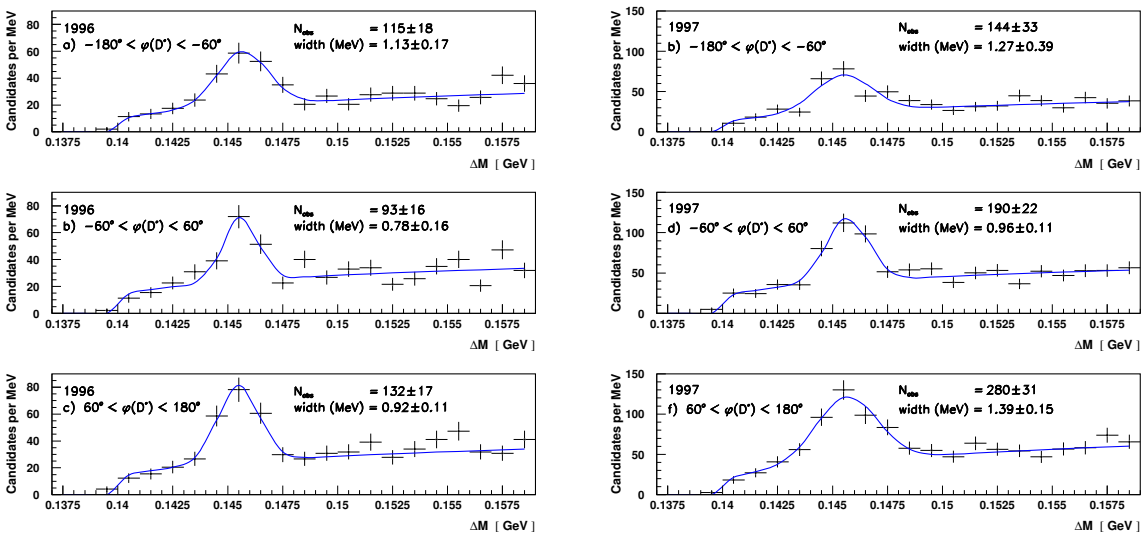

Figure 6.3: The ΔM distributions for three ranges in $\phi(D^*)$ for the 1996 [1997] data. (a)[(b)] $-180° < \phi(D^*) < -60°$ (c)[(d)] $-60° < \phi(D^*) < 60°$ (e)[(f)] $60° < \phi(D^*) < 180°$. The number of events, N_{obs}, and the width of the Gaussian after free fits to the distributions are shown in each plot.

The origin of the worsening resolution is unknown. Further study of this effect is non-trivial due to low statistics and correlations between the decay particles which makes identification of the problem with a particular track cut or momentum range difficult. The measured cross section as a function of $\phi(D^*)$ (see section 6.11) for the whole data sample is consistent with being flat, as expected, which suggests that the effect causing the badly described resolution does not affect the track reconstruction efficiency. This is further supported by confining all the decay particles of the D^* to a particular region in ϕ and measuring the D^* cross section in that ϕ region (see section 6.12).

6.5 Efficiency of the Track Cuts

The track cuts applied in the analysis aim to achieve a balance between high efficiency for D^* reconstruction and low background contamination. It is important that the efficiency of each cut evaluated from the data is shown to be compatible with that in the simulation. The efficiency of the track cuts, $\epsilon_{\text{track cuts}}$ is given by:

$$\epsilon_{\text{track cuts}} = \epsilon_{DCA} \times \epsilon_{\text{track length}} \times \epsilon_{\text{track start}} \tag{6.9}$$

where ϵ_{DCA}, $\epsilon_{\text{track length}}$ and $\epsilon_{\text{track start}}$ are the efficiencies of the track cuts in the distance of closest approach, track length and radius of the track start respectively. The efficiency of each track cut, in the data and simulation, is measured from the number of D^* mesons determined from fits to the ΔM distributions with (n) and without (N) the particular track cut under investigation applied. The efficiency and the error are calculated from an 'improved' binomial error [116], which remains valid even if either n, N or $N-n$ are small. The efficiency of a cut is then given by

$$\epsilon_{cut} = \frac{n+1}{N+2} \tag{6.10}$$

with the error on the efficiency by

$$\delta_{\epsilon_{cut}} = \sqrt{\frac{(n+1)(N-n+1)}{(N+2)^2(N+3)}} \tag{6.11}$$

In addition to the efficiency determination, the data and simulation are compared for all the K, π and π_{slow} candidates in the ΔM distribution for each track cut variable. These 'control distributions' serve only as a guide to where the simulation is giving a good description of the central tracker performance because the data are dominated by combinatorial background not present in the simulation. The efficiency evaluation described in the previous paragraph provides the best estimate of the effect on the cross section measurement. In the efficiency determination, in contrast to the control plots, only the 1996 and 1997 data sets are considered due to low statistics in the 1995 data.

6.5.1 Distance of Closest Approach

All tracks are required to have a distance of closest approach (DCA) to the primary vertex of less than 2 cm in the $r-\phi$ plane. Since all vertex fitted tracks are constrained to have a distance of closest approach of zero, the value of the DCA is taken from the parameters of the track before the vertex fitting was performed. The value of the DCA is non-vanishing due to multiple scattering in material either before or in the jet chamber and, at low momentum due to energy losses, such that a track parameterisation with constant curvature becomes insufficient. The cut on the DCA in the analysis is applied to reduce contamination from any secondary vertices such as beam induced background, random tracks in the reconstruction and cosmic rays.

A comparison of the DCA distribution in data and simulation for the K, π and π_{slow} candidates of the ΔM distribution is shown for the full data sample in figure 6.4. The analysis cut of $DCA < 2$ cm removes only the tails of the distribution so that the difference

in the widths between the data and simulation, which may be due to combinatorial background, has only a small effect on the efficiency of the cut. The efficiency of the DCA cut is shown in table 6.3, for the 1996 and 1997 data samples, and is close to 100% in both the data and simulation.

	DCA cut (cm)			efficiency (%)	
year	K	π	π_{slow}	data	simulation
1996	2	2	2	99.7 ± 0.3	99.9 ± 0.1
1997	2	2	2	99.8 ± 0.2	100.0 ± 0.1

Table 6.3: The efficiency of the cut in the distance of closest approach ($DCA < 2$ cm) for track candidates in data and simulation for the 1996 and 1997 samples.

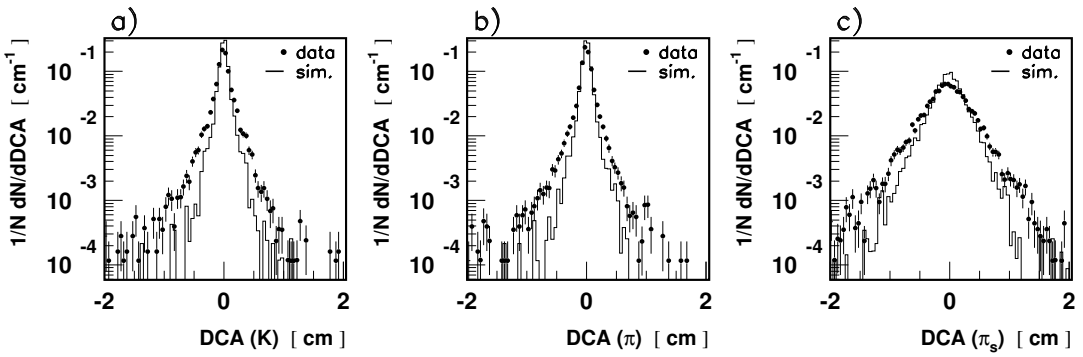

Figure 6.4: The distribution $\frac{1}{N}\frac{\Delta N}{\Delta DCA}\text{cm}^{-1}$ for the (a) K candidate (b) π candidate and (c) π_{slow} candidate, where DCA is the the distance of closest approach and N is the number of entries in the ΔM distribution for the full data sample (points) and detector simulation (full line).

6.5.2 Radial Track Length

The radial track length, R_{length}, is the radial distance measured between the first and last measured hits of the track. All tracks are required to have $R_{length} > 10$ cm, which guards against the possibility of broken tracks (i.e. a single charged particle reconstructed as two separate tracks - typically one in CJC1 and the other in CJC2).

The distribution of the radial track length for the K, π and π_{slow} candidates is shown for both data and the simulation in figure 6.5. The distributions peak at 20 cm and 60 cm which correspond to the thickness of CJC1 and CJC1 plus CJC2. The efficiency of the analysis cut is around 99% except for the 1997 data, as can be seen in table 6.4.

	track length(cm)			efficiency (%)	
year	K	π	π_{slow}	data	simulation
1996	10	10	10	99.0 ± 0.4	98.9 ± 0.2
1997	10	10	10	97.0 ± 0.6	98.7 ± 0.2

Table 6.4: The efficiency of the cut in the radial track length for track candidates in data and simulation for the 1996 and 1997 samples.

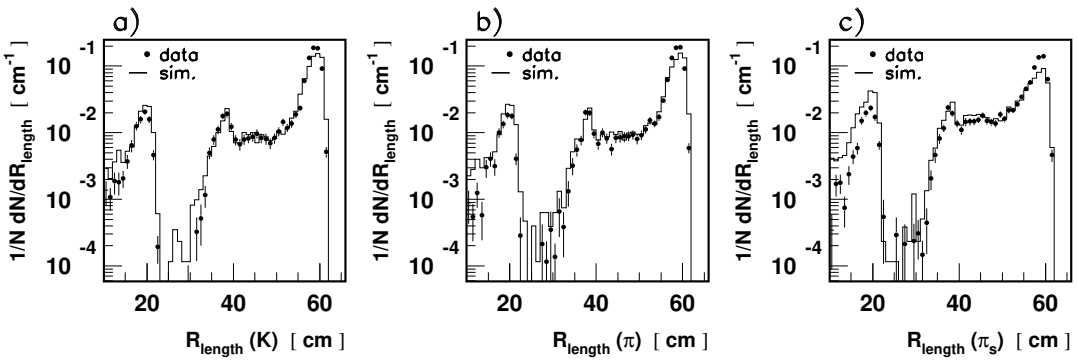

Figure 6.5: The distribution $\frac{1}{N}\frac{\Delta N}{\Delta R_{length}}\text{cm}^{-1}$ for the (a) K candidate (b) π candidate and (c) π_{slow} candidate, where R_{length} is the radial length of the track and N is the number of entries in the ΔM distribution for the full data sample (points) and detector simulation (full line).

6.5.3 Track Start

All tracks are required to start within 35 cm of the z-axis, except for the 1997 data where this cut is increased to 50 cm. This cut combined with the radial track length cut preferentially selects tracks that consist of a combination of one track segment in the inner and another in the outer chamber of the CJC. The distribution of the radial position of the start of the track, R_{start}, for the K, π, π_{slow} candidate is shown in figure 6.6. The small excess at around 28 cm is identified with an imperfect description of the efficiency of the lower half of CJC1 in 1997, since the tracks start at a larger radial distance in the data than in the simulation. To reduce any uncontrolled effect on the efficiency, the maximum distance for a track to start is increased to 50 cm for the 1997 sample. The efficiency of the analysis cut is around 95% in both data and simulation as can be in table 6.5. This cut is the most inefficient due to the effect of 'dead' regions in CJC1.

	track start(cm)			efficiency (%)	
year	K	π	π_{slow}	data	simulation
1996	35	35	35	95.3 ± 0.4	95.1 ± 0.2
1997	50	50	50	93.0 ± 0.7	94.9 ± 0.3

Table 6.5: The efficiency of the cut in the track start for track candidates in data and simulation for the 1996 and 1997 samples.

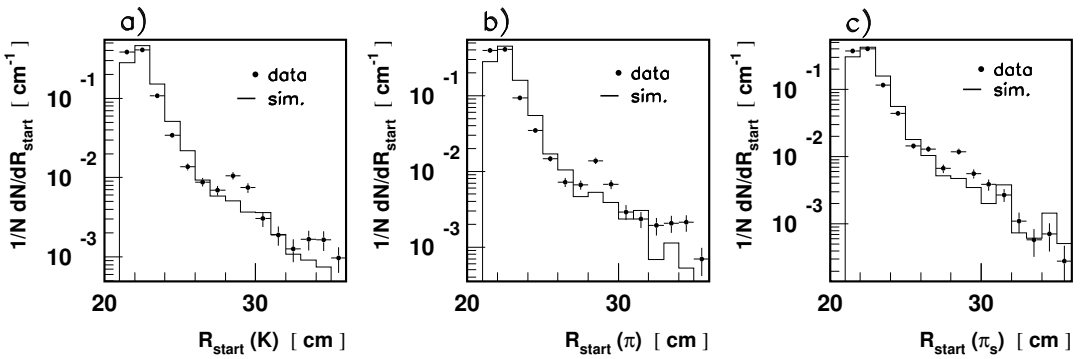

Figure 6.6: The distribution $\frac{1}{N}\frac{\Delta N}{\Delta R_{start}}\text{cm}^{-1}$ for the (a) K candidate (b) π candidate and (c) π_{slow} candidate, where R_{start} is the radial distance of the start of the track from the z axis and N is the number of entries in the ΔM distribution for the full data sample (points) and detector simulation (full line).

6.5.4 Combined Efficiency

The efficiency, $\epsilon_{\text{track cuts}}$, of the combined track cuts in the DCA, track length and track start as evaluated in sections 6.5.1-6.5.3 are shown in table 6.6. The discrepancy between the data and simulation, for the 1997 data sample, represents a difference of 1% per track candidate. Therefore, the results of the investigation into the efficiency of the track cuts give some confidence in the use of the simulated acceptance in the actual cross section measurement.

year	Data	simulation
1996	94.1 ± 0.6	94.0 ± 0.3
1997	90.0 ± 0.9	93.0 ± 0.4

Table 6.6: The combined efficiency, $\epsilon_{\text{track cuts}}$, of cuts in the DCA, track length and track start for the 1996 and 1997 data and simulation.

6.6 Studies of Vertex and Track Reconstruction Efficiency

The investigations of the hit multiplicities per track performed in section 6.4.1 and of the efficiency of the track cuts made in section 6.5 do not fully ascertain whether the simulation is providing a good description of the vertex fitting and track reconstruction efficiency. Therefore, information must be used from other investigations. The efficiency for reconstructing a DIS *event* without selecting an exclusive channel is known to be well described by the simulation from analysis of the inclusive structure function [16]. However, the efficiency for assigning a single track, in particular of low momentum, to the primary vertex may not be so well described. The vertex linking efficiency has been estimated for the 1994 [117] and 1996 data samples [118]. The efficiency for the vertex assignment of a track is obtained from a sample containing both vertex fitted and non-vertex fitted tracks. Track cuts, similar to those used in this thesis, are applied to the sample and the fraction passing these, which are assigned to the vertex by the reconstruction algorithm, provides a measure of the vertex linking efficiency. In data, where it is not known if the tracks originate from the primary vertex or not, the method provides a lower limit on the efficiency. In the 1996 analysis, and very similarly in the 1994 data, the simulation indicates almost a 100% vertex linking efficiency per track, whereas the lower limit from data is $98.5 \pm 0.5\%$. In this thesis no correction is made to the simulation for this effect and a systematic uncertainty of 1.5% is applied to each of the three daughter tracks of the D^* so that the combined vertex linking efficiency for the D^* is $1.00^{0.000}_{-0.044}$.

The reconstruction efficiency for detecting high-$p_\perp$ tracks (typically $p_\perp > 3$ GeV) in the CJC has been determined using cosmic rays for both the 1994 [117] and 1997 data [119]. The reconstruction efficiency for a cosmic muon track, when no minimum track length requirement is imposed, is found to be close to 100% in both years. For the analysis of 1994 data, the investigation was extended to a lower momentum range by the study of the $p_\perp$ spectrum from K^0_s decays [120], and by a visual scan of events [121]. The former method uses the decays of K^0_s into $\pi^+\pi^-$ and utilises the fact that the decay particles are known to be produced isotropically in the K^0_s rest frame. The angular distribution in the laboratory frame was assumed to be a function of the transverse momentum of the decay products only. This assumption was subsequently found to be unsafe because of different efficiencies for vertex and non-vertex fitted tracks due to the ϕ asymmetry inherent in the CJC design [122]. A visual scan to evaluate the track reconstruction efficiency would seem to be an ideal method for a future analysis.

Until a visual scan is performed it is wise to measure the cross section in a region where

the momentum of the π_{slow} is as high as possible, but low enough that the statistics of the measurement remain high. From the studies of the central tracker performance in this chapter an uncertainty in the reconstruction efficiency of 2% per track, increasing to 3% per track for the 1997 data, is quoted in this thesis.

6.7 Evaluation of the Trigger Efficiency

The analysis sub-trigger for the three years' data is described in section 4.4. The majority of the inefficiency is expected to be caused by the hard track conditions applied in the 1996 and 1997 data samples[3]. For example, the study of the detector simulation in section 6.3 shows that the hard track trigger conditions are, on average, 14% inefficient. In contrast, the efficiencies of the SPACAL IET threshold and the ToF vetos, which are not implemented in the simulation, are expected to be high. For example, the electron threshold of the IET trigger is much lower than the analysis cut of 9 GeV, so that the efficiency for electron identification is expected to be almost 100% [16]. The efficiency of the timing vetos is taken to be 100% and the systematic error is taken from [106].

The ability of the simulation to describe the efficiency of the $r-\phi$, $z-vtx$ and IET trigger elements is further investigated in this section by measuring their efficiency in the data. The efficiency of either the SPACAL or track trigger elements of the sub-trigger are evaluated in the data individually using a sub-trigger which is independent of that particular sub-system, called a monitor trigger. The trigger efficiency, ϵ_{trig}, is then calculated from the number of D^* candidates within the monitor trigger sample that are triggered by the analysis sub-trigger.

6.7.1 Electron Trigger Efficiency

For the 1996 running, the combination of the SPACAL IET trigger elements in the sub-trigger arrangement leads to an effective energy threshold for an electromagnetic cluster of 2 GeV for the inner and outer region of the SPACAL. For the start of the 1997 running, the sub-trigger continued in a similar form to 1996, however, for the later half of 1997 the SPACAL energy threshold of the sub-trigger was raised to around 6 GeV. The new sub-trigger was able to run with a lower prescale than previously because the background rate, in particular from photoproduction, was significantly reduced.

The efficiency for triggering an electron is calculated using D^* candidates triggered by a

[3]The trigger efficiency in the 1995 data is close to 100% and the systematic error is taken from [107].

monitor trigger which is independent of the SPACAL and is based on energy deposition in the LAr calorimeter. The number of entries in the ΔM distribution, rather than the number of D^* mesons obtained from the fit, is used in the determination of the efficiency in order to increase the statistical accuracy of the measurement. The assumption of the equivalence of the efficiency for the whole ΔM distribution with that of the D^* meson is valid because no difference between the monitor and analysis trigger, in the shape of the ΔM distribution, is observed. The results are shown in table 6.7 and the efficiency is seen to be 99% in all cases. In the analysis, no correction is made to the simulation for this effect and a small systematic error, the size of the measured inefficiency, is applied.

	data
1996 (low threshold)	99.26 ± 0.42
1997 (low threshold)	99.25 ± 0.74
1997 (high threshold)	98.84 ± 0.66

Table 6.7: The efficiency for the electron component of the trigger for the 1996 and 1997 data samples. The low threshold configuration involves a trigger threshold of around 2 GeV which is increased to 6 GeV for the high threshold.

6.7.2 Track Trigger Efficiency

The efficiency of the combination of track trigger elements in the sub-trigger is obtained by using a SPACAL sub-trigger designed to detect forward jets. The trigger combines the same energy threshold and veto conditions as either the low or high threshold trigger with energy deposition in the forward region of the LAr calorimeter. Hence, it is independent of any track trigger conditions.

Since the efficiency of the track trigger elements depends strongly on the production and decay characteristics of the D^* it is more sensible to evaluate the efficiency of the track components of the trigger from the number of D^* mesons obtained in fits of the ΔM distributions. This gives a larger statistical error than counting the entries in the ΔM distribution but has the advantage of being less sensitive to the effect of a difference in the behaviour of the background between the monitor and physics sub-triggers.

1996 data

For the 1996 data, only 70 events are available from the monitor trigger independent of track conditions. The results from the simulation and data are shown in table 6.8.

	data	simulation
$zvtx - sig$	79.1 ± 3.70	82.5 ± 0.6
$r\phi - T_{High}$	99.4 ± 1.4	95.9 ± 0.4
$zvtx - sig.\text{AND}.r\phi - T_{High}$	79.8 ± 3.7	78.0 ± 0.7

Table 6.8: The trigger efficiency for the track conditions for the 1996 data.

The simulation gives a reasonable description of the efficiency of the combined $zvtx$ and $r\phi$ trigger elements up to the accuracy of the monitor trigger statistics in the data. There appears to be a small discrepancy between the data and simulation for the efficiency of the $r\phi$ trigger element. The low statistics mean the efficiency of the trigger elements cannot be studied differentially as a function of y in the data with a completely independent trigger. However, adequate statistics are available using another sub-trigger that covers a different kinematic range and has only a weak $zvtx$ condition. This sub-trigger was designed as a minimum bias trigger for the measurement of the inclusive structure function, F_2, and is composed of

- An IET cluster threshold of 6 GeV which is operational in the outer region of the SPACAL only due to beam related background problems.
- A weak (i.e. at least one entry in the $zvtx$ histogram) $zvtx - t0$ condition is applied to reduce non-vertex fitted background, allowing the implementation of a low prescale factor.

The exclusion of a 'box' region in the inner part of SPACAL corresponds to the region of lowest Q^2. However, the excluded 'box' is positioned asymmetrically around the beampipe (see section 1.11.1) so that a fraction of the events are available at the lowest Q^2 values covered in the analysis. The number of D^* mesons collected by this sub-trigger is around 250. The 'box' region is excluded in the data and simulation so that the reduction in acceptance caused by the cut is the same for both. Due to the differences in the $zvtx$ trigger requirements, the measured trigger efficiency is different to that applicable in the analysis. However, the description of the $z - vtx$ and $r - \phi$ trigger by the simulation can still be investigated. The comparison of the track trigger element efficiency of this sub-trigger in the data and simulation is shown as a function of y in figures 6.7a-c. A reasonable agreement is observed with some deviations of small significance at low y for the $zvtx$ trigger element.

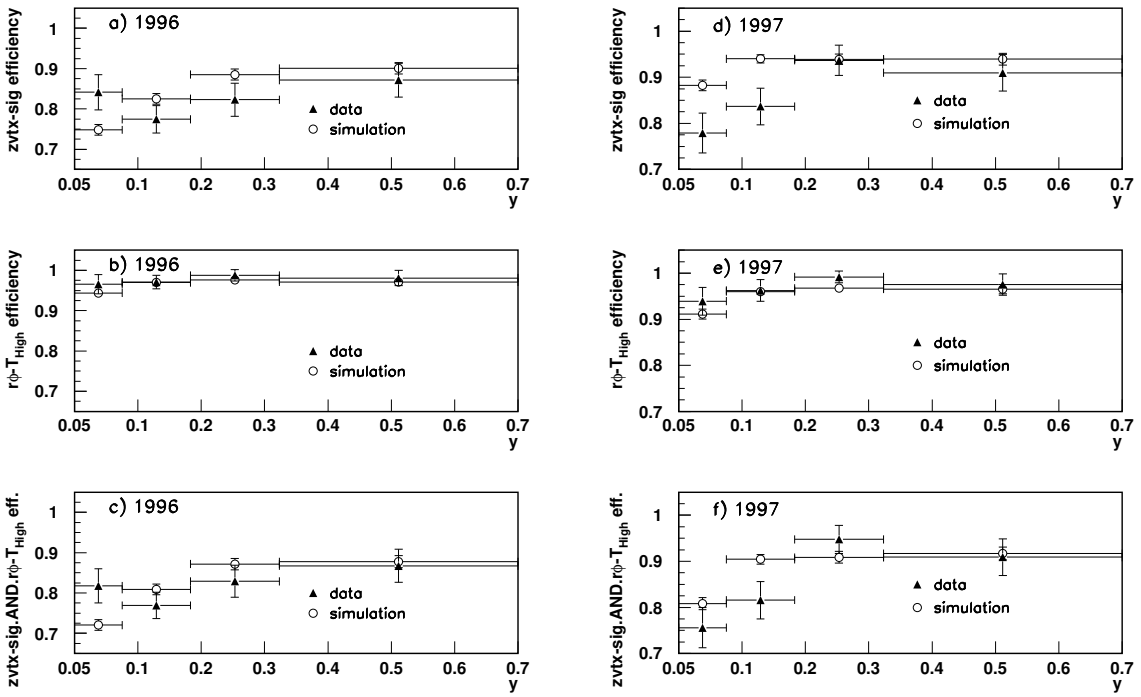

Figure 6.7: The efficiency of the $zvtx - sig$, $r\phi - T_{High}$ and $zvtx - sig.AND.r\phi - T_{High}$ trigger conditions. (a)-(c) The simulation is compared with the 1996 data for a monitor trigger with a $zvtx - t0$ requirement. (d)-(f) The simulation is compared with the 1997 data using a completely independent monitor trigger.

1997 data

For the analysis of the 1997 data, the monitor trigger collected around 190 events and the results of the efficiency measurement are shown in table 6.9.

	data	simulation
$zvtx - sig$	87.0 ± 2.1	92.5 ± 0.5
$r\phi - T_{High}$	98.1 ± 1.0	94.9 ± 0.5
$zvtx - sig.\text{AND}.r\phi - T_{High}$	86.0 ± 2.1	87.9 ± 0.6

Table 6.9: The trigger efficiency for the track conditions for the 1997 data.

The simulation and data both show a higher efficiency in 1997 when compared to 1996 for the $z - vtx$ trigger. This is due to a fine tuning of the trigger algorithm at the edges of the tracker in response to the inefficiency at low y [107]. There is an indication that the $z - vertex$ trigger is not as efficient in the data as expected in the simulation, and conversely that the $r\phi$ trigger in data is not as affected by the performance of the central tracker as expected in the simulation. The efficiency is determined differentially as a

function of y using the monitor trigger and is shown in figures 6.7d-f. The discrepancy between the data and simulation, within the limited statistics, appears to arise dominantly from the low y region for the $z-vertex$ trigger. Overall the description of the track trigger efficiency by the simulation is sufficient to justify its use for corrections, with an appropriately evaluated systematic error. The difference in the efficiency between the data and simulation for the $z-vtx$ and $r\phi$ trigger elements in each year are added in quadrature. This produces an uncertainty of 5.8% and 6.8% in the track trigger efficiency for the 1996 and 1997 data sets respectively.

Additional trigger elements from the $r-\phi$ trigger were applied to the high electron threshold sub-trigger in the 1997 running period to suppress background originating from protons interacting upstream of the detector. This background should be rejected by the timing vetos of the SPACAL. However, protons with incorrect beam timing (late satellite bunches) are accepted because they arrive just at the nominal time for ep interactions at these veto layers. Due to the large amount of dead material between the vertex and the central tracking detectors, these proton beam background induced events can cause an enormous number of hits in the drift and proportional chambers and require considerable time to be processed by the on-line level 4 trigger, which can cause inefficiency in the data taking. The newly introduced $r-\phi$ trigger elements serve as a veto of the 'large' background events by placing limits on the number of tracks found. From studies using the monitor trigger it is found that no events in the ΔM distribution are lost when the additional $r-\phi$ trigger elements are applied and the combination of trigger elements is assumed to be 100% efficient.

6.8 DIS Control Distributions

The efficiency for the reconstruction of the DIS electron and kinematics of the event is high. However, it is still important to make sure that the simulation describes the data, to ensure that the smearing is dealt with correctly. The ability of the detector simulation to describe this aspect of the event reconstruction is investigated by the use of 'control distributions'. In figure 6.8, the data and simulation are compared for events with at least one entry in the ΔM distribution. The agreement is reasonable for the radius of the cluster, R_{clus}, after the simulation values have been multiplied by a factor of 1.1 due to imperfect modelling of the transverse showering of the cluster [106]. The SPACAL cluster-BDC track link parameter, ΔR_{BDC}, and the radius of the electron in the SPACAL, R_{SPACAL}, are reasonably well described. The distribution of the z-vertex is also correctly described by the simulation.

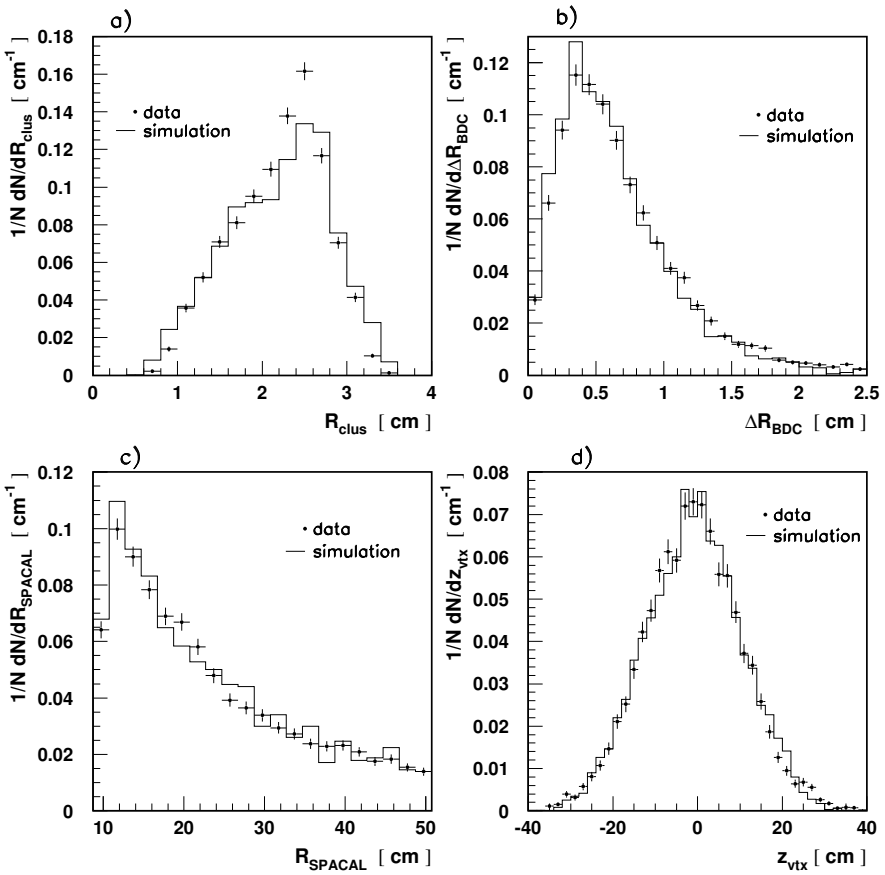

Figure 6.8: The simulation compared with the data for the (a) R_{clus} (b) ΔR_{BDC} (c) R_{SPACAL} and (d) z_{vtx} distributions. The plots are normalised to the number of entries within the ΔM distribution, N.

In figure 6.9 further distributions are compared for D^* candidates within 2 MeV of the signal position in the ΔM distribution, after background subtraction. The shape of the background is modelled by the distribution from D^* candidates with ΔM values in the range $0.15 - 0.17$ GeV and the normalisation is determined by the number of D^* mesons obtained from the fitting procedure. The cluster energy, E_{clus}, and polar angles θ and ϕ of the scattered electron are well described by the simulation. The agreement between the data and the simulation for the $\sum(E - p_z)$ distribution (figure 6.9d) is not as good. However, the position of the distribution, which peaks at twice the electron beam energy, is compatible between the data and the simulation, confirming that the electromagnetic energy scale is correct. The excess in the data at lower $\sum(E - p_z)$ is due mainly to radiative effects not included in the simulation.

The description of the final state is hindered further by the modelling of large rapidity

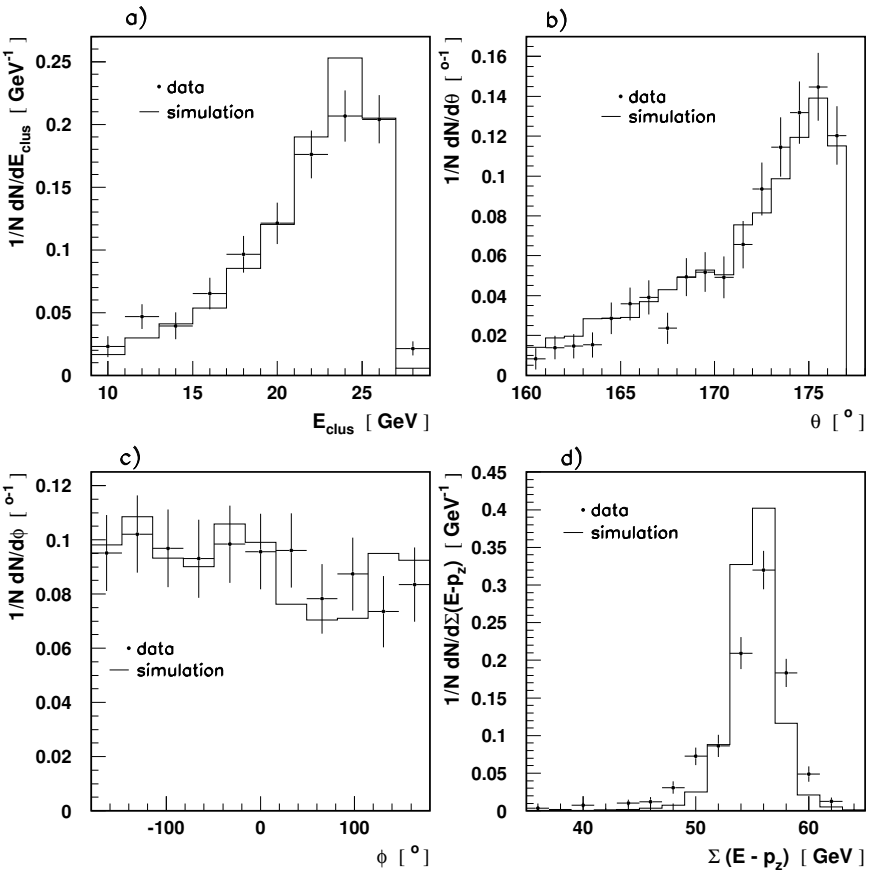

Figure 6.9: The simulation compared with the data for the (a) E_{clus} (b) θ (c) ϕ and (d) $\sum(E - p_z)$ distributions. The plots are normalised to the number of D^* candidates in the ΔM distribution, N.

gaps produced by soft colour interactions in the fragmentation scheme within AROMA (see section 3.7.3). These events usually have extremely low hadronic energy in the detector. This leads to a poor description of the hadronic final state, as shown in figure 6.10, for the hadronic energy, E_{had}, and the hadronic longitudinal momentum, p_{zhad}, reconstructed from track and calorimeter information. The large rapidity gap events produced by AROMA are discussed further in chapter 8.

6.9 The Background Correction - r

The AROMA Monte Carlo simulation that is used to correct the data models only the process under study $D^{*+} \rightarrow (K^-\pi^+)\pi^+_{slow}$ and not the remainder of the combinatorial background. The majority of this background is light quark induced and is expected to

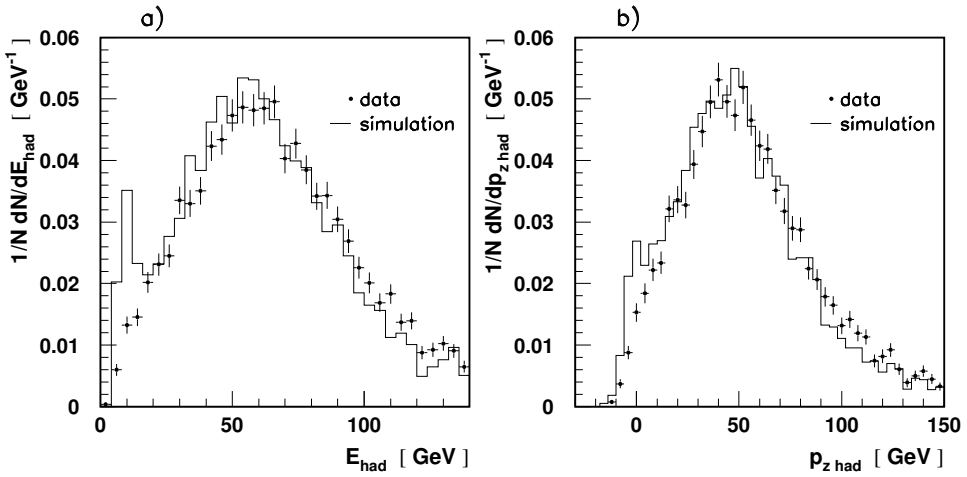

Figure 6.10: The simulation compared with the data for (a) the hadronic energy of the final state, E_{had} (b) the longitudinal momentum of the hadronic final state, p_{zhad}. The large rapidity gap events in AROMA produce events with low hadronic mass. The data are normalised to the number of entries within the ΔM distribution, N.

to follow the threshold behaviour. Therefore this makes no extra contribution around the signal region. However, there is a small contribution to the signal from other heavy flavour decay modes. The dominant source is decay modes of the D^0 other than $D^0 \to K^-\pi^+$, such as $D^0 \to K^-K^+$ and $D^0 \to \pi^-\pi^+$. In these cases, the assignment of the wrong mass hypothesis to one of the D^0 decay tracks leads to a shifting of the measured two particle invariant mass, but a fraction remains within the 80 MeV mass window around the nominal D^0 mass. If the D^0 originates from the $D^* \to D^0\pi$ decay, then the kinematic constraint of the π_{slow} is such that a peak is formed in the ΔM spectrum. The fraction of these events, referred to as reflections, contributing to the signal is estimated from further simulations of the largest contributing decays using the AROMA Monte Carlo. The correction increases with the size of the mass window around the D^0 mass, and for a window of 80 MeV leads to a contribution of $3.5 \pm 1.5\%$ [123].

6.10 Error Determination

There is one contribution to the statistical error on each cross section which arises from the result of the fit to the ΔM distribution (see section 5.7). The majority of systematic effects are considered for each bin by the variation of important parameters in the extraction procedure by equal amounts in either direction. The systematic error assigned is then equal to the average change in the cross section. The systematic uncertainties which

affect all data points in the same way are assigned to the correlated errors. The sources of systematic uncertainty considered are

- **Track and Vertex Reconstruction Efficiency**
  The systematic error due to the uncertainty in the track reconstruction for three particles (see section 6.6) results in an uncertainty, for each measured point, of $\pm 7.5\%$. The uncertainty in the efficiency for linking the tracks to the fitted vertex results in a correlated error of $^{+4.4\%}_{-0.0\%}$.

- **Track Trigger Efficiency**
  An uncertainty of 5.8%[4] in the efficiency of the $zvtx$ and $r-\phi$ components of the analysis sub-trigger, is determined from studies using independent triggers (see section 6.7).

- **Hadronic Energy Scale**
  A 4% uncertainty in the energy scale of the LAr calorimeter, a 7% uncertainty in the hadronic energy scale of the SPACAL, and a 3% uncertainty in the fraction of final state energy contained in the tracks affect the reconstruction of the event kinematics giving a systematic uncertainty at the level of 1.9% on average for all bins.

- **Electromagnetic Energy Scale and Electron Angle**
  The uncertainty on the measured angle of the scattered electron of 0.5 mrad, and an uncertainty of the electromagnetic energy scale in the SPACAL of 1%(3%) at 27.5(8) GeV affect the reconstruction of the event kinematics and determination of the $\gamma^{\star}p$ collision axis, which affects the boost into the hadronic centre of mass frame, such that the uncertainty on the cross sections is, on average, 3.4%.

- **Electron Trigger Threshold and Veto Conditions**
  An error of 1% is applied to account for the uncertainty in the threshold of the IET trigger and the veto conditions applied in the analysis sub-trigger (see section 6.7).

- **Electron Identification**
  The uncertainty in the electron identification and BDC reconstruction efficiency is 1% [10].

- **Luminosity**
  The uncertainty in the determination of the luminosity of the data sample is 1.5% [10].

[4]This error includes a contribution of 3.2% for the uncertainty in the trigger efficiency for the 1995 data [107]

- **Input Kinematic Distributions**
  The uncertainty due to the input momentum distributions in the AROMA MC model is estimated using a simulation of the RAPGAP Monte Carlo generator which has, for example, a different $p_\perp(D^*)$ and y distribution. This affects both the track reconstruction and trigger efficiency. Uncertainties of 6.0% are obtained when averaged over all distributions.

- **The z Cut**
  The uncertainty due to the efficiency of the $z(D^*)$ cut is estimated by not applying the cut. This results in a uncertainty of 4.0% when averaged for all the differential cross sections.

- **Photoproduction Background**
  The uncertainty on the contamination from photoproduction processes is quoted as $^{+0}_{-1}$% [48].

- **Beauty Production**
  The contribution of beauty production to the signal is small. No subtraction of this contribution is performed since the D^* cross section is defined for all production processes. A 1% error is applied due to uncertainty in the effect of b production on the acceptance [48].

- **ΔM Fitting Procedure**
  The systematic uncertainty in the determination of the number of D^* mesons from the fits to the ΔM distribution is estimated in the following way. The effect of fixing the width and position of the Gaussian, in the fits for the differential distributions, to that obtained from a free fit to the total sample, is estimated for each bin by variation of the Gaussian width by $\pm 1\sigma$ as determined from the total sample. This produces correlated errors of around 3%.

- **Reflections Correction**
  The uncertainty in the determination of the correction due to reflections produces a correlated uncertainty of 1.5% (see section 6.9).

- **Branching Fraction**
  The uncertainty in the branching fraction of the decay mode used leads to a correlated uncertainty of 3% on the cross sections [111].

6.11 Results

The cross section $\sigma(ep \to eD^*X)$ in the kinematic range $2 < Q^2 < 100$ GeV^2, $0.05 < y < 0.7$, $p_\perp(D^*) > 2$ GeV and $|\eta(D^*)| < 1.5$ is found to be

$$4.21 \pm 0.23 \pm 0.53 \text{ nb} \tag{6.12}$$

where the first error is statistical and the second systematic.

The inclusive D^* cross section is shown as a function of the variables Q^2, y, x_{BJ}, $\eta(D^*)$, $p_\perp(D^*)$, $p^*_\perp(D^*)$[5], $z(D^*)$, x_g^{obs}, $|\phi^*(D^*)|$ and $\phi(D^*)$ in figures 6.13 and 6.14. As an illustration of the statistics available with the combined data set the individual ΔM distributions are shown differentially in $p_\perp(D^*)$ and y in figures 6.15 and figure 6.16 respectively. The cross sections are compared with a leading order QCD calculation performed in AROMA. For the prediction, the GRV LO [124] parton densities have been used. The value of Λ_{QCD} and the number of flavours used in the first order expression for α_s were 0.2 GeV and 4 respectively. The mass of the charm quark was taken to be 1.5 GeV. With these settings the prediction of AROMA for the total cross section in the measured kinematic range is 4.13 nb which is in good agreement with the data[6]. The program is also found to give a reasonable description of the shape of the differential distributions. There is a slight discrepancy between the data and simulation in the distribution of x_g^{obs} and $\eta(D^*)$. The difference in both distributions is related to the gluon distribution in the proton at higher values of x_g. In order to reduce the uncertainty in the acceptance calculation, the generated x_g^{obs} distribution has been reweighted so that the simulation better describes the data. The agreement between the data and AROMA implies the measurement is generally compatible with published data performed on 1995 and 1996 data and measured in a slightly different kinematic range [48].

6.12 Stability of the Cross Section

The D^* cross section measured for each of the three years of data are in agreement within statistical errors. In order to test further the ability of the simulation to describe the deteriorating performance of the detector, the cross section is measured, for the 1996 and 1997 data, within different regions of the central tracking detector. The cross section is measured in the upper (lower) region of the central tracking detector by demanding that

[5]Note that the cross section for $p^*_\perp(D^*)$ is shown with the momentum cut in the laboratory applied and no extrapolation to the full phase space is made.

[6]For a precise comparison the data needs to be corrected for higher order QED effects. For the Σ reconstruction method, which is used throughout, these corrections are expected to be small [107].

the D^* meson, and all three of the reconstructed decay candidates, have an azimuthal angle in the range $\phi > 0^o$ ($\phi < 0^o$). Around two thirds of the full sample of D^* mesons satisfy the criteria of either having all decay products in the upper hemisphere or all decay products in the lower hemisphere. The total cross section measured in the two regions of the central tracking detector for the 1996 and 1997 data is shown in table 6.10. All four measurements are in agreement within their statistical errors. The number of D^* mesons used to evaluate the cross sections is obtained from free fits to the ΔM distribution because the width of the signal region differs between the two hemispheres.

Year	CJC Region	cross section (nb)
1996	upper	4.05 ± 0.51
	lower	4.75 ± 1.02
1997	upper	4.52 ± 0.55
	lower	4.42 ± 0.57

Table 6.10: The total cross section, shown with statistical errors only, measured for the 1996 and 1997 data samples when all the decay products of the D^* are demanded to be either in the upper ($\phi > 0^o$) or lower ($\phi < 0^o$) half of the central tracking detector.

6.13 Conclusion

The total and differential inclusive D^* cross section has been measured in a well defined kinematic range for the combined 1995, 1996 and 1997 data sample. The measured cross section is found to be consistent between each year. The main contribution to the losses in acceptance comes from the inefficiency in reconstructing 3 tracks within the central tracking detector, especially in the 1997 data, where the inefficiency increases considerably. The ability of the simulation to describe the performance of the central tracking detector has been investigated in detail. Although it is unable to reproduce all the studied distributions in detail, in particular the width of the ΔM distribution, the general properties such as the hit multiplicity per track and the efficiency of the track cuts are well described.

The hard track trigger conditions applied to the level 1 sub-trigger in the analysis are also a large source of inefficiency. The description of their efficiency in the data by the simulation has been investigated. The simulation is sufficient to be used in the evaluation of the trigger efficiency for the cross section measurement.

The LO AROMA program gives a good description of the rate and shape of the differential cross sections. A small reweighting of the x_g distribution in the proton towards higher x_g

was found to improve the description of the data by the program. The poor description of the hadronic final state at low energy indicates that the implementation of large rapidity gap events in AROMA, via the mechanism of soft colour interactions, will have difficulty in providing the correct description of large rapidity gap events. However, the program may be used to model the 'standard' DIS regime in the measurement of the diffractive D^* cross section in chapter 8.

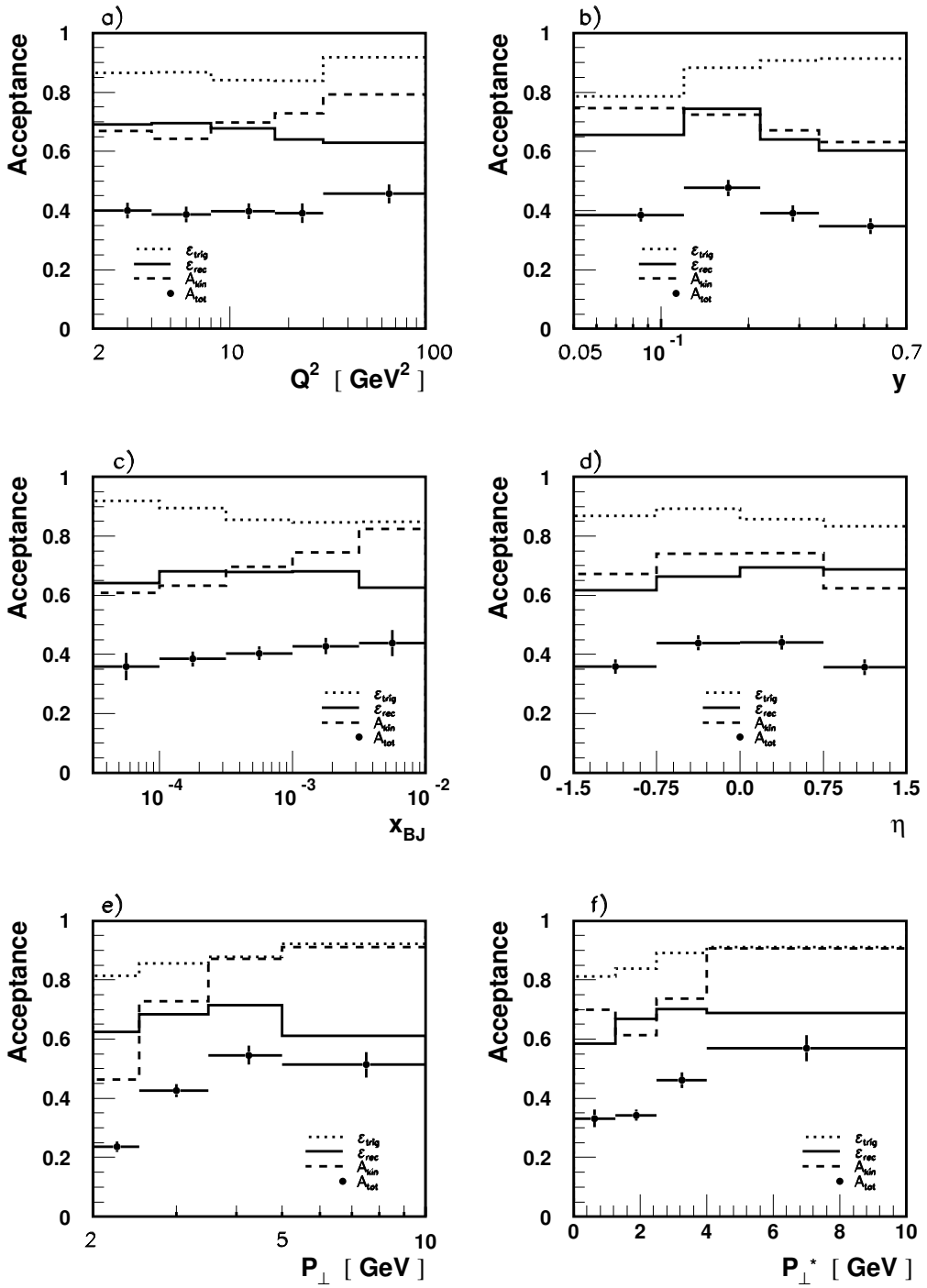

Figure 6.11: The 'smeared' acceptance as calculated from Monte Carlo simulations as a function of (a) Q^2 (b) y (c) x_{BJ} (d) η (e) $p_\perp$ and (f) $p_\perp^*$. The solid line indicates the reconstruction efficiency, ϵ_{rec}, the dashed line the kinematic acceptance, A_{kin}, the dotted line the trigger efficiency, ϵ_{trig}, and the points with error bars the overall 'smeared' acceptance, A_{tot}.

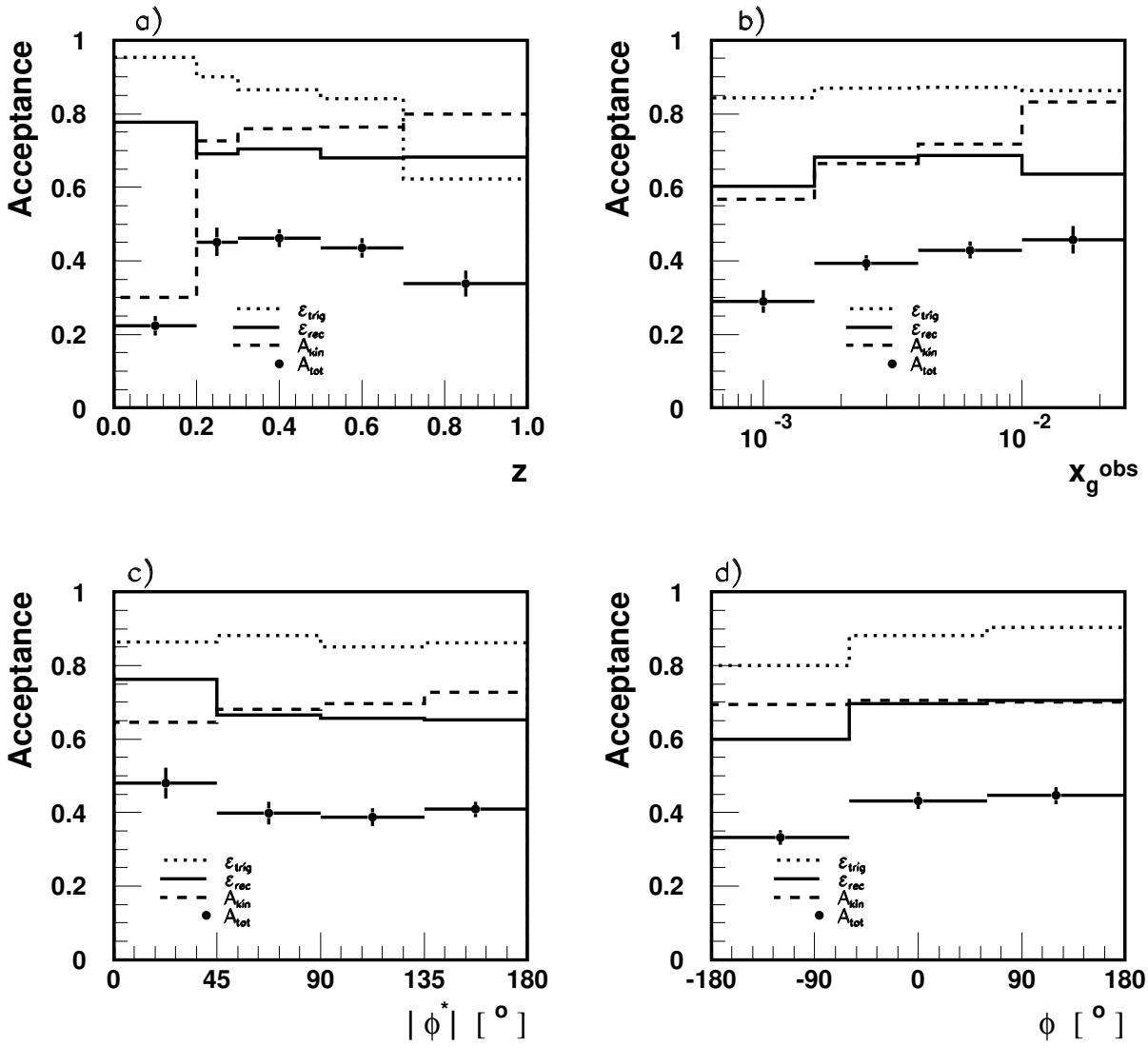

Figure 6.12: The 'smeared' acceptance as calculated from Monte Carlo simulations as a function of (a) z (b) x_g^{obs} (c) ϕ^* and (d) ϕ. The solid line indicates the reconstruction efficiency, ϵ_{rec}, the dashed line the kinematic acceptance, A_{kin}, the dotted line the trigger efficiency, ϵ_{trig}, and the points with error bars the overall 'smeared' acceptance, A_{tot}.

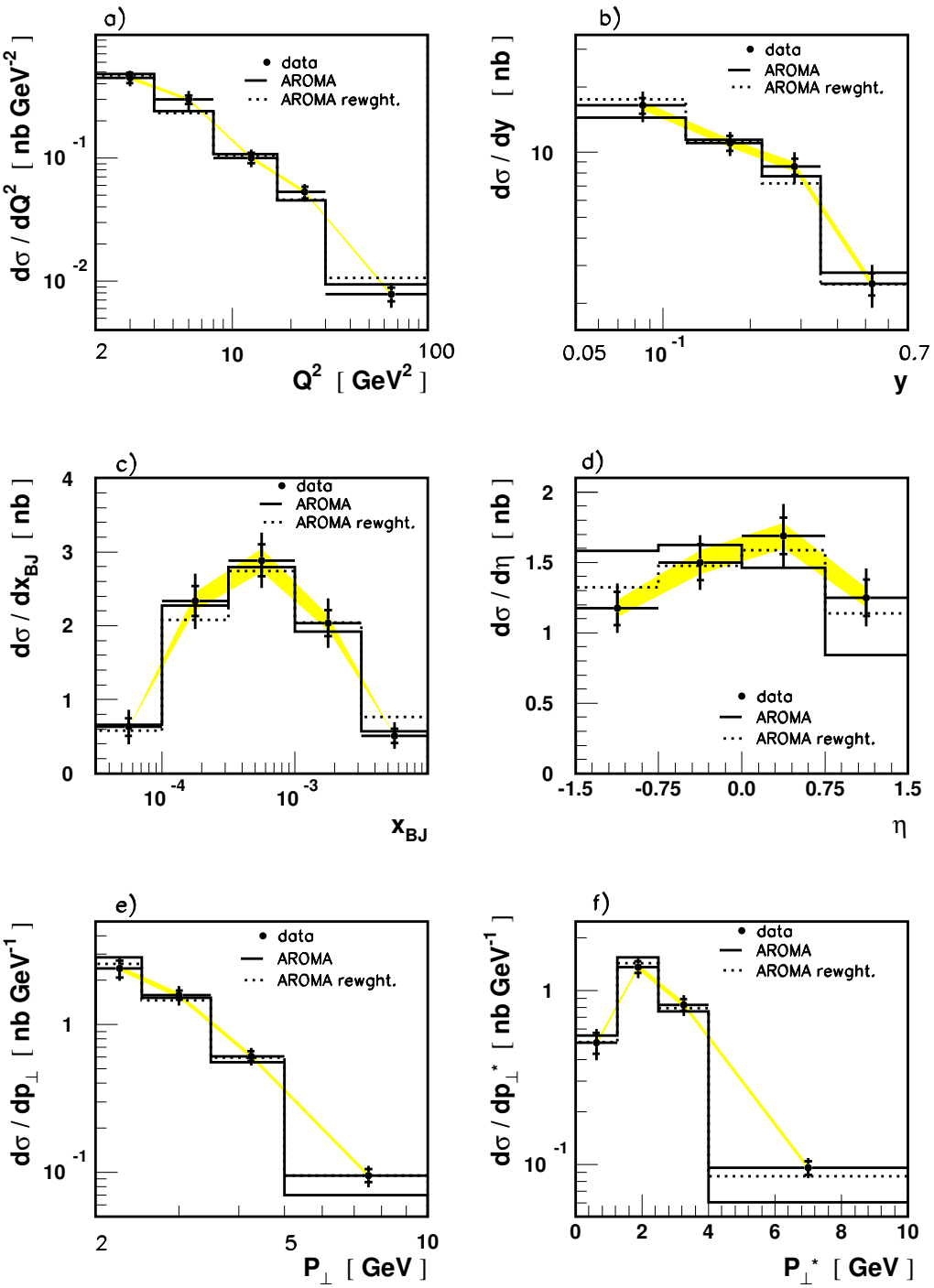

Figure 6.13: The inclusive D^* cross section plotted differentially as a function of (a) Q^2 (b) y (c) x_{BJ} (d) $\eta(D^*)$ (e) $p_\perp(D^*)$ and (f) $p^*_\perp(D^*)$. The data are shown as circles with error bars; the inner bar is the statistical error and the full bar is the statistical plus systematic error added in quadrature. The shaded band represents the overall normalisation uncertainty. The data are compared with a LO prediction calculated within AROMA (full line). The AROMA prediction is also shown reweighted (dotted line) to the x_g^{obs} distribution (figure 6.14b) which improves the description of the data, in particular the $\eta(D^*)$ distribution.

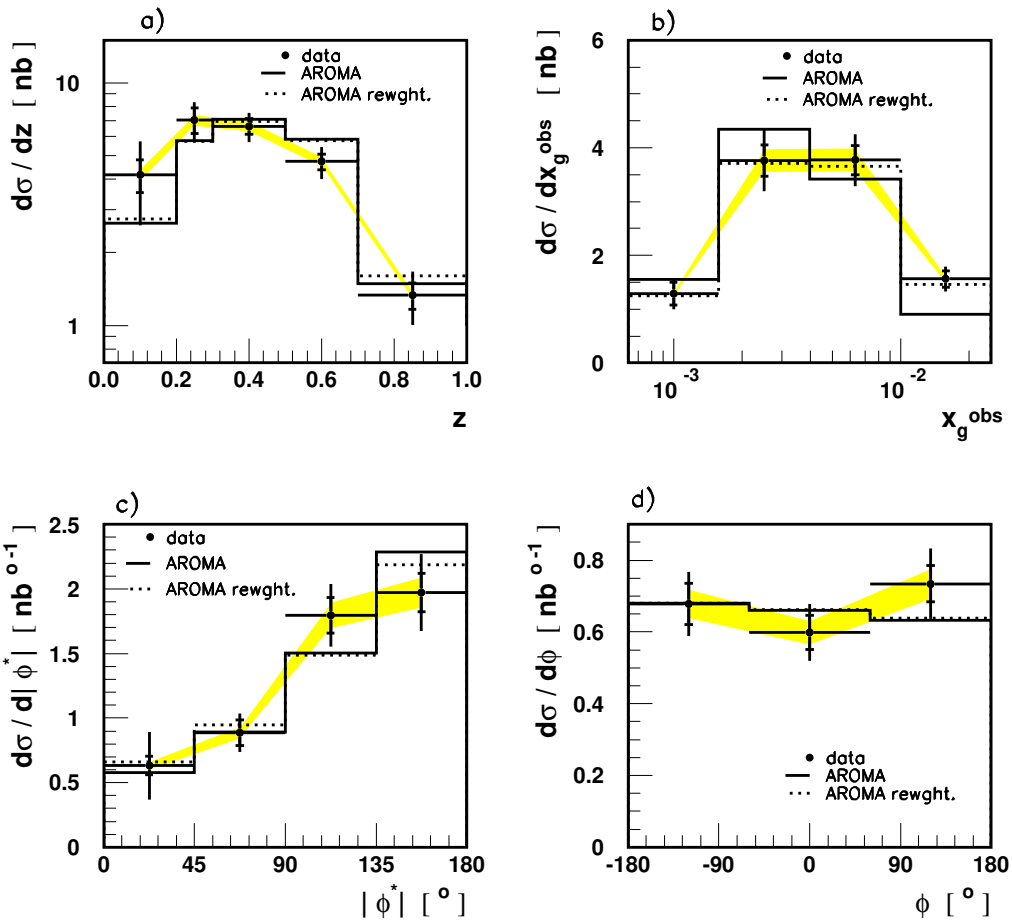

Figure 6.14: The inclusive D^* cross section plotted differentially as a function of (a) $z(D^*)$ (b) x_g^{obs} (c) $|\phi^*(D^*)|$ and (d) $\phi(D^*)$. The data are shown as circles with error bars; the inner bar is the statistical error and the full bar is the statistical plus systematic error added in quadrature. The shaded band represents the overall normalisation uncertainty. The data are compared with a LO prediction calculated within AROMA (full line). The AROMA prediction is also shown reweighted to the x_g^{obs} distribution (dotted line) which improves the description of the data.

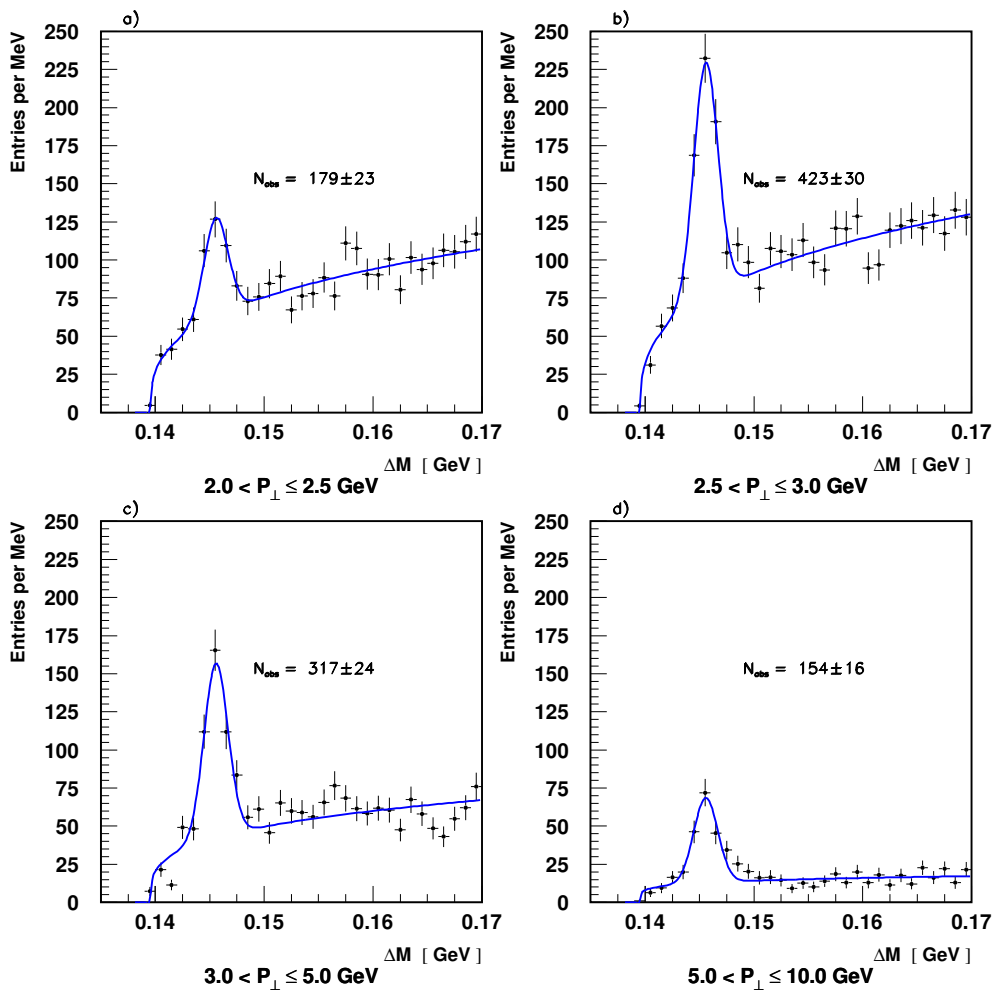

Figure 6.15: The individual ΔM distribution for the four bins in $p_\perp(D^*)$. (a) $2.0 < p_\perp(D^*) \leq 2.5$ GeV (b) $2.5 < p_\perp(D^*) \leq 3.0$ GeV (c) $3.0 < p_\perp(D^*) \leq 5.0$ GeV and (d) $5.0 < p_\perp(D^*) \leq 10.0$ GeV. For each bin the number of D^* mesons obtained from the fit to the ΔM distribution, N_{obs}, (including the error) is shown.

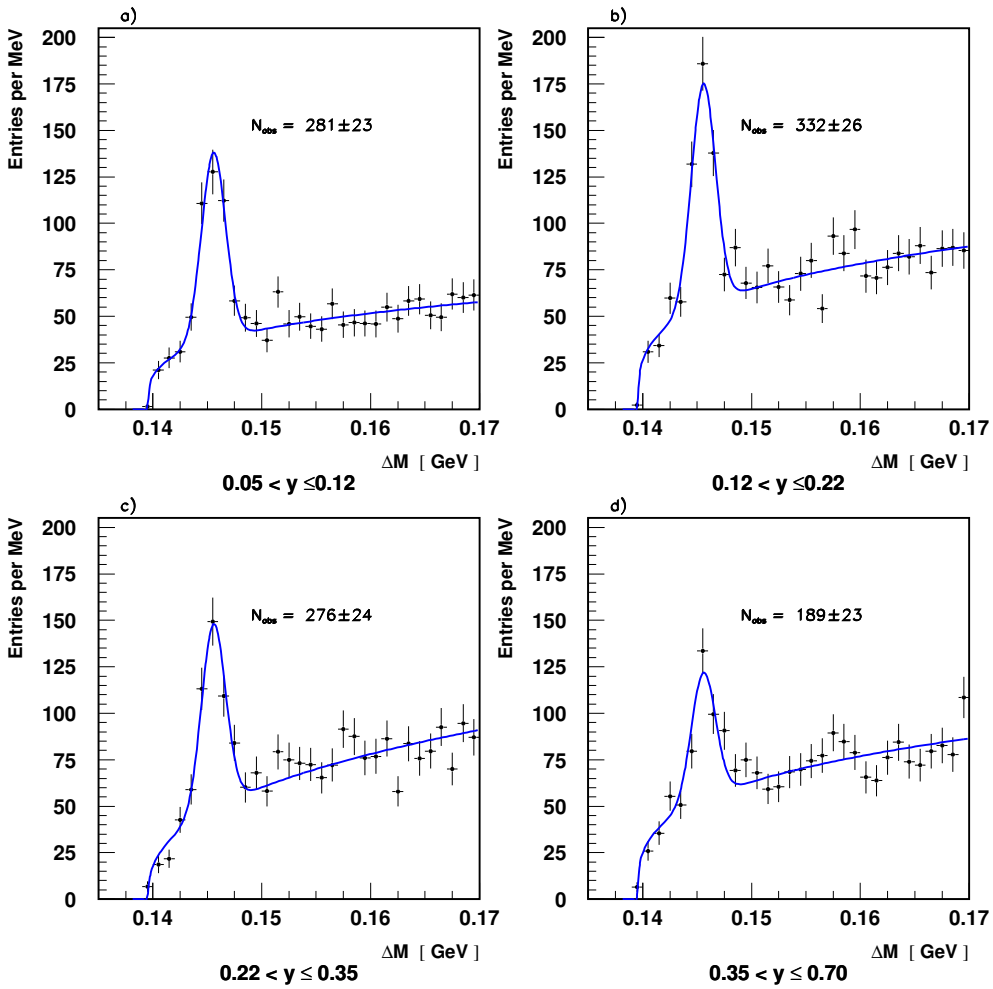

Figure 6.16: The individual ΔM distribution for the four bins in y. (a) $0.05 < y \leq 0.12$ (b) $0.12 < y \leq 0.22$ (c) $0.22 < y \leq 0.35$ and (d) $0.35 < y \leq 0.70$. For each bin the number of D^* mesons obtained from the fit to the ΔM distribution, N_{obs}, (including the error) is shown.

Chapter 7

Selection and Reconstruction of Diffractive Events

7.1 Introduction

This chapter contains a discussion of the experimental techniques used in the extraction of the DIS diffractive cross sections presented in chapter 8. Firstly, in section 7.2, the Monte Carlo models which are used to correct the data for the measurement of the diffractive cross section are introduced. In section 7.3 it is shown that the presence of a large gap in rapidity between the final state hadrons in colour singlet exchange processes allows a very pure sample of colour singlet exchange events to be selected.

The procedure for selecting large rapidity gap events utilises the detectors in the forward region of H1. A set of cuts using these forward detectors is formulated in section 7.4. The response of the detectors for the three years of data are investigated in section 7.5. A comparison of the performance of the forward detectors in data with Monte Carlo simulations is made in section 7.5.1 to investigate the ability of the models themselves, and the detector simulation, to describe the data. It is found that the response of the proton remnant tagger in the simulation differs considerably from that observed in the data. Therefore a correction procedure is applied to the simulation of the proton remnant tagger in section 7.5.2.

The kinematic range of the diffractive cross section measurement is completely defined by the three variables M_Y, t and $x_{I\!P}$[1]. Since the final state proton is not reconstructed directly, the cross section is integrated over both M_Y and t. In section 7.6, detector simulations of the forward region of the detector are used to investigate the acceptance

[1]See section 3.3.1 for the definition of these variables.

for detecting the final state proton in order to determine the range in M_Y and t over which the cross section is measured. The hadronic final state algorithm used to reconstruct $x_{I\!P}$ is explained in section 7.7. The kinematic range in $x_{I\!P}$ over which the cross section is measured is also detailed in this final section.

7.2 Monte Carlo Models

As in the measurement of the cross section for inclusive D^* production in chapter 6, Monte Carlo simulations are used to calculate the acceptance and smearing. However, the method is more involved for the measurement of the diffractive D^* cross section. A mixture of models has to be used in order to reproduce the data, because no single event generator gives a complete description of the available phase space.

7.2.1 RAPGAP

The Monte Carlo generator RAPGAP is used to generate the process $ep \to e(c\bar{c}X)Y$ for the kinematic range $x_{I\!P} < 0.1$ and $M_Y = m_p$. The model has two components in which the proton couples to a pomeron or a meson which then undergoes a hard scattering with the incident electron. The pomeron and meson fluxes are provided by a simple Regge form with an exponential t dependence so that the diffractive structure function is given by

$$F_2^{D(4)}(x_{I\!P}, \beta, Q^2, t) = \frac{e^{B_{I\!P}\, t}}{x_{I\!P}^{2\alpha_{I\!P}(t)-1}} F_2^{I\!P}(\beta, Q^2) + \frac{e^{B_{I\!R}\, t}}{x_{I\!P}^{2\alpha_{I\!R}(t)-1}} F_2^{I\!R}(\beta, Q^2) \tag{7.1}$$

where the pomeron and meson trajectories, $\alpha_{I\!P}(t)$ and $\alpha_{I\!R}(t)$, are taken from the results of a Regge phenomenological fit to the H1 diffractive structure function $F_2^{D(3)}$ [4]. The pomeron structure function is taken from the parton distributions obtained from a LO QCD fit to the H1 diffractive structure function. The meson structure function used is the GRV parameterisation of the pion [125].

The charm quark anti-quark pair is produced through the boson-gluon fusion process calculated to leading order in QED and QCD (see section 5.4). Higher order QCD corrections are provided either by the colour dipole model as implemented in the ARIADNE program [51] or the parton shower model similar to that used in LEPTO [49]. The hadronisation is performed using the Lund string model which is implemented in the JETSET [52] program.

7.2.2 DIFFVM

Since the RAPGAP program can only generate events with an elastic proton, the vector meson Monte Carlo generator DIFFVM [126] is used to model proton dissociation in the low mass range $M_Y < 5$ GeV. The J/Ψ is chosen as the vector meson most suitable for the simulation. In the DIFFVM model, the cross section for dissociation in the lowest mass region ($M_Y < 1.9$ GeV) is based on a parameterisation of proton dissociation on deuterium [127]. The dissociation at larger masses is assumed to have the Regge form $d\sigma/dM_Y^2 \sim 1/M_Y^2$. The constituent quarks of the proton are fragmented according to the Lund string model implemented within the JETSET [52] Monte Carlo program. The dependence of the dissociation cross section on t is parameterised in the exponential form $d\sigma/dt \sim e^{bt}$ with the slope parameter $b = 1.6$ GeV^{-2}. In the simulation, the ratio of elastic to proton dissociation interactions is taken to be $1:1$.

7.2.3 AROMA

In the region of either large M_Y or high $x_{I\!P}$ ($M_Y > 5$ GeV or $x_{I\!P} > 0.1$), the process $ep \to e(c\bar{c}X)Y$ is modelled by the AROMA Monte Carlo program which was shown in chapter 6 to reproduce well the general features of inclusive DIS D^* production, including the overall normalisation. The large rapidity gap events, which can be generated through soft colour interactions within AROMA, are suppressed in the kinematic range $M_Y > 5$ GeV or $x_{I\!P} > 0.1$ which avoids double counting.

7.3 Large Rapidity Gap Event Selection

7.3.1 Separation of the System X and System Y

In measurements of events containing a large rapidity gap, a precise definition of the hadron level cross section is essential. The definition employed by the H1 experiment decomposes the hadronic final state into two distinct topological systems, labelled X and Y (see figure 7.1). The two systems are separated by the largest gap in rapidity between the final state hadrons in the photon-proton centre of mass frame. The system closest to the direction of the proton is labelled the system Y.

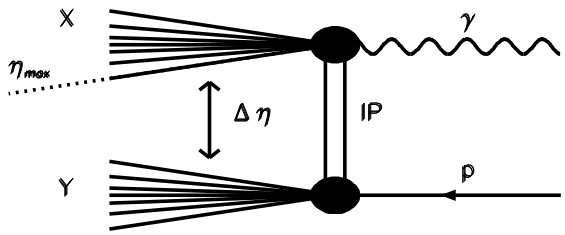

Figure 7.1: Diagram of the photon system X and the proton system Y in a diffractive event. The systems are separated by the largest gap in rapidity of the final state hadrons in the centre of mass frame. The pseudo-rapidity of the most forward hadron of the system X detected in the main calorimeter is called η_{max}.

7.3.2 Final State Rapidity Distributions

The signature of a colourless exchange process (such as diffraction) is a large region in rapidity in which no hadrons are produced, indicating the absence of any colour string connecting the photon and proton fragmentation regions. At HERA, the γp centre of mass is typically boosted in the forward direction in the laboratory so that at least part of the photon fragmentation system X is contained within the main detector. Conversely, except when M_Y is large ($M_Y \gtrsim 10$ GeV) the system Y is not visible in the main detector.

In events where there is a colour string connecting the photon and proton fragmentation regions, a hadronic plateau of low but detectable activity is produced. The fragmentation models discussed in section 2.6.1 have an exponential distribution in the size of the rapidity gap between successive parton emissions which decreases along the parton ladder in the direction from the proton to the photon. Therefore, the separation in rapidity of adjacent energy clusters in the calorimeter falls off exponentially, and the most forward cluster observed in the LAr calorimeter is typically very near to the edge of its acceptance.

Figure 7.2a shows a DIS D^* candidate without a large rapidity gap. It can be seen that there is significant activity in the forward region and that the most forward cluster in the LAr calorimeter is close to the edge of its acceptance ($\eta \sim 3.5$). In contrast, the event shown in figure 7.2b, a diffractive DIS D^* candidate, has very little activity in the forward region and there is a large rapidity gap which extends up to the most forward LAr cluster ($\eta \sim 0.5$).

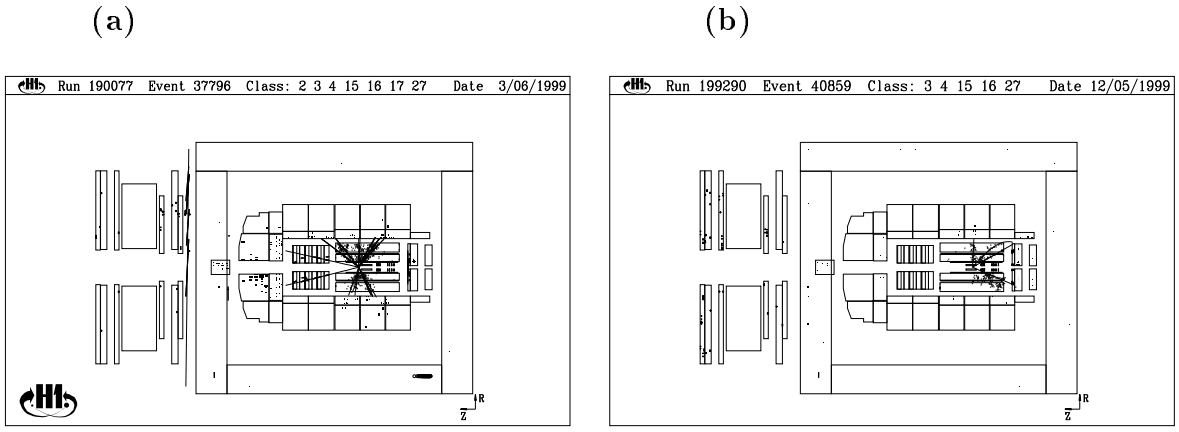

Figure 7.2: Example DIS D^* candidate events (a) non-diffractive, with considerable forward activity, and (b) diffractive, with little forward activity.

7.3.3 The η_{max} cut

The primary cut used to select diffractive events is in the variable η_{max}, which is defined as the rapidity of the most forward calorimeter energy deposit above a specified energy threshold to reject noise (see section 7.4.5). As is shown in figure 7.3a, for Monte Carlo events generated with AROMA, colour singlet exchange processes (denoted 'proton elastic' and 'proton dissociation') produce a plateau in the η_{max} distribution which extends to the lowest values ($\eta_{max} \sim -2$). The extent of the plateau in η_{max} can be inferred, for example, when multiperipheral models [128], which describe the fragmentation of the photon system as a function of rapidity, are combined with the expectations from triple Regge theory[2]. In contrast to colour singlet exchange processes, the η_{max} distribution for non-colour singlet exchange processes ('standard DIS' events) falls off steeply; and is negligible for $\eta_{max} \lesssim 2.5$.

In the first studies made on events with large rapidity gaps at HERA by ZEUS [130] and H1 [131] the cut $\eta_{max} \leq 2$ was used to select a pure sample of colour singlet exchange events. However, with this cut the kinematical range in M_X, and hence $x_{I\!P}$, is severely limited to values $M_X \lesssim 15$ GeV ($x_{I\!P} \lesssim 0.01$). The kinematic range in M_X accessed in the measurement can be extended to values $M_X \lesssim 30$ GeV if the η_{max} cut is increased to be close to the edge of acceptance of the calorimeter ($\eta \lesssim 3.3$). In order to reduce the contamination of 'standard' DIS events in the sample after this extension of the η_{max} cut, information from detectors forward of the liquid argon calorimeter can be used to limit

[2]For a full description see [129].

the activity from the system Y (see figure 7.3b). The removal of events with activity in the forward detectors will preferentially select colour singlet exchange events with an elastic proton rather than those in which the proton dissociates. The resulting rapidity gap then spans approximately 4 units in rapidity, from the edge of the LAr calorimeter ($\eta \sim 3.3$) to the acceptance of the most forward lying detector ($\eta \sim 7.5$).

Increasing the η_{max} cut to 3.3 also improves the $x_{I\!P}$ range accessible to $x_{I\!P} \lesssim 0.04$ (see section 7.7). The fact that there is no activity in the forward detectors restricts the system Y to values $M_Y \lesssim 1.6$ GeV with $|t| \lesssim 1$ GeV^2 (see section 7.6). Therefore, the cross section measured in chapter 8 is quoted for these kinematic ranges. In this kinematic range the system Y is dominantly a proton [132]. How the forward detectors are used in selecting a large rapidity gap sample is explained in the next section.

7.4 The Forward Detector Selection

There are two components of the H1 detector positioned forward of the LAr calorimeter which are used to tag particles at large pseudo-rapidities. They are the proton remnant tagger and the forward muon detector. The proton remnant tagger was designed to veto proton dissociative events in the forward direction (see section 1.9.1). The forward muon detector was designed to detect high energy muons in the forward direction (see section 1.6.2). However, it has proved also to be extremely sensitive to particles from the proton remnant which scatter in the beam pipe or surrounding material, making it an effective tag for particles with large pseudo-rapidities. These 'forward detectors' therefore have useful acceptance for larger values of pseudo-rapidity than would be expected from their geometrical acceptance alone.

The run selection applied to ensure that the forward detectors were fully functional during the data taking period is described in section 7.4.1. The large rapidity gap sample is selected by demanding an absence of activity in the forward detectors. The measurement must take account of residual noise levels in the detectors, and therefore, a noise analysis of all three years of the data is presented in section 7.4.2. The results of the noise analysis determine the appropriate cuts to be made in each of the forward detectors and the liquid argon calorimeter and they are presented in sections 7.4.3 to 7.4.5.

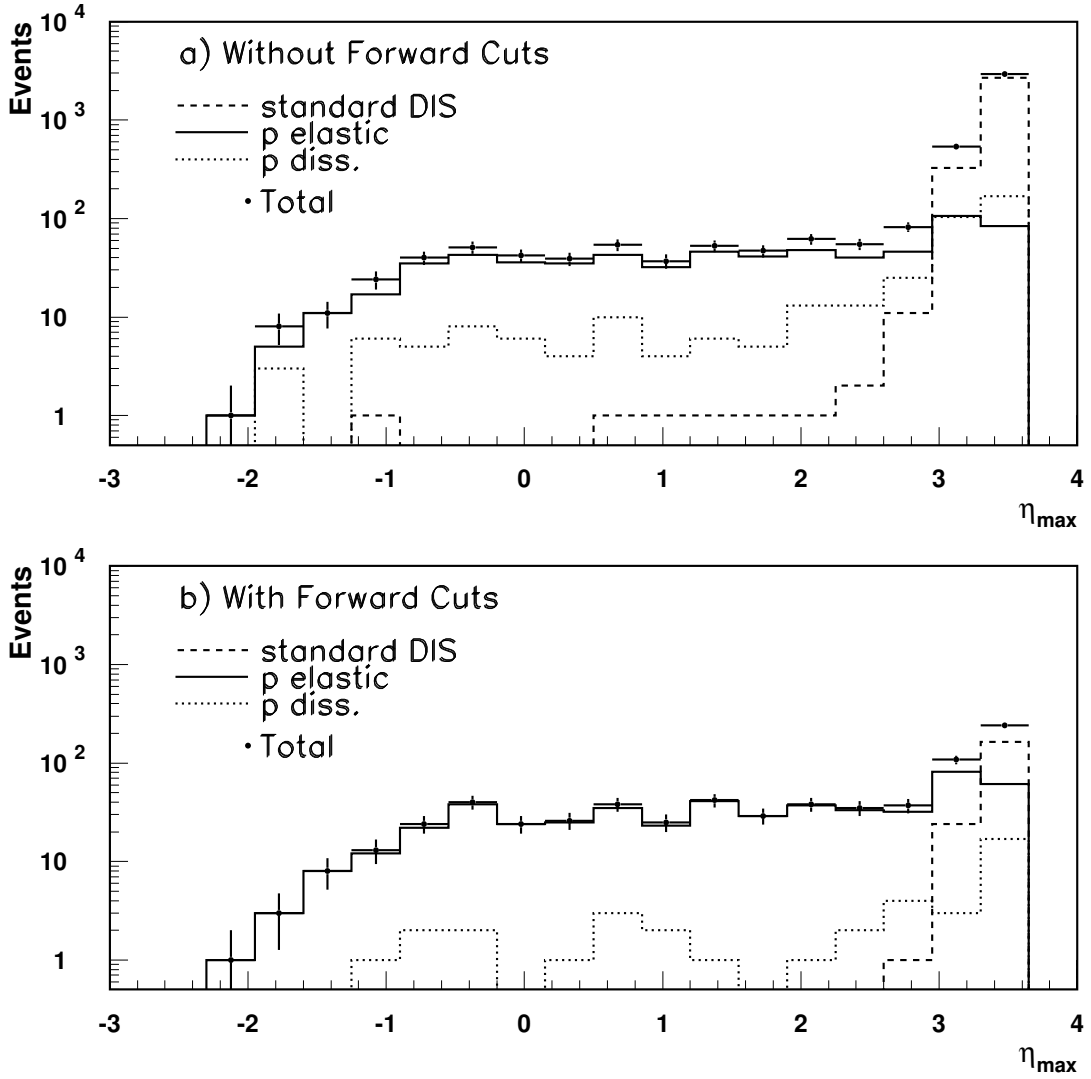

Figure 7.3: The η_{max} distribution in the LAr calorimeter using detector simulations based on the AROMA Monte Carlo program (a) without and (b) with the cuts on activity in the detectors in the forward region (forward cuts) applied. The 'standard DIS' kinematic range is given by $x_{I\!P} > 0.1$ or $M_Y > 5$ GeV and is shown by the dashed line. The 'proton dissociation' kinematic range is given by $x_{I\!P} < 0.1$ and $1.6 < M_Y < 5$ GeV, and is indicated by the dotted line. The 'proton elastic' kinematic range is defined as $x_{I\!P} < 0.1$ and $M_Y < 1.6$ GeV and is shown by the full line. The total of the three contributions is shown by the points with error bars. The application of the forward cuts combined with $\eta_{max} < 3.3$ is seen to be effective in preferentially selecting proton elastic events above 'standard DIS' and proton dissociative processes.

7.4.1 Forward Detector Run Selection

The data used for the studies described in this chapter and for the measurement of both the inclusive and diffractive D^* cross sections is restricted to periods when the high voltage and read out systems of the forward muon system[3] were operational. At the beginning of the 1997 data taking period approximately 1.7 pb^{-1} of luminosity are excluded due to a readout problem with the forward muon detector in which information from different events was mixed. Uniquely, no high voltage requirement is demanded for the proton remnant tagger and the periods when it was not functioning are treated as an inefficiency that is incorporated into the detector simulation. This is only a small fraction of the total data sample, so the effect of dropping this high voltage requirement is small.

7.4.2 Residual Noise in the Forward Detectors

The choice of activity thresholds in the forward detectors, above which events are rejected from the diffractive sample, is a compromise between maximising efficiency for rejection of non-diffractive events and minimising the number of diffractive events rejected due to noise. A genuine diffractive event may be rejected because there is a signal in the forward detectors caused by either beam backgrounds or electronic noise. To establish the rate at which the loss of diffractive events occurs, use is made of the 1% of all events which are written to tape during standard data taking that are triggered on random bunch-crossings, in which both the electron and proton bunches are filled but there are usually no actual sub-triggers in the event. The random noise present in the liquid argon calorimeter is monitored over regular periods of the data and incorporated into the detector simulation, whereas the noise present in the proton remnant tagger and the forward muon detector is not incorporated into the detector simulation and is studied separately here. A selection of randomly triggered events from the same run range as used for the cross section measurement is analysed.

7.4.3 The Forward Muon Detector (FMD)

The random electronic noise in the forward muon detector can be reduced to an acceptable level if the hit information within each layer is combined into pairs. The pairing algorithm is extended from that used in the normal reconstruction in order to recognise tracks originating from secondary scattering in the beam-pipe which enter the detector at a

[3]The high voltage requirement was demanded only for the pre-toroid layers of the forward muon detector, which were used in the selection.

steeper angle. The hit pairs are combined if they lie within 9 cm of each other in the radial co-ordinate. The information from full tracks is not used because the efficiency for background rejection is greatly reduced. Only the information from the pre-toroid layers is used because the post-toroid layers are susceptible to intermittent high levels of synchrotron radiation from the incoming electron direction; the pre-toroid layers being protected by the iron toroid.

Figure 7.4 shows the residual noise level for hit pairs in the forward muon detector obtained from the random trigger files. The noise level is seen to remain similar for the three years of the analysis. Approximately 25% of the random events have, at least, a single pre-toroid hit pair so that requiring no hit pairs in the analysis would result in unacceptably large losses. Therefore, to avoid this loss the large rapidity gap selection is chosen to require one or less hit pairs in the pre-toroid layers, i.e.

$$N_{FMD} < 2 \tag{7.2}$$

As is shown in table 7.1 this requirement reduces the loss of diffractive events to approximately 8%. It is corrected for in the calculation of the final cross section.

	1995	1996	1997
FMD noise correction ν	0.932	0.923	0.922

Table 7.1: The correction, ν, to the acceptance, for each of the three data samples, due to residual noise in the forward muon detector.

7.4.4 The Proton Remnant Tagger (PRT)

The residual noise level in the proton remnant tagger is found to be at the level of 10^{-3} hits per event and so is neglected. An event is accepted into the large rapidity gap sample if there are no hits in any of the seven scintillators, i.e.

$$N_{PRT} < 1 \tag{7.3}$$

7.4.5 The Liquid Argon Calorimeter

Experimentally η_{max} is chosen to be the pseudo-rapidity of the most forward cluster in the liquid argon calorimeter with energy above 300 MeV. This limit excludes the majority of random noise in the calorimeter; only around 1% of colour singlet exchange events are lost after this cut [133]. The η_{max} cut, used in the investigation described in section 7.3.3

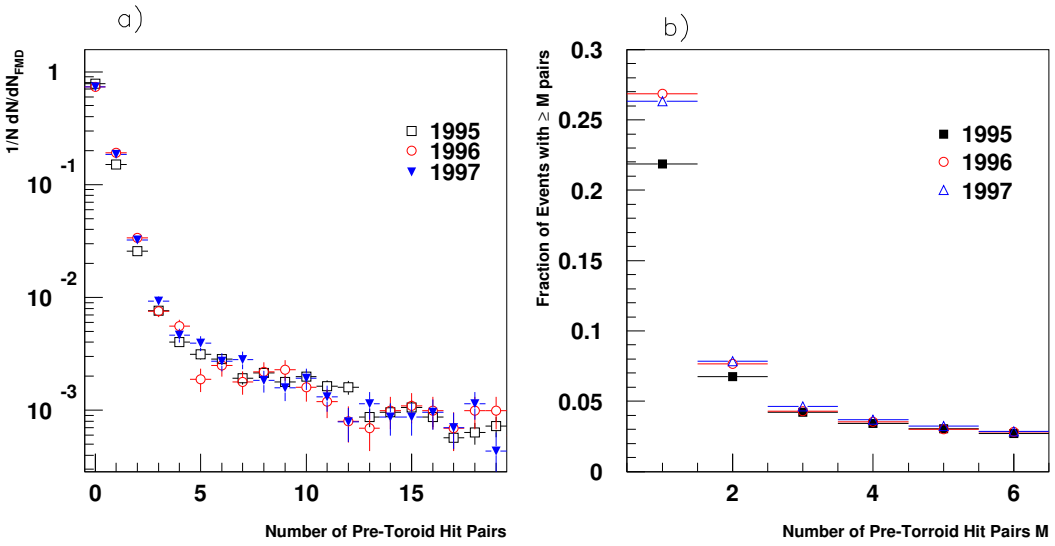

Figure 7.4: The level of residual noise in the forward muon detector for the data samples 1995 (open squares), 1996 (open circles) and 1997 (closed triangles) as determined using randomly triggered events (a) the number of forward muon pre-toroid hit pairs. The distributions are normalised to the number of events in the noise sample, N. (b) The fraction of randomly triggered events which satisfy the minimum levels of activity in the forward muon detector. For example, the first bin in plot (b) refers to the fraction of events which have one or more hits in the pre-toroid layers of the forward muon detector.

and also in the measurement of F_2^D in 1994 data [4], which provides good acceptance for colour singlet exchange processes whilst simultaneously rejecting the majority of non-colour singlet exchange background, is

$$\eta_{max} < 3.3 \tag{7.4}$$

7.5 Performance of the Forward Detectors

As described above the forward detectors are mainly used to reject 'standard' DIS events where hadronic activity associated with the photon fragmentation region extends forward of the main calorimeter and cannot be reconstructed. It is therefore important that the rate of activity in the forward detectors for all DIS events (both diffractive and non-diffractive) is observed to be constant for the whole data taking period and to be well simulated by the Monte Carlo programs. This requires, firstly, that the small fraction of diffractive events with low forward activity are correctly simulated. Then secondly, and equally importantly, it is necessary that the larger fraction of events with significant forward activity are also correctly simulated, because the fraction of these events which are not rejected by the forward cuts affects the measurement of the diffractive cross section.

In the following sections the requirement that the events with forward activity are well simulated is addressed first and so 'anti-diffractive' cuts are imposed on the data. The outcome of the study is that with careful corrections the simulation is able to give a good description of the detected forward energy flow. Equally it will be seen that the distributions of hits in the FMD and PRT plotted for Monte Carlo events does reproduce the data well in the crucial region of low hit multiplicities where the diffractive events make a large contribution.

The data sample of DIS events used for the investigation of the forward cuts should be in the same kinematic range, in terms of y and Q^2, as the data used in the D^* cross section measurements. The events used for the investigation come from a wider sample of inclusive DIS D^* candidates than that used in the analysis in chapter 6. The events are required to pass the identical run quality and DIS event selection as in chapter 4 but with extremely loose requirements on the D^* track quantities, transverse momenta and the mass windows so as to produce a high statistics sample of kinematically similar DIS events. For example, there are over 178 000 such 'DIS D^*' events in the 1997 data sample.

In figure 7.5 the levels of activity in the forward detectors are shown separately for the three years of data taking. To investigate their behaviour in more detail, the percentages of the 'DIS D^*' event sample remaining after applying combinations of 'anti-diffractive' cuts are given in table 7.2. The 'anti-diffractive' cuts indicate activity above noise thresholds and are precisely opposite to those stated in section 7.4. The response of each detector is summarised as follows:

- **FMD**
  The spectrum of the number of hit pairs in the pre-toroid layers of the forward muon detector for the three data samples is shown in figure 7.5a. The shape of the distribution is consistent between the three years. As expected, the percentage of DIS events which have activity above the noise cut $N_{FMD} > 1$ in table 7.2 are also similar between the three years.

- **LAr**
  The distribution shown in figure 7.5b of the most forward energy cluster of the liquid argon calorimeter, described by the variable η_{max}, is also consistent between the three years as are the efficiencies for the cut $\eta_{max} > 3.3$ in table 7.2.

- **PRT**
  The fraction of DIS events for which there is activity in a particular scintillator of the PRT is shown in figure 7.5c. It can be seen in the figure that the scintillators of the proton remnant tagger show a gradual worsening in performance which becomes

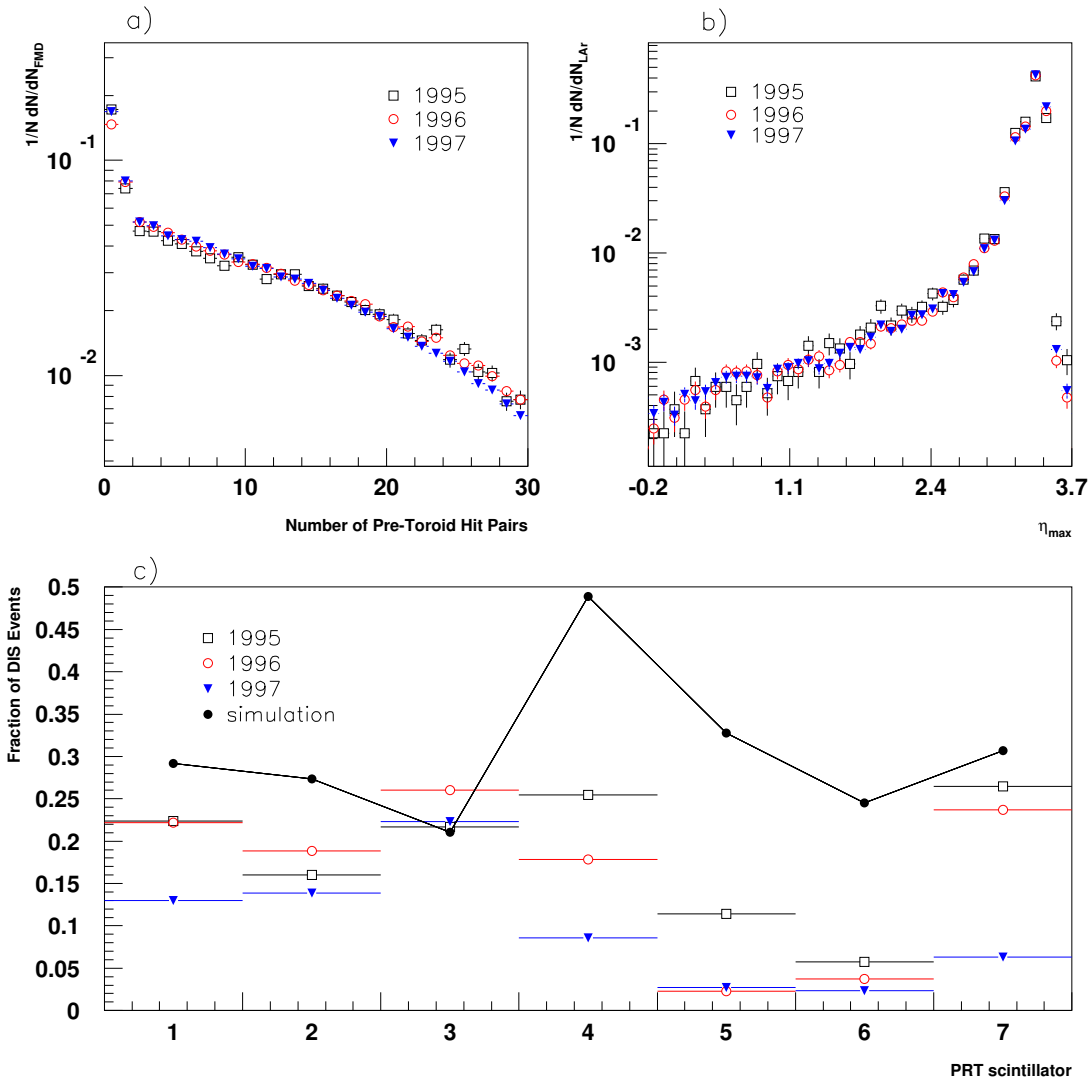

Figure 7.5: The levels of activity in the forward detectors for DIS events from the three data samples 1995(open squares), 1996(open circles) and 1997(closed triangles). (a) The forward muon detector (b) the LAr calorimeter and (c) the proton remnant tagger. In (c) the activity in the PRT given by the simulation is indicated by the full circles connected with a straight line. The data are normalised to the number of events, N, passing the standard DIS D^* selection.

dramatic for the first, fourth and seventh scintillators in the 1997 data. The worsening response of these scintillators results in a reduction of the overall efficiency of the proton remnant tagger by around 30%. For example, the condition $N_{PRT} > 0$ is satisfied by $\sim 40\%$ of all events in the 1995 and 1996 data samples which falls to 28% in the 1997 data sample. This can be seen from inspection of table 7.2.

7.5.1 Monte Carlo Comparison

Discrepancies between the Monte Carlo simulations and the data can arise because of two main reasons;

- the simulation of the sub-detector, the material surrounding the sub-detector or the beam optics is inadequate;
- the underlying physics model in the Monte Carlo is unable to describe the energy flow in the forward region. This may be due to deficiencies in either the simulation of the 'standard' DIS process, the simulation of diffractive processes or both.

An attempt is made to quantify the effect that these two contributions have on the quality of the simulation. If the simulation of the forward detectors, their surrounding material and beam optics is correct then the variation in performance of the proton remnant tagger for the 1997 data, seen in the previous section, should be described. To estimate the effect of the underlying physics model on the quality of the Monte Carlo simulation two independent physics models are used.

The 'DIS D^*' data sample is used to validate simulations with the ARIADNE and the LEPTO 6.5 Monte Carlo generators. ARIADNE uses the colour dipole model which is known to give a good description of forward particle production for the dominating DIS processes (see section 2.7). The program produces large rapidity gap events by a simple implementation of the resolved pomeron model. The LEPTO 6.5 Monte Carlo, which was introduced in section 2.6.1, is based on leading order QCD matrix elements with higher order corrections modelled by parton showers plus the additional exchange of soft colour between the outgoing partons. The soft colour interactions provide a mechanism for increased energy flow in the forward direction and a mechanism to produce events with a large rapidity gap. The simulation contains a detailed modelling of the forward detectors and their environment, including the beam pipe and collimators in the forward region. The effects of noise in the forward muon detector are included in the detector simulation by adding the signal of a randomly triggered data event to each Monte Carlo event.

The fraction of DIS events passing the forward activity thresholds are calculated from simulations of the LEPTO and ARIADNE Monte Carlo generators and are shown for 1996 running conditions in table 7.3. Only the results of the 1996 simulation are shown because very similar results for each activity threshold (to the order of $\sim 2\%$) are obtained from simulations of the 1995, 1996 and 1997 running periods. Therefore, by the comparison of the data, shown in table 7.2, and the typical response of the simulation for all years, shown in table 7.3, the following conclusions can be made:

- **Efficiency of the PRT**
  The efficiency of the PRT given by the simulation, which is almost identical for each year of the simulation, is too high. For example, the efficiency for the condition $N_{PRT} > 0$ in the 1996 data, shown in table 7.2, is 39% and can be compared to the value of $\sim 60\%$ for the simulation given in table 7.3. No description of the worsening response of the PRT in the 1997 data is given by the simulation and this is due to a failure in the simulation of the detector. Additional differences between the data and the simulation are due to a combination of the modelling of the energy flow in the forward region and the simulation of the beam optics and detector material. To ensure that large errors are not introduced in the calculation of the acceptance due to the poor description of the PRT, the simulation needs to be corrected. This correction is described below in section 7.5.2.

- **Forward Energy Flow**
  From the comparison of table 7.2 with table 7.3 it can be seen that for either of the two conditions ($N_{FMD} > 1$) or ($\eta_{max} > 3.3$) the differences in the efficiency between the ARIADNE and LEPTO models is the order of 4%; with the ARIADNE model in slightly better agreement with the data then LEPTO. The difference between the two models is diminished, and the agreement with the data improved, when more 'anti-diffractive' cuts are applied. For example, the two models and the data all agree to the level of 1%, when the joint condition ($FMD > 1 \& \eta_{max} > 3.3$) is applied. Therefore, by using combinations of forward detectors the sensitivity of the forward energy flow to the different physics models is reduced.

7.5.2 Correction of the Proton Remnant Tagger Simulation

As discussed in section 7.5.1, the description in the simulation of the efficiency of the PRT scintillators is unsatisfactory and becomes exacerbated in the 1997 data by the poor performance of the detector. The discrepancy between the data and simulation is resolved

	efficiency%		
condition	1995	1996	1997
$\eta_{max} > 3.3$	75.31 ± 0.28	77.23 ± 0.14	78.47 ± 0.12
$N_{FMD} > 1$	75.38 ± 0.28	77.40 ± 0.14	75.16 ± 0.12
$N_{PRT} > 0$	40.47 ± 0.17	39.25 ± 0.09	28.44 ± 0.05
$\eta_{max} > 3.3 \& N_{PRT} > 0$	31.17 ± 0.12	31.02 ± 0.06	22.68 ± 0.03
$\eta_{max} > 3.3 \& N_{FMD} > 0$	60.11 ± 0.25	63.17 ± 0.14	62.64 ± 0.11
$N_{FMD} > 1 \& N_{PRT} > 0$	32.92 ± 0.13	32.08 ± 0.07	22.34 ± 0.03
$\eta_{max} > 3.3 \& N_{FMD} > 1 \& N_{PRT} > 0$	25.82 ± 0.10	25.95 ± 0.05	18.34 ± 0.03

Table 7.2: The percentage of DIS events which satisfy various levels of activity in the forward detectors for the 1995, 1996 and 1997 data samples.

by calibrating the response of the PRT in the simulation using the study of its response in data. The PRT response changes a lot with time and this needs to be considered first (see section 7.5.3). The correction procedure, which is performed in two steps, is described in sections 7.5.4 and 7.5.5.

7.5.3 Performance History of the Proton Remnant Tagger

When there are high count rates in any of the scintillators of the proton remnant tagger, caused either by beam induced backgrounds or instability in the electronics, the high voltage of the photomultiplier, and hence its gain, is reduced. This procedure produces a tolerable data taking rate, although with a considerably reduced efficiency, for the problematic scintillator. In particular, the high voltage had to be reduced in all years for the scintillators number five and six because of synchrotron radiation (figure 7.5c). Similarly, the voltage of the seventh scintillator during the 1997 data taking period was reduced due to a high count rate, although the cause of this high rate remains unknown. The gain of the first and fourth scintillator was not altered and the reason for the reduction in their efficiency for the 1997 data period is unknown.

In view of the variable performance of the PRT in the data sample analysed in this thesis all the scintillators of the PRT are used in order to gain maximum detection efficiency from the device. This is in contrast to the analysis of the diffractive structure function performed on 1994 data [4] which used only the first three and the seventh scintillators. For this data period, and similarly for 1995 and 1996, the agreement between the data and simulation for that limited range of scintillators was of the order of 20%.

	efficiency%		
condition	ARIADNE	ARIADNE indiv	ARIADNE overall
$\eta_{max} > 3.3$	76.46 ± 0.08	76.46 ± 0.08	76.46 ± 0.08
$N_{FMD} > 1$	76.24 ± 0.08	76.24 ± 0.08	76.24 ± 0.08
$N_{PRT} > 0$	58.76 ± 0.07	46.42 ± 0.05	39.53 ± 0.04
$\eta_{max} > 3.3 \& N_{PRT} > 0$	45.50 ± 0.05	35.96 ± 0.04	30.61 ± 0.03
$\eta_{max} > 3.3 \& N_{FMD} > 0$	59.85 ± 0.07	59.85 ± 0.07	59.85 ± 0.07
$N_{FMD} > 1 \& N_{PRT} > 0$	47.06 ± 0.05	36.87 ± 0.04	31.45 ± 0.03
$\eta_{max} > 3.3 \& N_{FMD} > 1 \& N_{PRT} > 0$	36.91 ± 0.04	29.04 ± 0.03	24.74 ± 0.02
	efficiency%		
condition	LEPTO 6.5	LEPTO indiv	LEPTO overall
$\eta_{max} > 3.3$	73.35 ± 0.03	73.35 ± 0.03	73.35 ± 0.03
$N_{FMD} > 1$	72.34 ± 0.03	72.34 ± 0.03	72.34 ± 0.03
$N_{PRT} > 0$	60.76 ± 0.03	47.64 ± 0.02	40.50 ± 0.02
$\eta_{max} > 3.3 \& N_{PRT} > 0$	48.43 ± 0.02	38.10 ± 0.02	32.38 ± 0.01
$\eta_{max} > 3.3 \& N_{FMD} > 0$	60.62 ± 0.03	60.62 ± 0.03	60.63 ± 0.03
$N_{FMD} > 1 \& N_{PRT} > 0$	48.21 ± 0.02	37.81 ± 0.02	32.07 ± 0.01
$\eta_{max} > 3.3 \& N_{FMD} > 1 \& N_{PRT} > 0$	40.70 ± 0.02	31.96 ± 0.01	27.07 ± 0.01

Table 7.3: The percentage of simulated DIS events that pass various cuts on activity in the forward region of the detector using the ARIADNE Monte Carlo program (upper table) and the LEPTO 6.5 Monte Carlo program (lower table) under 1996 detector conditions. The second and third columns show the effect of each stage in the calibration of the proton remnant tagger.

7.5.4 Correction of the Individual Scintillators

The first part of the calibration procedure corrects the response of the individual scintillators of the PRT in the simulation to that obtained from data. The correction factors are calculated from events which have activity in both the LAr calorimeter and the forward muon system ($\eta_{max} > 3.3 \& N_{FMD} > 1$), because this limits the dependence of the calibration on the different Monte Carlo models. The condition $\eta_{max} > 3.3 \& N_{FMD} > 1$ produces a distribution in the data and simulation which looks very similar to that shown for all DIS events in figure 7.5c. The ratio of the acceptance for data and for the simulation gives the correction factor for each scintillator. The difference in the correction factors as calculated from the ARIADNE and LEPTO 6.5 Monte Carlo programs are small and the former model is used throughout for the results in this section. The efficiency of each scintillator in the simulation is reduced by the factors given in table 7.4. The efficiency for scintillator number three is left unchanged because its efficiency for the data is higher than that given by the simulation. The effect of this first step of the calibration on the ARIADNE and LEPTO 6.5 Monte Carlo programs is shown for the 1996 detector simulation in the second column of table 7.3. The calibration of the individual scintillators

has improved the description of the data by the simulation but the simulation efficiency for registering activity in any of the seven scintillators remains around 20% larger than the data.

Scintillator	1995	1996	1997
1	0.7910 ± 0.0043	0.7821 ± 0.0029	0.4604 ± 0.0015
2	0.5996 ± 0.0030	0.7032 ± 0.0025	0.5172 ± 0.0017
3	1.0000 ± 0.0000	1.0000 ± 0.0000	1.0000 ± 0.0000
4	0.5658 ± 0.0033	0.3977 ± 0.0015	0.1914 ± 0.0007
5	0.3617 ± 0.0017	0.0714 ± 0.0002	0.0868 ± 0.0003
6	0.2305 ± 0.0009	0.1512 ± 0.0005	0.0954 ± 0.0003
7	0.9112 ± 0.0052	0.8133 ± 0.0031	0.2170 ± 0.0007

Table 7.4: The individual scale factors for each scintillator of the PRT calculated using the ARIADNE Monte Carlo. The scale factors represent the difference between the probability of registering activity in each scintillator of the PRT between data and simulation for DIS events under the condition $\eta_{max} > 3.3 \& N_{FMD} > 1$.

7.5.5 Overall Correction of the PRT efficiency

The fact that the PRT shows more activity in the simulation than in the data after calibration of the individual scintillators suggests that in the simulation the shower in the material surrounding the PRT or the primary particle multiplicities are too large. This results in correlations between hits in different scintillators that are larger than they should be. The efficiency given by the simulation remains higher than the data after calibration of the individual scintillators and it has to be degraded by an overall factor, corresponding to the probability of registering activity in any of the seven scintillators, to match the data. The values of the overall scale factor, obtained for each of the data samples, are given in table 7.5.

year	1995	1996	1997
reduction	0.88	0.85	0.77

Table 7.5: The factors by which the overall activity detection probability in the simulation of the PRT is reduced in order to match the data, after the calibration of each individual scintillator has been performed.

These modifications do not otherwise affect the simulation because it is seen that the efficiency of the forward detectors agrees well between the last column of table 7.3 with the middle column of table 7.2 for a variety of cuts. The actual spectrum of the activity in

the forward detectors for the various conditions as well as the efficiency values themselves also show good agreement between the data and Monte Carlo. This can be seen for various conditions of activity in the forward region in the 1997 data sample in figure 7.6.

7.5.6 Summary of the Calibration

The difference in the response of the proton remnant tagger between the data and simulation was found to be significant, particularly for the 1997 data sample. The worsening performance of the PRT in the 1997 data sample was not described by the Monte Carlo simulation. The solution proposed in this thesis was to correct the response of the PRT in the simulation to that obtained in the data using a sample of events with high activity in the forward region.

The important features for the diffractive D^* DIS analysis, which follows in chapter 8, are as follows:

- The number of pre-toroid hit pairs in the forward muon detector shown in figure 7.6a show good agreement between the data and Monte Carlo. The agreement is also reasonable at low numbers of paired hits where the modelling of diffractive events and residual noise is important.
- The number of PRT scintillator hits shown in figure 7.6b also agree well between data and simulation.
- The energy deposition in the LAr calorimeter shown in figure 7.6c for events with activity in both the PRT and FMD shows good agreement between the data and simulation, which extends down to low values of η_{max}. This demonstrates that the data is well described by the simulation for diffractive events involving proton dissociation.

7.6 The Kinematic Range in M_Y and t

The Monte Carlo generator DIFFVM for J/ψ production is used to model proton dissociation at low M_Y ($M_Y < 5$ GeV). The efficiency for detecting the proton dissociation system, Y, in the forward detectors calculated from the DIFFVM Monte Carlo generator is shown in figure 7.7a. The proton remnant tagger response is shown after the calibration using DIS events described in section 7.5.2-7.5.6. At large M_Y ($M_Y > 5$ GeV) the

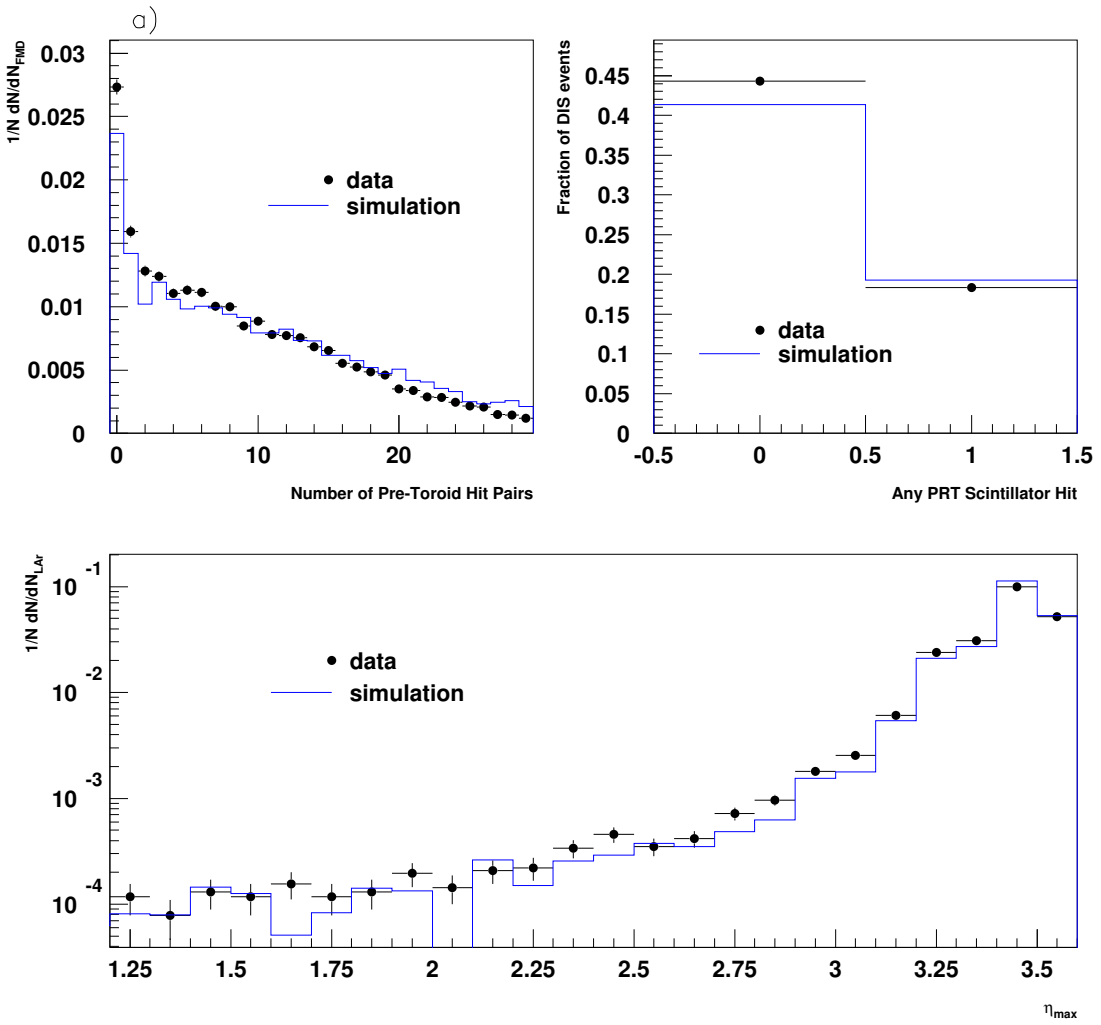

Figure 7.6: A comparison of the activity in the forward region of the detector between data and simulations of the ARIADNE Monte Carlo program for the 1997 data sample. The distributions are shown after the calibration of the proton remnant tagger. (a) The activity in the FMD with the condition $\eta_{max} > 3.3 \& N_{PRT} > 0$ (b) the activity in the PRT with the condition $\eta_{max} > 3.3 \& N_{FMD} > 0$ and (c) the activity in the LAr calorimeter with the condition $N_{FMD} > 1 \& N_{PRT} > 0$. The data is shown by the points with error bars and the simulation by the solid line. The distributions are normalised to the number of events, N, passing the standard DIS selection.

combined efficiency of the detectors for tagging the system Y reaches a plateau at around 90%. The most efficient detector over the whole range of M_Y is the forward muon detector. The high efficiency of the FMD is due to the showering of secondary particles from the dissociating proton. The proton remnant tagger has a constant efficiency with M_Y which is a consequence of its proximity to the beam line. The liquid argon calorimeter has a slowly rising threshold behaviour and becomes most efficient at larger values of M_Y.

Figure 7.7a shows that the efficiency for detecting proton dissociation decreases as the mass tends towards that of the proton. This failure of the forward detector selection to reject low M_Y proton dissociation events must be corrected for in any measurement of the cross section for an elastic proton ($M_Y = m_P$). Such a procedure results in large systematic uncertainties. These uncertainties can be avoided by measuring in a wider M_Y region. The detection efficiency is around 60% at $M_Y = 1.6$ GeV and the cross section measurement is defined in the range $M_Y < 1.6$ GeV. According to the DIFFVM Monte Carlo generator, the reduction in cross section when this cut is changed from $M_Y < 1.6$ GeV to $M_Y = m_p$ is around 8%. The efficiency as a function of t for dissociative events remains approximately constant at around 80% for all values of t as can be seen from the figure 7.7b.

Simulations of the DIFFVM Monte Carlo generated with an elastic proton for J/ψ production are used to investigate the acceptance of the forward selection for truly elastic events as a function of t and the results are shown in figure 7.7c. The efficiency of detection at $|t| = 1$ GeV^2 is around 30% and the cross section is corrected to the range of $|t| < 1$ GeV^2. The overall acceptance for events with an elastic proton in this t range is around 95% and the majority of the losses are caused by protons scattered into the PRT.

The simulation of proton dissociation is used to determine the correction, P, due to the net smearing of events across the kinematic boundary $M_Y = 1.6$ GeV defining the measured cross section. This correction is applied to the 'smeared' acceptance calculated using RAPGAP and is necessary because proton dissociation is not modelled in the RAPGAP program. The correction factor P is calculated as the ratio of the net migrations out of the kinematic range ($M_Y < 1.6$ GeV, $|t| < 1$ GeV^2) to the number of events generated in that kinematic range, and is given by the formula:

$$1 - P = \frac{N^{PD}_{gen}(M_Y < 1.6 \text{ GeV}, |t| < 1 \text{ GeV}^2) - N^{PD}_{rec}}{N^{PD}_{gen}(M_Y < 1.6 \text{ GeV}, |t| < 1 \text{ GeV}^2) + R^{EL}_{PD} \times N^{EL}_{gen}(|t| < 1 \text{ GeV}^2)} \qquad (7.5)$$

where R^{EL}_{PD} is the ratio of the proton elastic to the proton dissociation cross section and $N^{PD}_{gen}(N^{EL}_{gen})$ and $N^{PD}_{rec}(N^{PD(EL)}_{rec})$ are the number of generated and reconstructed proton dissociation(elastic) events.

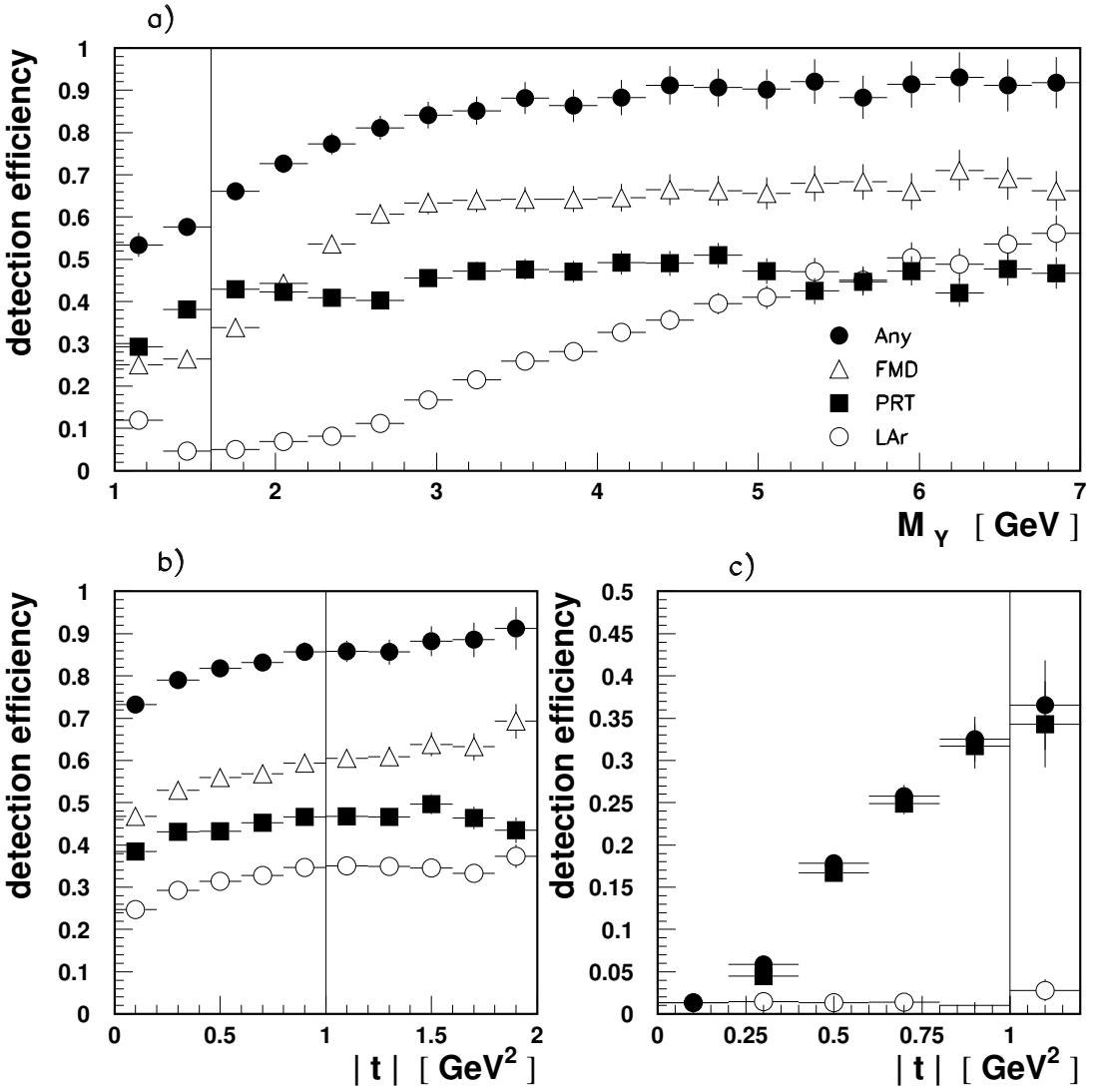

Figure 7.7: The efficiency for detecting the system Y, as a function of M_Y and t, calculated using detector simulations of the DIFFVM Monte Carlo for 1996 running conditions. (a) The efficiency for detecting proton dissociation as a function of M_Y. (b) The efficiency for detecting proton dissociation as a function of t. (c) The efficiency for detecting an elastic proton as a function of t. In all cases the efficiency is shown for activity above noise thresholds in; any forward detector (full circles), the forward muon detector (open triangles) the proton remnant tagger (full squares) and the liquid argon calorimeter (open circles).

The value of P, calculated for simulations of the three data years, is shown in table 7.6. The fact that the correction is larger than 1 indicates a net smearing into the range $M_Y < 1.6$ GeV. The increase in the size of the correction over the running period is caused by the worsening performance of the proton remnant tagger. If the proton remnant tagger is omitted from the forward selection, the correction due to dissociation for the 1997 sample increases to 1.13. The systematic error on the correction due to smearing across the boundary $M_Y = 1.6$ GeV, given in table 7.6, includes contributions from the following sources:

- Variation of the ratio of proton elastic to proton dissociation cross sections (R_{PD}^{EL} in equation 7.5) to either 1:2 or 2:1, so that the range covers that measured in various proton dissociation processes in both fixed target and DIS experiments [79, 134, 135].
- Variation of the generated M_Y distribution by $(\frac{1}{M_Y^2})^{\pm 0.3}$.
- Variation of the simulated t dependence by changing the slope parameter of the distribution in the proton dissociation simulation by ± 1 GeV^{-2} and ± 2 GeV^{-2} for the proton elastic simulation.
- Variation in the efficiency of the forward detectors based on the studies described earlier in this chapter. The efficiency of the forward muon detector is altered by $\pm 4\%$ and the value of the overall correction made in the calibration of the proton remnant tagger is varied by $\pm 100\%$.

	1995	1996	1997
M_Y smearing correction P	1.032 ± 0.038	1.040 ± 0.043	1.076 ± 0.062

Table 7.6: The correction to the acceptance, for each of the three data samples, due to smearing across the $M_Y = 1.6$ GeV boundary.

7.7 Kinematic Reconstruction

The fraction of the momentum of the initial state proton carried by the colour singlet exchange, $x_{I\!P}$, may be reconstructed from the final state by:

$$x_{I\!P} = \frac{Q^2 + M_X^2}{Q^2 + W^2} \tag{7.6}$$

where M_X is reconstructed from the 4-vector of the system X, and Q^2 and W^2 are reconstructed from the hadronic final state and/or the scattered electron (see section 4.6).

The sensitivity to losses in the reconstruction of the mass M_X and to initial state radiation can be reduced [136] if $x_{I\!P}$ is reconstructed as:

$$x_{I\!P} = \frac{\sum_{X+e'}(E + p_z)}{2E_p} \tag{7.7}$$

where the sum is over both the final state electron and the system X. The hadronic final state system X is reconstructed from clusters in the SPACAL and LAr calorimeters together with tracks from the central tracking detector, which provides a more accurate momentum determination for charged tracks. In order to avoid double counting of energy, the tracks are extrapolated to the calorimeter and a cylinder of radius 30 cm about the extrapolated track is masked off. If the energy accumulated in the resulting cylinder is larger than twice that of the track, then the energy in the calorimeter is taken, otherwise the track energy is used.

At low masses, the reconstruction of the system X is sensitive to low level noise in the forward part of the LAr calorimeter because $\sum_{X+e'}(E + p_z)$ is maximal in this region. Therefore, low energy isolated clusters in the forward direction, which are compatible with being noise, are not considered in the reconstruction of the invariant mass of the system X [79].

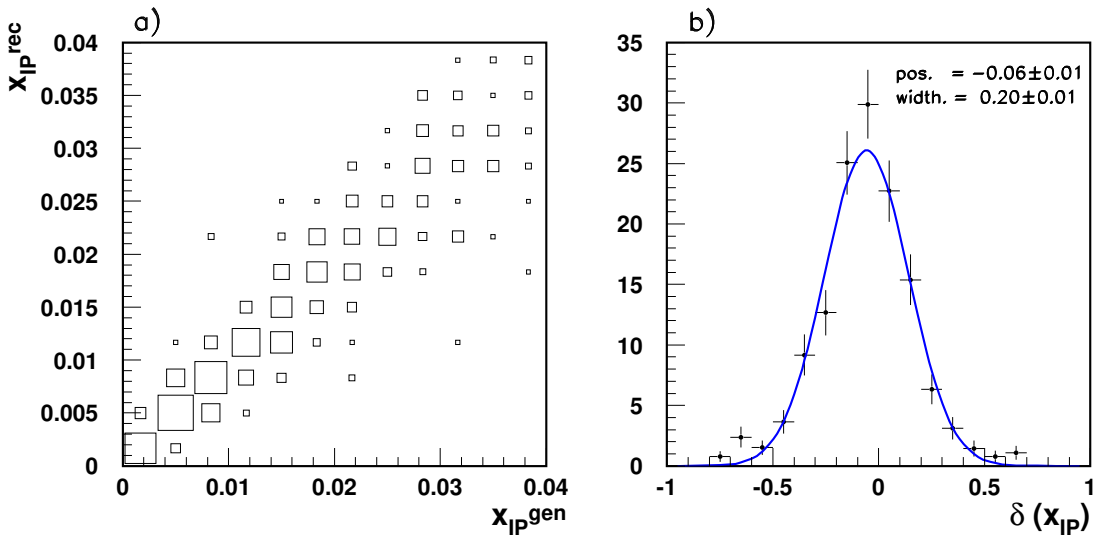

Figure 7.8: Illustrations of the resolution in $x_{I\!P}$ using equation 7.7 and the RAPGAP Monte Carlo program. (a) The correlation of the generated and reconstructed $x_{I\!P}$. (b) The $\delta(x_{I\!P})$ distribution defined in equation 7.8. Also shown is the resolution, given by the width, and the shift, given by the position.

The quality of the reconstruction of $x_{I\!P}$ in the detector achieved by using equation 7.7 may be estimated using the RAPGAP Monte Carlo program. Figure 7.8a shows the

reconstructed value of $x_{I\!P}$, $x_{I\!P}^{rec}$, against the generated value, $x_{I\!P}^{gen}$. A good correlation is seen over the whole range of $x_{I\!P}$. The shift and the resolution implicit in the method of reconstruction for $x_{I\!P}$ may be estimated using the following function:

$$\delta(x_{I\!P}) = \frac{x_{I\!P}^{rec} - x_{I\!P}^{gen}}{x_{I\!P}^{gen}} \tag{7.8}$$

The shift in the reconstruction of $x_{I\!P}$ is then defined as the mean of $\delta(x_{I\!P})$ and the resolution is defined as the width of $\delta(x_{I\!P})$ obtained in a Gaussian fit. Figure 7.8b shows the $\delta(x_{I\!P})$ distribution for the range in $x_{I\!P}$ for which the cross section is measured. The shift in $\delta(x_{I\!P})$, which is mainly caused by losses in the reconstruction of the hadronic energy of the system X, is small $\sim 6\%$, and no correction to the hadronic energy measurement is made. The resolution is around 20% and is found to be reasonably constant across the whole $x_{I\!P}$ range. The range in $x_{I\!P}$ over which the cross section is measured is

$$x_{I\!P} < 0.04 \tag{7.9}$$

For this region of $x_{I\!P}$ the contribution of sub-leading reggeon exchange, as opposed to the leading diffractive exchange, is small. The cut also gives good acceptance in $x_{I\!P}$ for the cut $\eta_{max} < 3.3$ [4].

7.8 Summary

It has been shown, that provided adequate care is taken, the detectors in the forward region of H1 are effective in selecting a sample of large rapidity gap events with a low mass final state Y which is dominantly a single proton. The residual noise levels and the response of the forward detectors in the data have been shown to be roughly constant with time, except in the case of the proton remnant tagger, for all three years of data. The description of the response of the detectors in the data by the simulation, after correction of the simulation of the proton remnant tagger, has been shown to be satisfactory to unfold acceptances with appropriately evaluated systematic errors. Monte Carlo simulations reveal that there is good acceptance to measure the diffractive cross section in the kinematic range

$$M_Y < 1.6 \text{ GeV} \tag{7.10}$$

$$|t| < 1 \text{ GeV}^2 \tag{7.11}$$

$$x_{I\!P} < 0.04 \tag{7.12}$$

Chapter 8

Measurement of the Diffractive D^* Cross Section

8.1 Introduction

This chapter contains the description of the measurement of the cross section for the diffractive production of D^* mesons $ep \to e(D^{*\pm}X)Y$, and this is presented differentially as a function of the various kinematic variables. The ratio of the diffractive D^* cross section found here to the inclusive D^* cross section measured in chapter 6 is also extracted.

8.2 Calculation of $\sigma(ep \to e(D^{*\pm}X)Y)$

The diffractive D^* cross section, $ep \to e(D^{*\pm}X)Y$, is measured in the range of $x_{I\!P} < 0.04$, $M_Y < 1.6$ GeV and $|t| < 1$ GeV^2. The ranges in y, Q^2, $p_\perp(D^*)$ and $\eta(D^*)$ are chosen to be identical to those for the inclusive measurement presented in section 6.11. In an analogous way to the measurement of the inclusive D^* cross section (see equation 6.2), the diffractive D^* cross section, $ep \to e(D^{*\pm}X)Y$, is evaluated using the following equation:

$$\sigma(ep \to e(D^{*\pm}X)Y) = \frac{N_{obs}\ (1-r)}{(\int \mathcal{L}\ dt)\ B\ A_{tot}} \tag{8.1}$$

where N_{obs} is the number of D^* mesons obtained from the fit to the ΔM distribution, r is the contribution to the signal from reflections, $\int \mathcal{L}\ dt$ is the integrated luminosity, B is the branching fraction for the decay mode used and A_{tot} is the 'smeared' acceptance. The extraction of the number of events, N_{obs}, from the ΔM distribution is explained in section 8.4. The calculation of the 'smeared' acceptance A_{tot} for the diffractive measurement is described in section 8.5. The integrated luminosity $\int \mathcal{L}\ dt$ and the branching fraction

B are identical to the values used in the calculation of the inclusive D^* cross section (see chapter 6). The value for the reflections correction r is assumed to be the same as for the inclusive case (see section 6.9). As with the inclusive D^* analysis the measurement of the total cross section is extended to the measurement of further differential distributions (see section 6.2).

8.3 Reconstruction of $z_{I\!P}$

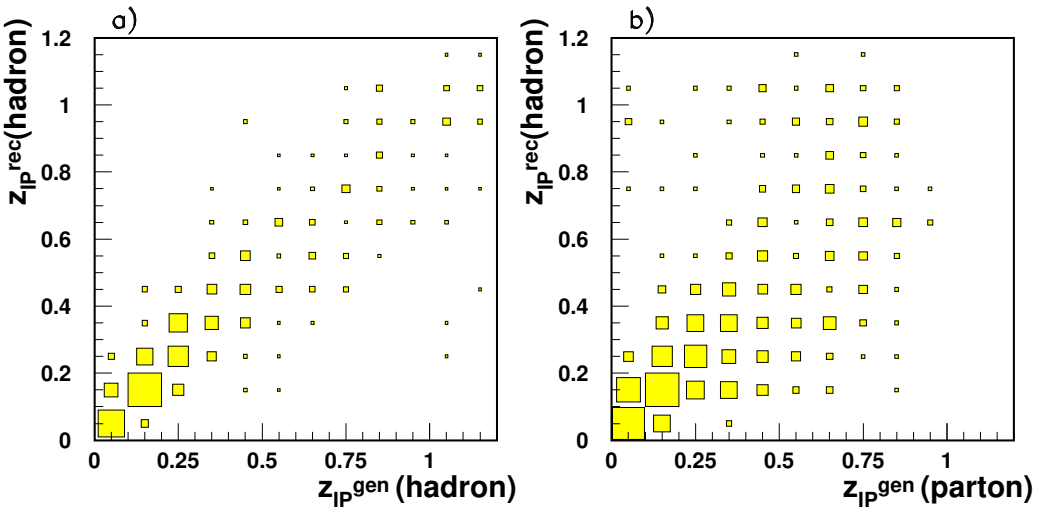

Figure 8.1: The correlation between the reconstructed value of $z_{I\!P}$ at the hadron level ($z_{I\!P}^{rec}$(hadron)) and the generated value of $z_{I\!P}$ ($z_{I\!P}^{gen}$) (a) at the hadron level $z_{I\!P}^{gen}$(hadron) and (b) at the parton level, $z_{I\!P}^{gen}$(parton).

Before the calculation of the diffractive cross section it is first instructive to discuss the reconstruction of $z_{I\!P}$ which is defined as

$$z_{I\!P} = \beta \left(1 + \frac{\hat{s}}{Q^2}\right) \tag{8.2}$$

As discussed in section 3.7, $z_{I\!P}$ is sensitive to the underlying partonic process in diffractive D^* production. If $\hat{s}$ is calculated from the partons entering or leaving the hard subprocess then $z_{I\!P}$ is said to be defined at the *parton level*. Alternatively, if $\hat{s}$ is reconstructed from the properties of the D^* meson then $z_{I\!P}$ is defined at the *hadron level*. The hadron level definition of $z_{I\!P}$ provides an estimate of the parton level or 'true' value of $z_{I\!P}$.

In this chapter the cross section differential in $z_{I\!P}$ is measured at the hadron level only and the cross section is not unfolded to the parton level. The hadron level estimate of $z_{I\!P}$ is

labelled $z_{I\!P}^{obs}$ because it is analogous to the variable x_g^{obs} studied in inclusive D^* production (see equations 2.40–2.42).

The effect of the detector on the reconstruction of $z_{I\!P}^{obs}$ may be estimated using Monte Carlo simulations. The correlation of $z_{I\!P}$ reconstructed in the detector, $z_{I\!P}^{rec}$(hadron), with the generated value of $z_{I\!P}$ at both the hadron, $z_{I\!P}^{gen}$(hadron), and parton level, $z_{I\!P}^{gen}$(parton), is shown, calculated using the RAPGAP Monte Carlo program, in figure 8.1a and figure 8.1b respectively. The level of correlation between $z_{I\!P}^{rec}$ and $z_{I\!P}^{gen}$(hadron) produces a resolution in $z_{I\!P}^{gen}$(hadron) of around 25% across the whole $z_{I\!P}$ range. The correlation of $z_{I\!P}^{rec}$(hadron) and $z_{I\!P}^{gen}$(parton) achieves a resolution of 45%. This is sufficient to demonstrate that there is indeed a relationship between the measured hadron level observable and the underlying parton level process. The correlation between the hadron level and the parton level is equally as good when other physics models are used e.g. SCI and two gluon exchange.

8.4 Evaluation of the Number of D^* Mesons - N_{obs}

The ΔM distribution from the combined data sample 1995-1997, after the diffractive selection, is shown in figure 8.2. The number of D^* mesons, N_{obs}, obtained from the ΔM distribution is measured in a similar manner to that for the inclusive sample of D^* mesons which is described in section 5.7. Due to the low statistics in the diffractive sample, it is sensible to constrain the width and the position of the Gaussian to the values obtained from free fits to the corresponding ΔM distribution in the inclusive sample[1]. A total number of 54 ± 11 D^* mesons are obtained from the fit to the ΔM distribution.

8.5 Calculation of the 'Smeared' Acceptance - A_{tot}

The Monte Carlo program RAPGAP is used to calculate the 'smeared' acceptance, A_{tot}, for the majority of the phase space covered in the diffractive measurement ($x_{I\!P} < 0.1$ and $M_Y = m_p$). The AROMA program is used to model the 'standard' DIS phase space ($x_{I\!P} > 0.1$ or $M_Y > 5$ GeV). The 'smeared' acceptance obtained using RAPGAP is subjected to two corrections. The first correction, ν, is due to the effect of residual noise in the forward muon detector (see section 7.4.3). The second correction, P, is due to smearing across the border $M_Y = 1.6$ GeV and is calculated using the DIFFVM Monte Carlo (see section 7.6).

[1]Detector simulations show that the width of the Gaussian in the ΔM distribution is compatible for inclusive and diffractive D^* production.

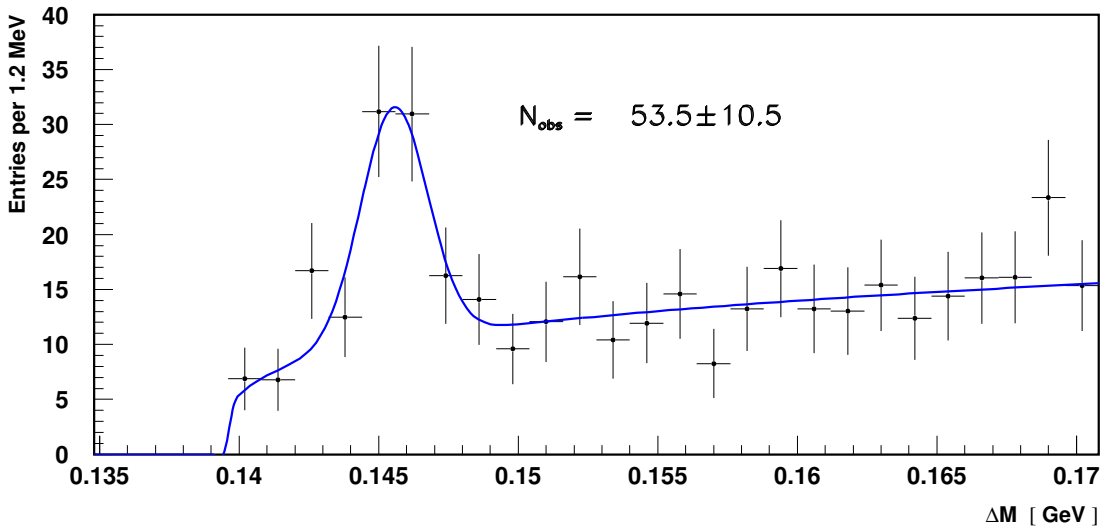

Figure 8.2: The ΔM distribution for the combined 1995-1997 data sample after the diffractive selection. The number of D^* mesons obtained from the fit (see section 5.7) , N_{obs}, is shown together with the statistical error.

The 'smeared' acceptance is shown as a function of all kinematic quantities for which the cross section is measured, using the same binning, in figures 8.3 and 8.4. The 'smeared' acceptance for the total diffractive cross section is 41%, which is similar to the value obtained from the simulation of inclusive D^* events. The 'smeared' acceptance is seen to be constant, with no large variations, for all the kinematic variables measured. The contribution of the trigger efficiency, ϵ_{trig}, (see section 6.3) to the acceptance is also shown in the figures. The trigger efficiency for the measurement of the diffractive cross section is 90%, and, as in the inclusive D^* measurement, varies most strongly as a function of y. The purity (see section 6.3), which indicates the level of smearing between the bins, is also shown in the figures. The purity is high in all bins which demonstrates that the smearing of events between bins is small.

8.6 Error Determination

The contribution to the statistical error on each cross section measurement arises from the result of the fit to the ΔM distribution. The same sources of systematic error are considered for the measurement of the diffractive cross section as were considered in the case of the inclusive cross in section 6.10. The magnitude of the systematic error for

many effects is taken to be the same for the diffractive and inclusive measurement. These include the errors due to the uncertainty in the track and in the vertex reconstruction efficiency, in the track trigger efficiency[2], in the branching fraction, in the reflections correction, in the effect of beauty production, in the photoproduction background, in the luminosity measurement, in the electron identification efficiency, and in the IET trigger efficiency. Sources of systematic error particular to diffraction or where the magnitude of the systematic error differs significantly from the inclusive measurement are listed below.

- **Hadronic Energy Scale**
  A 4% uncertainty in the energy scale of the LAr calorimeter, a 7% uncertainty in the hadronic energy scale of the SPACAL and a 3% uncertainty in the fraction of final state energy contained in the tracks affect the reconstruction of the event kinematics, in particular the $x_{I\!P}$ reconstruction, giving a systematic uncertainty at the level of 5.5% on average.

- **Electromagnetic Energy Scale and Electron Angle**
  The uncertainty in the angle of the scattered electron of 0.5 mrad, and an uncertainty in the electromagnetic energy scale of the SPACAL of 1%(3%) at 27.5(8) GeV affect the reconstruction of the event kinematics and determination of the $\gamma^* I\!P$ collision axis. This in turn affects the boost into the hadronic centre of mass frame, such that the uncertainty on the cross sections is, on average, 7.4%.

- **Input Kinematic Distributions**
  The generated β and t distributions are varied by factors chosen to result in changes that are larger than the level of precision determined by more inclusive measurements. Reweighting the generated value of β by $(1 \pm 0.3\beta)$ [4] results in average uncertainties of 4.6%. The uncertainty from varying the t distribution by $e^{\pm 2t}$ [132] is 5.2% when averaged for all bins. Since the $x_{I\!P}$ distribution in the data is not so well described by the RAPGAP program (see figure 8.3), the uncertainty in the $x_{I\!P}$ distribution is estimated by reweighting the Monte Carlo $x_{I\!P}$ distribution to match that in the data. An uncertainty of 8.1% is obtained when averaged over the differential cross sections. The uncertainty in the shape of the distributions due to different fragmentation models is estimated from the differences in results when using simulations of RAPGAP with parton showering or with the colour dipole model. Uncertainties of 6.0% are obtained when averaged over all distributions.

- **High $x_{I\!P}$ and/or Large M_Y Background**
  An error is assigned to account for smearing of events from kinematic regions outside

[2]The track multiplicity in the central tracking detector is found to be similar in the diffractive and inclusive D^* data samples.

the measured diffractive region. This is estimated by varying the number of events in the AROMA Monte Carlo model generated with $x_{I\!P} > 0.1$ and/or $M_Y > 5$ GeV by 100% and leads to an average uncertainty in the cross sections of 7%.

- **Migrations in M_Y**
  The uncertainty in the correction due to smearing of events across the boundary $M_Y < 1.6$ GeV produces a correlated error of 5.3% (see section 7.6).

- **PRT Efficiency**
  The uncertainty in the calibration of the PRT is estimated by varying the overall correction factor (see section 7.5.2) by $\pm 100\%$. This results in an uncertainty of less than 0.5% in all distributions.

- **FMD Efficiency**
  The uncertainty in the efficiency of the FMD is estimated by varying the efficiency by $\pm 4\%$ (see section 7.6). This results in an uncertainty of 4.4% averaged across all distributions.

- **Noise Correction**
  The uncertainty in the correction for events lost due to noise in the forward muon detector leads to an uncertainty of 4% in the overall normalisation of the cross section measurement.

- **The $z(D^*)$ Cut**
  The uncertainty due to the efficiency of the $z(D^*)$ cut is estimated by observing the change in the measured cross section when not applying the cut. This results in a uncertainty of 9.1% when averaged over all the differential cross sections.

- **ΔM Fitting Procedure**
  The systematic uncertainty in the determination of the number of D^* mesons from the fits to the ΔM distribution is estimated in the following way. The effect of fixing the width of the Gaussian in the fits for different distributions to that obtained from a free fit to the total sample is estimated for each bin by variation of the Gaussian width by $\pm 1\sigma$ as obtained from the inclusive D^* sample. This produces correlated errors of around 3.8%.

8.7 Cross Section Result

The cross section $\sigma(ep \to e(D^*X)Y)$ in the kinematic range $2 < Q^2 < 100$ GeV^2, $0.05 < y < 0.7$, $p_\perp(D^*) > 2$ GeV, $|\eta(D^*)| < 1.5$, $x_{I\!P} < 0.04$, $|t| < 1$ GeV^2 and $M_Y < 1.6$ GeV is

found to be

$$203 \pm 40 \pm 41 \text{ pb} \tag{8.3}$$

where the first error is statistical and the second systematic.

The diffractive D^* cross section is shown differentially in the variables Q^2, y, β, $x_{I\!P}$, $p_\perp(D^*)$, $z_{I\!P}^{obs}$, $\eta(D^*)$, $|\phi^*(D^*)|$, $p_\perp^*(D^*)$ and $z(D^*)$ in figures 8.5 and 8.6. The ΔM distributions for the individual bins are shown in figures 8.7, 8.8 and 8.9. A detailed discussion of the comparison of the cross section with the prediction of theoretical models is made in section 8.10.

8.8 Stability of the Cross Section Measurement

The cross section is found to be stable under variation of the cuts and reconstruction procedures. For example, the cross section has been measured repeatedly, in each case performing one of the following alterations; using the forward detectors only (i.e. omitting the η_{max} cut), reducing the η_{max} cut to $\eta_{max} < 2$ or $\eta_{max} < 3$, omitting the PRT(FMD) from the forward detector selection and using an alternative sub-trigger with lower statistics but only a weak $zvtx$ requirement ($zvtx - t0$). The measured cross section is found to be the same within 15% in all cases. In addition, the diffractive cross section measured in the 1996 data is in agreement with that measured in 1997. The level of statistics in the 1995 data do not allow a measurement of the cross section for this year alone.

8.9 The Ratio to the Inclusive D^* Cross Section

The ratio of the diffractive D^* cross section, with the diffractive kinematic range defined in terms of the $x_{I\!P}$, M_Y and t restrictions, to the inclusive D^* cross section measured in chapter 6 is found to be

$$4.8 \pm 1.0 \pm 1.3\% \tag{8.4}$$

where the first error is statistical and the second systematic. The ratio is shown as function of Q^2, y, $\eta(D^*)$, $p_\perp(D^*)$, $p_\perp^*(D^*)$ and $|\phi^*(D^*)|$ in figure 8.10. The discussion of the model comparison is included in the next section.

Model	Parton Distribution	cross section (pb)
Factorisable $\mathbb{P}$	$\mu^2 = Q^2 + p_\perp^2 + 4m_c^2$, $m_c = 1.5$ GeV, $\Lambda_{QCD} = 0.25$ GeV, $N_f = 5$	
	$F_2^{D(3)}$ fit 1	50
	$F_2^{D(3)}$ fit 2	435
	$F_2^{D(3)}$ fit 3	531
2 gluon ($c\bar{c}$)	$\mu^2 = Q^2 + p_\perp^2 + 4m_c^2$, $m_c = 1.5$ GeV, $\Lambda_{QCD} = 0.25$ GeV, $N_f = 5$	
	GRV LO	122
	GRV HO	80
SCI P(SCI)=0.5	$\mu^2 = \hat{s}$, $m_c = 1.5$ GeV, $\Lambda_{QCD} = 0.2$ GeV, $N_f = 4$	
	GRV LO	400

Table 8.1: The predictions for the total diffractive cross section of three models; factorisable pomeron, two gluon exchange and SCI, where μ^2 is the factorisation scale, m_c the mass of the charm quark, and Λ_{QCD} and the number of active quark flavours N_f are used in the first order expression for α_s in the hadronisation. These predictions should be compared to the measured cross section of $203 \pm 40 \pm 41$ pb.

8.10 Model Comparison

The total diffractive cross section is compared to predictions from the factorisable pomeron, perturbative two gluon exchange and soft colour interaction models in table 8.1 (see section 3.7 for a description of the models). The predictions of the factorisable pomeron model, calculated with parton distributions extracted from QCD fits to $F_2^{D(3)}$ which are dominated by gluons at the starting scale (fits 2 and 3), are seen to be a factor of $2-3$ larger than the data. There is some dependence of the factorisable pomeron model on the scales used in the calculation. For example, variation of the factorisation scale μ^2, from $Q^2 + p_\perp^2 + 4m_c^2$ to $p_\perp^2 + 4m_c^2$ produces an increase of 25% in the predicted cross section. Similarly, altering Λ_{QCD} from 0.25 GeV to 0.239 GeV and N_f from 5 to 4 reduces the cross section by 11%. Variation of the charm quark mass from $m_c = 1.5$ GeV to $m_c = 1.35$ GeV produces an increase of 20% in the cross section. However, the variation of scales in the calculation within the range of their standard values are unable to explain the discrepancy of the prediction with the measured cross section which is at the level of 3σ. The cross section lies midway between a gluon dominated and a quark dominated pomeron. As discussed in section 3.3.1, the latter parameterisation fails to describe $F_2^{D(3)}$ and other diffractive hadronic final state measurements.

The prediction for two gluon exchange, which models the system X by a $c\bar{c}$ pair at the parton level, is seen to be approximately a factor of 2 too small, although the discrepancy is less than 2σ. From table 8.1 the dependence of the cross section on the parameterisation of the gluon density within the proton (GRV LO c.f. GRV HO) is seen to be large ($\sim 50\%$),

which is a reflection of the fact that the predicted cross section varies with the square of the gluon density in the proton. The variation of the cross section with the scales in m_c, Λ_{QCD} and N_f chosen for the calculation is similar to that obtained with the factorisable pomeron model. For example, variation of the charm quark mass from $m_c = 1.5$ GeV to $m_c = 1.35$ GeV produces an increase of 10% in the cross section. Varying Λ_{QCD} from 0.25 GeV to 0.239 GeV and N_f from 5 to 4 reduces the cross section by 25%.

The SCI model is seen to suffer from a similar normalisation problem to the factorisable pomeron model. The model prediction shows a similar variation to the two other models with the values chosen for m_c, Λ_{QCD} and N_f (i.e. each produces variations of the order $10 - 20\%$). Using different input proton parton distributions, which describe inclusive proton structure function measurements, for the calculation produces variations of up to 20%. In addition to these variations, the overall normalisation can be altered by changing the free parameter P(SCI) which is the probability for soft colour interactions to occur. However, the probability of 0.5 used for the predicted cross section shown in table 8.1 is found to be appropriate for the description of $F_2^{D(3)}$ and diffractive dijet data [100]. For values of P(SCI) above 0.2 the fraction of all events produced that are diffractive is insensitive to the exact value of P(SCI) used [96]. Therefore, even after variation of the parameters used in the calculation within their standard values the prediction differs by more than 2σ from the data.

The differential cross sections are compared to the three models discussed above in figures 8.5 and 8.6. Due to the failure in the description of the overall cross section, the predictions of both the factorisable pomeron and SCI model are renormalised to the total cross section of the data. The shape of the distributions for the factorisable pomeron and SCI models are similar for most observables. Therefore, in the figures the SCI model prediction is shown only for those distributions in which the shape differs considerably from the factorisable pomeron model. These are the $x_{I\!P}$, β and $z_{I\!P}$ distributions.

The factorisable pomeron model is seen to give a good description of the shape of all the distributions. This would suggest that the shape of the gluon distribution in the model is appropriate to the description of diffractive charm production and only the normalisation is inappropriate. The $z_{I\!P}$, $x_{I\!P}$ and β distributions indicate that the mass of the system X in diffractive charm production can be large and is not confined to masses around the threshold region.

The SCI model, which has a similar shape to the resolved pomeron model for most variables (both are based on the BGF process), describes the shape of the data well, except in the $z_{I\!P}$, $x_{I\!P}$ and β distributions. The SCI model is unable to describe the high

mass region of the system X. As discussed in section 3.7.3 large masses are not modelled by the SCI generator due to the suppression of gluon radiation from the final state $c\bar{c}$ system.

The perturbative two gluon exchange model, in which the system X is modelled by a $c\bar{c}$ pair, describes the low mass region of the phase space, i.e. low $p_{\perp}^{*}$, low $x_{I\!P}$, high β and high $z_{I\!P}$. The normalisation of the model in this region appears satisfactory. The contribution of higher order fluctuations of the photon (e.g. $c\bar{c}g$) are therefore necessary to describe the high mass phase space [100]. The limited statistics do not allow any conclusions, concerning the dynamics of the exchange, to be made from the $|\phi(D^{*})|$ distribution.

The ratios of the diffractive differential D^{*} cross sections to the inclusive differential D^{*} cross sections are shown in figure 8.10. The low statistics of the measurement mean that all the distributions are consistent with being flat around the average value for the cross section ratio of 4.8%. The data are compared with the ratio of the diffractive cross section given by the factorisable pomeron model in RAPGAP[3] to the inclusive cross section given by the AROMA program.

8.11 Conclusion

The diffractive cross section $ep \to e(D^{*\pm}X)Y$ is found to account for approximately 5% of the inclusive D^{*} cross section in the kinematic range measured, and within the limited statistics is consistent with being constant for all kinematical variables. The differential cross section in $z_{I\!P}$ shows a large fraction of events at low $z_{I\!P}$ which suggests that the mass of the diffractively scattered system in diffractive charm production may be large. The predictions for the diffractive cross section given by the factorisable pomeron model, where the parton distributions extracted from fits to $F_2^{D(3)}$ are dominated by gluons at the starting scale, fail to describe the normalisation of the cross section by a factor of around 2-3 where standard fragmentation and hadronisation parameters are used. This is in contrast to the measurement of the diffractive dijet cross section which is the other hadronic final state process sensitive to the normalisation of the gluon content of the pomeron. However, the shapes of the differential distributions are very well described by the factorisable pomeron model. The large discrepancy in the normalisation between the data and the factorisable model suggests that a simultaneous description of $F_2^{D(3)}$ and charm production may be difficult within the present model.

[3]The total diffractive cross section in RAPGAP is renormalised to the total cross section measured in the data.

The SCI model as implemented in AROMA 2.2 suffers from a similar normalisation problem as the factorisable pomeron model. This is a consequence of the fact that the ratio of diffractive to inclusive D^* production in this model is predicted to be at the level of 10%. Alteration of the probability for soft colour interactions to occur could correct this. However, in order to describe simultaneously all diffractive data with one parameter would then be difficult. In the AROMA model of charm production, gluon radiation from the final state $c\bar{c}$ pair is suppressed with respect to light quark production due to the mass of the charm quark. This suppression, which is determined by QCD splitting functions, causes problems for the description of large diffractive masses by the SCI model.

The model for perturbative two gluon exchange, in which the photon fluctuates into a $c\bar{c}$ pair, describes the region of phase space where the mass of the photon fragmentation system is small. Both the normalisation and the shape of the diffractive cross section suggest that fluctuations of the photon to $c\bar{c}g$ and other higher order Fock-states are necessary to describe the full phase space for large diffractive masses. The normalisation of the calculation for the $c\bar{c}$ Fock state lies below the data, which allows higher order states to contribute within this model.

The measurement of the diffractive charm cross section has proved to be a powerful and direct test of the role of gluons in diffraction. The measured cross section suggests that the theoretical pictures presently available for diffractive charm production are in need of refinement. The statistics of the measurement remain small and the collection of more luminosity will be important in confirming the present measurement and guiding the formulation of the theoretical models of diffraction.

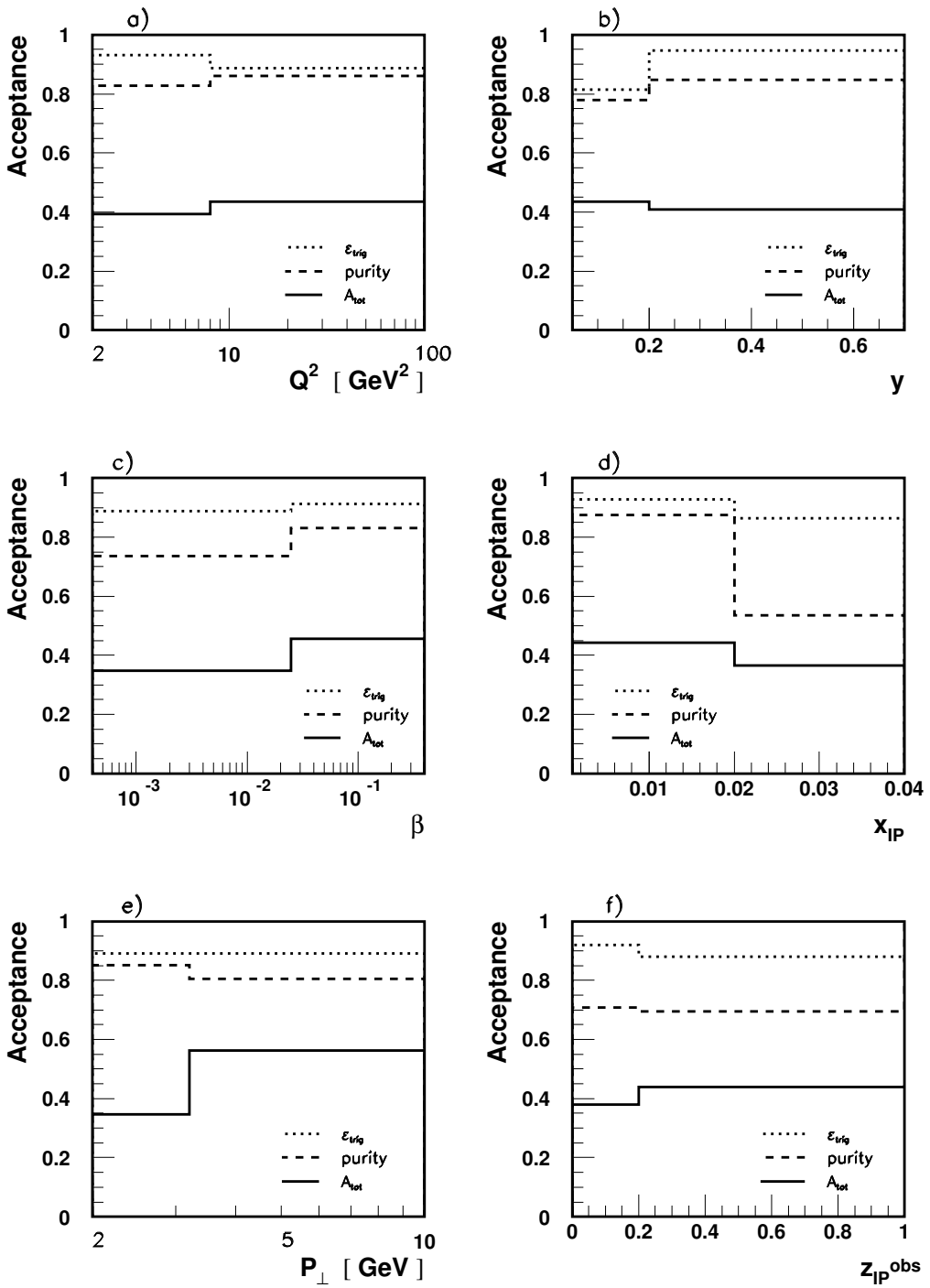

Figure 8.3: The 'smeared' acceptance for diffractive D^* production as calculated from Monte Carlo simulations as a function of (a) Q^2 (b) y (c) β (d) $x_{I\!P}$ (e) $p_\perp$ and (f) $z_{I\!P}^{obs}$. The dotted line indicates the efficiency of the track trigger, ϵ_{trig}, the dashed line the 'purity' of the sample and the full line the 'smeared' acceptance.

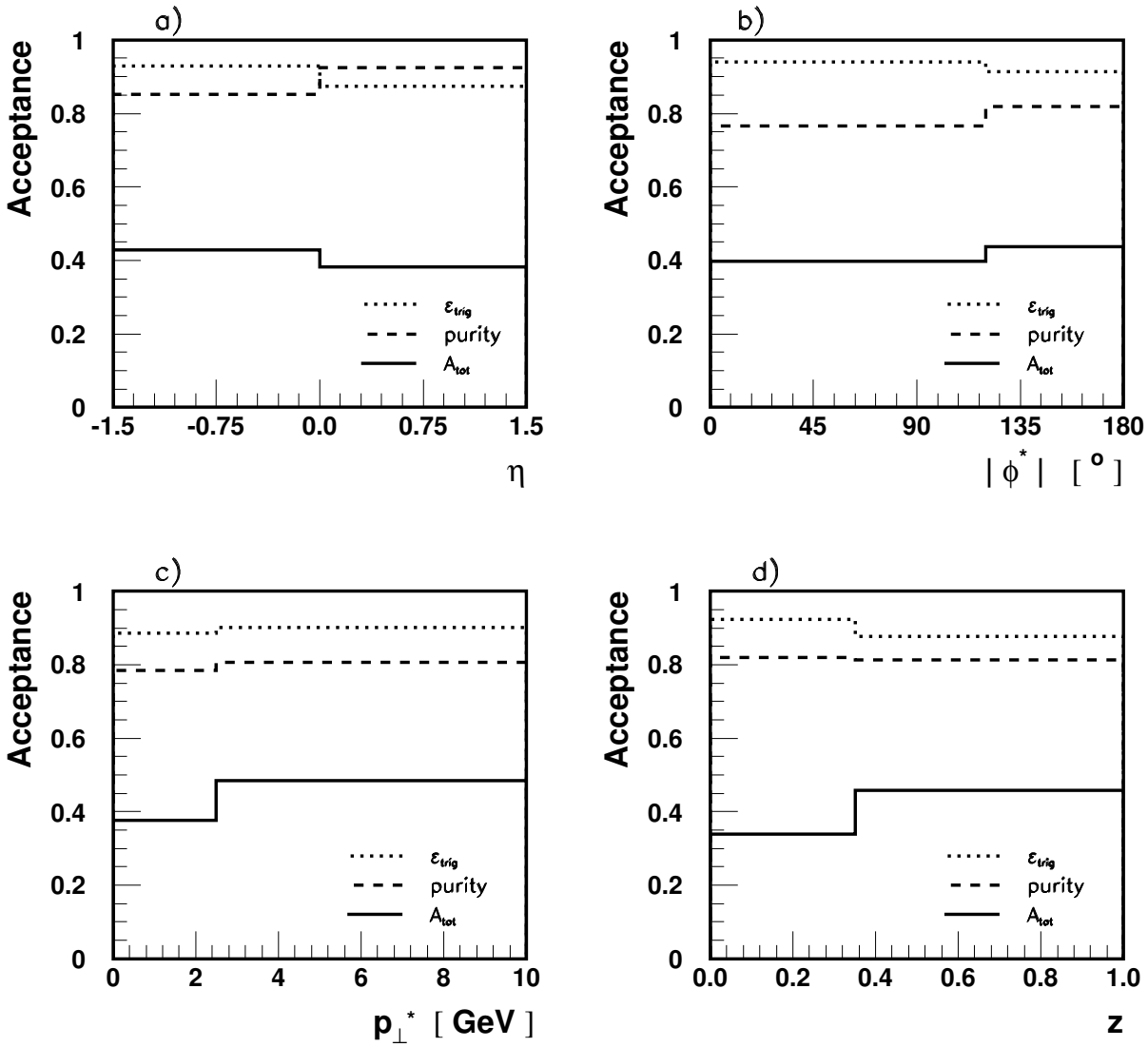

Figure 8.4: The 'smeared' acceptance for diffractive D^* production as calculated from Monte Carlo simulations as a function of (a) η (b) $|\phi^*|$ (c) $p_\perp^*$ and (d) z. The dotted line indicates the efficiency of the track trigger, ϵ_{trig}, the dashed line the 'purity' of the sample and the full line the 'smeared' acceptance.

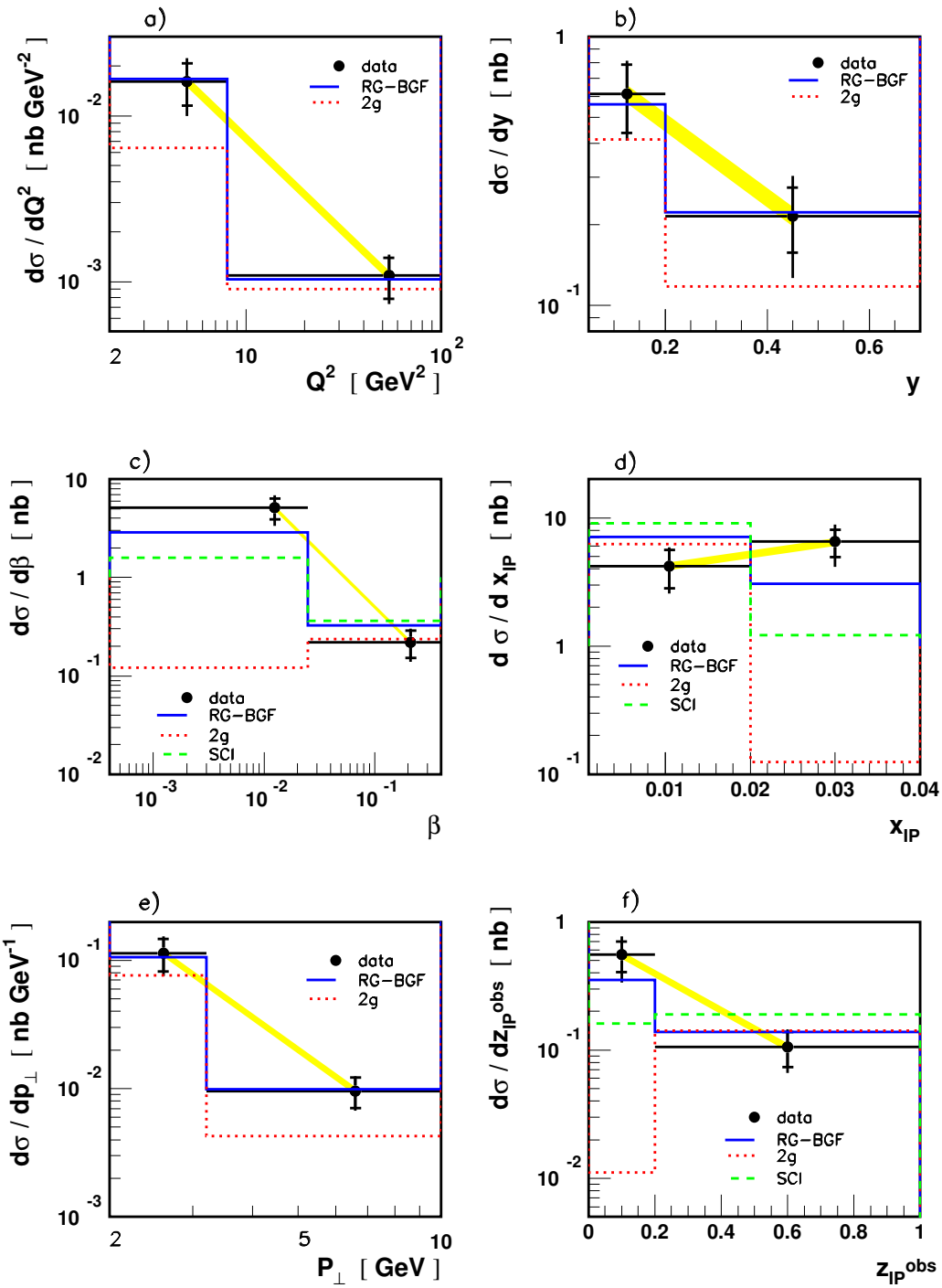

Figure 8.5: The diffractive D^* cross section plotted differentially as a function of (a) Q^2 (b) y (c) β (d) $x_{I\!P}$ (e) $p_\perp$ and (f) $z_{I\!P}^{obs}$. The shaded bands show the overall normalisation uncertainties. The data are compared with; a factorisable pomeron model (RG-BGF) [Full line], the total cross section for which is renormalised to that in the data, and a perturbative two gluon exchange model for the $c\bar{c}$ fluctuation of the photon (2g) [dotted line]. In (c), (d) and (f) the data are also compared with the model of soft colour interactions (SCI) [dashed line], the total cross section of the SCI prediction is renormalised to that measured in the data.

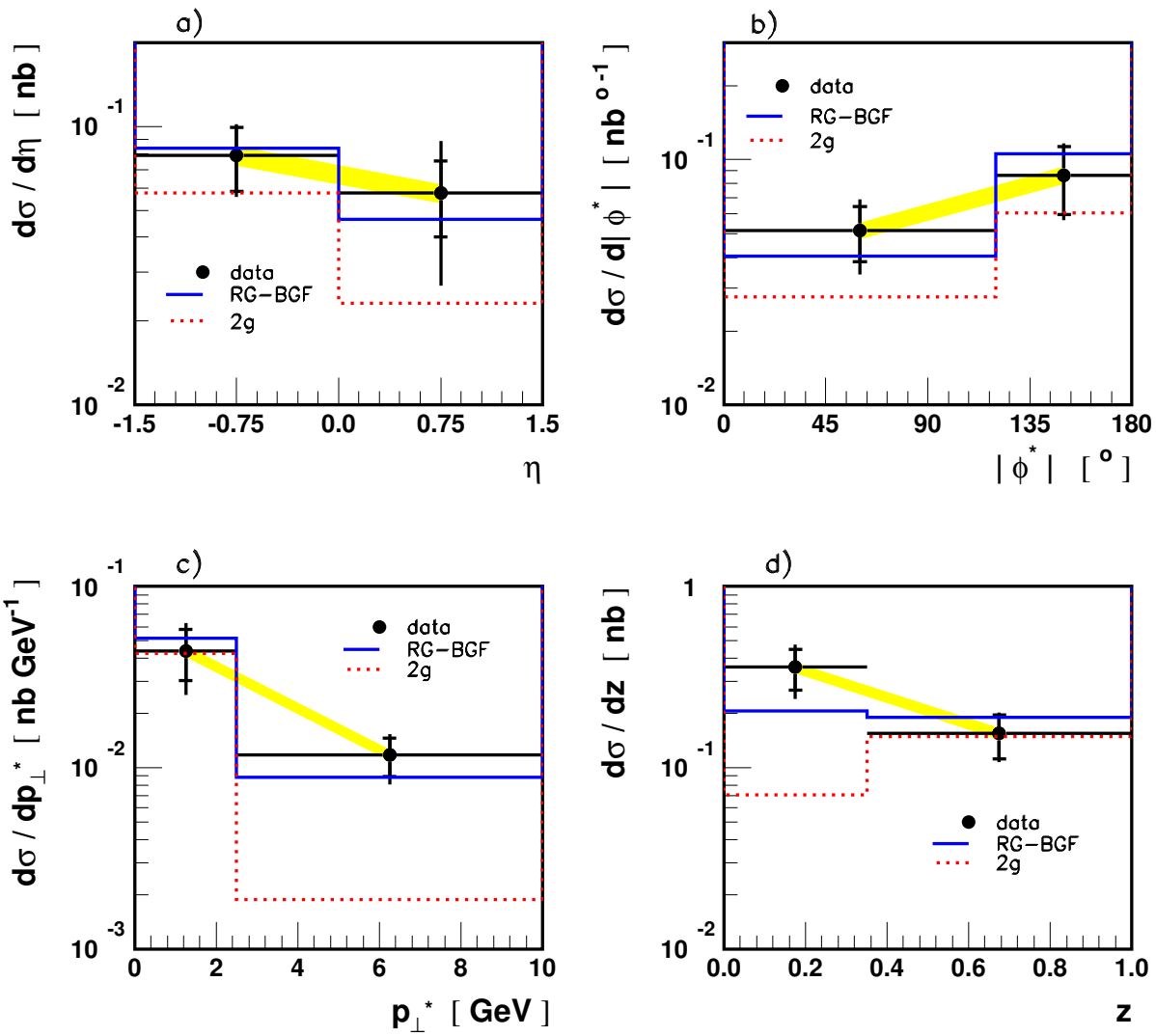

Figure 8.6: The diffractive D^* cross section plotted differentially as a function of (a) η (b) $|\phi^*|$ (c) $p_\perp^*$ and (d) z. The shaded bands show the overall normalisation uncertainties. The data are compared with; a factorisable pomeron model (RG-BGF) [Full line], the total cross section for which is normalised to that in the data, and a perturbative two gluon exchange model for the $c\bar{c}$ fluctuation of the photon (2g) [dotted line].

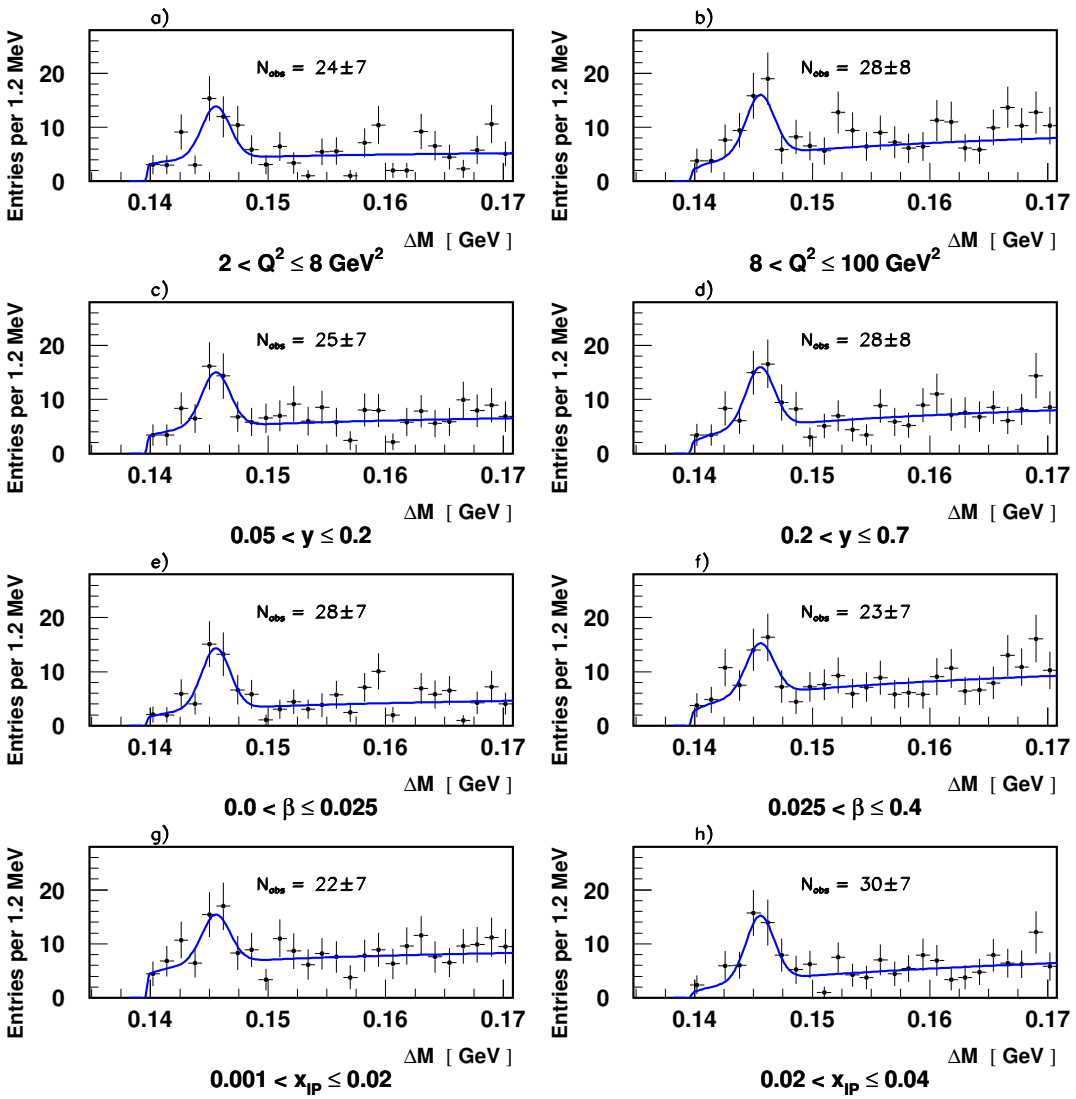

Figure 8.7: The individual ΔM distributions for the bins in (a)-(b) Q^2 (c)-(d) y (e)-(f) β (g)-(h) $x_{I\!P}$. The number of D^*, N_{obs} obtained from the fit for each bin are displayed in each distribution.

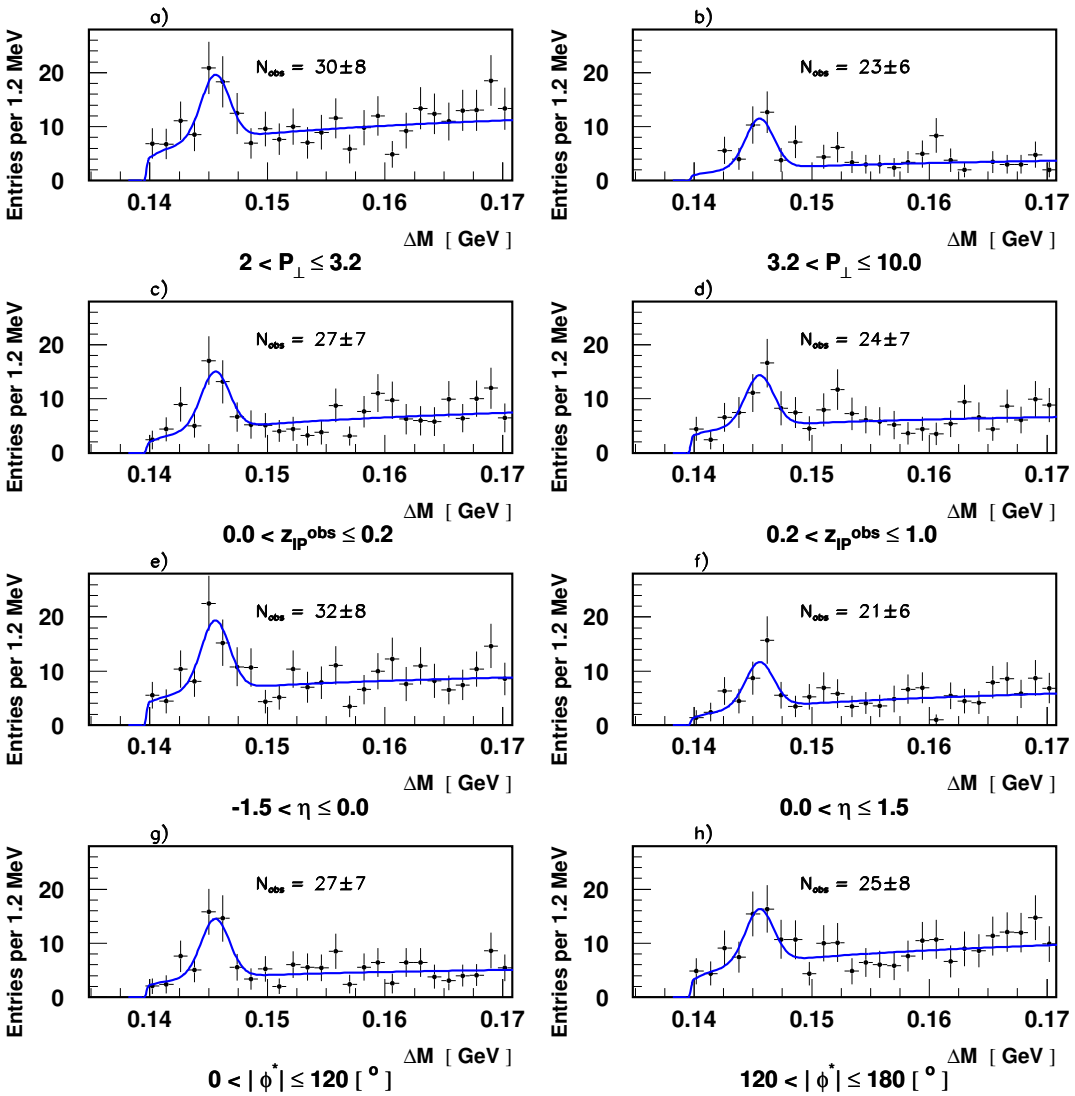

Figure 8.8: The individual ΔM distributions for the bins in (a)-(b) $p_\perp$ (c)-(d) $z_{I\!P}^{obs}$ (e)-(f) η (g)-(h) $|\phi^*|$. The number of D^*, N_{obs} obtained from the fit for each bin are shown in each distribution.

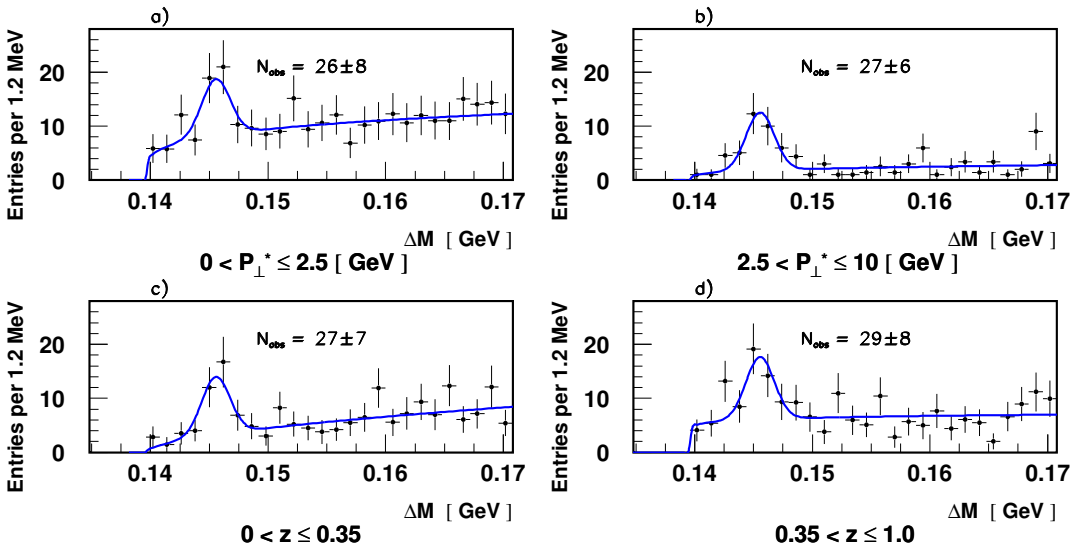

Figure 8.9: The individual ΔM distributions for the bins in (a)-(b) $p^*_\perp$ (c)-(d) z. The number of D^*, N_{obs} obtained from the fit for each bin are shown in each distribution.

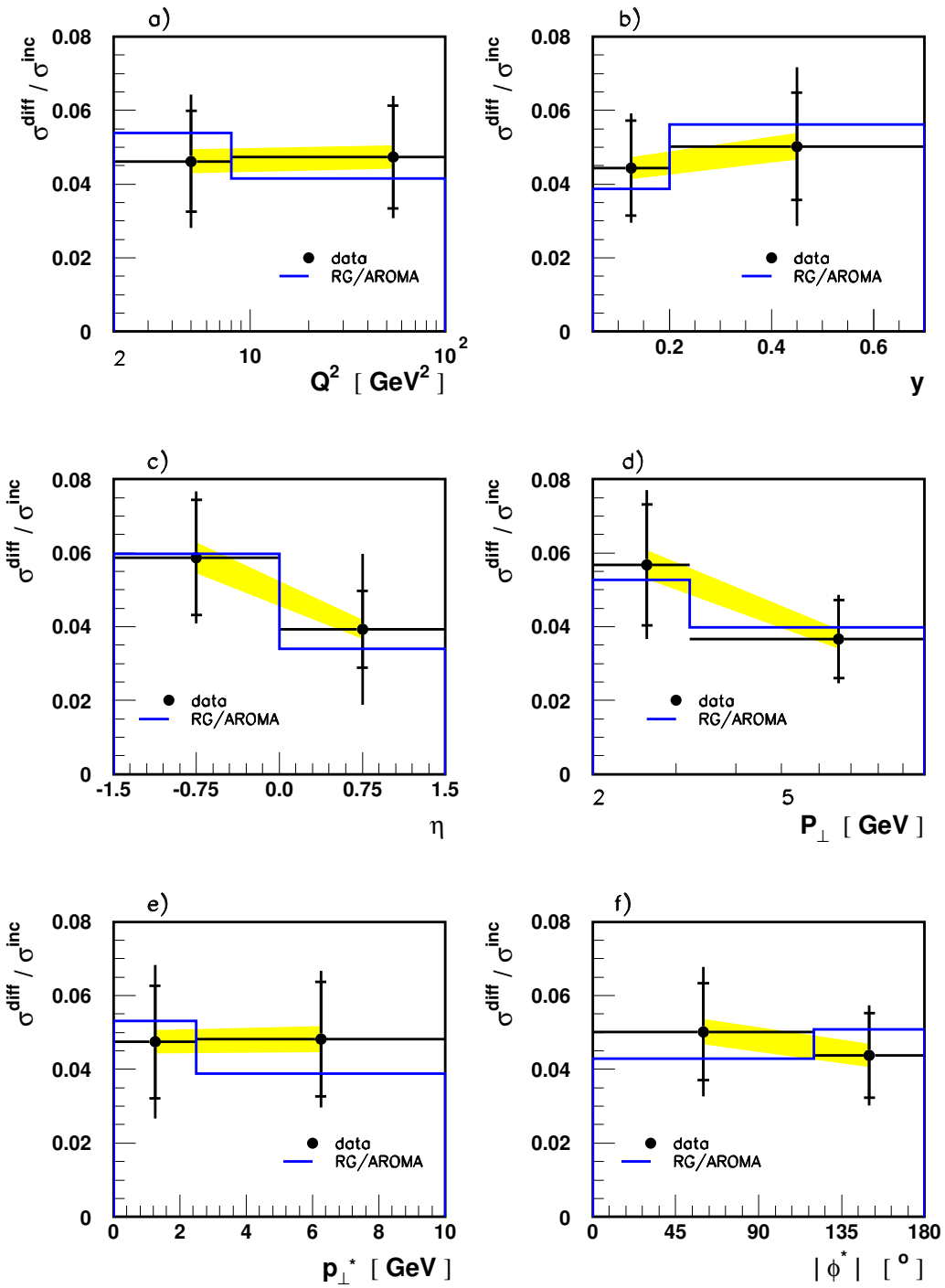

Figure 8.10: The ratio of the diffractive to the inclusive D^* cross section $\sigma^{diff}/\sigma^{inc}$ plotted as a function of (a) Q^2 (b) y (c) η (d) $p_\perp$ (e) $p_\perp^*$ and (f) $|\phi^*|$. The shaded bands show the overall normalisation uncertainty. The data are compared with the ratio of the RAPGAP factorisable pomeron model (RG), the total cross section for which is renormalised to the measured diffractive cross section, to the prediction for the inclusive D^* cross section as calculated by the AROMA Monte Carlo.

References

[1] S. Glashow, Nucl. Phys. **B8** (1961) 579.
S. Weinberg, Phys. Rev. Lett. **19** (1967) 1264.

[2] M. Breidenbach et al., Phys. Rev. Lett. **23** (1969) 935.

[3] T. Regge, Nuovo Cimento **14** (1959) 951.
T. Regge, Nuovo Cimento **18** (1960) 947.

[4] H1 Collaboration, Z. Phys. **C76** (1997) 613.

[5] J. Bürger et al., NIM. **A279** (1989) 217.

[6] S. Egli et al., NIM. **A283** (1989) 487.

[7] K. Müller et al., NIM. **A312** (1992) 457.

[8] S. Burke et al., RAL **95-037**. DESY **95-132**.

[9] H1 Collaboration, *Technical Proposal to Upgrade the Backward Scattering Region of the H1 Detector,* DESY PRC 93/02.

[10] H1 Collaboration, *Precision Measurement of the Inclusive Deep Inelastic ep Scattering Cross Section at Low* Q^2, Abstract 534, contribution to 29th International Conference on High Energy Physics, July 1998, Vancouver, Canada.

[11] H1 Calorimeter Group, NIM. **A336** (1993) 460.

[12] H1 Collaboration, NIM. **A386** (1997) 310.

[13] H1 SPACAL Group, *The H1 Lead/Scintillating-Fibre Calorimeter.* DESY **96-171**.

[14] H1 SPACAL Group, NIM. **A374** (1996) 149.

[15] K.C. Hoeger, *Proceedings of the Workshop Physics at HERA*, vol. 1, eds. W. Buchmueller, G. Ingelman, DESY (1992) 43.

[16] A.A. Glazov, *Measurement of the Proton Structure Functions $F_2(x,Q^2)$ and $F_L(x,Q^2)$ with the H1 Detector at HERA.* Ph.D. thesis, University of Berlin (1998).

[17] R. Maracek, Ph.D. thesis, Kosice (1997).

[18] M. Dirkmann, H1 Internal Note, **H1-05/96-477** (1996).

[19] C. Arndt, Diploma thesis, Hamburg (1995).

[20] C. Mueller, Diploma thesis, Heidelberg (1997).

[21] J. Tutas, *A Level 1 Trigger from the Limited Streamer Tube system.* H1 Internal Note **91-185**.
H. Itterbeck et al., *Improvement of the Trigger Timin g of the H1 Digital Muon System.* H1 Internal Note **95-427**.

[22] H. Cronstrom et al., NIM. **A340** (1994) 304.

[23] T. Ahmed et al., NIM. **A364** (1995) 456.

[24] H1 Collaboration, *Luminosity Measurement in the H1 Experiment at HERA*, contributed paper pa17-026 to ICHEP 1996, Warsaw.

[25] H. Bethe, W. Heitler, Proc. Roy. Soc. **A146** (1934) 83.

[26] H1 Collaboration, *Proposal for a Forward Proton Spectrometer for H1*, DESY **94-03**.

[27] M. Beck et al., Nucl. Instr. and Meth. **A355** (1995) 351.

[28] H1 Collaboration, Eur. Phys. J. **C6** (1999) 587.

[29] E. Elsen, *The H1 Trigger and Data Acquisition.* Proc. of the 'International Symposium on Electronic Instrumentation in Physics', Dubna, May 1991. H1 Internal Note **93-262**.
F. Sefkow et al., *Experience with the First Level Trigger of H1.* Proc. of the 1994 IEEE Nuclear Science Symposium, Norfolk, Virginia. H1 Internal Note **94-407**.

[30] J.C. Bizot et al., *Status of Simulation for a Topological Level 2 Trigger.* H1 Internal Note **92-212**.
J.C. Bizot et al., *Strategy Studies for the H1 Topological L2-Trigger (L2TT).* H1 Internal Note **97-508**.

[31] J.H. Köhne et. al., *Realization of a Second Level Neural Network Trigger for the H1 Experiment at HERA.* H1 Internal Note **97-509**.

[32] V. Blobel, *The BOS System (Fortran 77 Version)*, DESY, December 1987.

[33] S. Eichenberger et al., NIM. **A323** (1992) 532.

[34] T. Wolff et al., NIM. **A323** (1992) 537.

[35] R. Feynman, Phys. Rev. Lett. **23** (1969) 1415.
J. Bjorken, E. Paschos, Phys. Rev. **185** (1969) 1975.

[36] F. Halzen, A. Martin, *Quarks and Leptons*. John Wiley (1984).

[37] H1 Collaboration, Nucl. Phys. **B470** (1996) 3.

[38] C. Callan, D. Gross, Phys. Rev. Lett. **22** (1969) 156.

[39] R. E. Taylor, Rev. Mod. Phys. **63** (1991) 573.
H. W. Kendall, Rev. Mod. Phys. **63** (1991) 597.
J. I. Friedman, Rev. Mod. Phys. **63** (1991) 615.

[40] K. Bodek et al., Phys. Rev. **51B** (1974) 417.

[41] V. Gribov et al., Sov. J. Nucl. Phys. **15** (1972) 438.
G. Altarelli, G. Parisi, Nucl. Phys. **B126** (1977) 298.

[42] A. Schäfer, W. Reya. *Quantum Chromodynamics*. Springer-Verlag (1995).

[43] A. Martin, R. Roberts, J. Stirling, Phys. Lett. **B354** (1995) 155.

[44] E. Kuraev, L. Lipatov, V. Fadin, Sov. Phys. JETP. **44** (1976) 443.
Y. Balitsky, L. Lipatov, Sov. J. Nucl. Phys. **28** (1978) 822.

[45] V. S. Fadin and L. N. Lipatov, Phys. Lett. **B429** (1998) 127.

[46] H1 Collaboration, Phys.Lett. **B406** (1997) 256.
H1 Collaboration, Nucl. Phys. **B504** (1997) 3.

[47] H1 Collaboration, Eur. Phys. J. **C5** (1998) 625.

[48] H1 Collaboration, Nucl. Phys. **B545** (1999) 21.

[49] G. Ingleman, *Proc. of the HERA workshop*, eds W. Buchmüller and G. Ingelman, vol. 3, DESY (1992) 1366.

[50] G. Gustafson, Phys. Lett. **B175** (1986) 453.

[51] L. Lönnblad, Comp. Phys. Comm. **71** (1992) 15.

[52] T. Sjöstrand, Comp. Phys. Comm. **39** (1986) 347.

[53] H1 Collaboration, Nucl.Phys. **B538** (1999) 3.

[54] H. Jung, Phys. Comm. **86** (1995) 147.

[55] G. A. Schuler, T. Sjöstrand, Phys. Lett. **B376** (1996) 193.

[56] L. Lönnblad, Z. Phys. **C65** (1995) 285.
A. H. Mueller, Nucl. Phys. **B415** (1994) 373.
L. Lönnblad, Z. Phys. **C70** (1996) 107.

[57] H. Kharraziha, L. Lönnblad, **hep-ph/9709424** (1997).

[58] B. Anderson, G. Gustafson, J. Samuelsson, Nucl. Phys. **B467** (1996) 443.
B. Anderson, G. Gustafson, H. Kharraziha, J. Samuelsson, Z. Phys. **C71** (1996) 613.

[59] M. Ciafaloni, Nucl. Phys. **B296** (1998) 49.
S. Catani, F. Fiorani, G. Marchesini, Phys. Let. **234B** (1990) 339.
S. Catani, F. Fiorani, G. Marchesini, Nucl. Phys. **B336** (1990) 18.

[60] J. Bartels et al., Phys. Lett. **384** (1996) 300.

[61] S. Catani, M. H. Seymour, Nucl. Phys. **485** (1997) 291, Erratum-ibid. **B510** (1997) 503.

[62] S. J. Brodsky, P. Hoyer, C. Peterson, N. Sakai, Phys. Lett. **B93** (1980).
S. J. Brodsky, C. Peterson, Phys. Rev. **D23** (1981) 2745.

[63] B. W. Harris, J. Smith, R. Vogt, Nucl. Phys. **B461** (1996) 181.

[64] H1 Collaboration, Nucl.Phys. **B470** (1996) 3.

[65] CDHS Collaboration, Z. Phys. **C15** (1982) 19.
E531 Collaboration, Phys. Lett. **B206** (1988) 380.

[66] ALEPH, DELPHI, L3 and OPAL Collab., Nucl. Instrum. Meth. **A378** (1996) 101.

[67] S. Riemersma et al., Phys. Lett. **B347** (1995) 143.

[68] M. Glück et al., Z. Phys. **C53** (1992) 127.

[69] A. D. Martin et al., Phys. Rev. **D50** (1994) 6743.

[70] A. D. Martin et al., Phys. Lett. **B306** (1993) 145.

[71] M. Glück, E. Reya, M. Stratmann, Nucl. Phys. **B422** (1994) 37.

[72] J. C. Collins, W. K. Tung, Nucl. Phys. **278** (1986) 934.

[73] M. Buza et al., Eur. Phys. J. **C1** (1998) 301.

[74] E. Laenen, M. Buza, B. W. Harris, Y. Matiounine, R. Migneron, S. Riemersma, J. Smith, W.L. van Neerven, *Proc. of the Workshop on Future Physics at HERA*, vol. 1, Eds. G. Ingelmann et al., DESY (1996) 393.

[75] R. S. Thorne, R. G. Roberts, Phys. Rev. **D57** (1998) 6871.

[76] B. W. Harris, J. Smith, Phys. Rev. **D57** (1998) 2806.

[77] C. Peterson, D. Schlatter, I. Schmitt, P. M. Zerwas, Phys. Rev. **D27** (1983) 105.

[78] H. Lai et al., Phys. Rev. **D55** (1997) 1280.

[79] H1 Collaboration, Z. Phys. **C74** (1997) 221.

[80] J. Phillips, *The Deep-Inelastic Structure of Diffraction.* Ph.D. thesis, University of Manchester (1995).

[81] J. Jackson, Rev. Mod. Phys. **37** (1965) 484.

[82] D. Perkins, *Introduction to High Energy Physics.* Second Ed. AWP (1982).
I. R. Kenyon, *Elementary Particle Physics.* RKP (1987).

[83] A. Barnes et al., Phys. Rev. Lett. **37** (1976) 76.

[84] K. Goulianos, Phys. Rep. **101** (1983) 169.

[85] G. Chew, S. Frautschi, S. Mandelstam, Phys. Rev. **126** (1962) 1202.

[86] A. Donnachie, P. Landshoff, Nucl. Phys. **B231** (1983) 189.

[87] CHLM Collaboration, Nucl. Phys. **B108** (1976) 1.

[88] T. Chapin et al., Phys. Rev. **D31** (1985) 17.

[89] UA4 Collaboration, Phys. Lett. **B186** (1987) 227.

[90] R. Cool et al., Phys. Rev. **47** (1981) 701.

[91] ZEUS Collaboration, Zeit. Phys. **C68** (1995) 569.
H1 Collaboration, Phys. Lett. **B348** (1995) 681.

[92] A. Donnachie, P. V. Landshoff, Phys. Lett. **B191** (1987) 309.

[93] L. Alvero, J.C. Collins, J. Terron, J.J. Whitmore, Phys. Rev. **D59** (1999).

[94] J. Bartels, J. Ellis, H. Kowalski, M. Wüsthoff, Eur. Phys. J. **C7** (1999) 443.

[95] W. Buchmüller, T. Gehrmann, A. Hebecker, Nucl. Phys. **B537** (1999) 477.

[96] A. Edin, G. Ingelman, J. Rathsman, Phys. Lett. **366** (1996) 371.

[97] H1 Collaboration, Eur. Phys. J. **C1** (1998) 495.

[98] H1 Collaboration, Phys. Lett. **B428** (1998) 206.

[99] H1 Collaboration, Eur. Phys. J. **C5** (1998) 439.

[100] H1 Collaboration, Eur. Phys. J. **C6** (1999) 421.

[101] ZEUS Collaboration, Eur. Phys. J. **C5** (1998) 41.

[102] J. Bartels, H. Lotter, M. Wüsthoff, Phys. Lett. **379** (1996) 239.
J. Bartels, C. Ewerz, H. Lotter, M. Wüsthoff, Phys. Lett. **386** (1996) 389.

[103] L. Alvero, J.C. Collins, J.J. Whitmore, **hep-ph/9806340**.

[104] E. M. Levin, A. D. Martin, M. G. Ryskin, T. Tenbner, Z. Phys. **C74** (1997) 671.

[105] J. Bjorken, J. Kogut, Phys. Rev. **D8** (1973) 1341.
G. Bertsch, S. Brodsky, A. Goldhaber, J. Gunion, Phys. Rev. Lett. **47** (1981) 297.

[106] A. Meyer, *Measurement of the Structure Function $F_2(x, Q^2)$ of the Proton at Low Q^2 with the H1 Detector at HERA Using the New Detector Components Spacal and BDC.* Ph.D. thesis, University of Hamburg (1997).

[107] D. Müller, *A Measurement of the Gluon Density in the Proton Based on Charm Production at HERA.* Ph.D. thesis, University of Zürich (1998).

[108] C. Pfeiffer, M. Dirkmann, Internal Note **H1-01/97-512** (1997).

[109] *GEANT Detector Description and Simulation Tool.* CERN Program Library Long Writeup W5013, 1993.

[110] G. J. Feldman et al., Phys Rev. Lett. **38** (1977) 1313.

[111] C. Caso *et al.* (Particle Data Group), Eur. Phys J. **C3** (1998) 1.

[112] G. Ingleman, J. Rathsman, G. A. Schuler, Comput. Phys. Commun. **101** (1997) 135.

[113] G. A. Schuler, Nucl. Phys. **B299** (1988) 21.

[114] F. James. *MINUIT: Function Minimisation and Error Analysis.* CERN Program Library Long Writeup **D506** (1994).

[115] J. Meyer (Ed.), *Guide to the Simulation Program H1SIM*, H1 Internal Document (1991).

[116] C. Royon, Ph.D. thesis, Universitié de Paris-Sud (1994).

[117] H1 Collaboration, Nucl. Phys. **B472** (1996) 32.

[118] H. Niggli, *Direct Gluon Density Determination in Tagged Charm-Photoproduction at HERA.* Ph.D. thesis, ETH Zürich (1998).

[119] A. Schwank, Diploma thesis, University of Hamburg (1998).

[120] W. Erdmann. Ph.D. thesis, ETH Zürich (1996).

[121] D. Milstead. Private communication.

[122] A. Küpper, *Minutes of H1 Heavy Flavour Working Group Meeting.* July 16^{th} (1998).

[123] S. Hengstmann, Private communication.

[124] M. Glück, E. Reya, A. Vogt, Z. Phys. **C67** (1995) 433.

[125] M. Glück, E. Reya, A. Vogt, Z. Phys. **C53** (1992) 651.

[126] B. List, Diploma thesis, Techn. Univ. Berlin, unpublished (1993).

[127] K. Goulianos, Phys. Rep. **101** (1983) 169.

[128] D. Amati, A. Stanghellini, S. Fubini, Nuovo Cimento **26** (1962) 896.

[129] P. Newman, *A study of the Dynamics of Diffractive Photoproduction at HERA*, Ph.D. thesis, University of Birmingham (1996).

[130] ZEUS Collaboration, Phys. Lett. **B315** (1993) 481.

[131] H1 Collaboration, Nucl. Phys. **B429** (1994) 377.

[132] ZEUS Collaboration, Eur. Phys. J. **C1** (1998) 81.
ZEUS Collaboration, Eur. Phys. J. **C2** (1998) 237.

[133] Andrew Mehta, Private Communication.

[134] H1 Collaboration, Z. Phys. **C75** (1997) 607.

[135] H1 Collaboration, Phys. Lett. **B338** (1994) 507.

[136] C. M. Cormack, *Measurements of Hadron Production in Deep Inelastic Diffractive Scattering.* Ph.D. thesis, University of Liverpool (1997).

Acknowledgements

There are many people who I would like to acknowledge for their patient help for the duration of my Ph.D. studies. Firstly, my supervisor Ian Kenyon for his continued support and advice. The other Birmingham academics involved in H1, John Dowell and John Garvey who have also been on hand to give helpful advice and guidance. I would also particularly like to thank Paul Newman for his encouragement during both the high and low points of my Ph.D. studies. It is from Paul that I have learned most about the topic of diffraction and how to perform an analysis. I would also like to thank Paul Sutton and Lee West for their help.

I would like to thank Dave Milstead for welcoming me to building 10b. Dave provided me with invaluable training and it was a privilege to share an office with such an experienced physicist. I would like to thank the rest of the inhabitants of 10b who have helped me to produce the work in this thesis. In particular I would like to thank Andrew Mehta for his patience and willingness to answer questions. Working with Andrew allowed me to learn rapidly the good techniques necessary in experimental physics. Thanks also to Julian Phillips for introducing me to the topic of diffraction. I am also grateful to Ben Waugh and Chris Hilton for their knowledge of heavy flavour physics. I would also like to thank John Dainton for his support.

Throughout the course of my Ph.D. I have been fortunate to interact with the students and academics at the University of Zürich from whom I have learnt the techniques and procedures for performing a heavy flavour analysis. In particular I would like to thank Stefan Hengstmann for his efforts and vital help during my Ph.D., and for his enthusiasm which kept me going during the most stressful stages of the analysis. I would also like to thank Felix Sefkow, Martin zur Nedden and David Müller.

There are very many people whose friendship has been an inspiration throughout the past three years. To Robert Waugh for being the best man at my wedding, although I would hate to have seen the worst. To the players past, present and future of the Bleicherstrasse Theatrical Workshop - you were all simply wonderful: Dave Waters, Vicki Hudgson, Stuart Cocks, Eram Rizvi, Andrew Mehta, Rob Waugh, Paul Bate, Monika Biddulph, Sabine Lammers and Nick Malden. To Dave Lamb for putting up sharing an office with me whilst I was writing my thesis. I wish Dave and Carrie Goodwin good luck in their future studies. Finally, for immeasurable support and motivation to complete my Ph.D., profound thanks to my wife, Asia, and my son, William, to whom this thesis is dedicated.